# Understanding The Effect of Ionising Radiation on The Properties of Vitrified Nuclear Waste

A thesis submitted to the University of Manchester for the degree of Doctor of Philosophy in the Faculty of Science and Engineering

2023

**Natasha A. Brown**

School of Engineering

Department of Mechanical, Aerospace, and Civil Engineering

# Contents

Word Count - 50485

# Abbreviations

| | |
|---|---|
| Ateliers de Vitrification de Marcoule | AVM |
| Back Scattered Electron | BSE |
| Boron Oxygen Hole Center | BOHC |
| Dalton Cumbrian Facility | DCF |
| Diamond Light Source | DLS |
| Electron Paramagnetic Resonance | EPR |
| Electron Spin Resonance | ESR |
| Electron Trapped center | ET center |
| Hole Center | HC |
| Extended X-ray Absorption Fine Structure | EXAFS |
| Fast Half-life | $t_{\text{half-life 1}}$ |
| GEneral Materials diffractometer | GEM |
| Geological Disposal Facility | GDF |
| Glass Transition Temperature | $T_g$ |
| High Level Waste | HLW |
| Highly Active Liquor | HAL |
| Highly Active Residue Vitrification Experimental Studies | HARVEST |
| Hole Center$_1$ | $HC_1$ |
| Inductively Coupled Plasma Optical Emission Spectroscopy | ICP-OES |
| Intermediate Level Waste | ILW |
| International Atomic Energy Agency | IAEA |
| International Simple Glass | ISG |
| Low Level Waste | LLW |
| Magic Angle Spinning | MAS |

| | |
|---|---|
| Magic Angle Spinning Nuclear Magnetic Resonance | MAS-NMR |
| Materials Characterisation Center Test 1, Standard Test Method for Static Leaching of Monolithic Waste Forms for Disposal of Radioactive Waste | MCC-1 |
| Mixture Windscale | MW |
| Molecular Dynamics | MD |
| Monte Carlo | MC |
| Multi Quantum Magic Angle Spinning | MQMAS |
| Non Bridging Oxygen | NBO |
| Non Bridging Oxygen Hole Center | NBOHC |
| Normalised Boron Content | [B] |
| Normalised Silicon Content | [Si] |
| Normalised Sodium Content | [Na] |
| Nuclear Magnetic Resonance | NMR |
| National Nuclear Laboratories | NNL |
| Pair Distribution Function | PDF |
| PerOxy Radical | POR |
| Plutonium Uranium Reduction EXtraction | PUREX |
| Post Operational Clean Out | POCO |
| Product Consistency Test ASTM Standard Test Methods for Determining Chemical Durability of Nuclear, Hazardous, and Mixed Waste Glasses and Multiphase Glass Ceramics | PCT |
| Radiofrequency Field | rF |
| Scanning Electron Microscopy | SEM |
| Scanning Electron Microscopy - Energy Dispersive Spectroscopy | SEM-EDS |
| Slow Half-life | $t_{\text{half-life 2}}$ |

| | |
|---|---|
| THermal Oxide Reprocessing Plant | THORP |
| Trapped electron | ET |
| UV-Visible-Near IR | UV-Vis-NIR |
| Waste Vitrification Plant | WVP |
| X-Ray Diffraction | XRD |
| X-ray Fluorescence | XRF |

# List of Tables

# List of Figures

## Hypothesis

In Geological Disposal Facility conditions contact with steel, and radiation-induced changes in glass structure, will increase glass leaching rate in the early stages of container breach.

## Abstract

The structure of Mixture Windscale and CaZn UK base glass and International Simple Glass has been investigated for the first time through the direct simultaneous fitting of X-ray and neutron Pair Distribution Functions, with the aid of Magic Angle Spinning -Nuclear Magnetic Resonance data collected by the University of Liverpool. The structural data from the direct fitting of ISG has been verified against existing data collected through indirect fitting of PDFs with atomistic models. The direct fitting of these PDFs has revealed vital structural information regarding the bonding present in the glass network that will be of use in future attempts at creating a comprehensive atomistic model of UK base glass, and improving existing models of ISG.

The PDF structural data collected has been used to improve the analysis of both structural and leaching data collected from gamma irradiated glass. This has revealed strong evidence for regions of potential aluminium based crystalline phase separation, believed to be too small to be detected using standard laboratory XRD instrumentation, and has demonstrated that electronic defect formation and structural changes have vastly different gamma radiation dose thresholds. As part of this, a method of partially characterising electronic defects though selective recombination with UV light, while preserving major structural changes, has been demonstrated.

The proposed structural changes have been used to rationalise changes in the glass alteration behaviour observed with increased gamma radiation dose and contact with a steel based crevice environment. This has provided strong evidence that the overall impact

of gamma radiation on glass alteration is the result of the balance of changes that occur due to the presence of different network components and modifiers. Strong evidence has been found that indicates the presence of a steel crevice environment will have an undesirable effect on the early stages of UK base glass alteration. It has been proposed that the undesirable effect is largely the result of the sorption of soluble silicates by steel and the potential for this to be enhanced by an electrochemical reaction between certain glass components and steel has been identified. As a result of this, both steel crevice contact and radiation effects on glass alteration are strongly dependant on glass formulation and require further investigation with simulant glasses.

## Declaration

No portion of the work referred to in the thesis has been submitted in support of an application for another degree or qualification of this or any other university or other institute of learning;

## Copyright Statement

i. The author of this thesis (including any appendices and/or schedules to this thesis) owns certain copyright or related rights in it (the "Copyright") and they have given the University of Manchester certain rights to use such Copyright, including for administrative purposes.

ii. Copies of this thesis, either in full or in extracts and whether in hard or electronic copy, may be made only in accordance with the Copyright, Designs and Patents Act 1988 (as amended) and regulations issued under it or, where appropriate, in accordance with licensing agreements which the University has from time to time. This page must form part of any such copies made.

iii. The ownership of certain Copyright, patents, designs, trademarks and other intellectual property (the "Intellectual Property") and any reproductions of copyright works in the thesis, for example graphs and tables ("Reproductions"), which may be described in this thesis, may not be owned by the author and may be owned by third parties. Such Intellectual Property and Reproductions cannot and must not be made available for use without the prior written permission of the owner(s) of the relevant Intellectual Property and/or Reproductions.

iv. Further information on the conditions under which disclosure, publication and commercialisation of this thesis, the Copyright and any Intellectual Property and/or Reproductions described in it may take place is available in the

University IP Policy (see

http://documents.manchester.ac.uk/DocuInfo.aspx?DocID=24420 ), in any

relevant Thesis restriction declarations deposited in the University Library, the

University Library's regulations (see

http://www.library.manchester.ac.uk/about/regulations/ ) and in the

University's policy on Presentation of Theses.

# Acknowledgements

The author would like to thank the following :

My supervisors Dr Laura Leay, for giving me the opportunity to conduct this research by providing the foundations of this project, and Prof Francis Livens for stepping in and helping me finish the project.

My industrial supervisor Dr Mike Harrison (National Nuclear Laboratories (NNL)) for providing continued help in understanding the industrial and regulatory aspects of this work

Dr Alex Hannon, of ISIS Neutron and Muon source and Dr Gavin Mountjoy, for teaching me everything I know about neutron scattering and the analysis of glass pair distribution functions.

Prof Paul Bingham and Dr Maulik Patel for their help in understanding the specifics of experimental technique and data analysis used with amorphous materials.

Everyone at the Dalton Cumbrian Faculty especially Morven Willson and Dr Ruth Edge.

# The Author

The Author graduated from Keele University in 2018 with an MChem degree in Chemistry awarded after completing a project based on the structure of synthetic and natural zeolites. From 2019 – 2022 she was sponsored by NNL to conduct the research presented in this thesis. This research was initially supervised by Dr Laura Leay before supervision was transferred to Prof Francis Livens in 2021.

# Introduction

This thesis is divided into six main sections; the introductory literature review section that is designed to provide context and provide a critical review of the literature and analytical techniques surrounding this body of work, then three papers are presented in chronological order each written with the aim of building on the findings of the previous paper, a conclusion providing context for future work, and an analytical theory and method section describing the underlying theory behind the methods discussed in previous chapters.

The first paper was written by the author while working in partnership with researchers from ISIS Neutron and Muon Source, University of Kent, University of Liverpool, and Sheffield Hallam University. This paper is based on Pair Distribution Function (PDF) data collected and analysed by the author and has been supplemented by (Magic Angle Spinning Nuclear Magnetic Resonance) MAS-NMR work carried out by researchers from University of Liverpool. The second and third papers feature research carried out solely by the author. The second paper investigates the impact that high dose gamma radiation has on the amorphous glass structures studied in the first paper. This body of work was carried out with the aim of establishing a baseline for both the electronic defects formed as result of radiation exposure, and the impact that gamma radiation has on the structure of UK base glass. The third and final paper brings together the first two papers to explore the impact that gamma radiation damage has on glass alteration through the use of a standard leaching environment and a steel crevice environment. The steel crevice environment was explored, as the negative effects of proposed gamma radiation induced changes and proposed glass steel interactions have the potential to amplify each other in the early stages of glass alteration. The conclusion summarises the findings of the three papers and provides context for future work exploring these interactions in simulant base glasses.

# 1. Literature review

## 1.1. Context

Globally borosilicate glass is amongst the most commonly used material for high level radioactive waste immobilisation through vitrification. The final disposal location of this glass is typically a Geological Disposal Facility (GDF) where the glass, functioning as part of a multi barrier system, must be able to contain the waste until the radioactivity has naturally decayed to safe levels.

To ensure a stable homogenous glass is produced various borosilicate glass compositions, known as base glasses, used globally are tailored to the waste stream being immobilised. In the UK two base glass formulations are used, Mixture Windscale (MW), and CaZn (mol% composition shown table 1) (1,2). International Simple Glass (ISG) (also shown in table 1) is a six component simulant glass based on a simplified version of the French R7T7 glass and was developed to allow for comparison between leaching studies involving differing base glass formulations (3). As a simulant glass ISG is not designed to be radiation tolerant. MW has been in use since the 1980s with the only significant change in glass formulation being the use of half lithia MW frit with the remaining lithium required to bring the glass to specification added as part of the vitrification process (2). CaZn was developed to address issues with molybdenum solubility in Post Operational Clean Out (POCO) and is based on the MW formulation, with the addition of additional aluminium, calcium , and zinc being the only significant deviations from the original MW formulation (1).

*Table 1 Oxide mol % formulations of MW, CaZn and ISG glasses*

| Mol% | $SiO_2$ | $B_2O_3$ | $Na_2O$ | $Li_2O$ | $Al_2O_3$ | CaO | ZnO | ZrO |
|---|---|---|---|---|---|---|---|---|
| MW | 60 | 19.0 | 10.5 | 10.5 | | | | |
| CaZn | 48.7 | 20.6 | 8.5 | 8.6 | 2.5 | 6.6 | 4.5 | |
| ISG | 60.2 | 16.0 | 12.6 | | 3.8 | 5.7 | | 1.7 |

Despite many years of widespread use in the UK very little is known about the structure of MW and CaZn glasses with no full atomistic models available. Current investigations are limited by the lack of structural data needed to produce a start point for atomistic modeling. The lack of atomistic model start point prevents the impact of radiation on the glass structure over the full lifetime of the radioactivity from being fully understood. It is vital the radiation induced changes in the glass are better comprehended to ensure the future safety of the glass and immobilised waste in a GDF.

### 1.1.1. Vitrification and Waste Classification

High level radioactive waste is expected to show elevated levels of radiation for a minimum of $10^8$ years and generate significant heat in its early life time (4). Few materials are able to withstand the high levels of radioactivity and temperature generated in the early stages of waste immobilisation without undergoing significant structural changes or degradation. Borosilicate glass, however, has the potential to tolerate both radiation damage and exposure to the storage environment, in order to contain radionuclides for longer than the predicted radioactive lifetime of the immobilised waste.

Radioactive waste is anything in a gaseous, liquid or solid form that is no longer considered useful and contains or is contaminated with radionuclides at concentrations or activities greater than established by regulatory bodies. In the UK this waste is divided into three categories depending on activity level, Low Level Waste (LLW), Intermediate Level Waste (ILW), and High Level Waste (HLW) with any waste having a half-life >31 years being classed as long lived (5). HLW is defined as waste with an activity greater than 4 GBq per tonne of alpha activity, or 12 GBq per tonne of beta/gamma activity that generates a significant amount of heat due to its radioactivity (5). Vitrification followed by a minimum of 50 years storage in an above ground facility before disposal in a GDF is the standard method

proposed for management of HLW in England and Wales (4). There will be no requirement to dispose of HLW in Scotland.

Historically the majority of HLW in the UK came from spent fuel reprocessed through the Plutonium Uranium Reduction EXtraction (PUREX) process (2). This process gave a nitric acid based waste stream that contained fission products, residual actinides, corrosion products, process additives, fuel additives, impurities and residual cladding material in varying quantities (2). Any base glass used for vitrification must be able to tolerate variations in waste composition and give a homogenous stable glass.

Vitrification using borosilicate glass was first proposed in the 1950s (2,6). In the UK, glass systems based on alkali silicate and alkali phosphate were initially explored, with the phosphate systems being abandoned as these were found to be corrosive to materials used in melters and the generic alkali silicate having too high a melting point to be of practical use (6). A sodium silicate glass was originally chosen as this had an acceptable melting point and waste loading (6). This was replaced with a more stable sodium borosilicate formulation that was then refined as part of the early Highly Active Residue Vitrification Experimental Studies (HARVEST) process to give the MW glass formulation (6). The batch HARVEST process was superseded by a continuous Ateliers de Vitrification de Marcoule (AVM) based process shown in figure 1 (1).

In the UK spent fuel was reprocessed on an industrial scale where the Highly Active Liquor (HAL) originating from the UK's two PUREX facilities, namely Magnox, for reprocessing of natural uranium based metallic fuel from first generation Magnox reactors, and THermal Oxide Reprocessing Plant (THORP) for enriched oxide fuels was vitrified at Sellafield in the Waste Vitrification Plant (WVP) (2). The two different types of HAL were blended according to vitrification plant feed requirements and transferred to a vitrification feed tank (7). A sugar solution is added to the vitrification feed tank to act as a reducing agent, then the

material is fed into a heated rotary calciner to produce a dry granular material (7). The calcine is gravity fed along with a measured quantity of glass frit into an inductively heated crucible and heated to ~1050°C (2). In the crucible the calcine reacts with the frit to produce a stable glass. The glass is gravity fed into a steel container and the lid is welded shut before the container is tested for surface contamination and transferred to the vitrified product store for short term interim storage before eventually being moved to a future GDF (2).

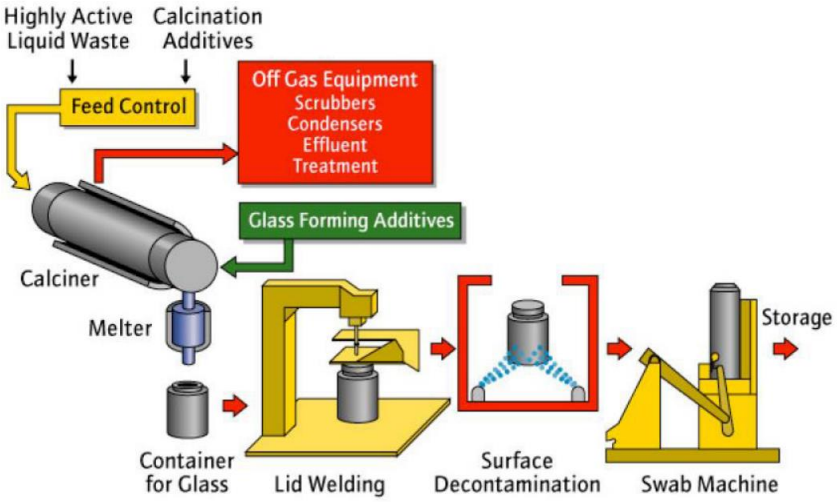


*Figure 1 Diagram showing AVM based process used in the production of UK HLW glass (taken from (1))*

As the waste package and multiple engineered barriers fail over many millennia, the glass will ultimately be exposed to ground water. The glass structure must be studied in order to model the release of radionuclides that takes place when the glass is exposed to ground water. This ensures the radioactive elements present are confined below surface level until the radioactivity has decayed to safe levels.

## 1.2. Glass Structure

### 1.2.1. Definitions

Glass is defined by Shelby as “as an amorphous solid completely lacking in long range, periodic atomic structure, and exhibiting a region of glass transformation behaviour” (8). A

key part of this definition is that, while this work has focused only on borosilicate glass, glass is not necessarily silicate based and other formulations, such as the mainly sulfur based chalcogenide glasses, exist.

Expanding on this definition, the materials making up a glass can be defined as network formers, network modifiers, and intermediates (8). Network formers such as $SiO_2$ and $GeS_2$ will form a stable binary glass without the addition of any other materials (8). Network modifiers will modify the glass network by changing the charge balance without being covalently bonded to network formers in the structure (8). Intermediates can act as either a network former or network modifier by becoming part of the glass network but cannot form a stable glass without the presence of network modifiers or glass formers (8). The line between intermediate and network former is blurry, leading to some debate as to if certain oxides can be classed as a network former or intermediate (9). The network formers, intermediates and modifiers present in UK base glass and ISG are shown below in figure 2.

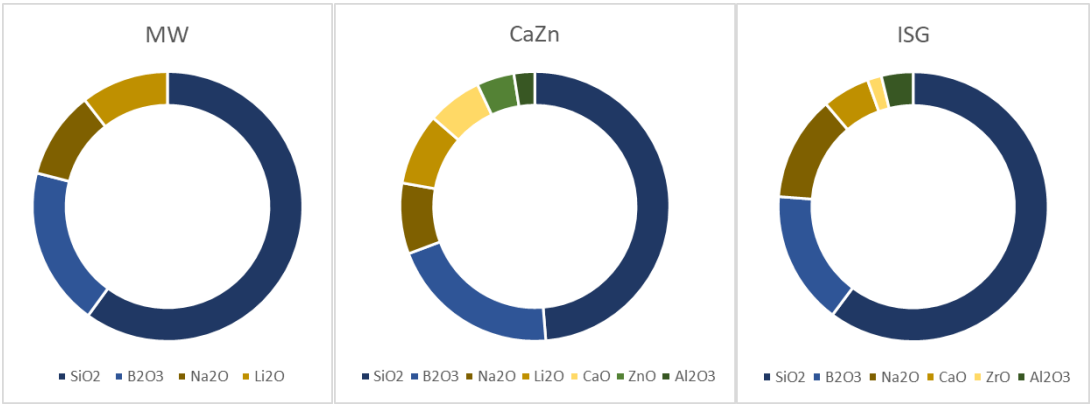


*Figure 2 Diagram showing oxide mol% ratios of network formers (blue), modifiers (yellow), and intermediates (green) present in MW, CaZn, and ISG.*

The structural model of silicate glass as an amorphous material was first proposed by Zachariasen in the random network theory (10). This theory states that glass is fully lacking in periodicity and forms a continuous network (10). This provides a broad definition of a glass but is only truly correct for very simple binary glasses containing only glass Formers; more complex glasses can display varying degrees of short range order. This leads to the

Modified Network Theory, sometimes called Greaves Modified Network theory, that better allows for the inclusion of network modifiers by proposing regions of microsegregation containing network modifiers (11). This is further expanded on by Compensated Continuous Random Network theory where charged network components, such as aluminium or four coordinate boron are directly compensated for by charged network modifiers (as shown in figure 3), resulting in a reduction in the amount of negatively charged oxygen single bonded to one silicon atom, known as a Non Bridging Oxygen (NBO) present (11).

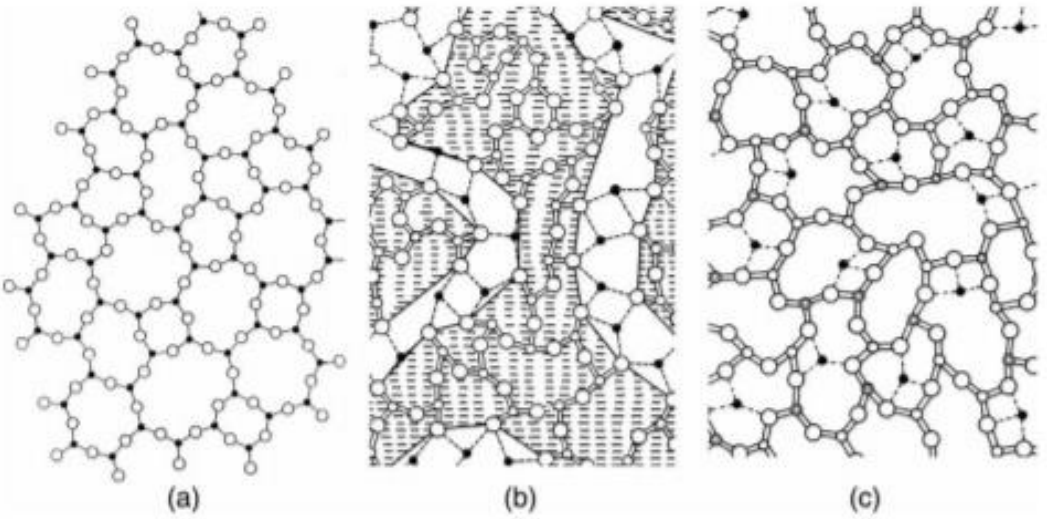


*Figure 3 2D representations of the three main glass structural models, a) Zachariasens continuous random network, b) Greaves modified random network with regions of microsegregation show unshaded, and c) compensated random network with charged network modifiers shown shaded (taken from (11)).*

The amount of NBO in a silicate glass and hence the network connectivity is described by $Q_n$ notation. In $Q_n$ notation the n represents the average number of bridging oxygens connected to silicon, such that $Q_4$ is a fully bridged silicon tetrahedron and $Q_0$ is a non-bridged silicate tetrahedron (as shown in table 2) (8). In a multicomponent glass the $Q_n$ notation is typicity only used to describe the NBO on silica, while other network formers or Intermediates present will use alternative abbreviations when describing the average NBO ratio present.

*Table 2 Qn numbers shown with their corresponding structural units*

| $Q_0$ | $Q_1$ | $Q_2$ | $Q_3$ | $Q_4$ |
|---|---|---|---|---|
| 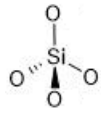 | 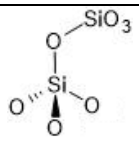 | 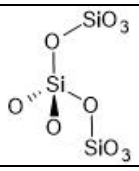 | 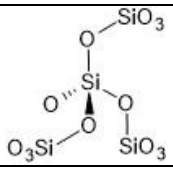 | 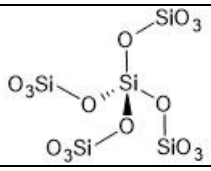 |

### 1.2.2. Variable Coordination Number in Oxide Glass Components.

Many of the Intermediates and network modifiers, and some network formers added to silicate glass will display a variable coordination number. This number can be influenced by a range of factors, such as the oxide concentration, the melt temperature, and the environment the molten glass is exposed to. The average coordination number of these will impact the physical properties of the glass. These coordination numbers can vary greatly from those seen in crystalline structures and are often present in varying ratios. B, Al and the smaller group 1 elements are of note and these are discussed in this section.

One of the more well-known examples of variable coordination in glass is the boron anomaly. $B_2O_3$ is a network former that on its own forms a stable glass composed of mainly three coordinate borate structures. When added to silicate glass, the boron becomes part of the glass network and a borosilicate glass is produced, again with mostly three coordinate boron present (8). If a network modifier is introduced to the glass melt, a percentage of these will be converted to a charged four coordinate borate forming a structural unit similar to silicate, and the four coordinate borate can then form a range of structural units (examples of these are shown figure 4) resulting in a phenonemon known as the boron anomaly (12,13).

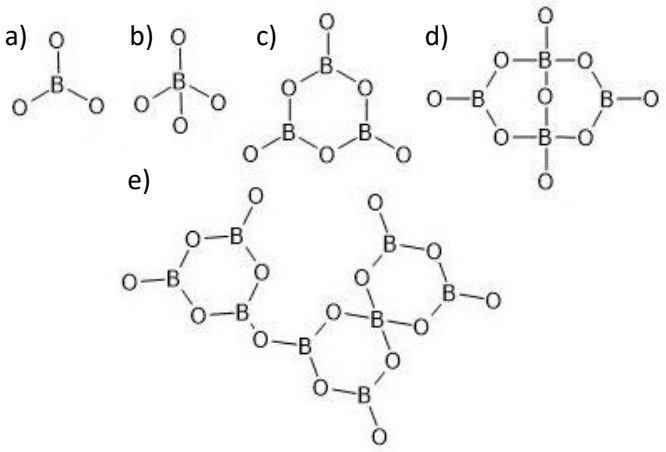


*Figure 4 Borate structural units a) three coordinate, b) four coordinate, c) borate ring, d) diborate and, e) tetraborate formed in the presence of four coordinate borate.*

The boron anomaly refers to an inflection point observed as a sudden change in thermal expansion, hardness, and other properties that are observed in a borate or borosilicate glass as the amount of alkaline or alkaline earth metal modifier is increased. In a simple alkali borate or alkali borosilicate this occurs between 15-20 mol% alkaline metal oxide (12,14,15).

In multicomponent glass the prediction of boron coordination ratio with the addition of alkali oxides becomes more complex due to charge competition, charge compensation, and increased impact of silicon boron mixing (12). Charge competition and charge compensation are related but not identical phenomena seen in glass. Charge compensation is the ability of a network former or intermediate to compensate for charged network modifiers. Charge competition refers to the preferential charge compensation of network modifiers by a given network former or intermediate present in a multicomponent glass. In a borosilicate glass the preferential charge compensation of $BO_4^-$ tetrahedra will reduce the amount of NBO present in the glass structure through charge competition.

A notable intermediate present in many waste glasses is alumina. In an aluminium containing glass three different coordination environments can potentially be found $AlO_4^-$, $AlO_5^{2-}$ and $AlO_6^{3-}$, with the $AlO_4^-$ tetrahedra being the most common form found in silicate or

borosilicate glass. In a silicate glass the negatively charged Al will occupy the same structural sites as Si, while preferentially charge balancing any positive cations ions found and thereby reducing the amount of NBO present and increasing the $Q_n$ number (8). In a borosilicate glass the Al is expected to again be the preferred charge compensator; though the impact this will have on $Q_n$ number and $BO_3$:$BO_4$ ratio is more difficult to accurately predict as the two possible negatively charged network components, the $AlO_4^-$ tetrahedra and the $BO_4^-$ tetrahedra, will compete for charge compensation with certain Modifiers acting as preferential charge compensators (13).

Variable coordination is also observed in network modifiers, such as the group 1 metals. In a glass the coordination number of a group 1 metal can vary from as low as 4 for lithium, to as high as 12 for cesium (16,17). Within this range each element will have a preferred range of coordination with the average coordination mainly dependant on network modifier concentration (16). The exact mechanisms behind the variability of coordination numbers in network modifier cations is poorly understood but is thought to be related to size mismatch and charge distribution. Variable coordination is not unique to glass and can be found in related materials, such as sodium silicates (18). However, unlike crystalline materials where a dominant coordination number is usually seen, the coordination numbers found in glasses, particularly for network modifiers, are best described as a spread of probable values. This is further complicated by the mixed alkali effect, where the properties of a glass containing one or more alkali metals show a deviation from what would be expected, if only additive effects were present (19). Combined with the amorphous nature of the material this results in further challenges when performing structural analysis.

### 1.2.3. Atomistic Modeling of Glass Structure

Atomistic modeling is typically used to model simple two to four component glasses. When modeling glasses three main approaches can be taken, creating a purely theoretical atomistic model using data extracted from existing models of related structures, fitting experimental data to extract necessary structural data, and using experimental data to refine a starting model. Given that, unlike in crystalline materials, in amorphous materials the structure that best fits experimental data may not be lowest system energy structure the use of high quality experimental data is necessary to ensure a representative atomistic model is produced (20).

At the time of writing there are no known complete atomistic models of UK base glass and only few complete models of ISG are known (21,22). These models were created by using existing data to create a starting model then altering a model till a satisfactory fit to experimental data was found. Creating a structure through this method relies on the assumption that the starting point combined with the fitting method used gives a reasonable approximation of the final structure. The difficulties seen in fitting the Zr-O peak by Bouty *et.al* and the poor fit by Lu *et.al* in the O-O region demonstrates the difficulty in using this method. In particular the poor fit for the O-O region seen in the data fitted by Lu *et.al* using Molecular Dynamics (MD) demonstrates how certain computational methods are unable to properly distinguish intermediate range O-O interactions (21). While the contrast between the Zr-O region fit carried out by Bouty *et.al* and the fit carried out by Lu *et.al* demonstrates the importance of using experimental data to refine a model (21,22). Overall this shows that in order to produce a full and accurate atomistic model, whilst using minimal assumptions, data on the interatomic distance, distribution of interatomic distances, and coordination number for all the oxide pairs present in the glass should be known, and in the absence of this data an accurate atomistic model cannot be created.

In studies of more simple glass formulations atomistic modeling has been used to predict the impact of radiation damage on glass structure and leaching rate (23,24). While many of these models were produced with the aim of investigating radiation effects glass structure, the results produced by Jan *et.al* shown a that a good match for experimentally observed glass leaching performance is only found up to up to a certain dose threshold (23–25). Once this dose threshold is reached the results begin to deviate, presumably due to changes occurring within the irradiated glass that are not present in the model, again demonstrating the need for experimental data to verify atomistic models (23,25).

Of the glasses used in this thesis ISG is the only glass with full atomistic models known, and from these models insights into structural differences between the surface and bulk of ISG has been gained, presumably with the eventual goal of gaining a better understanding of the leaching behaviour of ISG (3,21). It is hoped that by directly fitting glass PDFs and thereby providing a starting point the same insights can be gained by enabling future work towards a full atomistic model of MW and CaZn.

### 1.2.4. Summary of Glass Structure

The structure of glass is well understood but difficult to predict due to its amorphous nature. A borosilicate glass, such as those used in waste vitrification, will consist of a randomly linked network of silicon-oxygen tetrahedra, and boron-oxygen triangles and tetrahedra. In addition to this network, the waste glass will contain various network modifiers, which can cause both positive and negative structural changes, and Intermediates, many of which will become part of the glass network, further altering the glass structure and properties. Due to the complexity of these interactions, it is not possible to reliably model the glass structure without sufficient experimental data to use as a starting point. This data is not currently available for UK base glass and a complete atomistic model for these glasses is therefore not possible.

## 1.3. Factors Affecting HLW Glass

### 1.3.1. Radiation

Materials used for the immobilisation or storage of HLW will be exposed to significant amounts of radiation. Borosilicate glass is used for containment of HLW, as glass is one of the few materials able to tolerate both the radiation and heat produced from HLW without undergoing significant degradation and structural failure. However, due to the long lifetime of the waste, glass is not entirely able to withstand the high levels of radiation and some changes will take place. These changes take the form of electronic defects, ionisation effects, and atomic displacements, with the quantity and type of defects present depending on the type and amount of radiation present (26–29). Knowledge of these effects is vital to model the degradation of the wasteform to ensure the waste stays contained until the radioactivity has decayed to safe levels. In UK HLW alpha, beta, and gamma activity are expected to be the main types of radiation present, with the radioactivity expected to take $10^8$ years to decay to safe levels, as shown in figure 5 (4).

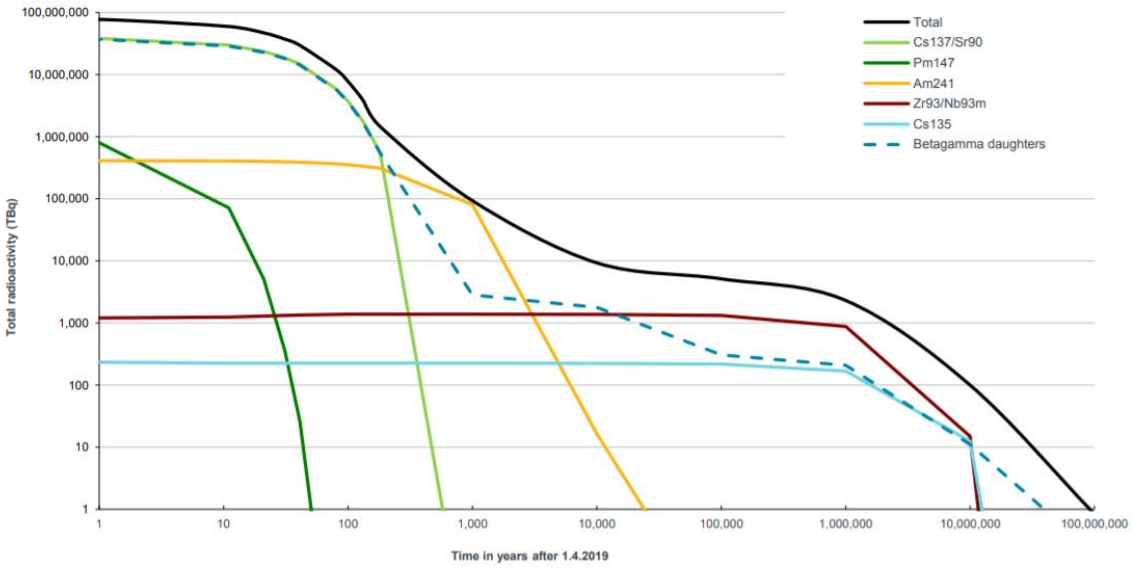


*Figure 5 Predicted total lifetime of all UK HLW (taken from (4))*

#### *1.3.1.1. Ionising vs Non Ionising Radiation*

Ionising radiation is defined in UK legislation as "the transfer of energy in the form of particles or electromagnetic waves of a wavelength of 100 nm or less or a frequency of 3 x

$10^{15}$ Hz or more capable of producing ions directly or indirectly" (30). The alpha, beta and gamma radiation produced by the HLW waste contained within the glass has enough energy to act as ionising radiation. Of the radiation present within the glass the alpha radiation will typically have the highest ionising power and lowest penetration while gamma radiation will have the lowest ionising power but highest penetration. The three different types of radiation present are produced by the following processes.

Alpha radiation is produced by the decay of heavy elements such as $^{241}$Am and $^{238}$U. In this decay process the atomic nucleus emits an alpha particle that is identical to a $^{4}$He nucleus, consisting of two protons and two neutrons. As part of this process the original nucleus, known as a parent nucleus, is transformed into a different nucleus known as a daughter nucleus (as shown in figure 6). In order for alpha emission to take place the mass of the parent nucleus must be greater than the combined mass of the daughter nucleus and the alpha particle as when decay takes place this mass difference is converted into energy. Most of this energy will be transferred to the alpha particle and some of the energy will be transferred to the daughter nucleus in the form of alpha recoil. Despite having a lower energy the alpha recoil of large daughter nucleus is more likely to lead to direct displacements within a structure whilst collisions with the alpha particle will lead to ionisation effects.

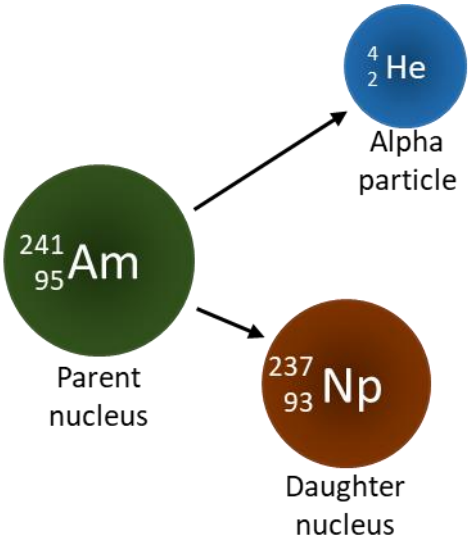


*Figure 6 Simplified diagram showing alpha radiation*

Beta decay is somewhat unique in that it can proceed via either conversion of a neutron into a proton resulting in antineutrino and electron emission, known as $\beta^-$ decay, or via conversion of a proton into a neutron resulting in neutrino and positron emission, known as $\beta^+$ decay (as shown in figure 7). In both these processes a daughter nucleus is produced, however as the beta particle is smaller and lighter than the alpha particle the daughter nucleus does not undergo recoil effects. Instead the energy is transferred from the beta particle to its surroundings mainly via ionisation effects.

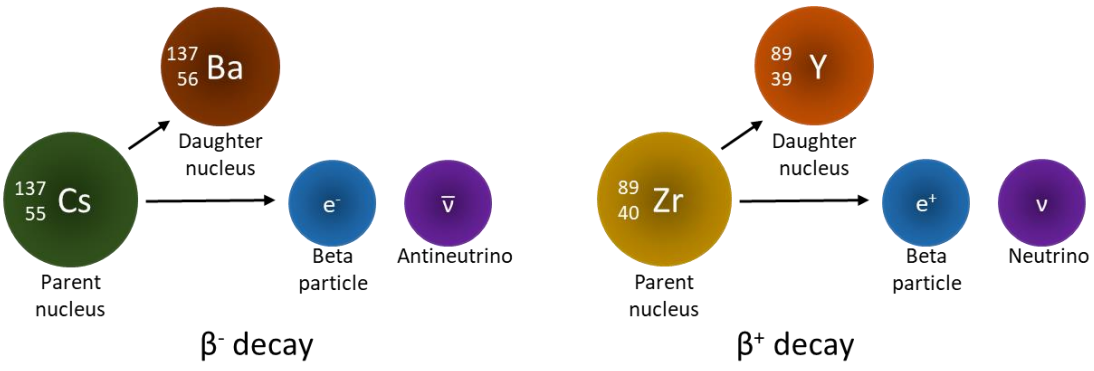


*Figure 7 Simplified diagram showing beta$^+$ and beta$^-$ decay*

Gamma decay is produced by the emission of a high energy photon from an unstable nucleus. The unstable nucleus is often a formed as an excited daughter nucleus from either alpha or beta decay (as shown in figure 8). Gamma radiation is the most penetrating out of

the three types of radiation produced by the HLW contained within the glass. As the gamma ray passes through a material it interacts with the material through three main ionising processes, the photoelectric effect, Compton scattering, and pair production.

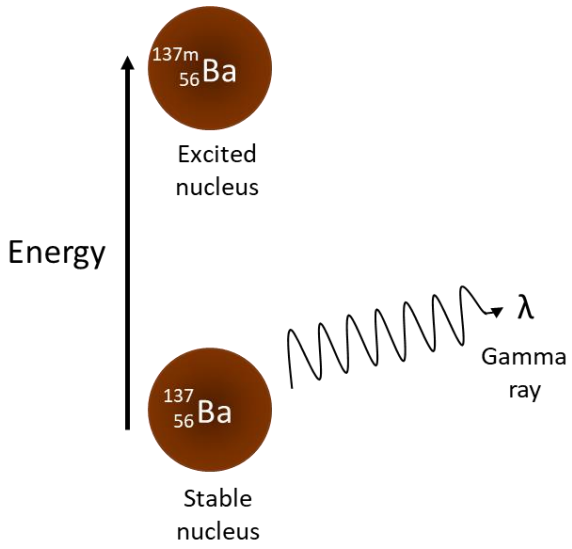


*Figure 8 Simplified diagram showing gamma emission*

#### *1.3.1.2. Gamma Radiation Induced Defect Formation*

Electronic defects typically take one of two forms, an excess of electrons often termed an electron trapped center (ET center) or a deficiency in electrons termed a hole center (HC center) (31). These defects are found in a range of crystalline materials and can either be present as result of conditions present as the crystal forms, impurities within the crystal or induced through the use of thermal treatment or radiation (31). The presence of electronic defects can change both the physical and optical properties of a material with the classical example of a colour causing defect being the F center (from Farbezentrum). The F center colour originates from a trapped electron occupying an anion site and transitioning between different orbitals as a result of absorbing specific light wavelengths (31).

As with crystalline materials electronic defects in borosilicate glass can also cause a colour change and a change in physical properties. These defects are typically induced by exposing

the borosilicate glass to high energy photons such as those in the upper UV (λ=193nm) to gamma irradiation range, or electron beams though depending on the elements present some glasses can be discoloured by exposure to visible light (32–35). The general mechansim responsible for the formation of the UV X-Ray and gamma radiation induced defects is identical, when the glass exposed to the high energy photons electrons are excited and move from their normal position throughout the glass network forming an HC center, this free electron then becomes trapped forming an ET center (35). When the defect is recombined the trapped electron is freed and able to move back into a hole center. In some materials this transition occurs at room temperature as soon as radiation exposure is stopped, whereas in borosilicate glass the glass must be heated to near the glass transition temperature ($T_g$) for defects to be fully recombined (36). This stability may originate from pre-existing defect precursors found within the structure or irradiation induced structural changes (32,37).

One of these changes that is of interest is the structure of the $HC_1$ and $HC_2$ center (specific types of related hole centres found in alkali silicate and borosilicate glass shown in figure 9) proposed by Griscom and the related clustering of alkali metal ions within the glass structure (38,39). In this mechanism an electron is lost from a NBO and the hole created becomes trapped on the 2p orbital of a NBO (as shown figure 9) with $HC_1$ being the preferred orientation and $HC_2$ only being observable at low temperatures (38). The hole trapping removes the negative charge from the NBO and, in the absence of this negative charge the alkali modifier ion becomes mobile as demonstrated by the $HC_2$ to $HC_1$ transition. The alkali modifier ion is also able to trap electrons which leads to the clustering proposed by Griscom (39). In the proposed clustering mechanism electrons are trapped on alkali ions which are then able to agglomerate into larger clusters with these clusters expected to be partially or fully EPR silent due to the presence of spin paired electrons (39).

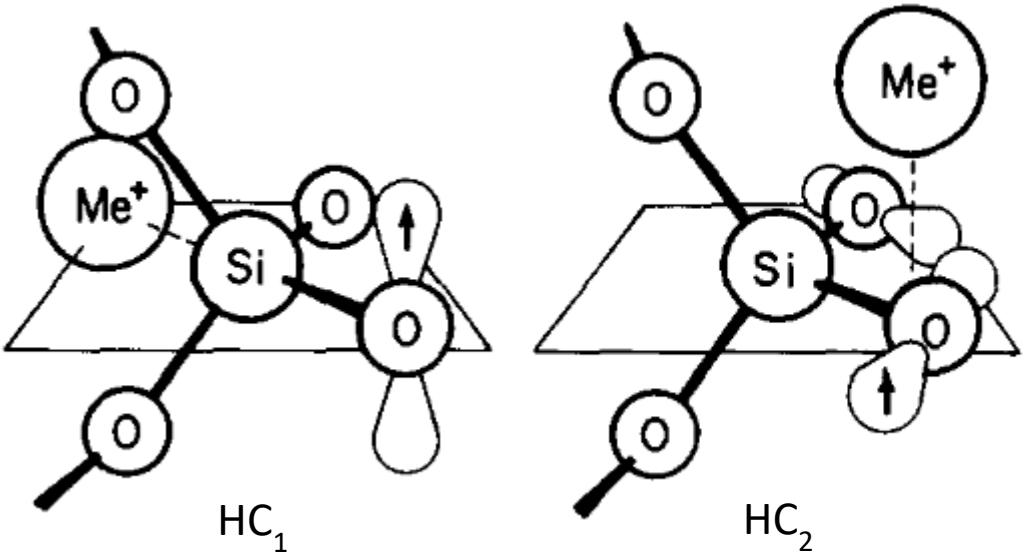


*Figure 9 Model of $HC_1$ and $HC_2$ centres formed by irradiation of alkali silicate glass. In $HC_1$ the cation is in plain with the hole located on a more distant NBO. In $HC_2$ the cation is above or below the NBO (taken from (38)).*

This clustering has the potential to change both the optical and physical properties of a glass while being nearly entirely EPR silent. Due to this it may only be possible to identify these defects through matching UV-Vis data to EPR data. Although, due to the complexity of EPR spectra produced by multicomponent glass and inherent difficulties in matching the defects observed in complex UV-VIS data with defects observed in complex EPR data it is not always possible to directly identify specific defects responsible for colour centres and instead the identification is based on existing data from related materials (35,36). This method suffers from an intrinsic flaw in that the glass matrix can also impact the formation of defects and absorption behaviour of the defects making the identification of EPR silent defects difficult if not entirely impossible (32). The most suitable means of overcoming these difficulties would be through the selective recombination of specific defects in the glass.

#### *1.3.1.3. Effects on Glass*

The primary waste stream vitrified in the UK is blended HAL from Magnox and THORP with plans currently in place to vitrify HLW from POCO operations (2). In the resulting waste streams, a mix of active and non-active elements are present with the POCO waste

containing significantly increased quantities of molybdenum. The increased molybdenum level has been found to lead to undesirable phase separation during vitrification with MW that results in the formation of a soluble and corrosive “yellow phase” hence the need to develop CaZn as a means of reducing this phase separation (2).

Many of the active elements are beta emitters such as $^{137}Cs$ and $^{147}Pm$ that, in the early days of the waste lifetime, are expected to be the dominant form of radiation and for the first 600 years generate a significant amount of self-heating (up to ~500°C) from radioactive decay (4,26,40). Due to this self-heating the waste glass will be stored for a minimum of 50 years before being disposed of in the proposed GDF (40). The beta decay can proceed via $\beta^+$ or $\beta^-$ emission producing either a positron or an electron and a daughter nucleus. The daughter nucleus is often unstable decaying further and emitting other forms of radiation in combination with gamma radiation. The beta particles are not expected to significantly impact the glass structure, as these are relatively light and transfer energy through ionisation effects, producing significant self-heating within the glass, but resulting in less than one displacement expected per decay event (26).

In the latter stages of the waste lifetime, alpha radiation from longer lived isotopes, such as $^{241}Am$ is expected to be the dominant form of radiation. Alpha decay of elements present produces both alpha particles and large heavy recoil nuclei. These alpha particles and recoil nuclei transfer energy through, ionisation processes, elastic collisions, and alpha recoil, with enough energy transferred through both collisions and recoil effects to lead to several hundred displacements in the structure (27). These displacements are expected to lead to a loss in network connectivity increasing the amount of NBO present (27,29). Both alpha and beta radiation effects can be simulated through ion beam techniques or through doping glass with short lived active elements. Ion beam techniques are more commonly used as these do not generally require active handling. However, there is some debate surrounding

the use of electron beams to simulate beta radiation, and the heavy ions used to simulate alpha recoil effects have poor penetration and will only damage the first few μm of the glass surface (34,41). The impact that alpha and beta radiation will have on glass has not been studied here due to time constraints and concerns about the gel layer thickness exceeding the heavy ion irradiation damaged area (42).

The gamma radiation present originates from the production of a high energy photon from an excited nucleus. This nucleus is generally created by alpha or beta decay. The damage that gamma radiation induces is expected to mostly consist of electronic defects and ionisation effects, as gamma photons are too light to directly cause displacements (36,43). Gamma radiation induced changes may lead to increased ion mobility with the potential for irradiation induced clustering of the smaller group 1 network formers proposed (27,36). The full impact of this on leaching performance is unclear as, while an increase in ion mobility would be expected to cause an increase in reactivity and has been shown to cause an increase in the rate of the early stages of glass leaching, overall leaching rate is controlled both by hydrolysis of and ion exchange through a gel layer (explained in detail in section 1.3.3) formed during this early stages of glass leaching (27,44).

The electronic defects formed in glass by gamma irradiation (explained in detail in sections 1.3.1.3 and 3.2.1) are relatively stable and lead to a distinct colour change with a clear dose dependence seen. These defects are unstable to both heat and UV light, though a thorough investigation of the exact impact of these on defect recombination is lacking. This is likely due to the precise nature of the defects themselves being poorly understood. These defects are difficult to characterise due to all having similar g-factor values (explained in more detail in sections 3.4.2 and 6.1.3) when carrying out Electron Paramagnetic Resonance (EPR) and similar absorbance when carrying out UV-Visible-Near IR (UV-Vis-NIR)

spectroscopy (36). The electronic defects present in both MW and CaZn have not previously been fully characterised, so an attempt has been made to characterise these.

In previous literature the following electronic defects have been identified in a gamma irradiated MW-like glass: an E' center, electron trapped centres, boron oxygen hole centres and $Fe^{3+}$ (silicate glass typically contains approx 0.5 % iron impurity) (36). These gamma irradiation induced defects were primarily identified through UV-Vis-NIR, which in glass will not show defects that absorb in the UV range as these will be obscured by UV absorption from the glass, no attempt was made in Rautiyal *et.al.* to properly simulate the EPR spectra collected (36). No attempts to directly identify irradiation induced electronic defects in CaZn are found in literature but examples of EPR analysis and simulation carried out using related irradiated borosilicate glass formulations are known (45–47). From these CaZn is expected to contain similar defects to MW with the exception of a strong sharp band associated with either aluminium or calcium (47,48). These defects and their identification are discussed more comprehensively in sections 3.2.1. and 3.3.4 of this work.

### 1.3.2. Storage Environment

The final location of the UKs vitrified HLW will be a GDF. A site for the UK's GDF has not been selected, though talks are currently in place with local government and communities to select the final location, so it is not possible to comment on ground water chemistry and other aspects of local geology that may impact long term disposal (49). GDFs are currently in use, or have been proposed, for the disposal of HLW and ILW in many countries and typically follow guidance set by the International Atomic Energy Agency (IAEA) that states the waste must be contained, isolated, have a multi-barrier function, and be passively safe (50). Containment is not identical to isolation and refers to minimising the direct release of radionuclides; waste must be contained until radioactive decay has significantly reduced the hazard posed by the waste. Isolation refers to minimising the possibility of contact with

the radioactivity released by the waste, which is partly achieved through the depth of the facility. Passive safety requires that the facility needs only minimum maintenance after closure with the assumption made that the location of the site will, at some point during the expected radioactive lifetime of the waste, be lost to history (50). Early versions of repository design took a slightly different approach with various solutions proposed to prevent future civilisations disturbing near surface waste repositories (51).

Where the waste is vitrified the glass forms the first element of the multi-barrier system. When this glass comes into contact with ground water the ground water chemistry can have a dramatic effect on the stability of the glass, and its ability to retain the radioactive material. The radioactivity will also impact glass durability but, one aspect of the system that has not been fully considered is the steel container. In early stages of barrier failure the steel container will corrode and eventually breach, resulting in the glass and steel being exposed to the GDF environment simultaneously.

Over the long lifetime of the GDF, the barriers in the GDF will fail, most likely due to slow water ingress. As part of the passive safety concept the GDF is designed with this in mind. In this design the glass forms the first barrier preventing waste from being released into the environment, due to this the slow dissolution of glass, known as alteration, and its interaction with subsequent GDF barriers must be modelled to ensure that radionuclides are contained until the radioactivity has naturally decayed to safe levels.

### 1.3.3. Water Ingress

The primary method of containment failure will be water ingress, and because of this, a large body of literature documenting the effects of water on waste glass is available (52–56). It is generally agreed that the ability of a glass to resist aqueous corrosion is not an intrinsic property of a glass but is instead determined by the environment a glass is placed

in. Conditions such as pH, Eh and ion concentration in the environment the glass is exposed to will impact the processes responsible for glass alteration (55,56).

Glass alteration is expected to proceed through the stages shown figure 10. These stages will be governed by the following processes:

Stage 1 - The initial fast alteration rate is controlled by the concentration of rate limiting species, such as soluble silicates, in solution and the formation of a gel layer that is analogous to the passive layer formed on many metals (56). This stage is highly dependent on the ground water temperature, chemistry and flow rate, such that, if the rate limiting species are removed from solution, either by the formation of insoluble minerals or mechanically, a stable gel layer will not form (55).

Stage 2 – Primarily controlled by either diffusion through the gel layer or formation of secondary silicate mineral phases (56). During this stage the glass alteration rate is at its lowest, ideally the waste glass will rapidly progress through stage 1 onto stage 2, with stage 2 being the dominant stage (55,56).

Stage 3 – The resumption of rapid glass alteration occurs if the gel layer is disrupted by physical damage to the gel layer or by chemical changes in the surrounding water, such as a sudden change in pH leading to the rapid precipitation of silica-containing minerals (56).

The impact of the steel container on glass alteration has been poorly studied, with most existing studies focussing solely on the interaction of corrosion products with the glass and the potential for these to initiate stage 3 or extend stage 1 alteration (57,58). In the early days of glass studies the impact of the container was explored but this does not seem to be fully considered in more recent works (59). This results in an incomplete picture as it is highly unlikely the container will fail through uniform corrosion in a manner that results in the glass only being exposed to corrosion products. The possibility exists that the steel

container may disrupt glass alteration through the precipitation of silicate on the steel surface resulting in a feedback loop that extends stage 1 of glass alteration (60). This has not been fully explored in current literature.

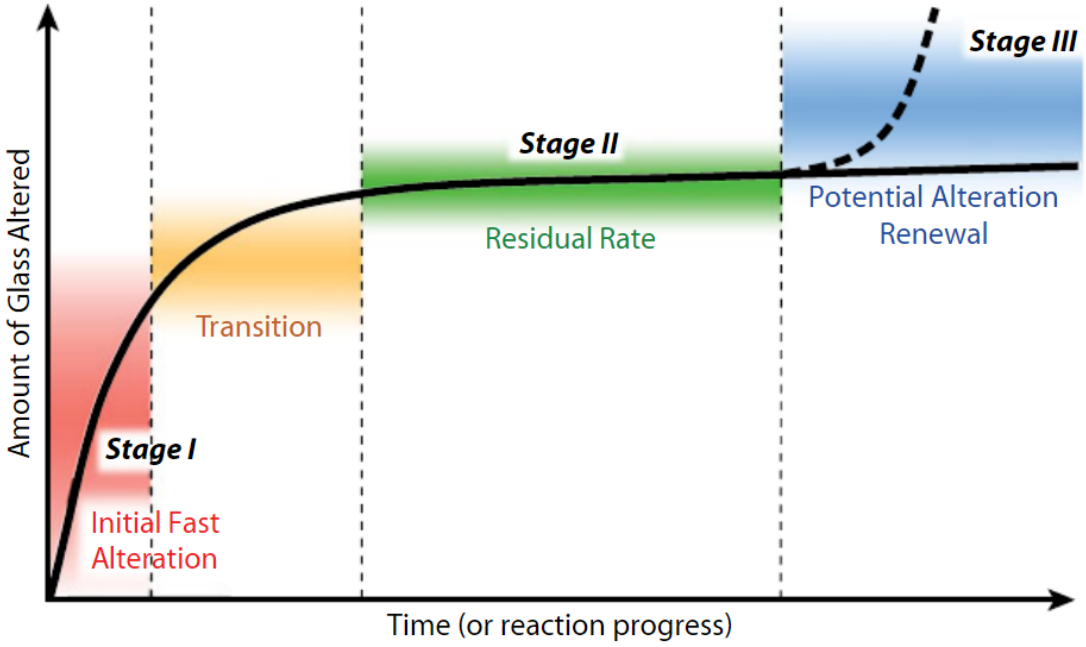


*Figure 10 Diagram showing glass alteration rate during stage I through III of the glass alteration process (taken from (56))*

Glass alteration is measured using leaching experiments. The two most common leaching methods used are as follows

- The Product Consistency Test, ASTM Standard Test Methods for Determining Chemical Durability of Nuclear, Hazardous, and Mixed Waste Glasses and Multiphase Glass Ceramics (PCT) powder based leaching technique (61).
- The Materials Characterisation Center Test 1, Standard Test Method for Static Leaching of Monolithic Waste Forms for Disposal of Radioactive Waste (MCC-1) based monolith leaching technique (62).

The PCT method is designed with a high glass surface area to solution volume ratio. The high surface area to volume ratio results in the glass rapidly progressing through stage 1 to

stage 2 of alteration, making this method ideal for simulating the latter stages of glass alteration. The MCC-1 method has a comparatively low surface area to volume ratio, resulting in glass alteration progressing more slowly than in the PCT method, the slower rate and single glass monolith used make this method ideal for studying the earlier stages of alteration and bulk gel layer properties.

### 1.3.4. Galvanic and Electrochemical Interactions with Steel

In current glass alteration studies the interaction between iron one of the main steel corrosion products and glass has been thoroughly investigated, however the interaction between glass and bulk steel has been all but entirely ignored (57–60,63,64). One of two assumptions seem to have been made that the glass will not interact with the container during alteration, or that the container will fail via uniform corrosion in a manner that only exposes the glass to steel corrosion products. Both early and more recent studies indicate that these assumptions are incorrect and an interaction between glass and bulk steel takes place and that this interaction potentially related to the crevice corrosion of steel (59,60,65).

#### 1.3.4.1. Crevice Corrosion

Crevice corrosion is a form of corrosion that tends to occur in small shielded areas of metal where aqueous solutions can become trapped, such as on the edges of spot welds or under gaskets. In stainless steel crevice corrosion is thought to be initiated by a drop in solution oxygen concentration caused by a cathodic reduction mechanism occurring in solution (66). Initially the cathodic reduction mechanism occurs uniformly across the steel surface and is charge balanced by anodic dissolution of metal however, once oxygen has been consumed the cathodic reduction mechanism ceases (66). In the absence of the negative charge provided by cathodic reduction negative ions (typically chloride or sulphide/thiosulphate) will migrate into the crevice in order to charge balance anodic dissolution (66,67). These

negative ions can attack the passive layer, which in the absence of oxygen cannot reform. In an environment containing chloride ions this attack will form soluble metal chlorides that will then hydrolyse to form metal hydroxides and HCl resulting in a harsh acidic environment within the crevice. This mechanism is shown in figure 11.

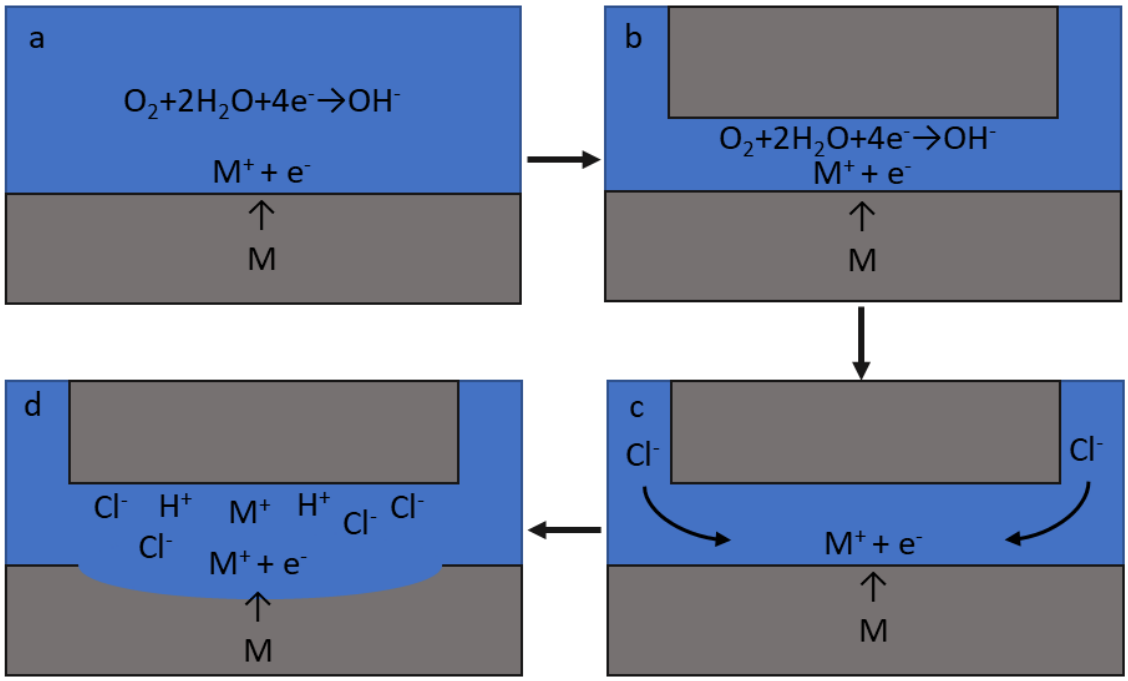


*Figure 11 Simplified mechansim for initiation of crevice corrosion. A shows slow uniform corrosion in absence of crevice. B shown oxygen consumption by cathodic reduction. C shows migration of chloride ions into crevice environment due to charge imbalance. D shows harsh environment formed in crevice during crevice corrosion.*

This process shares some similarities with galvanic corrosion however galvanic corrosion is initiated by a potential difference between metals where one metal is more reactive than the other. In galvanic corrosion the more reactive metal acts as an anode and is preferentially corroded over the less reactive metal acting as a cathode whereas in crevice corrosion the two metals or metal and conductive nonmetal are of identical reactivity and electrochemical changes in solution chemistry are the driving force for the increased corrosion rate within the crevice.

1.3.4.2. Galvanic Corrosion

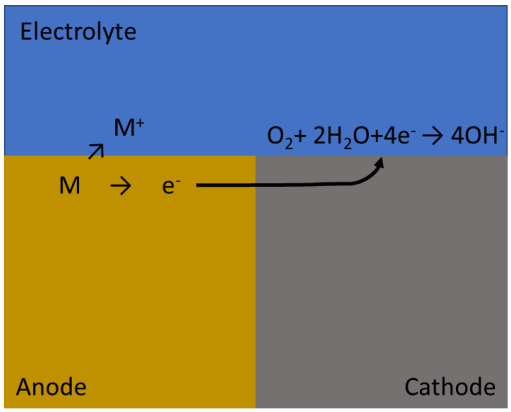


*Figure 12 Simplified diagram of galvanic corrosion*

Galvanic corrosion is a specific type of corrosion in which an electrochemical cell is formed by the direct contact of two metals with dissimilar reactivities and an electrolyte solution, in the absence of any of these requirements galvanic corrosion cannot occur. The driving force behind galvanic corrosion is the anodic dissolution of the more reactive metal at the anode, that is charge balanced by reduction at the cathode (as shown in figure 12). This can lead to the rapid degradation of the less noble metal while the more noble material remains uncorroded, this can be a desirable process in the case of sacrificial anodes or galvanised steel or it can be an undesirable process in the case of poor materials selection.

The simplest way of preventing galvanic corrosion is selection of compatible materials and consideration of the environment they will be exposed to with the typical example of an electrolyte being a saline solution such as sea water as shown in the example galvanic series shown in figure 13 (68). Additionally if the anode is significantly larger than the cathode or a nonconductive coating is applied to one or both of the materials then galvanic corrosion will not occur, although caution must be taken when using coatings as these may facilitate crevice corrosion and any breaches in the coating may allow galvanic corrosion (68).

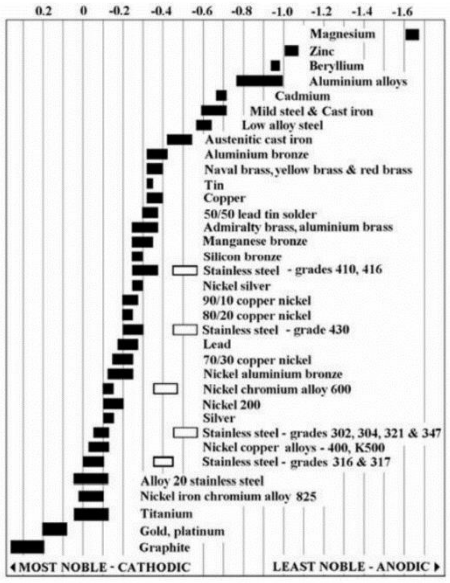


*Figure 13 Example galvanic series used to assess the risk of galvanic corrosion occurring in seawater. Taken from (68).*

Given that a large quantity of the groundwater found within deep UK aquifers is either brackish or saline it is likely there will some chloride present in groundwater when water ingress occurs in the proposed GDF making galvanic corrosion a possibility (69).

#### 1.3.4.3. Graphite and Steel

The interaction between graphite and steel demonstrates the destructive potential of both crevice corrosion and galvanic corrosion in a system containing two materials which in isolation are considered to be reasonably inert, this is of interest as in isolation glass and steel are considered to be inert materials. In the graphite steel electrochemical system the steel acts as a sacrificial anode and is preferentially corroded over the graphite. Where graphite gaskets have been used with steel piping exposed to a saline environment galvanic corrosion assisted crevice corrosion has also been observed (68).

Due to the presence of stainless steel structural materials and graphite in both the aerospace and nuclear industries this system has been extensively studded in a range of relevant electrolyte materials (68,70–73). In these different systems the graphite took the form of solid graphite (68,70), a graphite polymer composite (71,72) and suspended graphite particles (73), and either an aqueous saline environment (68,71,72) or a molten flouride containing salt (70,73) was used as an electrolyte. Despite the different grade of steel used, different electrolytes, and different methods used to introduce graphite into the system in all cases indications of crevice corrosion characteristics were observed in the steel graphite systems (68,70–73). In these systems the only factor that had any effect on the corrosion characteristics of the steel graphite system was the electrolyte used. In an aqueous environment crevice corrosion characteristics tend to dominate over galvanic corrosion resulting in galvanic corrosion assisted crevice corrosion occurring in these systems (68,71,72), whereas in molten salt electrolytes crevice corrosion is the dominant form of corrosion seen (70,73). The crevice corrosion observed when using a molten salt

electrolyte is believed to be related to the presence of small amounts of moisture in the salt used (70). Given the use of molten salt as a coolant in proposed molten salt rectors methods of controlling and monitoring crevice corrosion must be well developed in order to use these reactors on a commercial scale.

Galvanic corrosion assisted crevice corrosion is of interest in modeling the conditions likely to be observed in the early stages of GDF breach. Given the unreactive nature of glass if glass or the materials contained within the glass are able to participate in galvanic corrosion then galvanic corrosion assisted crevice corrosion becomes a strong possibility.

#### 1.3.4.4. Glass and Steel

The system formed by glass in contact with steel has not been extensively studied with only two papers known that attempt to directly study this phenomena. In these papers the flat glass monolith was held against a flat piece of steel and the glass steel coupon was submerged in either a NaCl solution or ultrapure water at 90°C for 30 days (60,65). The papers by Guo et.al conclude that in the presence of a saline environment acidic conditions are produced by metal ions trapped within the crevice and this leads to crevice corrosion like conditions and that in ultra-pure water crevice corrosion characteristics are not observed due to the absence of anions necessary for the formation of an acidic environment (60). These harsh conditions formed within the crevice have an unfavourable effect on glass alteration rate and may lead to enhanced pitting corrosion in the stainless steel container (65).

While the few studies available tend to agree that the glass steel interaction will have a negative effect on glass alteration, the overall impact on the steel container is somewhat debated with the more recent studies by Guo et.al coming to the conclusion that, despite the enhanced pitting corrosion observed the glass steel interaction may have an overall protective effect on the steel, due to the formation of a silicate coating on the steel surface

(65). This is in contrast to the earlier studies by McVay et.al that suggest glass metal interactions will increase both glass alteration and metal corrosion rates (64).

The different conclusions observed in these studies indicate a system related to surface area effects, Si concentration, and some form of electrochemical interaction that forms when glass is in direct contact with steel. In the different glass metal systems used, Guo et.al uses ISG pressed against a much larger stainless steel coupon (60). Whereas McVay et.al uses PNL 76-68 glass, which has both a lower overall Si content and more complex formulation than ISG, with an iron coupon the same size as the glass monolith, this coupon was not in direct contact with the glass (64).

These contrasting results indicate that the size of the crevice has an impact in the glass steel system and given that a poor crevice is created by pressing two flat surfaces together this system requires further study involving the use of a true crevice environment and other glass formulations. The crevice environment should be similar to the environment created by the crevice washers used in the ASTM G48-11 procedure for assessing the crevice corrosion of steel (74).

## 1.4. Summary

Glass is a commonly used but extremely complex material. To ensure the safety of current and future vitrified waste, the structure of the waste glass used, the impact of radiation on this structure, and its interaction with all aspects of the future GDF environment must be properly understood. In order to model these interactions a detailed understanding of the comparably simple base glasses is needed. This understanding is lacking in some areas for both the MW and CaZn UK base glasses due to large gaps in current structural data. An aim of this work is to fill in these gaps to create a starting point to enable the future creation of a complete atomistic model of UK base glass. Future work to develop an atomistic model of

UK base glass will facilitate a better understanding of current experimental data on the impact of radiation on the glass structure.

It is widely agreed that a GDF will be the safest method of disposing of HLW, although there are some gaps in the understanding of the GDF environment. It is not currently possible to study the impact of specific groundwater chemistry on glass alteration, as a location for the UK GDF has not been chosen. Additionally, the direct interaction of glass and steel has been all but completely disregarded in current literature, despite the possibility of unfavourable glass-steel interactions being recognised in early literature. This, in combination with the impact of gamma radiation on stage 1 glass alteration, may lead to extensive glass alteration. This leads to my hypothesis "In GDF conditions, contact with steel, and radiation-induced changes in glass structure, will increase glass leaching rate in the early stages of container breach".

# 2. New Insights Into MW, CaZn, and ISG Glass Structure from X-Ray and Neutron Scattering Combined with MAS-NMR.

## 2.1. Abstract

An understanding of the initial structure of a glass is needed to predict its long term performance under radiation and ground water leaching conditions. The complex chemistry of many glasses creates numerous difficulties in evaluating their structure. Hence, a comprehensive atomistic structural model describing the short and intermediate range order of UK MW and CaZn base glass does not currently exist and only limited models of ISG are known. Here, we report on the full structure analysis of $^{11}B$ doped MW, CaZn base glass, and ISG glass using high momentum transfer X-ray and neutron pair distribution function data (27 $Å^{-1}$ and 60 $Å^{-1}$ respectively), complemented by $^{11}B$ and $^{27}Al$ MAS NMR data. Analysis of the short range order in terms of nearest neighbour distances and coordination numbers shows the distinct boron and aluminium coordination numbers present, and provides strong indications that in all formulations the glass network is highly polymerised . This information has been verified against current models of ISG, and will underpin future atomistic modelling of UK MW and CaZn base glasses.

## 2.2. Introduction

The UK uses two base glass formulations, Mixture Windscale (MW) and CaZn, to vitrify High Level Waste (HLW) , while International Simple Glass (ISG) was developed as part of an international initiative for use as a glass standard (1,2,75). The physical properties of these glasses have been and continue to be well studied, however, compared to ISG, little is understood about the structure of the UK base glasses (53,76–80). This is due to the

multicomponent nature of these glasses introducing a significant challenge in the analysis of structural data.

The MW and CaZn compositions are shown in table 3 along with ISG. The three glasses studied here were developed for different purposes. MW was developed for the vitrification of mixed waste streams containing waste material from the reprocessing of both Magnox and enriched uranium oxide fuels (81). MW is formulated to make use of the high aluminium content found in Magnox waste as a means of improving glass durability (81). CaZn, a modified version of the MW glass formulation, is a later development designed to address issues with undesirable "yellow phase" formation during the vitrification of Post Operational Clean Out (POCO) wastes containing high level of molybdenum (82). ISG is a non-active simulant glass that was developed as a standard formulation for use in studies of glass leaching behaviour (75).

*Table 3 MW, CaZn, and ISG designated glass specifications*

| mol % | $SiO_2$ | $B_2O_3$ | $Na_2O$ | $Li_2O$ | $Al_2O_3$ | CaO | ZnO | $ZrO_2$ |
|---|---|---|---|---|---|---|---|---|
| MW | 60.0 | 19.0 | 10.5 | 10.5 | | | | |
| CaZn | 48.7 | 20.6 | 8.5 | 8.6 | 2.5 | 6.6 | 4.5 | |
| ISG | 60.2 | 16.0 | 12.6 | | 3.8 | 5.7 | | 1.7 |

Detailed information on the structure of these three glasses can be extracted from fitting a Pair Distribution Function (PDF) with a series of partial corelations. There is currently no know PDF data available for MW or CaZn. The few known PDF data sets produced from ISG have been primarily collected using X-ray scattering, which have a comparatively low momentum transfer (Qmax) of 17, and 26 $Å^{-1}$ (21,22). Neutron PDF data of glass formulations related to ISG have been collected and analysed to aid in atomistic modeling, although again this analysis used a comparatively low Qmax of 30 $Å^{-1}$ (83). The low Qmax leads to a poorly resolved PDF. All of these previous data sets have been fitted through the use of an atomistic model. This method relies on the creation of an accurate starting model

and is typically not able to accurately fit atom pairs described by more than one Gaussian curve, such as the B-O and O-O region of PDF data (21). These difficulties can be overcome through directly fitting a PDF data set.

The PDF obtained from a multi component glass consists of a series of highly complex overlapping peaks each corresponding to an atom pair. This peak overlap is typically sufficient to prevent the direct fitting of PDF data and results in the need for atomistic modeling. However, through the use of simultaneous fitting of high momentum transfer X-ray and neutron scattering data in combination with $^{11}B$ and $^{27}Al$ MAS NMR, this can be overcome. In this work a method for the direct fitting of three multicomponent glass PDFs has been demonstrated using MW, CaZn and ISG.

## 2.3. Experimental, Materials and Methods

### 2.3.1. Glass Synthesis

In order to minimise neutron absorption by $^{10}B$, samples of glass were prepared from batch using $^{11}B$ isotopically enriched $H_3{}^{11}BO_3$ and a melt quench anneal method. The following quantities (listed in table 4) of high purity dried reagent grade powders and $^{11}B$ boric acid (supplied by 3M enriched to 99.98%) were weighed into polymer bags and thoroughly mixed to ensure homogeneity.

*Table 4 Reagent quantities used in glass manufacture.*

| Sample / g | MW | CaZn | ISG |
|---|---|---|---|
| $SiO_2$ (Sand) | 10.40 | 7.62 | 12.38 |
| $H_3{}^{11}BO_3$ | 6.79 | 6.66 | 6.79 |
| $Na_2CO_3$ | 3.21 | 2.35 | 4.58 |
| $Al(OH)_3$ | | 1.03 | 2.02 |
| $CaCO_3$ | | 1.72 | 1.95 |
| $Li_2CO_3$ | 2.25 | 1.65 | |
| $ZrO_2$ | | | 0.72 |
| ZnO | | 0.95 | |

The powders were placed in fresh alumina crucibles, transferred to an electric furnace, and heated in air at a rate of 2 °C/min to 1150 °C for MW and CaZn, and 1350 °C for ISG, with a hold time of approximately 4 hours. ISG was melted at a higher temperature to allow for increased melt viscosity due to the presence of zirconium. The molten glasses were poured into a room temperature small circular steel mould on a steel plate, allowed to cool until hardened enough to be removed from the steel plate, removed from the plate, and annealed at 480 °C for 2 hours before being allowed to cool to room temperature at a rate of approximately 0.5 °C/min inside the annealing furnace. The crucibles were retained as these contained a significant quantity of glass, adhered to the crucible walls.

The nominal composition of the glass produced is shown with the final composition in table 6 section 2.3.5. This differs slightly from the final composition due to alumina absorbed from the crucibles during the melt process.

### 2.3.2. Sample Preparation

Glass fragments were removed from the crucible walls using a small hand tool and inspected to ensure no crucible material remained adhered to them. The glass disks were crushed using a vice to fragments of no larger than ~1 cm, then transferred to a small laboratory grinder with the fragments recovered from the crucible walls. A small quantity of ethanol was added to the grinder to minimise dust generation and the samples were ground to a fine powder, then dried in an oven until free flowing. The free flowing powder was placed in a small glass screw top vial, and returned to the oven to dry further and the vials were sealed while still hot. After drying the following masses of glass powder were measured MW: 6.2901 g, CaZn: 8.1238 g, ISG: 6.6230 g.

### 2.3.3. Density Measurements

Density measurements of the glass powers were carried out using a Accupyc II 1340 helium pycnometer. Prior to each analysis the pycnometer was calibrated using a 10 $cm^3$

calibration sphere. A known quantity of powder (shown table 5) was measured into a standard 10 $cm^3$ sample cup and run with 20 purge fill cycles.

*Table 5 Density values determined by He pycnometry*

| Glass | Quantity / g | Density / g $cm^{-3}$ |
|---|---|---|
| MW | 4.5205 | 2.4206 ± 0.0013 |
| CaZn | 6.1264 | 2.5340 ± 0.0015 |
| ISG | 4.8581 | 2.4484 ± 0.0015 |

### 2.3.4. Sample Composition

Sample composition was determined by Sheffield Assay Office (Sheffield, UK) using Inductively Coupled Plasma Optical Emission Spectroscopy (ICP-OES) for lithium, sodium, and boron and by Glass Technology Services (Sheffield, UK) using X-ray Fluorescence (XRF) for all other elements present. The results of the analysis are shown in table 6 with the nominal compositions calculated from the weighed precursors. It can be seen that the glass melts had absorbed extra alumina from the crucibles used and that some lithium had been lost potentially through volatilisation. All glasses were transparent and very pale blue green in colour. The pale green colour originates from a yellow tint caused by a slight (0.1-0.2 at%) iron impurity in the sand used.

*Table 6 Nominal and actual glass compositions determined by ICP-OES and XRF*

| | MW | | CaZn | | ISG | |
|---|---|---|---|---|---|---|
| mol% | Nominal | Actual | Nominal | Actual | Nominal | Actual |
| $SiO_2$ | 59.98 | 62.24 | 48.69 | 47.67 | 60.20 | 55.35 |
| $B_2O_3$ | 18.97 | 18.75 | 20.61 | 20.58 | 16.00 | 14.44 |
| $Al_2O_3$ | | 3.87 | 2.53 | 9.92 | 3.78 | 11.43 |
| $Na_2O$ | 10.50 | 10.13 | 8.51 | 7.78 | 12.63 | 10.93 |
| CaO | | | 6.60 | 6.02 | 5.7 | 5.01 |
| ZnO | | | 4.48 | 5.46 | | |
| $Li_2O$ | 10.55 | 5.00 | 8.57 | 2.57 | | |
| $ZrO_2$ | | | | | 1.7 | 2.83 |

### 2.3.5. Nuclear Magnetic Resonance

All experimental NMR spectra were acquired in collaboration with researchers from University of Liverpool on a 400 MHz Bruker Avance III HD spectrometer using a Bruker 4 mm HXY Magic Angle Spinning (MAS) probe in double resonance mode. MAS frequency of 8 kHz was used. The nuclear spin quantum number (I) and Larmor frequency ($\nu_0$) of each nucleus are indicated below. Glass powder samples were packed into commercial 4 mm zirconia Bruker rotors. Experimental 1D MAS NMR spectra were fitted using a version of the Czjzek distribution using the software DMFit (84). Spectra were optimised to achieve the best possible fit with an error of +/- 1.

$^{11}B$ (I =3/2, $\nu_0$= 128 MHz) MAS NMR spectra were acquired using small nutation angle pulses corresponding to a $\pi/18$ flip angle to ensure quantitative spectra (85). A radiofrequency field (rf) amplitude of 50 kHz as measured on the reference $NaBH_4$ was used on all three glasses. A recycle delay of 50 seconds was found to be sufficient to allow for complete longitudinal relaxation by carrying out a saturation recovery experiment on the $^{11}B$ nuclear spins in all three glass compositions. Rotor-synchronised $^{11}B$ Hahn echo MAS NMR spectra were acquired using the Hahn echo ($\pi/18 - \tau - \pi/9$ -τ- acq) pulse sequence. $^{11}B$ shifts were referenced externally to the field-independent $NaBH_4$ signal at 41.4 ppm that corresponds to the primary reference $BF_3.Et_2O$ resonating at 0.0 ppm.

$^{27}Al$ (I = 52, $\nu_0$ = 104 MHz) MAS NMR spectra were acquired using a $\pi/2$ flip angle. A radio frequency field amplitude of 56 kHz as measured on the reference, 0.1 M $Al(NO_3)_3$, was used for all three glass compositions. A recycle delay of 5 s was found to be sufficient to allow for complete longitudinal relaxation of $^{27}Al$ nuclear spins in each of the three glass compositions. Recycle delay times were determined by carrying out a saturation recovery experiment. $^{27}Al$ shifts were referenced externally to the field-independent 0.1 M $Al(NO_3)_3$ in $H_2O$ resonating at 0.0 ppm. Triple quantum Multi-Quantum MAS (MQMAS) with a Z-filter

pulse sequence were recorded on all samples to determine the number of aluminium sites in the glass network (86,87).

### 2.3.6. Pair Distribution Function Data Collection

X-ray scattering measurements were performed at the i15 beamline at Diamond Light Source (DLS) (Didcot, UK) using high energy synchrotron X-rays with a photon energy of 76.69 keV (wavelength λ = 0.161669 Å). The glass powder was loaded into a 1.1 mm polyamide tube with a wall thickness of 0.05 mm and the ends of the tube sealed with a small quantity of cyanoacrylate adhesive. Measurements were carried out on an empty tube to act as a background, and sample measurements were made using 10 min intervals with sample spinning used and the sample position shifted slightly to reduce damage caused by high energy X-ray radiation.

The scattering data was processed using GudrunX software to remove the sample background and self-scattering effects, merge the data sets, and extract the distinct scattering (S(Q)) (88). A top hat function within GudrunX was applied to the S(Q) to minimise any remaining background effects. The T(r) was obtained by Fourier transforming the S(Q) using a Lorch modification function with a Qmax = 27 $Å^{-1}$ and the density measurements shown in table 5 (89).

Neutron scattering measurements were carried out using the GEM beamline of the ISIS pulsed neutron source (Didcot, UK). Samples of glass were placed in a 10.3 mm vanadium can. The packing height and weight of the sample were recorded and used to calculate the packing fraction for use in sample corrections. A rod of vanadium-niobium null alloy and an empty sample can were also measured to enable calculation and subtraction of the sample background. GudrunN and the ATLAS suite of programs were used to analyse and normalise the data using the technique described by Alderman *et al.* (88,90,91). The distinct scattering was collected to Qmax = 60 $Å^{-1}$ and Fourier transformed with a Lorch and

Step function to produce two differing neutron data sets for each glass. The atomic density and $T_0r$ were calculated using XSect, initial atomic density and $T_0r$ values were calculated using the nominal composition, and the final values used were calculated with the actual composition and densities shown in tables 8 and 9. Initial fitting of the first three peaks in the neutron data was carried out using PNfit. The latter portions (> ~ 1.8 Å) were fitted using NXfit to enable the simultaneous fitting of both sets of corelation functions (92). Data analysis was performed using the nominal composition as a starting point for data normalisation, the data were later renormalised using the actual composition resulting in the early portion of the neutron data being nonlinear.

The $^{27}Al$ and $^{11}B$ NMR data collected was used to determine the Al-O coordination of four and constrain the $BO_3$ to $BO_4$ peak area ratio, respectively. The Si-O peak coordination was also fixed at 4 as the glass network is expected to only contain silicate tetrahedra. The σ values (where σ represents the standard deviation of the average interatomic distance for a given pair of atoms in a PDF) of the Ca-O peak for ISG, Na-O and, Li-O peaks in all glasses were fixed based on previous literature values (17,18). The Ca-O σ value for CaZn was constrained based on literature values (17). In all samples the end fit was obtained through varying the neutron and X-ray weighting from 0.5:0.5 to 0.7:0.3 with the B-O and Si-O values fixed to values obtained from neutron data.

### 2.3.7. Raman Spectroscopy

Raman data was collected using a Senterra Ramanscope Spectrometer on fragments recovered from the crucible walls. The following settings were used on all samples a 532 nm laser set at a power of 20 mW with a 50x magnification lens. To reduce noise during collection a spectrum collection time of 15 s with 30 accumulations and a 25x1000 µm aperture was used. The data was baseline corrected, temperature and excitation line

corrected using a method adapted from Long, and normalised to the highest peak position (93).

The $Q_n$ region was fitted with a Pseudo Voigt function using the default PsdVoigt2 function in OriginPro 9.1. In accordance with values obtained from previous literature, the $Q_n$ region (where n represents the quantity of bridging oxygen present on a silicon oxygen tetrahedra) in CaZn and ISG was fitted with five peaks and the following peak position constraints were applied to fitted peaks positions: 900 -930 ($Q_1$), 950-1000 ($Q_2$), 990-1040 (Al-O), and 1050 – 1100 $cm^{-1}$ ($Q_3$) (79,94,95). Due to the low quantity of alumina present in MW it was not possible to fit the Al-O peak separately and a four peak fit was carried out.

## 2.4. Results

### 2.4.1. Nuclear Magnetic Resonance

The $^{27}$Al-MAS-NMR spectra of all glasses (shown in figure 14) contained a single broad site at approximately 55 ppm which featured tailing to the right-hand side. This is characteristic of a tetrahedrally coordinated aluminum species (96) . Multi Quantum Magic Angle Spinning (MQMAS) measurements (shown in figure 15) showing a single broad site further confirmed the presence of a single aluminum environment (97).

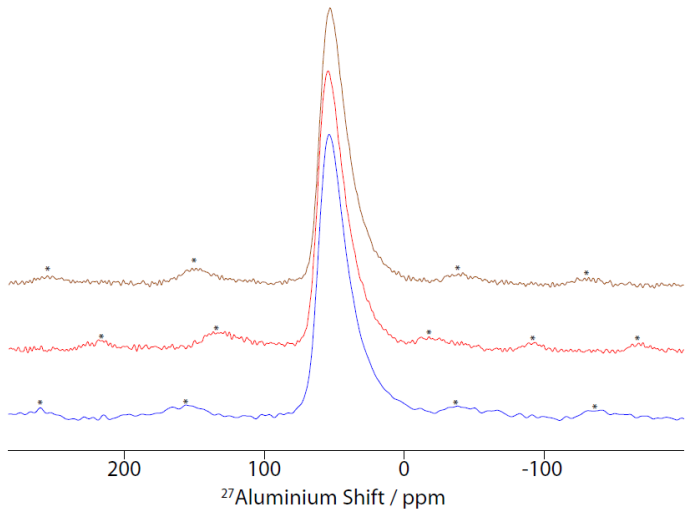


*Figure 14 $^{27}$Al MAS NMR spectra of the three glass compositions MW (blue), CaZn (red) and ISG (brown) with spinning side bands marked with *.*

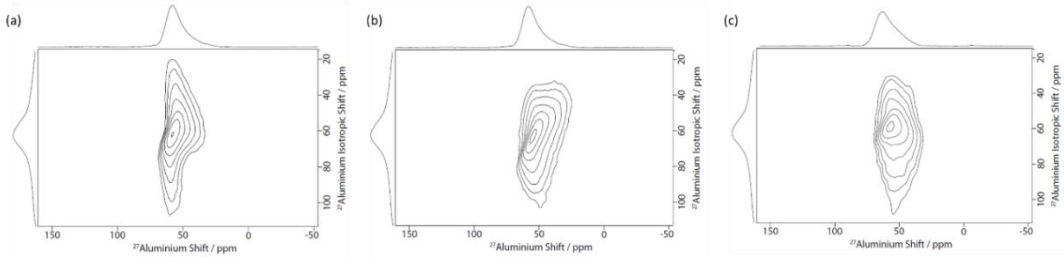


*Figure 15 $^{27}$Al MQMAS spectra of the three glass compositions (a) CaZn (b) ISG and (c) MW.*

The $^{11}$B-MAS-NMR (in figure 16) shows two sites corresponding to B-$O_3$ and B-$O_4^-$ structural units; however, these two sites did not fully resolve at the field strength used. The three coordinate borate site was located at approximately 15 ppm whereas the four coordinate borate site was located at approximately 0 ppm. The ratio of the two sites varied depending on the quantity of boron and the amount of charged network modifiers present. In all cases the B-$O_3$ site consisted of a single wide peak, with differing degrees of peak tailing present and the B-$O_4^-$ site consisted of a single signal with minimal tailing present. The B-$O_3$:B-$O_4^-$ ratios shown in table 7 were obtained through fitting both the main peaks and any side bands present using DMfit and the Czjzek distribution (84).

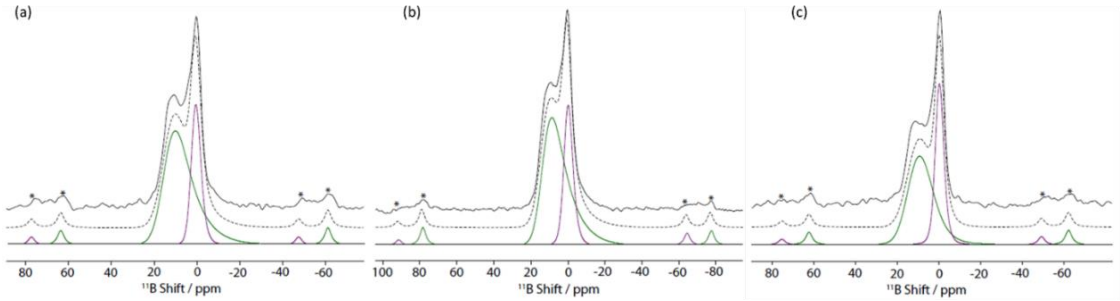


*Figure 16 $^{11}B$ MAS NMR spectra of the three glass compositions, (a) CaZn (b) ISG and (c) MW. Spinning sidebands denoted by asterixis. (a) and (c) carried out at MAS frequency 8 kHz and (b) at 10 kHz all at magnetic field 9.4 T.*

*Table 7 $BO_3$:$BO_4$ ratio obtained from NMR. ± refers to error on set of ratios.*

| Glass | $BO_3$:$BO_4$ site ratios |
|---|---|
| MW | 59:41 ± 1 |
| CaZn | 67:32 ± 1 |
| ISG | 68:32 ± 1 |

### 2.4.2. Pair Distribution Functions

With the exception of CaZn, the Q space data shown in figure 17 lacks the presence of Bragg peaks demonstrating the glass is amorphous with minimal phase separation present. The CaZn X-ray S(Q) spectra shows a very small quantity of Bragg peaks and, because these peaks are absent in the neutron data (as shown figure 18), their presence is believed to be the result of small amounts of X-ray damage to the sample. In all data sets the corrected and normalised X-ray S(Q) and neutron i(Q) shown in figure 17 were Fourier transformed with a Lorch function to give the PDFs shown in figure 19.

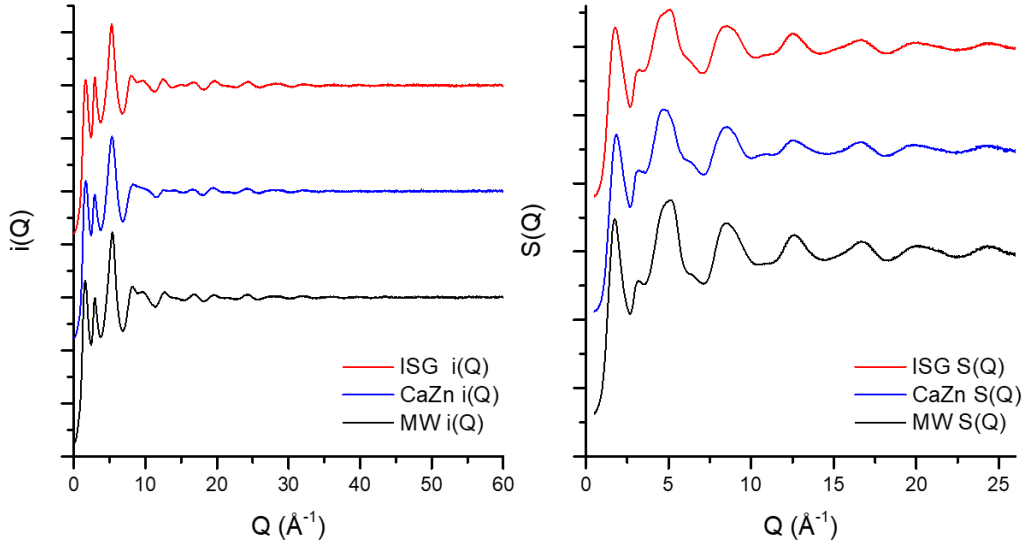


*Figure 17 ISG, CaZn, and MW normalised neutron i(Q) processed using ATLAS, and normalised X-ray S(Q) processed using Gudrun X, offset for clarity*

The resulting PDFs consisted of a complex series of overlapping peaks. The main features observed in each neutron data set prior to fitting correspond to B-O bonds (1.38-1.47 Å) (21,83,98), Si-O (~1.62 Å) (18,21,83), Li-O (17), Zn-O (99), and Zr-O (22) observed in MW, CaZn, and ISG respectively (between 1.95 and 2.10 Å), O-B-O (~2.42 Å) (98,100), and O-Si-O (~1.62 Å) (18). Due to the differing Qmax values obtained, the X-ray data set was less well resolved than the neutron data particularly in the B-O region, which was not clearly visible due to the poor X-ray scattering of boron and peak broadening originating from the lower Qmax value. In order to make full use of the high neutron

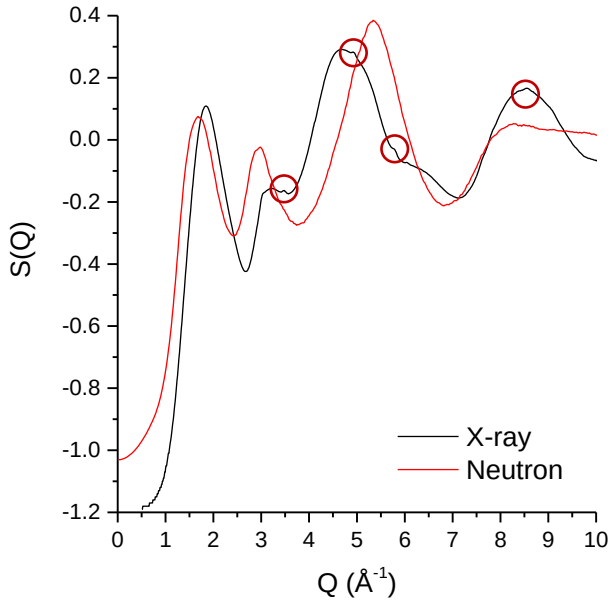


*Figure 18 Overlaid CaZn neutron and X-ray S(Q), overlaid and scaled to illustrate the presence of Bragg peaks (circled in red) in the X-ray S(Q)*

Qmax, the neutron i(Q) and S(Q) were also Fourier transformed using a Step correction. The Step corrected data is shown in figure s1 and s2 of the supplementary section. The full multi component simultaneous fits are shown in figure 20 and 21, and results are shown table 8. These are discussed further in text.

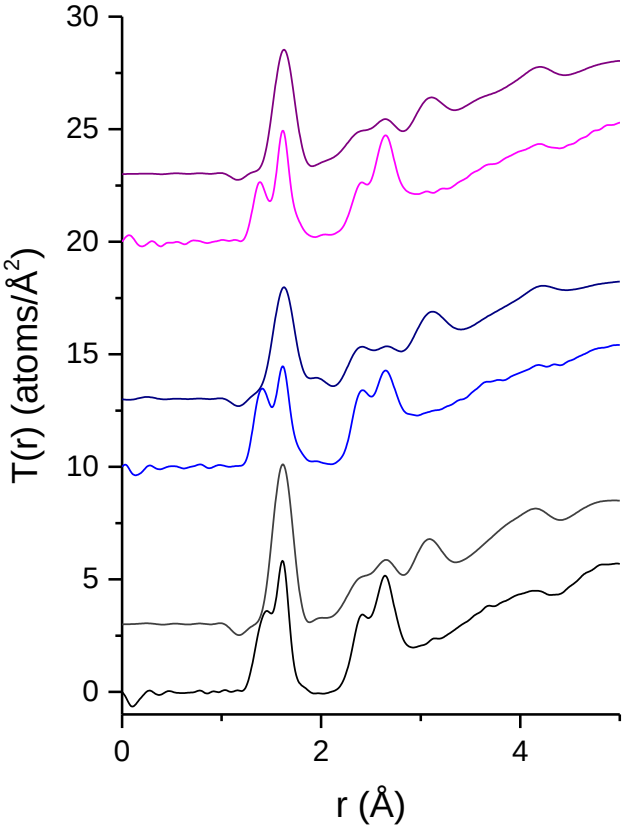


*Figure 19 Overlaid ISG (purple, top X-ray, bottom neutron) CaZn (blue, top X-ray, bottom neutron) and MW (black, top X-ray, bottom neutron) X-ray and neutron T(r) functions normalised to atoms/Å2, and offset for clarity*

*Table 8 PDF fit results. Values marked with * indicate fixed values*

| | MW | | | CaZn | | | ISG | | |
|---|---|---|---|---|---|---|---|---|---|
| | Bond length/ Å | Co-ord | σ | Bond length/ Å | Co-ord | σ | Bond length/ Å | Co-ord | σ |
| B-$O_3$ | 1.3822± 0.0006 | 1.655± 0.006 | 0.0632± 0.0006 | 1.378±0 .002 | 1.92± 0.02 | 0.057± 0.002 | 1.370± 0.003 | 1.943± 0.005 | 0.050± 0.001 |
| B-$O_4$ | 1.474± 0.001 | 1.534± 0.001 | 0.0510± 0.0008 | 1.481± 0.003 | 1.263± 0.003 | 0.057± 0.005 | 1.466± 0.006 | 1.22± 0.01 | 0.063± 0.003 |
| Si-O | 1.6156± 0.0002 | 4* | 0.0511± 0.0002 | 1.6168± 0.0002 | 4* | 0.050± 0.001 | 1.6135± 0.0005 | 4* | 0.0501± 0.0005 |
| Al-O | 1.775± 0.005 | 4* | 0.063± 0.001 | 1.7425± 0.0002 | 4* | 0.080± 0.006 | 1.731± 0.007 | 4* | 0.085± 0.002 |
| Zn-O | | | | 1.95± 0.05 | 4.1± 0.1 | 0.107±0 .004 | | | |
| Li-O | 1.85± 0.02 | 3±1 | 0.103* | 1.85* | 3* | 0.103* | | | |
| Li-O | 2.21± 0.02 | 1.2± 0.2 | 0.103* | 2.21* | 1.2* | 0.103* | | | |
| Zr-O | | | | | | | 2.03± 0.09 | 3.2± 0.3 | 0.06± 0.07 |
| Zr-O | | | | | | | 2.3± 0.2 | 2.4± 0.7 | 0.2± 0.1 |
| Na-O | 2.28± 0.01 | 1.84± 0.04 | 0.107* | 2.32± 0.04 | 1.8± 0.4 | 0.107* | 2.30± 0.09 | 1.8± 0.3 | 0.107* |
| Na-O | 2.60± 0.09 | 3.9± 0.2 | 0.229* | 2.5± 0.2 | 3.4± 0.6 | 0.229* | 2.55± 0.05 | 3.3± 0.5 | 0.229* |
| Ca-O | | | | 2.364± 0.003 | 6.0± 0.5 | 0.087± 0.003 | 2.368± 0.008 | 6.0± 0.6 | 0.13* |
| O-$BO_2$ | 2.3712± 0.0009 | 0.71± 0.06 | 0.09± 0.02 | 2.36± 0.01 | 0.830± 0.002 | 0.06± 0.02 | 2.39± 0.04 | 0.56± 0.07 | 0.094± 0.009 |
| O-$BO_3$ | 2.402± 0.003 | 0.99± 0.05 | 0.065± 0.001 | 2.45± 0.01 | 0.9± 0.1 | 0.06± 0.01 | 2.39± 0.02 | 0.5± 0.2 | 0.056± 0.009 |
| B-O-B | 2.60± 0.02 | 1.1± 0.1 | 0.11± 0.02 | 2.548±0 .008 | 0.28± 0.09 | 0.07± 0.03 | 2.68± 0.01 | 0.09± 0.02 | 0.012± 0.006 |
| Si-O-B | 2.81± 0.03 | 3.7± 0.4 | 0.20± 0.02 | 2.79± 0.04 | 5.4± 0.9 | 0.21± 0.06 | 2.8± 0.1 | 6.0± 0.9 | 0.16± 0.03 |
| O-Si-O | 2.638* | 3.22± 0.06 | 0.094± 0.002 | 2.6403* | 2.66± 0.05 | 0.090± 0.003 | 2.635* | 3.0± 0.1 | 0.094± 0.008 |
| O-Al-O | 2.899* | 0.448* | 0.08± 0.02 | 2.8455* | 1.141* | 0.107± 0.005 | 2.826* | 1.307* | 0.19± 0.04 |

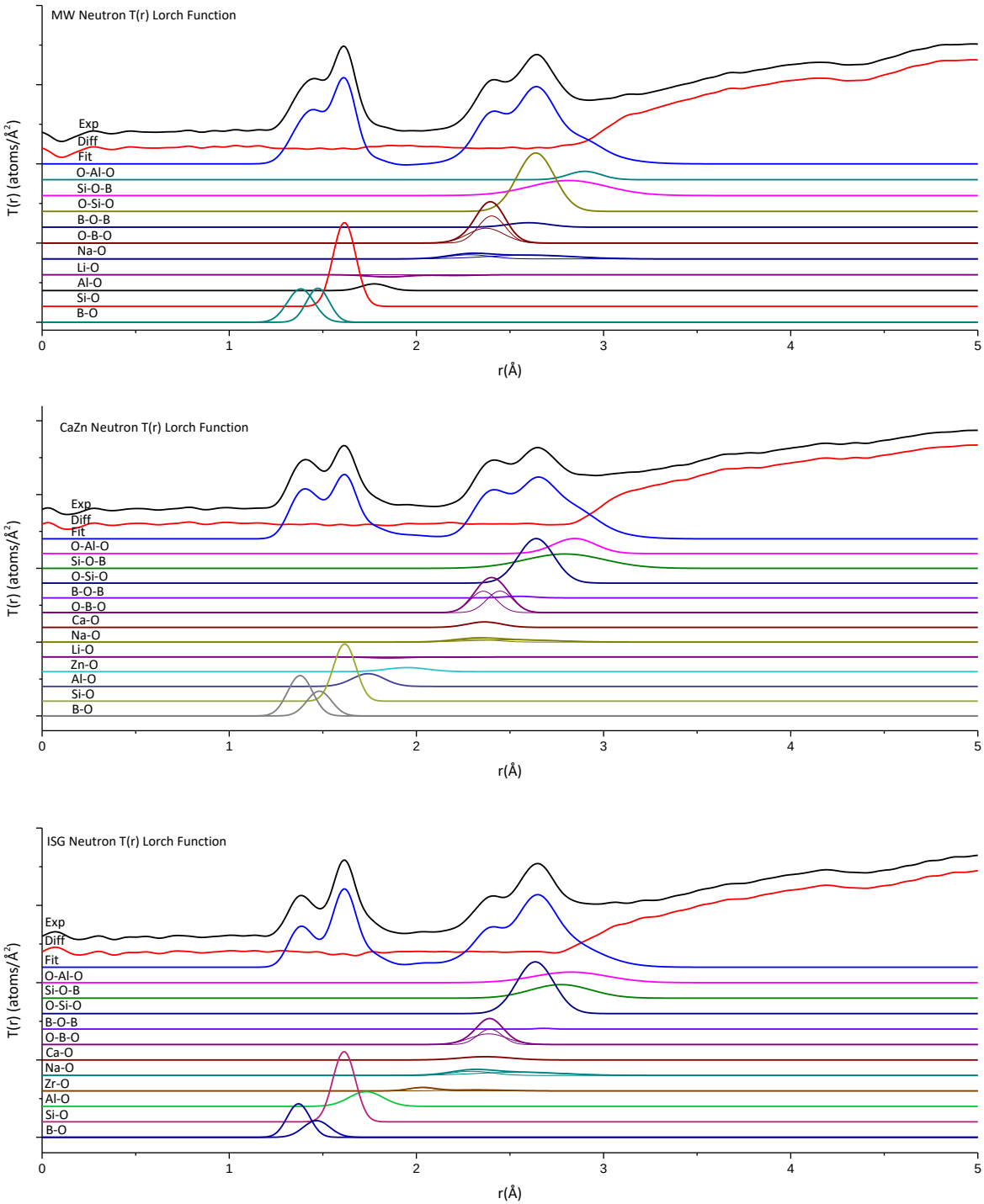


*Figure 20 Full neutron T(r) fits, individual peaks offset for clarity*

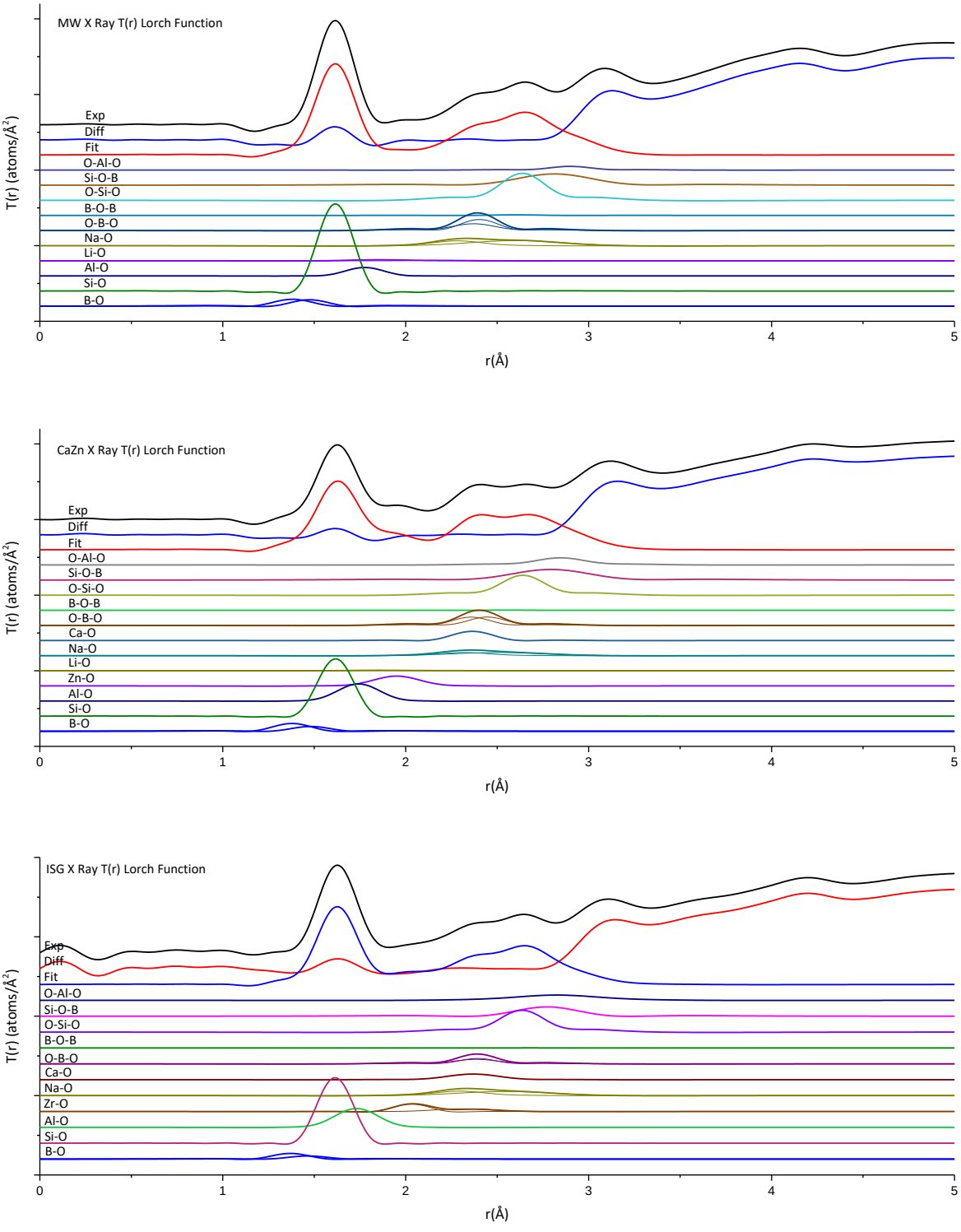


*Figure 21 Full X-ray T(r) fits, individual peaks offset for clarity*

### 2.4.3. Raman Spectroscopy

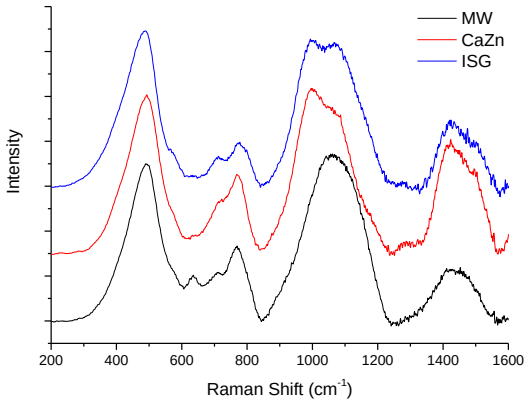


*Figure 22 Full MW, CaZn, and ISG Raman spectra showing key regions present in all glasses*

The $Q_n$ regions in CaZn and ISG glasses were fitted with five peaks corresponding to the $Q_1$ to $Q_4$ Si-O bonding and an expected Al-O contribution in order to estimate the $Q_n$ ratios. This showed that these glasses contain mainly $Q_3$ and $Q_4$ structural units. MW was fitted with four peaks, as no distinct Al-O peak was present. This resulted in a higher than expected $Q_2$ contribution; however, this peak was disregarded as despite the lack of distinct Al-O peak the $Q_2$ peak is likely to contain a comparably significant Al-O contribution. With the exception of the $Q_2$ region again the two most distinct peaks in MW were the $Q_3$ and $Q_4$ peak. The resulting fits and full spectra are shown in figures 22, 23 and table 9.

*Table 9 $Q_n$ percentages estimated using raman. The $Q_2$ region is intentionally omitted from MW due to difficulties in fitting the Al-O peak*

| | MW | | CaZn | | ISG | |
|---|---|---|---|---|---|---|
| Assignment | Raman Shift ($cm^{-1}$) | %$Q_n$ ratio | Raman Shift ($cm^{-1}$) | %$Q_n$ ratio | Raman Shift ($cm^{-1}$) | %$Q_n$ ratio |
| $Q_1$ | 919.62 | 9.83 | 913.02 | 10.34 | 924.02 | 7.64 |
| $Q_2$ | 1000.00 | | 959.98 | 16.70 | 971.67 | 15.59 |
| Al-O | | | 1000.00 | N/A | 999.79 | N/A |
| $Q_3$ | 1070.98 | 55.64 | 1078.00 | 55.05 | 1077.42 | 51.40 |
| Q4 | 1143.81 | 34.52 | 1156.43 | 17.92 | 1150.77 | 25.37 |

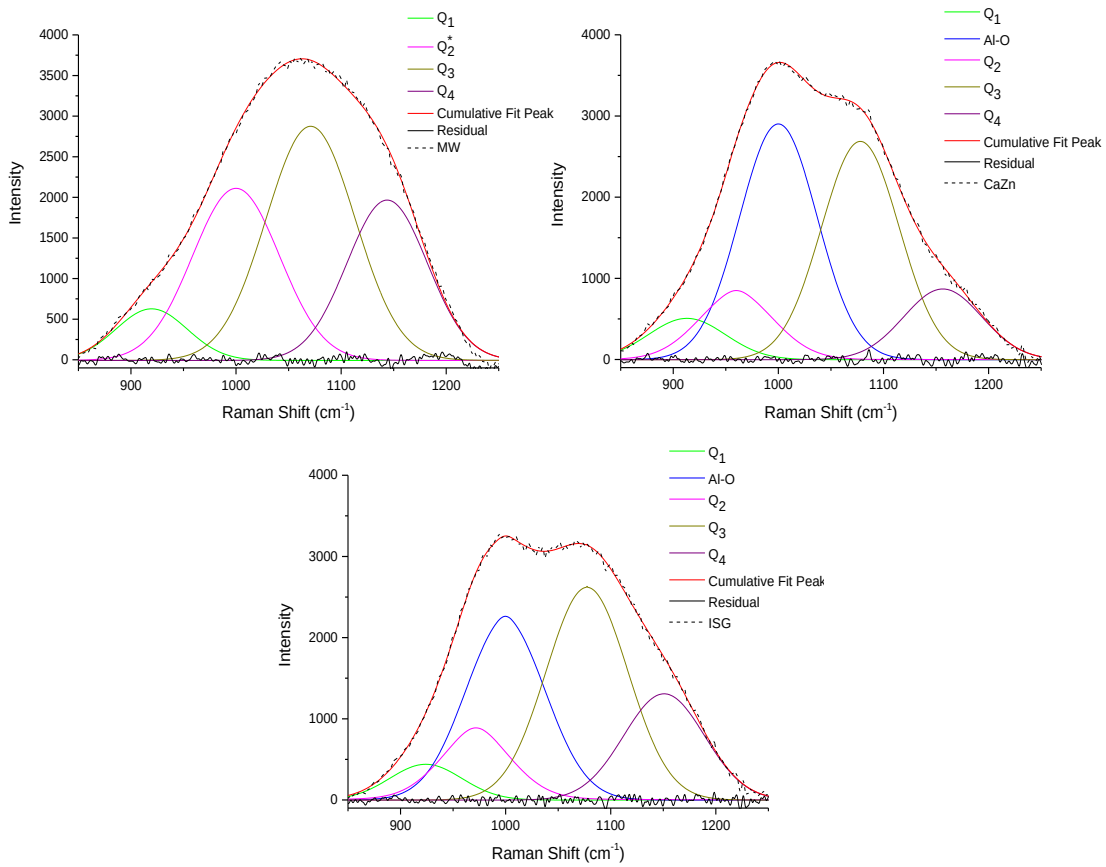


*Figure 23 $Q_n$ region Raman spectra fits*

## 2.5. Discussion

The use of simultaneous fitting of X-ray and neutron PDFs in combination with NMR has enabled the deconvolution and fitting of PDF data collected from MW, CaZn, and ISG glasses. If the PDF is thought of as the sum of the partial PDFs weighted according to scattering magnitudes, then fitting both data sets simultaneously becomes effectively the same as solving two simultaneous equations, where the individual equations have multiple complex answers. Using this method, it has been possible to deconvolute the latter regions (>2 Å) of the PDFs revealing structural information about the coordination and bonding of the network modifiers present.

This method is not well suited for fitting atom pairs where there is a significant difference between the X-ray and neutron scattering magnitudes of both atoms in an atom pair. This is demonstrated by the poor match between the X-ray and neutron data at <2 Å (shown in

figure s2 and s3) that occurs as a result of the B-O atom pair being both a poor X-ray scatterer due to boron and oxygen having a low atomic number and a strong neutron scatterer due to the comparably large coherent neutron scattering of $^{11}B$ and oxygen. This issue was further compounded by excessive broadening of the Si-O peak in the X-ray PDF data; this results in a mismatch between the X-ray and neutron PDFs, and nearly fully obscures both the B-O and Al-O region in all glasses. This was overcome through the use of $^{11}B$ and $^{27}Al$ MAS-NMR to gain information on the $B\text{-}O_3$:$B\text{-}O_4$ ratio (shown in table 7) and aluminum coordination number.

### 2.5.1. Nuclear Magnetic Resonance

$^{27}Al$-MAS-NMR was carried out to better understand the aluminium coordination as it can display variable coordination with 4, 5, or 6 coordinate species possible. Additionally, due to a combination of complex peak overlap and issues involving peak broadening of Si-O present in the X-ray PDF, it was not possible to accurately determine the aluminium coordination from PDF data alone. The $^{27}Al$-MAS-NMR contained a single site located at 55 ppm characteristic of tetrahedrally coordinated aluminium bonded to silicate as $[Al(OSi)_4]^-$. However, peak tailing resulting from the quadrupolar spin, 5/2, of the $^{27}Al$ nuclei was also present. The degree of quadrupolar tailing present was sufficient to obscure any potential minor peaks corresponding to small quantities of octahedrally coordinated aluminium (located at approximately 0 ppm) and aluminium bonded to borate as $[Al(OB)_4]^-$ (located between 40-45 ppm). In order to determine if any minor peaks were present $^{27}Al$-MQMAS was carried out. In all glasses studied the $^{27}Al$-MQMAS showed only the single site corresponding to $[Al(OSi)_4]$ was present. From this it can be inferred that the aluminium is directly incorporated into the silicate glass network, where the $AlO_4^-$ structural unit will charge balance positively charged network modifiers.

In order to deconvolute the B-O region in the PDF data the $B\text{-}O_3$:$B\text{-}O_4^-$ ratio (shown in table 7) was calculated through fitting of $^{11}$B-MAS-NMR using DMfit and the Czjzek distribution. The $^{11}$B-MAS-NMR spectra consisted of two partially resolved sites corresponding to the $B\text{-}O_3$ and $B\text{-}O_4^-$ structural units and, as $^{11}$B is a spin 3/2 nuclide, quadripolar broadening is also observed in the $^{11}$B-MAS-NMR. The two sites displayed differing degrees of quadrupolar broadening with the $B\text{-}O_3$ site showing the greatest degree of peak broadening resulting in an asymmetric tailing peak shape that overlaps the $B\text{-}O_4^-$ site. Compared to the $B\text{-}O_4^-$ site the $B\text{-}O_3$ sites show a greater degree of variation in peak tailing between the different glasses.

This introduces the possibility that a portion of the $B\text{-}O_3$ peak tailing is related to the presence of differing quantities of ring and non-ring borate with both the ring and non-ring sites expected to produce broad overlapping signals, where the non-ring site is located approximately 5 ppm lower than the ring site (101). It is not possible to comment on the degree of silicon boron mixing using this data due to the proximity, and thus overlap, of the $B\text{-}O_3$ and $B\text{-}O_4^-$ sites where the separation between boron bonded to borate $[B(OB)_4]^-$ and boron bonded to silicate $[B(OSi)_4]^-$ is expected to be approximately 1.8 ppm (101).

## 2.5.2. Pair Distribution Functions

### *2.5.2.1. B-O to Al-O Region*

The first three peaks, shown in figure 24 and table 8, were fitted using only the neutron data to allow for boron being a poor X-ray scatterer due to its low atomic weight. To allow for the poor fit shown by Si-O in the X-ray data, the Al-O peak position was fitted with a 0.9:0.1 neutron to X-ray weighting (fit shown in figure 24) and latter peak positions were fitted by varying the neutron to X-ray weighting from 0.5:0.5 to 0.7:0.3. This is illustrated in table 8, figure 20, and figure 21.

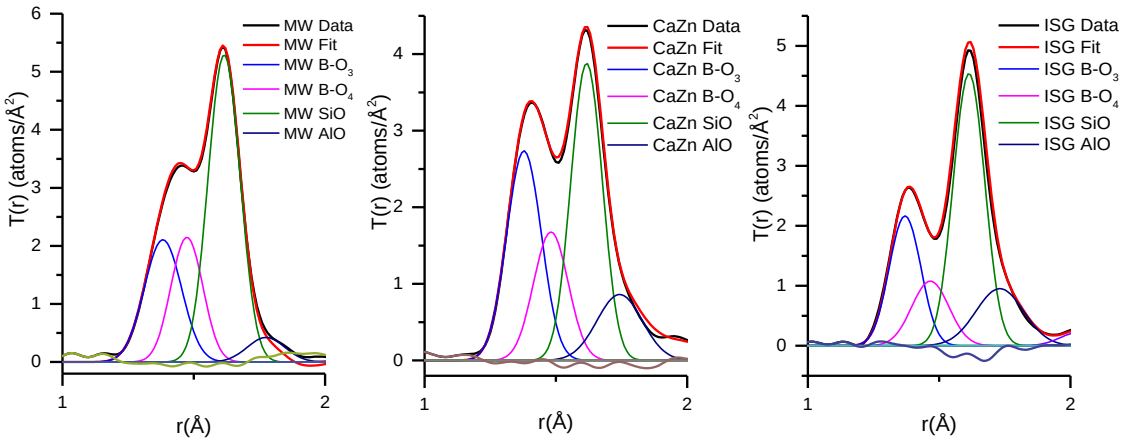


*Figure 24 First four peak fits in MW, CaZn, and ISG*

In all neutron PDF data sets, the two B-O peaks were closely overlapping and poorly resolved, resulting in the singular distorted Gaussian peak observed in the data Fourier transformed with the Lorch function. As discussed in the results section (section 2.4.2) the neutron data was also Fourier transformed with a Step correction to aid in deconvoluting PDF regions containing large and overlapping peaks. With the exception of ISG, the B-O peaks remained poorly resolved in the data Fourier transformed using a Step correction. In ISG these peaks were only partially resolved, and a direct fit was not possible due to overlap with both the Si-O peak and the termination ripples. In the X-ray data the weakly scattering B-O peaks were nearly completely obscured by both the large Si-O peak and a

slightly negative error peak originating from imperfect data correction, and were not directly fitted due to this.

In order to apply the $B\text{-}O_3$:$B\text{-}O_4$ ratio calculated through NMR, the expected observed B-O coordination for both was calculated and the ratio of peak areas were bound using PNFit with neighbouring Si-O and Al-O peaks fixed at a coordination number of four. The binding of the B-O ratios using this method enabled the single distorted B-O peak seen in the neutron PDFs (which were Fourier transformed with a Lorch function) to be deconvoluted. In order to further confirm these peak positions, the data was also fitted to the Step corrected neutron PDF.

In all cases the pre-normalisation boron coordination numbers calculated through binding peak ratios were approximately 0.1 lower than expected, which resulted in post normalisation coordination numbers that were typically 0.2 lower than expected. A slight reduction in coordination number obtained from neutron PDFs is expected to occur as a result of peak dampening due to finite Q space resolution. However, the peak dampening, which is a result of Q space resolution, is expected to be <1% of the expected coordination number given the high Qmax measured. However deviation from the expected B-O coordination was as high as 5.4% in one sample.

Two potential explantations are given for the slightly lower than expected B-O coordination number obtained. One explanation is that this is due to a cumulative peak dampening effect which arises from the coordination number of the neighbouring large Si-O and Al-O peaks being fixed at 4. The second explanation is this is due to the presence of overlapping ring and non-ring $B\text{-}O_3$ peaks causing the “total” $B\text{-}O_3$ peak to be slightly distorted such that the peak shape is no longer fully Gaussian and therefore, if fitted with a single Gaussian, is likely to be under or over fitted. The fixed peak areas of the neighbouring peaks would minimise overfitting but would not prevent underfitting. Due to the method of peak

binding used, any underfitting of the B-$O_3$ peak would cause the peak area binding to also underfit the B-$O_4$ peak.

The bond lengths obtained for the two B-O environments are in good agreement with previous literature values obtained through neutron diffraction of borate glass (1.37±0.01 Å and 1.47±0.02 Å for B-$O_3$ and B-$O_4$ respectively) (102), and atomistic modeling for borosilicate glass (1.388 Å and 1.47 Å for B-$O_3$ and B-$O_4$ respectively) (98). In the MW and CaZn data sets, the B-$O_3$ peak is the same as or wider than the B-$O_4$ peak. This is slightly unexpected as, due to a combination of greater thermal motion modes and tetrahedral distortion, a larger spread of bond lengths are expected in the B-$O_4$ region. This spread was observed in ISG, however. Additionally, the B-$O_3$ σ values seem to be related to total boron quantity where a higher total boron content, not boron coordination ratio, resulted in a higher σ. This adds further weight to the proposal that a mix of ring and non-ring B-$O_3$ structures are present in these glasses, with the higher boron content glasses containing a greater mix of ring and non-ring borate. The position of the B-$O_4$ peak showed slightly more variation between the three glasses studied than position of the B-$O_3$ peak. While there does not appear to be a clear relationship between peak position and boron content or peak position and borate coordination ratio, the changes in peak position are likely to be related to the degree of silicon boron mixing present, as the $[B(OB)_4]^-$ bond is expected to sit at approximately 1.47 Å and $[B(OSi)_4]^-$ bond expected to sit at approximately 1.485 Å (98).

As discussed previously both the Si-O and Al-O peaks were fixed at a coordination number of four. The silicate peak position was approximately 1.62 Å and the peak itself was very narrow in all glasses indicating minimal distortion of the Si-O bond was present. The Si-O bond length (1.616 – 1.1617 Å) in the glass used for this study was found to be slightly lower than has previously been found from direct fitting of lithium and sodium silicate glass

PDFs (1.622 Å and 1.6249 Å respectively), but is consistent with values of 1.60 ± 0.005 found through fitting with atomistic modeling of a multicomponent sodium borosilicate glasses (17,18,100).

The neighbouring Al-O peak showed the greatest variation in peak position of all the network component peaks. The peak positions observed seem to show a shortening in bond length with increasing Al content, with MW having the greatest Al-O bond length at 1.78 Å and ISG having the shortest at 1.73 Å. Given that the NMR data indicates that Al-O is primarily bonded to Si and that Al is four coordinate, the degree of variation in bond length is somewhat surprising. Typically variations in Al-O coordination are attributed to a change in coordination number ratio (103,104), however, NMR studies have demonstrated that this is not the case here in this work. This suggests an alternate mechanism, such as tetrahedral distortion, is responsible for the variation seen.

#### *2.5.2.2. O-O Region*

Theoretically the adjacent O-B-O peak region should contain two separate peaks corresponding to the different boron coordinations present. However, when the bond lengths of the two peaks are calculated geometrically the separation between the peaks in MW and ISG is <0.02 Å. CaZn has the greatest peak separation at ~0.03 Å which is reflected in both the Lorch function and Step corrected neutron data where clear evidence for the presence of two peaks is seen. Using values calculated from the two B-O peaks in the glasses, the O-B-O peaks are expected to lie between 2.37–2.42 Å in all glasses investigated in this study.

Following initial peak fitting, maximum values for all O-O peak coordinations were calculated using equations 1, 2, 3, and 4 shown below, where $N_a$ is the percentage of atoms of element a in a glass, $N_i$ is the percentage of atoms of element i in a glass, $N_3$ is the % of the total boron present as three coordinate, $N_4$ is the % of the total boron present as four

coordinate, and $N_{a\text{-}l}$ is the expected coordination number observed in the PDF (18). Fits of the O-O peaks caried out without peak area constraints gave unreasonably high coordination numbers when compared to the calculated values. This overfitting is the direct result of it not being possible to account for the B-O-B and Si-O-B peaks overlapping this region. Additionally, without the use of calculated values it was not possible to fit the O-B-O region as two separate peaks resulting in a poor match for peak shape in the O-B-O region. As the two O-B-O peaks did not resolve in any of the MW and ISG neutron data sets, these regions were fitted with peak constraints based on the calculated bond length and peak area values. The O-B-O peaks in CaZn were partially resolved in the Step corrected neutron data, due to this the peak areas were not constrained in the final fit of this region. The O-Si-O peak is fit is discussed in more detail in section 2.5.2.2.

$$N_{O-BO_3} = \frac{2 \times 6N_4N_B}{N_O}$$

*Equation 1 $N_4$ = % of total boron present as four cordinate, $N_B$ = atomic fraction of boron present, $N_o$= atomic fraction of oxygen presnt*

$$N_{O-BO_2} = \frac{2 \times 3N_3N_B}{N_O}$$

*Equation 2 $N_3$ = % of total boron present as three cordinate, $N_B$ = atomic fraction of boron present, $N_o$= atomic fraction of oxygen present*

$$N_{OSiO} = \frac{12N_{Si}}{N_O}$$

*Equation 3 $N_{Si}$ = atomic fraction of silicon present, $N_o$= atomic fraction of oxygen present*

$$N_{OAlO} = \frac{2 \times 12N_{Al}}{N_O}$$

*Equation 4 $N_{Al}$ = atomic fraction of Aluminium present, $N_o$= atomic fraction of oxygen presnt*

The results obtained for the O-B-O region coordination numbers in MW and CaZn as shown in table 8 and 10 were consistently higher than the calculated values by 5 – 10% while the value for ISG was near identical to the calculated values, however due to the complexity of this region in ISG this value was more heavily constrained for ISG. The increased coordination number is likely to be the result of uncertainties surrounding these peaks due to the complex nature of this region of the PDF. The results are expected to be close to the calculated values, due to minimal boron non-bridging oxygen formation, but not exceed them.

*Table 10 Fitted bond length and coordination values sown with calculated values for clarity. Fix used to indicate this value was fixed at the calculated value during PDF fitting.*

| | MW | | | | CaZn | | | | ISG | | | |
|---|---|---|---|---|---|---|---|---|---|---|---|---|
| | Fitted | | Calculated | | Fitted | | Calculated | | Fitted | | Calculated | |
| | Bond length/Å | Coord | Bond length/Å | Coord | Bond length/Å | Coord | Bond length/Å | Coord | Bond length/Å | Coord | Bond length/Å | Coord |
| O-$BO_2$ | 2.3712±0.009 | 0.71±0.06 | 2.3941 | 0.64 | 2.36±0.01 | 0.830±0.002 | 2.39 | 0.793 | 2.39±0.04 | 0.56±0.07 | 2.37 | 0.56 |
| O-$BO_3$ | 2.402±0.003 | 0.99±0.05 | 2.407 | 0.89 | 2.45±0.01 | 0.9±0.1 | 2.42 | 0.8 | 2.39±0.02 | 0.5±0.2 | 2.39 | 0.5 |
| O-Si-O | Fix | 3.22±0.06 | 2.638 | 3.60 | Fix | 2.66±0.05 | 2.6403 | 2.74 | Fix | 3.0±0.1 | 2.635 | 3.2 |
| O-Al-O | Fix | Fix | 2.899 | 0.448 | Fix | Fix | 2.8455 | 1.141 | Fix | Fix | 2.826 | 1.307 |

With the exception of ISG the fitted O-$BO_2$ bond length showed shortening compared to the calculated value (shown in table 10) whereas with the exception of MW the O-$BO_3$ bond showed a slight lengthening compared to the calculated value (shown in table 10). The deviation from calculated values is not entirely unexpected given the σ values seen in the B-O region indicated the presence of distortion in the B-$O_3$ triangles, what is unexpected is the magnitude of this distortion as due to thermal motion the distortion of B-$O_4$ tetrahedra and therefore change in O-$BO_3$ bond length is expected to be greater than the change in O-$BO_2$ bond length. Additionally, the σ values for the O-B-$O_2$ peak are smaller than the values calculated for the O-B-$O_3$ peak in MW and ISG indicating there is less variation in the distortion surrounding the B-$O_3$ providing further evidence for the presence of borate rings.

The O-Si-O peak was fitted using the method described in Hannon *et al*., where O-Si-O bond lengths are calculated and fixed using the assumption that minimal tetrahedral distortion is present in the glass (18). The calculated bond lengths showed a good match with the PDF data; however, the σ values and areas obtained from initial fits of this peak were higher than expected for a borosilicate glass. This was assumed to be a result of overlap between the O-Al-O and Si-O-B peaks as these are also expected to be present in this region, and in later fits these peaks were added to allow for this. Further evidence of there being additional peaks overlapping the O-Si-O peak was found due to the presence of a slight shoulder in the O-Si-O region of the MW and CaZn Step corrected neutron PDFs. In order to fit these peaks, the O-Si-O σ values were bound between 0.8 and 0.9 and the position of the O-Al-O peak was fixed using the previously discussed calculated area and approximate peak positions calculated using the same method as was utilised for the O-Si-O peak.

The variable bond lengths and comparably high σ values of the Al-O peak indicate that the actual O-Al-O peak position is highly likely to vary from the calculated peak position, due to tetrahedral distortion, and therefore the O-Al-O peak position used is seen as a rough approximation carried out with the aim of improving the fit of neighbouring peaks. The Si-O-B and B-O-B peaks were fitted with this same goal of improving the O-Si-O fit. These two sets of peaks were fitted using estimates taken from previous literature as a start point and were fitted without constraints (83,105). Due to the complexity of this region and the large degree of uncertainty surrounding these peaks the O-Al-O, B-O-B, and B-O-Si peak will not be discussed in any detail here. Once the initial fit for this region had been carried out, the O-Si-O σ value bounds were removed and a second fit was carried out. This unbound second fit showed σ values which are more consistent with previous literature values in all cases.

The coordination numbers obtained for the O-Si-O region (shown in table 10) were all lower than the calculated value indicating the expected presence of small quantities of NBO. When normalised by percentage against the theoretical maximum value of 6 the O-Si-O coordination number was approximately 5 in all glasses indicating the glass network is well bridged.

#### *2.5.2.3. Network Modifiers and Minor Intermediates*

Due to a combination of lithium being lost from the glass melt, lithium itself being both a poor X-ray and negative neutron scatterer, Li-O having an asymmetric line shape, and a slight iron impurity (0.1-0.2 at%) resulting in the presence of a small Fe-O peak in the Li-O region, it has not been possible to reliably fit the Li-O region present in MW and CaZn. Attempts have been made to fit the Li-O region in MW by varying the weighting ratios applied to the X-ray and neutron PDFs; however, all attempts have resulted in a mismatch between the data and its fit in the neutron PDF or unreasonable coordination numbers and bond lengths. The current fit has been achieved *via* fixing σ to values obtained in a study which investigated silicate glass containing a relatively high quantity of lithium when compared to the glasses used in this study (17). Additionally, the study by Vaishnav *et.al.* was also used to constrain the bond lengths and coordination numbers (17). Due to MW and CaZn having comparable compositions and the presence of a larger overlapping Zn-O peak in CaZn, the values used in CaZn were fixed at the most reasonable Li-O data set obtained from MW.

In CaZn the Zn-O peak sat at a near identical bond length to the Li-O peak. The Zn-O peak fit showed good agreement with bond length values of 1.95 ± 0.01 Å obtained from previous studies involving the structural role of zinc in simulant UK nuclear waste glasses (99). The only significant deviation from previous studies involving experimental data was seen in the

σ values, with the σ value obtained here being much greater than the σ value of 0.08 obtained from extended X-ray absorption fine structure data (EXAFS) (99).

The Zr-O peak in ISG was present at approximately 2.2 Å in both the neutron and X-ray PDF. No prior studies involving the direct fitting of PDFs for silicate, borate, or borosilicate glass containing zirconium are known. Previous studies involving the fitting of an MD model of ISG to an X-ray PDF have shown a poor match between PDF fit and calculated model for this area (21). Initial attempts at fitting a single peak to the Zr-O region here also resulted in an unreasonably low Zr-O coordination below 4 and a poor match between X-ray and neutron PDF fittings. What this, and the poor fits in earlier studies, suggests is that Zr-O displays an asymmetric line shape. Further evidence of this is seen in literature EXAFS data which showed that ISG has two main Zr-O environments present, one 6 coordinate and one 7 coordinate, with a minor 5 coordinate component (22). To allow for asymmetry resulting from the presence of multiple coordination environments, the Zr-O region was fitted with two peaks, which showed both a better agreement between the X-ray and neutron PDFs and a more reasonable coordination number than a single peak fitted in this region.

The Na-O peak has been fitted with two peaks to allow for the expected peak tailing observed in previous studies involving sodium silicate glass (17,18). The Na-O peaks have been fitted using σ values and bond lengths taken from sodium silicate glass as a starting point. Due to the large degree of overlap with the surrounding peaks, the Na-O σ values were fixed and the coordination number constrained such that the sum of peak areas cannot result in a coordination number greater than 6. Initial fits were done where bond lengths were fixed at values obtained from a sodium silicate glass (18). This resulted in a poor match between the X-ray and neutron data, and so bond lengths were allowed to vary to improve the overall fit. The coordination numbers obtained showed a slight increase with increasing boron content.

A relationship between boron content and sodium coordination has been previously observed in studies involving sodium borosilicate glass with alumina added (106). Upon plotting the sodium coordination number obtained here against the percentage of boron in the network formers present a comparable approximately linear relationship is observed, shown in figure 25. The relationship between aluminium network component percentage and sodium coordination number seems to be the inverse of the relationship between boron and sodium coordination number. While this relationship between Na-O coordination and aluminium network component percentage is not as distinct as it is with boron, this does add some support to the possibility that the variation in Al-O bond length is related to degree of charge competition between boron and aluminium.

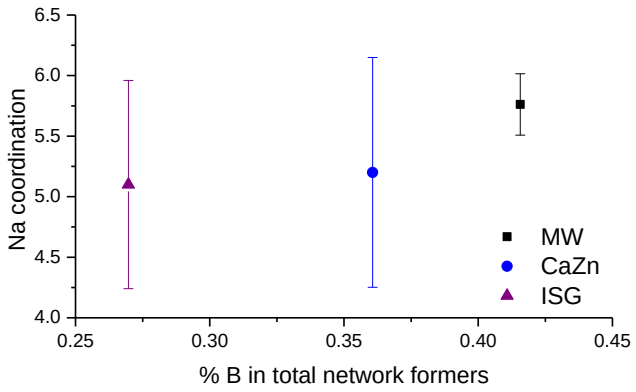


*Figure 25 Na coordination vs % B in total network formers. Error bars shown are sum of errors for both Na peak coordination numbers.*

The Ca-O peak in both CaZn and ISG were fitted in using the same method as the Na-O peak, but with data taken from a calcium silicate glass used as the starting point (17). The σ value was kept fixed in ISG and was allowed to vary slightly in CaZn. This decision was made as the Ca-O peak is much more prominent in CaZn than in ISG, due to its higher calcium content, and a poor match was found in CaZn between the neutron and X-ray data fit when the σ value was fixed. The Ca-O coordination number was found to be ~6 in both calcium containing glasses with a peak position of ~2.4 Å in both.

### 2.5.3. Raman Spectroscopy

The $Q_n$ region of the Raman spectra shown in figure 23 were fitted with the PsdVoigt2 function in accordance with the proposal that the peaks present in the $Q_n$ region of glass have a mixed Gaussian, Lorentzian line shape (107). In the PsdVoigt2 function the Gaussian Lorentzian character of a peak is given as a peak shape number, with a peak shape of 0 indicating the peak has a primarily Gaussian shape and peak shape number of 1 indicating the peak is primarily Lorentzian. In this case the peak shape number was found to be near 0 or 0 for many peaks indicating that overall the peaks present have a primarily Gaussian line shape.

With the exception of MW, which was fitted with four peaks in the $Q_n$ region, the $Q_3$ and $Q_4$ peaks are the largest Si-O peaks in the $Q_n$ region. Indicating the glasses studied contain mostly $Q_3$ and $Q_4$ units. It was not possible to fit five peaks in the $Q_n$ region of MW and this has resulted in an overly large peak seen in the $Q_2$ region. This peak was disregarded as this occurs in the same region as the Al-O peak seen in spectra fitted with five peaks, indicating the presence of a significant Al-O contribution.

While the fully bridged $AlO_4$ tetrahedron is expected to be the dominant Al-O structural unit occurring in the same region as the Si-O $Q_n$ contribution, the overall impact of Al-O on the Raman spectra both overlaps and has the same degree of complexity as the varying Si-O regions. In addition to the Al-O peak the presence of small quantities of Si-O-Al linkages are expected to produce a peak present between 900 - 940 $cm^{-1}$ , this may have further impacted the $Q_n$ region fitting (95). This contribution would be present in the same region as the $Q_1$ peak. Due to the presence of varying Al-O contributions the $Q_n$ ratios obtained from Raman are considered an estimate. The average $Q_n$ number obtained from Raman was ~3, which is slightly lower than expected given the O-Si-O coordination obtained from

PDF work, and is taken to be an indication that the presence of Al-O, in particular the Al-O-Si linkage, has not been fully taken into account during fitting of the Raman $Q_n$ region.

## 2.6. Conclusion

A method for use in the direct fitting of complex multicomponent glass PDF data has been demonstrated using MW, CaZn and ISG, and the ISG fit has been compared to previous fits (21,22,83). The combined use of X-ray and neutron PDF, and $^{11}B$ and $^{27}Al$ MAS NMR has revealed new information about B-O behaviour, by enabling the deconvolution of the B-O and O-B-O region in all glasses, and new information on Al-O structure and bond length by removing uncertainty surrounding aluminium coordination environment. Using information gained from simultaneous PDF fitting it has been possible to near fully deconvolute the O-O region of the three multicomponent glasses to reveal the underlying network modifier peaks. From this and the fitting of network modifiers occurring in earlier regions it is proposed that the asymmetric PDF line shapes observed in the smaller group one and two metals may also be encountered in other small metallic network modifiers, such as zirconium. The structural information gained from these three glasses will be of use in future attempts at both fitting multicomponent glass PDFs, and atomistic modeling of glasses.

# 3. Gamma Irradiation-Induced Structural Changes in Glass

## 3.1. Abstract

Samples of MW and CaZn base glass, and ISG glass have been irradiated to doses of ~5 and ~10 MGy and studied with Raman, UV-Vis-NIR and X and Q band EPR spectroscopy. Selective recombination with UV light combined with results obtained from UV-Vis-NIR have been used to partially simulate the EPR spectrum of gamma irradiated MW revealing evidence supporting the presence of sodium clustering, while the higher band EPR data has revealed evidence supporting potential calcium clustering in CaZn glass. Raman data indicates that structural rearrangement takes place in UK base glass at high doses though these changes have been partially obscured by fluorescence originating from electronic defect formation. Additional samples of these glasses irradiated to a dose of ~8 MGy have been studied using X-ray scattering. This has revealed distinct structural changes within the glass including the presence of potentially crystalline phase separation related to aluminum content occurring at doses at and above ~8 MGy. These results indicate that electronic defect formation and structural reorganisation within glass have different dose thresholds with structural reorganisation occurring at a higher dose then electronic defect formation.

## 3.2. Introduction

In the UK high level radioactive waste (HLW) is incorporated into glass in a process known as vitrification (2). The vitrified waste form will be exposed to large amounts of self-irradiation from the incorporated waste. It is therefore important to characterise radiation induced changes in glass to understand is long term stability during storage and eventual disposal. Three approaches can be taken in order to quantify the effects of radiation on glass, atomistic modeling, internal irradiation, where small quantities of short-lived radioactive material are included in glass, and external irradiation where the glass is exposed to a high dose radiation source.

Internal irradiation using doping with short-lived active isotopes is widely considered to be the most representative of the damage that will be found in the actual waste form, but it is also the most difficult technique to carry out due to requiring handling of active materials in the glass making process and subsequent analysis (108,109). While the resulting active glass can be stored until the radiation has decayed to safe levels, this does not seem to be a common practice and instead the glass is studied as the radiation decays. The use of internal irradiation mirrors the conditions that the HLW glass will be exposed to and is one of the few methods of accurately modeling homogeneous internal structural damage caused by alpha and beta radiation.

Atomistic modeling combined with experimental data has the potential to reveal detailed information about the structural changes that take place at a molecular level in a glass exposed to radiation over time scales and doses impractical for use in experimental studies (24,110). However, as discussed in previous publications (111), due to the nature of amorphous materials this technique suffers heavily from the lack of data needed to produce an accurate starting point to model the pristine non-irradiated glass structure. There are currently no full atomistic models of UK base glass so an aim of this previous study was to provide the key experimental data on bond lengths and coordination numbers needed to underpin a full atomistic model of UK base glass (111). The data collected here on the effects of radiation on UK base glass can be combined with the proposed atomistic model to further the understanding of radiation effects on glass.

External irradiation is the most commonly used method of studying radiation effects on glass. This method varies depending on the exact type of radiation being studied with the ballistic effects of alpha radiation and recoil, and ionising effects of beta radiation typically studied through the use of ion beam techniques, and electromagnetic radiation studied through exposure to gamma radiation produced by an external source such as $^{60}Co$. Ion

beam irradiation can produce doses equivalent to the predicted lifetime dose of the waste form in hours although due to the poor penetration depth of alpha radiation, beta radiation, and heavy ions used to simulate alpha recoil, this damage will be localised to a small region of the glass surface. This creates a range of issues with considerable debate surrounding how representative the effects of using a high dose rate and the effects of heavy ions are of the damage caused by alpha and beta decay of the elements contained within actual HLW glass (34,41,109,112). Additionally, common methods of calculating radiation damage depth may not give accurate results for glass (79), making it is difficult to determine the thickness of the radiation-damaged portion of the sample without physically damaging the irradiated portion of the sample surface. A poor understanding of radiation damaged sample thickness also makes the sample potentially unsuitable for use in leaching trials, as is it possible for the amount of altered glass to exceed the thickness of the radiation damaged portion of the glass surface and, because of this, the decision was made to focus on the impact of gamma radiation on glass behaviour.

Gamma radiation will penetrate the entire sample thickness, resulting in homogeneous radiation damage to a sample. As a result of this the damage caused by internal gamma radiation is expected to be near-identical to irradiation from an external source. While the damage occurs homogeneously across the entire sample thickness, when compared to ion beam techniques longer irradiations are needed to accumulate doses equivalent to those expected to during the waste lifetime. In an actual HLW glass alpha, beta, and gamma irradiation would occur simultaneously. Despite this, compared to alpha, beta radiation and associated ion beam techniques, the impact of gamma radiation on glass structure is poorly understood.

### 3.2.1. Gamma Irradiation Effects

As the photon has a zero rest mass, gamma radiation damage is expected to primarily consist of electronic effects with the most obvious impact of gamma radiation on glass structure observed in the form of a distinctive colour change (29). This colour change can be partially or fully reversed through exposing the glass to UV light or annealing the glass slightly below the Glass Transition Temperature ($T_g$) point (36,113). The colour change is the result of electronic defect formation within the glass structure. The electronic defects shown in table 11 are expected to form in sodium borosilicate glass as a result of gamma irradiation (45,46,114).

*Table 11 Defect centres observed in sodium borosilicate glass • denotes radical.*

| | |
|---|---|
| Boron Oxygen Hole Center (BOHC) | 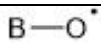 |
| Hole Center$_1$ ($HC_1$) | 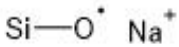 |
| E' center |  |
| PerOxy Radical (POR) | 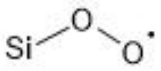 |
| Non Bridging Oxygen Hole Center (NBOHC) | 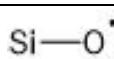 |
| $BO_3$ | 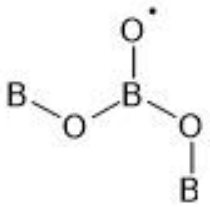 |
| BOSi | 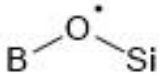 |
| BOB | 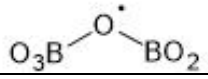 |

The persistence of these electronic defects leads to difficulty untangling structural changes such as changes in the amount of non-bridging oxygen from effects associated with the formation of electronic defects as both will be removed by annealing the glass near the $T_g$

point. Compared to defect recombination with UV light, thermal annealing following gamma irradiation is a more widely used method. This is typically caried out at >300 °C with the aim of simulating the self-heating aspect of vitrified HLW and comes to the conclusion that the impact of gamma radiation on waste durability will be minimal as a large portion of the structural changes and electronic defects will be annealed out of the glass by self-heating (33,36). What this method often fails to consider is the timeline of irradiation with the gamma-emitting daughter nuclei, produced by decay of long lived elements, expected to be present long after the elements responsible for self-heating have mostly decayed and the dose dependence of structural changes vs dose dependence of electronic defects. It is proposed that, in order to fully understand all the changes that take place as a result of gamma radiation, electronic defects should be considered separately from physical changes with the recombination of electronic defects with UV light being used to reveal underlying structural changes.

The electronic defects responsible for the colour change taking place are poorly understood, as are the effects of gamma radiation on the glass network structure. This is in part due to the structural changes that take place being highly dependent on glass structure, with elements such as transition elements and lanthanides which display variable coordination, improving the radiation resistance of glass by acting as a hole sink through a redox mechanism (43,115).

In the absence of interference originating from electronic defects, structural changes can then be more easily observed via techniques such as Raman spectroscopy, since electronic defects tend to introduce a strong fluorescent background in Raman spectra. This background is not removed through standard techniques, such as sample bleaching, used to reduce Raman fluorescence. The only method that has been found to be somewhat effective in removing this baseline is exposure to UV light prior to data collection.

The complexity of glass alteration mechanisms further complicates any attempts at modeling the impact of gamma radiation on stability of the vitrified waste form in a GDF environment. While it is widely agreed that structural degradation will increase the rate of glass alteration in the earlier stages of water exposure, the effects on the latter stages of glass alteration are less clear due to gel layer behaviour and precipitation of secondary phases being the controlling factors (44,116). The overall residual rate of glass alteration is controlled by rate limiting processes occurring within the gel layer. The exact nature of these rate limiting processes are somewhat debated and while it is unlikely the behaviour at the glass gel – layer interface will be a rate limiting process it will impact the gel layer thickness and formation rate (54).

The behaviour at the unaltered glass - gel layer interface can be broadly grouped into two categories: ion exchange of soluble elements through the gel layer, and hydrolysis of the silicate glass network. If ion exchange dominates, the effects of increased ion mobility with the glass due to radiation damage will be significant, whereas if hydrolysis dominates the effects of radiation on the later stages of glass alteration will be minimal (116,117). At elevated temperatures, such as those caused by beta radiation associated self-heating, hydrolysis at the glass gel layer interface is expected to be the dominant process (117). However, once the container temperature begins to lower, ion exchange through the gel layer can then become a more dominant process, which would result in the formation of a thicker gel layer (117).

A final aspect of gamma radiation induced damage that has not been well considered is the potential for phase separation and devitrification of glass. Evidence of phase separation and devitrification has been encountered during X-ray Pair Distribution Function (PDF) work carried out here (discussed in section 3.4.3), yet this does not seem to be well documented in current literature (82,118). The lack of previous data on phase separation is

believed to be in part due to dominant use of laboratory X-Ray Diffraction (XRD) in verifying that a glass is amorphous, combined with the strong amorphous glass background, and the size and quantity of the crystals potentially formed due to phase separation. Very small crystals will result in extensive peak broadening at the wavelength range used in typical laboratory XRD, and peaks originating from small quantities of small crystals will be invisible against the strong amorphous background produced by the glass. As demonstrated by the Scherrer equation this peak broadening will be greatly reduced at the high X-ray energy used in X-ray PDF work (119). Additionally, the use of long XRD measurement times may also induce small amounts of electronic defects and radiation damage in the glass sample. This can potentially interfere with establishing a non-irradiated baseline for a glass. This has been observed in UV-Vis-NIR studies (shown in figure s5 in Supplementary chapter) where a slight nonlinear background was observed in some samples subjected to long XRD measurements prior to UV-Vis-NIR analysis.

## 3.3. Experimental

### 3.3.1. Glass Preparation

ISG was prepared from batch using the following quantities of reagent grade materials: $SiO_2$-84.4 g $Na_2CO_3$-31.16 g, $H_3BO_3$ -46.17 g, $Al(OH)_3$-13.84 g, $CaCO_3$-13.32 g and $ZrO_2$-4.92 g. The MW and CaZn glasses were prepared from frit supplied by the NNL (Seascale UK). 50 g of full lithia MW frit, and 97.90 g of half lithia CaZn with 5.19 g $Li_2CO_3$ added to make this glass to the full lithium specification was used. All glasses were prepared using fresh alumina crucibles.

The glasses were prepared in two batches. The first batch was melted in an electric furnace with a ramp rate of 2 °C/min and a hold time of approximately 4 hours, with a hold temperature of 1150 °C used for MW and 1350 °C used for ISG. The molten glasses were poured onto a room temperature steel plate allowed to cool for a few seconds and cast

into ingots with the excess ISG from this melt being cast into a small glass disc. All glasses were annealed at 480 °C for 2 hours then allowed to cool to room temperature at a rate of approximately 0.5 °C/min inside the closed, turned off furnace. The ISG prepared from batch was intentionally improperly annealed as this batch of glass was produced with the intention of being ground, remelted and properly annealed at a later date to ensure homogeneity. This was, however, not possible due to Covid-19 related travel restrictions. The ISG and CaZn melt produced a clear very pale green/blue glass with the ISG displaying significant cracking due to poor annealing. The MW melt produced a clear, very pale-yellow glass. The colouration of the MW glass is believed to be due to trace impurities present in the glass.

A second batch of full lithia CaZn glass, designated CaZn 2, was prepared at a later date using the same ratio of $Li_2CO_3$, batch of frit, and electric furnace, as the initial batch. The following melting conditions and ramp rate were used 2 °C/min, with a hold temperature of 1050 °C, a hold time of 4 hours, and a covered crucible was used to prevent trace contamination from other glass melts prepared at the same time in the same furnace. The glass was poured on a room temperature steel plate, allowed to cool briefly, and shaped into ingots before being annealed at 500 °C for 3 hours then allowed to cool to room temperature at a rate of approximately 0.5°C/min inside the closed, turned off furnace. This melt produced a clear pale blue/green glass identical in colour to the first batch of CaZn glass produced.

Monoliths of glass were cut from the glass ingots using a Struers Accutom-5 cutting machine and a diamond tipped cutting blade then wet polished to a 5 µm surface finish using SiC paper. The remaining glass was powdered using the method, used for $^{11}B$ glass, described in Brown *et.al* (111).

### 3.3.2. Gamma Irradiation

Gamma irradiation was carried out using a Foss Therapy Services 812 $^{60}$Co irradiator. Five separate sets of gamma irradiations were carried out. The first irradiation was carried out using glass powder for use in the PDF work. The second was performed in two stages using selected monoliths and samples of powdered MW, CaZn and ISG. These samples were irradiated first to a dose of ~5 MGy then to a dose of ~ 10 MGy for use in leaching experiments. The third irradiation was carried out to a total dose of ~5 MGy using only MW and CaZn ingots for use in future leaching experiments, and to enable the collection of better quality UV-Vis-NIR data. A fourth irradiation of small fragments of MW and CaZn was carried out in two parts to enable the collection of EPR data from freshly irradiated glass to determine an appropriate dose for the higher EPR band experiments. A fifth and final batch of MW and CaZn powder was irradiated to a total dose of ~5 MGy for use in higher band EPR experiments. Tables 12, 13, 14, 15 and 16 show the exact dose and dose rate used.

*Table 12 Gamma irradiation parameters used for all PDF samples*

| Glass | MW powder | CaZn powder | ISG powder | $^{11}$B MW powder | $^{11}$B CaZn powder | $^{11}$B ISG powder |
|---|---|---|---|---|---|---|
| Duration h | 400 | 400 | 400 | 400 | 400 | 400 |
| Ave dose rate Gy/min | 328 | 328 | 315 | 328 | 328 | 315 |
| Total dose MGy | 7.862 | 7.862 | 7.556 | 7.862 | 7.862 | 7.556 |

*Table 13 Gamma irradiation parameters used for initial set of monolith samples*

| Glass | MW monoliths | CaZn monliths | ISG monoliths |
|---|---|---|---|
| Duration h | 402 | 402 | 402 |
| Ave dose rate Gy/min | 209 | 202 | 212 |
| Total dose MGy | 5.042 | 4.866 | 5.121 |
| Duration h | 373 | 404 | 373 |
| Ave dose rate Gy/min | 215 | 206 | 209 |
| Total dose MGy | 9.854 | 9.863 | 9.808 |

*Table 14 Gamma irradiation parameters used for second set of monolith samples*

| Glass | MW monoliths | CaZn monliths |
|---|---|---|
| Duration h | 465 | 441 |
| Ave dose rate Gy/min | 179 | 189 |
| Total dose MGy | 4.998 | 4.999 |

*Table 15 Gamma irradiation parameters used for 10 MGy EPR samples*

| Glass | MW fragment | CaZn fragment |
|---|---|---|
| Duration h | 336 | 336 |
| Ave dose rate Gy/min | 250 | 250 |
| Total dose MGy | 5.044 | 5.044 |
| Duration h | 385 | 385 |
| Ave dose rate Gy/min | 215 | 215 |
| Total dose MGy | 10.001 | 10.001 |

*Table 16 Gamma irradiation parameters used for 5 MGy EPR samples*

| Glass | MW powder | CaZn powder |
|---|---|---|
| Duration h | 465 | 441 |
| Ave dose rate Gy/min | 179 | 189 |
| Total dose MGy | 4.998 | 4.999 |

### 3.3.3. Raman Spectroscopy

Raman measurements were collected from pristine and irradiated polished glass monoliths using a Senterra Ramanscope Raman microscope. Initial measurements were carried out on the first set of ~5 MGy glass monolith samples using the following settings, a 532 nm laser set at 5 mW power, with 20x magnification, a 60 s integration time, 30 coadditions, and a 25x1000 µm aperture. With the exception of the ~5 MGy ISG sample these measurements were repeated using the following settings 532 nm laser set at 20 mW, 50x magnification, an integration time of 15 s, 30 coadditions and a 25x1000 µm aperture. The 50x magnification setting produced a less noisy data. In order to minimise the amount of noise present and reduce the impact of poor signal obtained from glass, the MW and CaZn Raman spectra were averaged using a minimum of three different spectra and the ISG samples were averaged using two different spectra. The averaged Raman data was baseline

corrected, temperature and excitation line corrected using a method adapted from Long, and normalised to the highest peak position (93). The normalised and corrected data was fitted using either the default PsdVoigt1 or PsdVoigt2 line shape in OriginPro 9.1.

### 3.3.4. UV-Vis-NIR Spectroscopy

UV-VIS-NIR measurements were carried out using a Cary 5000 UV-Vis-NIR spectrophotometer operated in dual beam mode with air as a baseline. The thickness of the polished glass monoliths was measured using digital calipers, and the monoliths were mounted on a standard solid sample holder using small quantities of reusable adhesive putty. Measurements were carried out at a range of 190 – 3300 nm and the default scan rate and detector change over points were used. Prior to running the samples, beam alignment was checked using zero order mode. The initial set of measurements were run at half beam height in order to ensure the beam of light was not clipped by the solid sample holder and these measurements were repeated at full beam height for MW and CaZn. ISG was not re-run due to time constraints and lack of sample availability. The spectra were averaged across a minimum of three measurements and processed using the method given in Rautiyal et al. (36). The resulting rescaled and normalised spectra were fitted using the default Gauss function in OriginPro 9.1.

### 3.3.5. Electron Paramagnetic Resonance Spectroscopy

Information on the EPR-active electronic defects were collected from pristine and irradiated MW and CaZn glass using a Bruker EMX Nano X band EPR spectrometer and a Bruker EMX Plus Q band EPR spectrometer. Measurements were carried out at room temperature using quartz glass tubes and the sample mass was recorded to enable normalisation by sample mass. The X band UV exposure EPR measurements were carried out in situ using a mercury arc lamp equipped with a fibre optic attachment with measurements taken at 3 min intervals for the first 2.5 h and then at 22 min intervals. The

Q band UV EPR measurements were carried out ex situ using a dark box fitted with a xenon arc lamp. Q band EPR measurements were taken at 5, 10, 15, 30, 60 and 120 min UV exposure intervals and the temperature in the dark box was monitored to ensure it did not exceed 50 °C to prevent excessive temperature-related recombination of EPR active defects. EPR data simulation and fitting was carried out using the EasySpin Matlab program.

### 3.3.6. X-Ray Scattering

Using the method described in Brown *et.al*, X-ray scattering measurements were performed at the i15 beamline at Diamond Light Source (Didcot, UK) using high energy synchrotron X-rays with a photon energy of 76.69 keV (wavelength λ = 0.161669 Å) (111). The samples of pristine and irradiated glass powder were loaded into 1.1 mm polyamide tubes with a wall thickness of 0.05 mm and the ends of the tubes were sealed with a small quantity of cyanoacrylate adhesive, measurements were carried out on an empty tube to act as a background, and sample measurements were made using 10 min intervals with sample spinning used and the sample position shifted slightly to reduce damage caused by high energy X-ray radiation.

The scattering data was processed using GudrunX software to remove the sample background and self-scattering effects, merge the data sets, and extract the distinct scattering (S(Q)) (88). A top hat function within GudrunX was applied to the S(Q) to minimise any remaining background effects. The S(Q) collected from the irradiated glass showed significant Bragg peaks, indicating phase separation of the irradiated glass has taken place. Due to evidence of phase separation and the absence of sufficient irradiated glass to collect accurate density measurements, the S(Q) data collected from irradiated glass was not Fourier transformed to r space to give a PDF.

## 3.4. Results and Discussion

### 3.4.1. Raman Spectroscopy

Raman spectroscopy is a non-destructive technique that can aid in understanding the changes that take place as a result of irradiation. Here attempts have been made at deconvoluting the $Q_n$ region in MW, CaZn, and ISG glasses irradiated to total doses of ~5 MGy and ~10 MGy. To allow for different magnification settings the Raman data discussed in this section were collected using two different sets of settings. Due to variations in signal to noise ratio and baseline caused by difficulties in collecting spectra, changes in peak height between regions are not discussed in detail as in weakly scattering materials, such as glass, peak height is highly susceptible to distortion originating from differing baselines and data collection settings.

Initial attempts at fitting were carried out using a Gaussian line shape, but this resulted in a poor fit, which was latter reattempted using the Pseudo Voigt functions in OriginPro 9.1 Within OriginPro 9.1 two Pseudo Voigt functions are available: PsdVoigt1, which fits a convolution of Gaussian and Lorentzian curves with a fixed linewidth and PsdVoigt2, which fits a convolution of Gaussian and Lorentzian with a mixed Gaussian, Lorentzian linewidth. In both functions a profile shape factor is calculated where a value of 0 represents a primarily Gaussian peak while a profile shape factor of 1 represents a primarily Lorentzian peak shape. As the peaks can contain varying degrees of Gaussian and Lorentzian character in all data sets fitting was attempted with both (107). The fit that gave the best $X^2$ value with minimal variations in peak width and change in peak position between the pristine and irradiated glass was considered to be the best fit. The Voigt function present in OriginPro 9.1 was not used as this uses Gaussian, Lorentzian peak width as a means of determining the Gaussian, Lorentzian character of the peak. This made the function unsuitable for use as it is not possible to apply constraints to peak width without also

applying constraints to the peak shape. While the use of a Pseudo Voigt function resulted in an overall improved fit compared to using a purely Gaussian line shape, a poor $X^2$ value was still observed across all samples studied. This is believed to be due to a combination of noise and small quantities of Al-O stretching modes also being present in this region overlapping the Si-O stretching modes (120). It was not possible to deconvolute the Al-O signal from the Si-O signal and, due to the use of alumina crucibles, all glasses are expected to contain alumina. The results presented in this section are therefore considered an estimate of the gamma radiation induced change in $Q_n$ ratio.

The same set of glass samples were used for pristine (un-irradiated), ~5 MGy, and ~10 MGy Raman spectra. Due to differences in instrument settings in the ISG glass data sets the signal collected from ~5 MGy glass using 20x magnification had a stronger baseline and was noticeably noisier than the signal collected from the ~10 MGy irradiated glass. The 50x set of parameters gave higher quality data but, due to time constraints and travel restrictions, it was not possible to obtain more glass to enable the ISG ~5 MGy sets of measurements to be repeated with the better set of parameters.

In CaZn a significant increase in the fluorescent background was observed following irradiation (discussed in section 3.4.1.2 shown in figure 27). This background partially obscured the final $BO_3$ peak and has potentially distorted the peak height within the $Q_n$ region. As demonstrated in here the fluorescence found in irradiated CaZn glass could be reduced to near pre-irradiation levels through recombination of electronic defects with UV light. This indicates that this fluorescence likely originated from electronic defects. However, due to differing sample preparation methods used for EPR it was not possible to obtain high quality Raman data from these samples. Compared to CaZn, the fluorescent background present in MW did not undergo significant change as a result of irradiation and was not greatly reduced following exposure to UV light.

There is a notable reduction in fluorescence in ISG irradiated to ~10 MGy. This reduction in fluorescence was seen to a lesser degree in samples irradiated to a ~5 MGy dose. However, due to the issues encountered during the analysis of the initial ~5 MGy data set discussed, it is not possible to state with any certainty if this is due to variations in the poor signal or changes in fluorescence. Due to time constraints ISG was not investigated in any detail using EPR and therefore not exposed to large quantities of UV light at any point in this investigation. As discussed previously the ISG sample was a poorly annealed test batch intended to be powdered, remelted, and annealed at a later date to improve sample homogeneity. As a result of this poor annealing the ISG sample was highly strained. The reduction in florescence suggests some form of structural origin with a possible explanation for the reduction in fluorescence being structural changes or relaxation as a result of exposure to gamma radiation. This was not explored further due to travel restrictions preventing the remelting and annealing of the ISG sample.

None of the glasses studied showed a significant change in Raman peak position (discussed in detail sections 3.4.1.1.- 3.4.1.3 figures 26 - 30 ) with irradiation although, a change in peak height was observed with the differing doses. Given the differing baselines present and the variation in instrument settings some caution must be used in the use of peak height to postulate structural changes. It is proposed that in future work data should be collected from the glass pre and post UV exposure, in order to minimise the impact of changes in baseline on peak height. The changes in spectra observed in each individual glass is discussed in detail below

#### *3.4.1.1. MW*

As with the MW-like mixed alkali Li-Na borosilicate glass previously studied in the literature a change in the peak height of the peak at ~630 $cm^{-1}$ corresponding to danburite units (four membered rings composed of two silicon oxygen and two boron oxygen tetrahedra) is

observed and this is clearly visible in the spectra both pre and post baseline application indicating changes in the glass structure (36). This is further supported by changes in the $Q_1$ and $Q_3$ portion of the $Q_n$ region seen in this glass. Spectra collected from the ~5 MGy sample showed a clear increase in peak height of the $Q_1$ peak and a corresponding potential slight decrease in the danburite peak. By contrast, the ~10 MGy sample showed a reduction in $Q_1$ peak height to near unirradiated glass levels and an increase in $Q_3$ peak height compared to both the ~5 MGy and pristine glass. This was accompanied by a slight increase in danburite peak height compared to ~5 MGy. The height of the Si-O peak also increased in the ~10 MGy data though, given the data processing method used it is not entirely clear whether this originates from structural changes or distortion caused by the baseline and normalisation process.

The fits shown in figure 26 were done using the PsdVoigt2 function to provide an indiction of the $Q_n$ bonding with table 17 (below) showing data parameters.

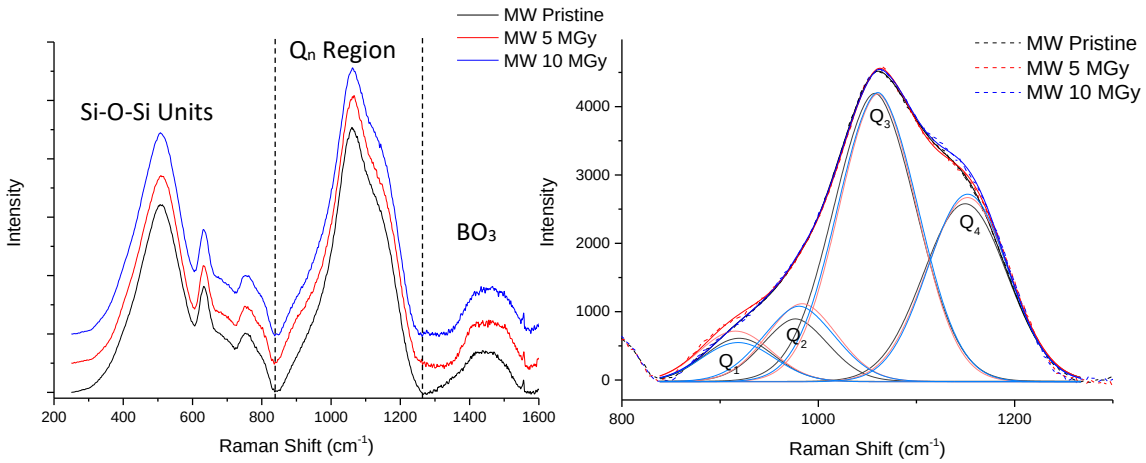


*Figure 26 Normalised MW Raman data (shown left) offset for clarity, with $Q_n$ region fits (shown right).*

*Table 17 MW $Q_n$ region fit results, $X^2$ indicates goodness of fit with a lower number indicating a better fit, FWHM – peak full width half max, wG Gaussian peak width, wL Lorentzian peak width*

| Assignment | Pristine | | | | 5.042 MGy | | | | 9.854 MGy | | | |
|---|---|---|---|---|---|---|---|---|---|---|---|---|
| $X^2$ | 618 | | | | 1413 | | | | 1560 | | | |
| | Wave No ($cm^{-1}$) | FWHM | Area (a.u) | Profile shape | Wave no ($cm^{-1}$) | FWHM | Area (a.u) | Profile shape | Wave no ($cm^{-1}$) | FWHM | Area (a.u) | Profile shape |
| $Q_1$ | 920 | wG 83 | 55942 | 0 | 916 | wG 87 | 68542 | 0 | 918 | wG 87 | 53340 | 0 |
| $Q_2$ | 977 | wG 81 wL 39 | 77405 | 0.06 | 983 | wG 86 wL 49 | 103574 | 0.06 | 980 | wG 90 wL 43 | 102927 | 0.06 |
| $Q_3$ | 1058 | wG 101 wL 34 | 444365 | 0.02 | 1061 | wG 95 wL 28 | 419251 | 0.01 | 1061 | wG 98 wL 24 | 434164 | 0.01 |
| $Q_4$ | 1150 | wG 100 | 277182 | 0 | 1152 | wG 98 | 281805 | 0 | 1152 | wG 97 | 279512 | 0 |

### *3.4.1.2. CaZn*

All gamma irradiated samples of CaZn showed a significant fluorescent baseline. This baseline was not reduced through using the default sample bleaching parameter of the Raman instrument used and attempts at changing the Raman laser wavelength resulted in no usable data being collected from CaZn. The background was only reduced once the electronic defects had been recombined through exposure to UV light (as shown in figure 27). This was carried out as part of the EPR investigation discussed in section 3.4.2. Due to the differing preparation methods used for EPR and the limited quantities of glass samples which necessitated all gamma irradiated glass be used for leaching experiments, it was not possible to repeat these measurements on glass that had been exposed to UV light in order to recombine the defects.

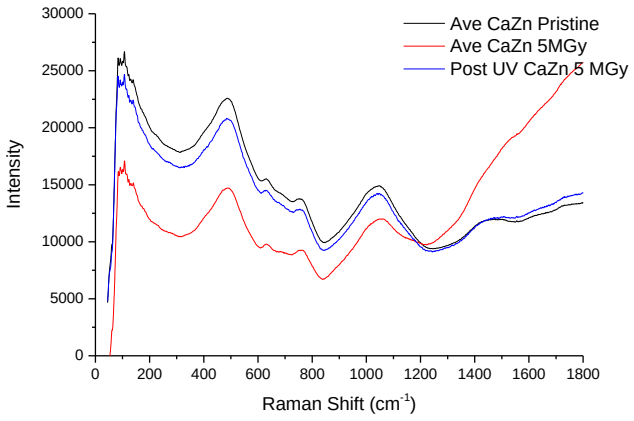


*Figure 27 Unnormalized CaZn Raman data showing reduced fluorescence*

Overall, a great deal of peak height variation was observed between the differing doses (as shown in figure 28), but the changes seen in the $Q_n$ region of the CaZn Raman spectra were

visibly more subtle than the changes seen in MW. In this case the change in peak height in the latter part of Si-O-Si regions and the $BO_3$ region, is likely to be in part due to the strong fluorescent background seen in gamma irradiated glass. Both the ~5 MGy and ~10 MGy data sets had a strong fluorescent background with the ~5 MGy sample being the strongest due to being collected on freshly irradiated glass.

The $Q_n$ region was fitted with the PsdVoigt2 function to give the data set shown in figure 28 and table 18. There is a clear dose dependence seen in the $Q_1$ region with both the peak height and area increasing with dose (shown in figure 28 and table 18). The changes seen in the other portions of the $Q_n$ region are less clear. The $Q_2$ region increases in height with dose but there does not seem to be an overall pattern of peak area and dose indicating the overlapping Al-O signal may be partly responsible for these changes. There is a slight decrease in $Q_3$ and $Q_4$ peak area seen in the ~5 MGy data, although this does not significantly change at ~10 MGy, conversely the $Q_4$ peak height decreases at ~5 MGy and increases at ~10 MGy.

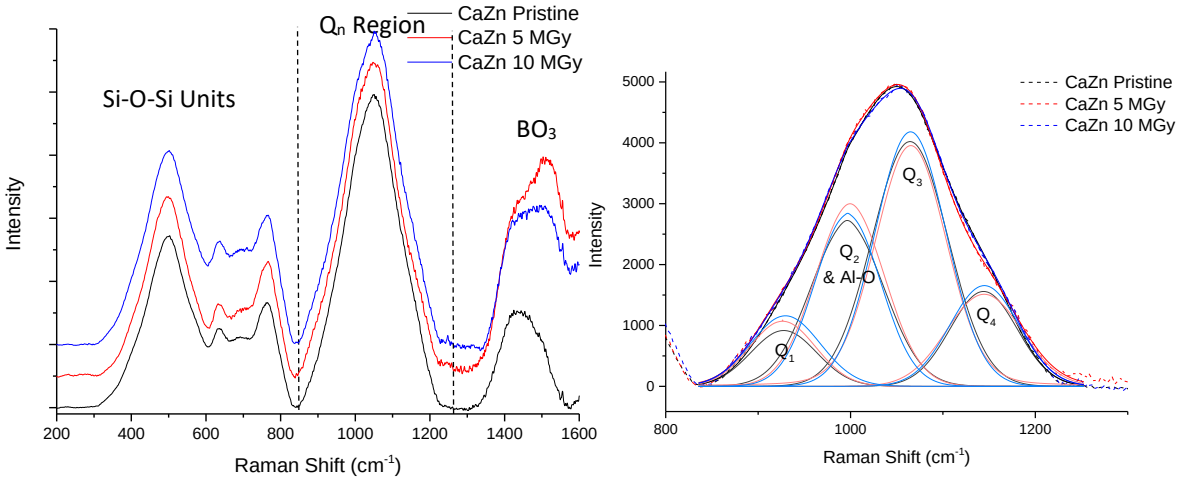


*Figure 28 Normalised CaZn Raman data (shown left) offset for clarity, with Qn region fits (shown right).*

*Table 18 CaZn Qn region fit results $X^2$ indicates goodness of fit with a lower number indicating a better fit, FWHM – peak full width half max, wG Gaussian peak width, wL Lorentzian peak width*

| Assignment | Pristine | | | | 4.866MGy | | | | 9.863MGy | | | |
|---|---|---|---|---|---|---|---|---|---|---|---|---|
| $X^2$ | 643 | | | | 1676 | | | | 1399 | | | |
| | Wave No ($cm^{-1}$) | FWHM | Area (a.u) | Profile shape | Wave no($cm^{-1}$) | FWHM | Area (a.u) | Profile shape | Wave no ($cm^{-1}$) | FWHM | Area (a.u) | Profile shape |
| $Q_1$ | 928 | wG 84 | 81765 | 0 | 927 | wG 84 | 97347 | 0 | 930 | wG 89 | 109341 | 0 |
| $Q_2$ + Al-O | 997 | wG 95 wL 22 | 267606 | 0.01 | 999 | wG 89 wL 27 | 280756 | 0.01 | 997 | wG 84 wL 7 | 252068 | 0.001 |
| $Q_3$ | 1064 | wG 97 | 414070 | 0 | 1065 | wG 89 wL 113 | 402999 | 0.15 | 1065 | wG 91 | 403436 | 0.00 |
| $Q_4$ | 1144 | wG 85 | 141835 | 0 | 1144 | wG 96 | 154577 | 0 | 1145 | wG 88 | 155616 | 0 |

### *3.4.1.3. ISG*

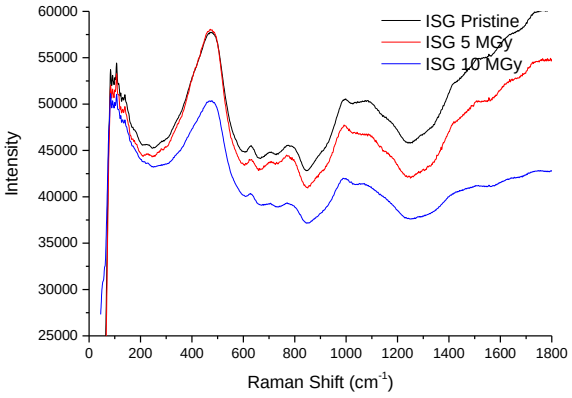


*Figure 29 Unnormalized ISG Raman data showing changes in fluorescence*

The ISG data set was collected in the early stages of the project, and as a result is noisier than other Raman data sets collected as part of this project. This data also shows an unusual decrease in the fluorescence with dose (shown in figure 29), which is not seen in any other data set studied here. As aluminosilicate glasses tend to display Raman fluorescence the reduction in fluorescence may be related to radiation induced structural changes within the glass involving aluminum (121).

Given the high aluminium content of ISG, the $Q_n$ region is also likely to contain a significant Al-O contribution. This will have contributed to the unusually large peak observed in the $Q_2$ region of all ISG samples. Due to the limited quantity of data collected preventing adequate data averaging, the ~5 MGy data set was plotted against a pristine glass collected with the 20x magnification settings, referred to as pristine 1, and the ~10 MGy data set was plotted against a pristine glass collected with the 50x magnification settings, referred to as pristine

2. The lack of averaging makes the impact of the differing settings more significant, as seen in the spectra plotted in figure 30 which were normalised to the highest peak across all four data sets. The pristine and irradiated glass were normalised to the highest peak in each pair of spectra prior to being fitted with the PsdVoigt1 function. The use of different sets of pristine data results in the change in peak area seen between pristine 1 (shown table 19) and pristine 2 (shown table 20). Both the ~10 MGy and ~5 MGy dose sample sets of data showed a significant reduction in the both the peak height and area of the $Q_3$ and $Q_4$ peaks but did not show and significant changes in the $Q_1$ and $Q_2$ regions of the Raman spectra suggesting the change in $Q_n$ number primarily occurred in bridged $SiO_4$ tetrahedra bonded to other network components.

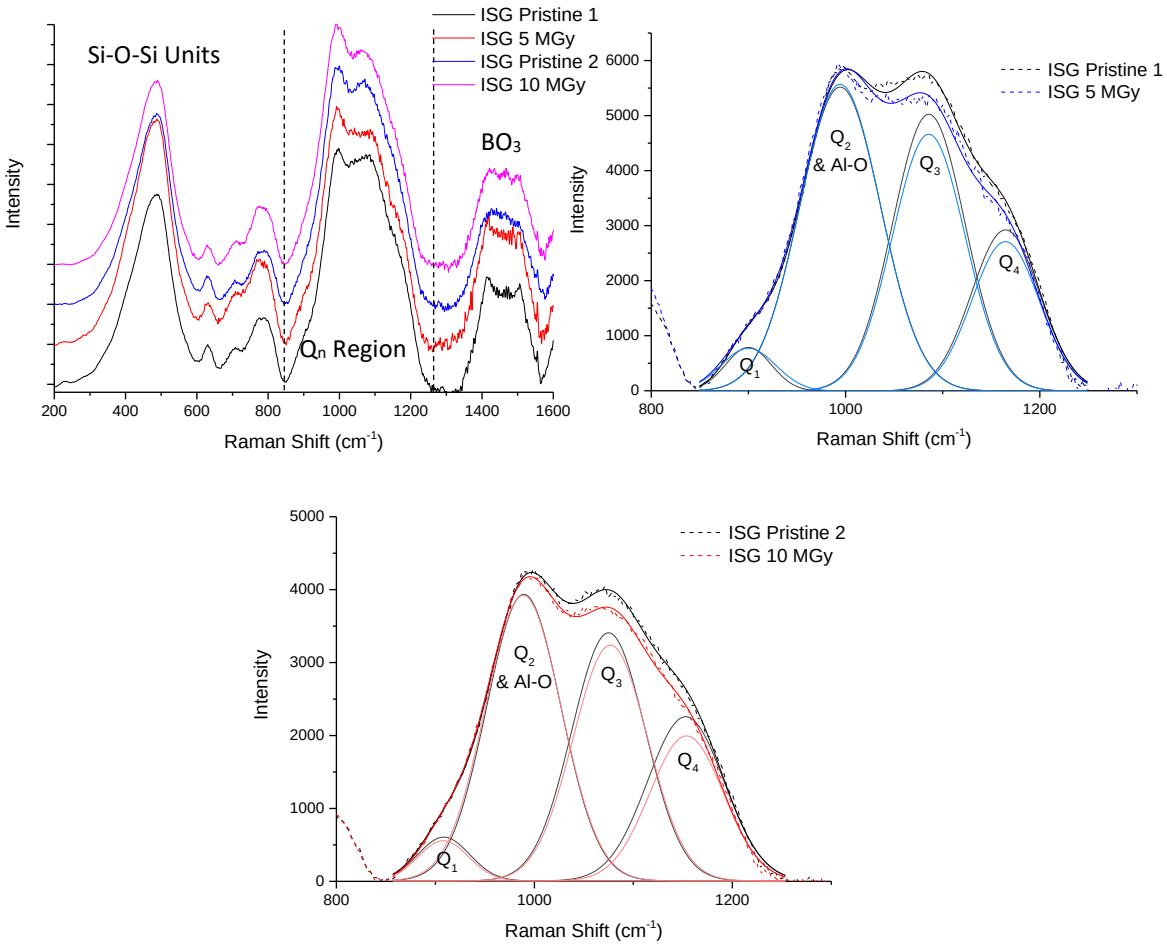


*Figure 30 Normalised ISG Raman data (shown top left) offset for clarity, with Pristine 1 and Pristine 2 Qn region fits*

*Table 19 ISG Pristine 1 Qn region fit results $X^2$ indicates goodness of fit with a lower number indicating a better fit, FWHM – peak full width half max*

| Assignment | Pristine 2 (50x magnification) | | | | 9.808 MGy ISG | | | |
|---|---|---|---|---|---|---|---|---|
| $X^2$ | 2261 | | | | 2301 | | | |
| | Wavenumber ($cm^{-1}$) | FWHM | Area (a.u) | Profile shape | Wavenumber ($cm^{-1}$) | FWHM | Area (a.u) | Profile shape |
| $Q_1$ | 908 | 61 | 39248 | 0 | 908 | 60 | 34987 | 0 |
| $Q_2$ + Al-O | 989 | 89 | 370742 | 0 | 988 | 90 | 376405 | 0 |
| $Q_3$ | 1075 | 87 | 317379 | 0 | 1076 | 89 | 304780 | 0 |
| $Q_4$ | 1653 | 91 | 218313 | 0 | 1154 | 88 | 185468 | 0 |

*Table 20 ISG Pristine 2 Qn region fit results $X^2$ indicates goodness of fit with a lower number indicating a better fit, FWHM – peak full width half max*

| Assignment | Pristine 1 (20x magnification) | | | | 5.121 MGy ISG | | | |
|---|---|---|---|---|---|---|---|---|
| $X^2$ | 7272 | | | | 12769 | | | |
| | Wavenumber ($cm^{-1}$) | FWHM | Area (a.u) | Profile shape | Wavenumber ($cm^{-1}$) | FWHM | Area (a.u) | Profile shape |
| $Q_1$ | 900 | 55 | 46751 | 0 | 900 | 66 | 54675 | 0 |
| $Q_2$ + Al-O | 994 | 98 | 577804 | 0 | 994 | 97 | 579057 | 0 |
| $Q_3$ | 1086 | 88 | 470348 | 0 | 1085 | 88 | 436159 | 0 |
| $Q_4$ | 1165 | 83 | 257720 | 0 | 1165 | 82 | 236123 | 0 |

Based on these results future work is needed on the use of EPR in combination with UV-Vis-NIR and UV light induced defect recombination to quantify the relationship between the presence of Raman fluorescence and electronic defects in glass. The anomalous change in fluorescence seen in ISG suggests that further work on the effect of cooling rate on Raman fluorescence in glass in combination with gamma irradiation and UV exposure are needed to better explore the structural origins of this change. This has the potential to reveal further details about radiation-induced structural healing a phenomenon that has only previously been observed in glass doped with active elements or subjected to dual ion beam irradiation (112,122). The impact of gamma radiation on internal strain is made all the more relevant by the conditions used in the production of HLW glass. HLW glass will not be subjected to controlled annealing, resulting in a highly strained glass. This demonstrates the importance of considering the electronic defects and physical changes as

separate but closely related phenomena as shown by the Raman investigation carried out here.

### 3.4.2. UV Vis and EPR for Electronic Defect Identification.

Many factors, such as melt temperature, oxidation environment, and trace impurities can influence the colour displayed by a glass. One of these factors is the presence of radiation-induced electronic defects. As discussed previously, these defects will be formed when glass is exposed to gamma radiation. The resulting colour can vary from blue to near black depending on the irradiated glass, type and quantity of defects formed. The quantity of certain electronic defects formed within the glass, and therefore the colour, shows a clear dose dependence (113).

Due to this UV-Vis-NIR has been used to aid in the identification of coloured electronic defects present. Using the method given in Rautiyal et al. the UV-Vis-NIR data collected from irradiated and pristine glass has been normalised using equation 5 to remove the dependence on pathlength, rescaled from wavelength to wavenumber, and the pristine unirradiated glass spectrum subtracted from the irradiated glass spectrum to give a UV-Vis-NIR spectrum containing only the electronic defects responsible for the observed colour change present in the glass (36). The normalisation and rescaling process enables the identification of defects present in the glass through fitting the spectra with a series of Gaussian peaks (as shown in figure 31, 32 and 33).

$$\alpha = \frac{ln10 \times a(\gamma)}{t(cm)}$$

*Equation 5 a = sample absorption, t = sample thickness*

The MW, CaZn, and ISG glasses studied here all displayed a colour change from pale blue green or pale yellow to dark brown when exposed to gamma radiation and this colour change showed the expected dose dependence. This was not initially reflected in all UV-

Vis-NIR data sets as, due to issues with the solid sample holder, the initial ~5 MGy glass monolith data was collected using the half beam height setting. This glass was then irradiated to a total dose of ~10 MGy for use in leaching experiments.

An attempt at re-running the initial measurements using the second set of ~5 MGy MW and CaZn samples was made. This set of measurements showed the expected change in colour intensity with increased dose in both glasses. A second set of samples cut from the same glass ingots was used for these measurements as, due to the sensitivity of UV-Vis-NIR to decolourisation caused by defect recombination, the UV-Vis-NIR data must be collected as close to irradiation as possible. The impact of the defect recombination based decolouration is most prominent in the decreased peak height of the large peak at ~275 nm observed in data collected at a later date from CaZn. Due to time constraints ISG was not studied in the later EPR experiments or the second set of UV-Vis-NIR measurements. The normalised and rescaled UV-Vis-NIR data was fitted using the Gaussian peak function in OriginPro 9.1, and the initial peak positions were taken from literature (36).

Pre-normalisation the UV-Vis-NIR data collected from pristine glasses showed a small broad peak at ~ 2700 to 2800 nm in the NIR region, corresponding to small quantities of water in the glasses, and a UV cut off at ~ 250 nm corresponding to UV absorbance of NBO in the glasses, apart from this the spectra were largely featureless (123). Pre-normalisation the irradiated glass showed the same water peak and UV cut off, with additional peaks corresponding to electronic defects present in the 250 nm to 700 nm region.

The ~10 MGy MW and CaZn data was initially fitted with four peaks according to the method used in previous literature (36). As the CaZn formulation is based on MW and is expected to contain additional defects associated with glass components not present in MW, an attempt at fitting CaZn with five peaks was made but this failed to converge. The results of the four peak fits are shown in figure 31 and the peak assignments in table 21

and 22. There is some uncertainty surrounding the precise identity of the large peak at ~275 nm in CaZn, which is discussed in further detail in this section.

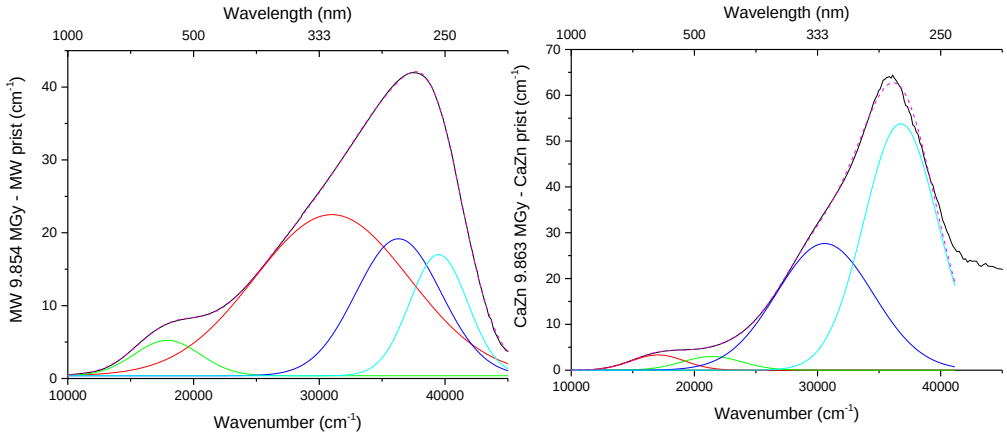


*Figure 31 Normalised 10 MGy MW and CaZn electronic defect UV-VIS-Nir spectra*

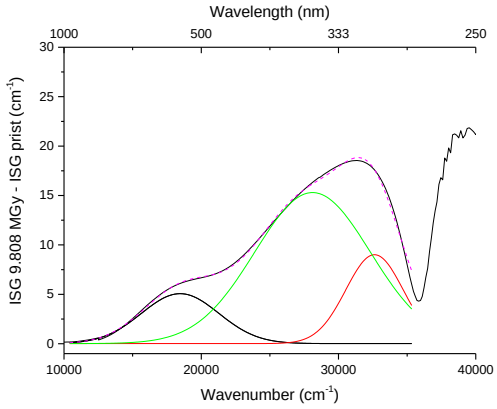


*Figure 32 Normalised 10 MGy ISG electronic defect UV-VIS-Nir spectrum*

The ~10 MGy ISG data was fitted with 3 curves (as shown in figure 32) and it was assumed the peak at ~260 nm (~38000 $cm^{-1}$) assigned to $Fe^{3+}$ centres was obscured by issues with the UV cut off (36). Due to these issues the region above ~285 nm (~35000 $cm^{-1}$) was excluded from all ISG fits. This region contains what is potentially a large band with very strong absorbance present on the edge of the UV cutoff region. As ISG is not designed to be radiation tolerant, this could correspond to a change in the amount of NBO present causing a shift in the UV cut off (123). However, this band could also be due to inhomogeneity in samples introducing changes in the UV cut off, as the ISG was produced as a test batch, and despite being cut from the same glass ingot a varying amount of cracking was present in the monoliths due to the glass being poorly annealed. Instead a peak at ~306 nm believed to correspond to a type of trapped electron (ET) or E' centres was found in ISG (32,36). This peak is shifted to a

slightly higher wavelength compared to the ET center peak in MW and CaZn (shown in tables 24 -26).

As discussed previously the glass samples irradiated to a dose of ~5 MGy were initially analysed with the half beam height setting. This glass was later irradiated to a dose of ~10 MGy for use in leaching experiments. A second set of ~5 MGy dose measurements were collected using a second set of MW and CaZn samples irradiated to a dose of ~5 MGy and the ISG measurements were not repeated. These measurements were fitted using the same method as the ~10 MGy data and are shown in figure 33. Note that a nosier spectrum is observed in ~5 MGy ISG due to using a reduced beam height.

As shown in figure 33 and table 21 and 22, the attempt at fitting the ~5 MGy MW and CaZn spectra also converged with four peaks present. As with the ~10 MGy data set the poorly annealed ISG sample showed the same shifted and weaker ET/E' centre band and a potential large band with very strong absorbance on the edge of the UV cutoff region. Again this could correspond to a change in the amount of NBO present causing a shift in the UV absorbance cut off, or inhomogeneity in the sample (123). The shifts in ET/E' band wavelength are unexpected as numerous identical ET centres are present in all three glasses.

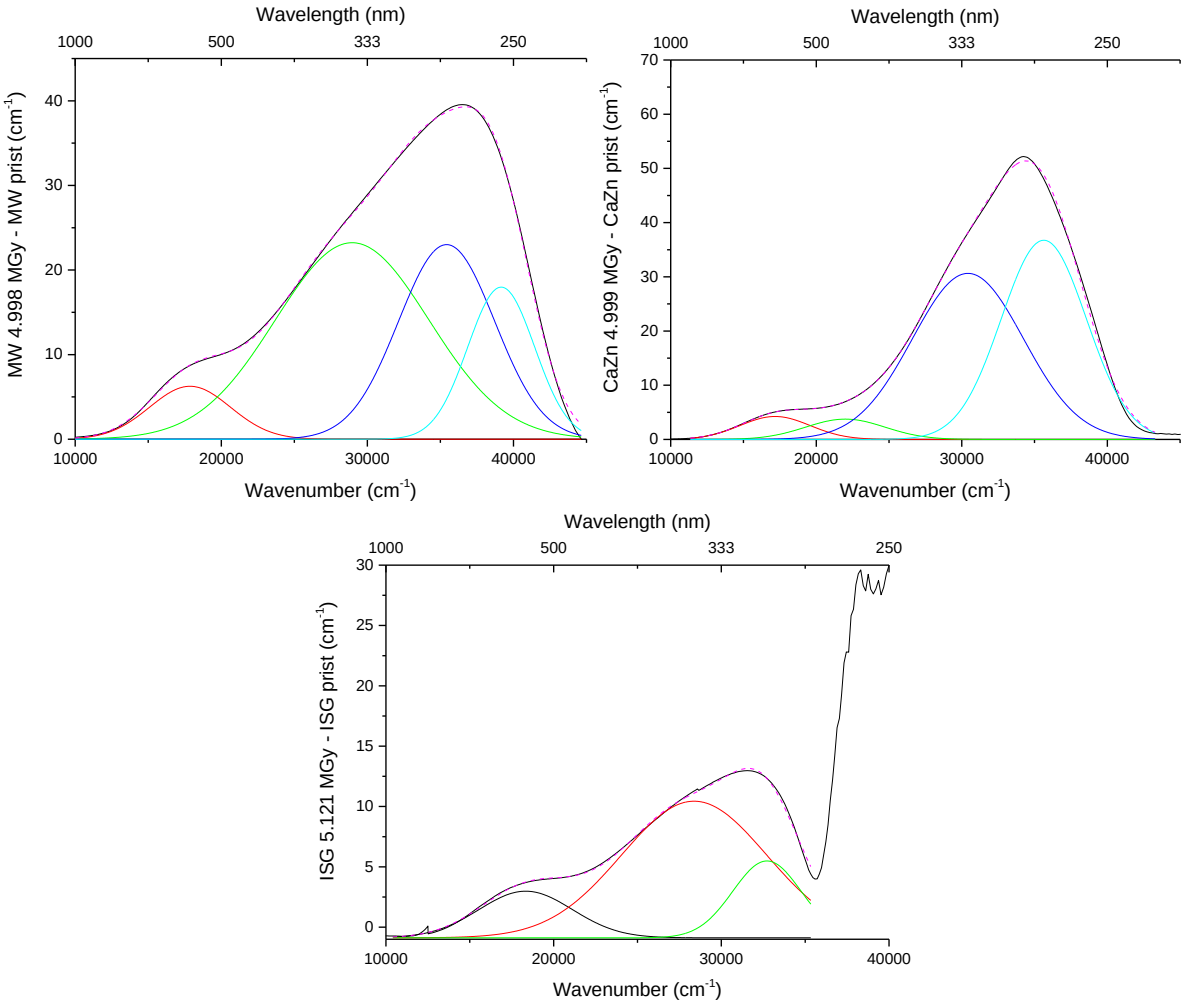


*Figure 33 Normalised 5 MGy MW, CaZn and ISG electronic defect UV-VIS-Nir spectra*

The ~5 and ~10 MGy dose spectra showed broadly the same features and peak positions (shown in table 21, 22, and 23). The assumption that peak assignments do not vary with the doses used here has been made on the basis of EPR data collected at both doses that showed minimal changes in peak intensity indicating the same set of peaks are present at ~5 and ~10 MGy. The UV-Vis-NIR peak assignments and justifications are as follows.

The peak observed at 253 nm in MW has been assigned to $Fe^{3+}$ based on the UV-Vis-NIR fit used as a start point carried out in Rautiyal *et al.*. (36). This peak is expected to occur in all glasses as a result of a trace iron impurity originating from the silica used in glass manufacture and $Fe^{2+}$ acting as a hole trap and undergoing a change from $Fe^{2+}$ to $Fe^{3+}$ (124). This peak has not been observed in ISG where the iron region is obscured by the UV

absorption cut off. A large peak is observed at ~ 272 nm in the $Fe^{3+}$ region of CaZn but has not been assigned to iron. While this peak is likely to contain some contribution from $Fe^{3+}$ the stability of this peak is not consistent with $Fe^{3+}$ behaviour. The behaviour of this peak is consistent with a large UV unstable defect observed in gamma irradiated CaZn EPR data. As a result of this the peak has instead been assigned as a calcium related HC defect. This assignment has been made based on the following literature information; a large sharp peak observed by Gac *et.al* in electron irradiated calcium aluminosilicate glass EPR data and a peak attributed to calcium colloid formation observed by Beuneu *et.al* in cryo EPR of electron irradiated natural fluorite crystals, both with a near identical g value to the large sharp UV unstable peak observed here in CaZn EPR data; combined with evidence of calcium cation migration observed by Patel *et.al* in borosilicate glass exposed to beta radiation, and the ability of alkali cations to associate with defects and potentially form colloids (37,47,48,125,126). Of note is the lack of distinctive strong UV-Vis-NIR absorbance at 580 nm expected in the presence of large calcium colloids, combined with the narrow room temperature EPR band, suggesting any calcium clusters formed are very small and unable to absorb enough light to be detectable through UV-Vis but are detectable through room temperature EPR (48,126).

The ET center observed at ~280 nm in MW has been assigned based on the fitting by Rautiyal *et al.* used as a start point (36). Given the calcium related HC defect seen in CaZn, the exact identity of this peak is likely to be a $HC_1$ center. The peak at ~305 nm in ISG was a partial fit for both an ET center observed by Rautiyal et al. and a $E^{'}$ center observed by Ehrt and Ebeling in UV-Vis-NIR data, due to the lack of EPR data it is not possible to definitively state if this peak is an $E^{'}$ center or a generic ET center (32,36). The BOHC in all glasses have been assigned based on the fit carried out by Ehrt and Ebling (32). The NBOHC has been assigned using the UV-Vis-NIR fit caried out by Ehrt and Ebling and the eV values calculated by Griscom and Mizuguchi from isochronal-anneal difference spectra (32,127).

This method suffers greatly from a lack of previous data to aid in peak identification. This has led to a great deal of uncertainty when trying to match the observed results with EPR data. The advantages of combining EPR with UV-Vis-NIR are best demonstrated by the large rapidly decolourised peak seen in CaZn, which was initially tentatively identified as a corresponding to a BOHC + POR electronic defect. However, when combined with EPR data collected from CaZn, where a large UV unstable peak believed to correspond to a defect associated with calcium is also present, the same UV unstable defect becomes a more likely explanation.

*Table 21 MW UV-VIS-Nir fit results*

| | MW 9.854 MGy | | MW 4.998 MGy | |
|---|---|---|---|---|
| Assignment | $cm^{-1}$ | nm | $cm^{-1}$ | nm |
| NBOHC (114,127) | 17909.16 | 558.37 | 17860.61 | 559.89 |
| BOHC (32) | 30996.24 | 322.62 | 28957.63 | 345.33 |
| ET centres (36) | 36303.95 | 275.45 | 35424.03 | 282.29 |
| $Fe^{3+}$ (36) | 39493.96 | 253.20 | 39160.90 | 255.36 |

*Table 22 CaZn UV-VIS-Nir fit results*

| | CaZn 9.863 MGy | | CaZn 4.999 MGy | |
|---|---|---|---|---|
| Assignment | $cm^{-1}$ | nm | $cm^{-1}$ | nm |
| NBOHC (114,127) | 17053.93 | 586.37 | 17172.52 | 582.33 |
| BOHC (32) | 21434.63 | 466.53 | 21997.51 | 454.60 |
| BOHC (32) | 30583.98 | 326.97 | 30424.11 | 328.69 |
| Potential Ca HC center (39,47) | 36764.25 | 272.00 | 35637.29 | 280.60 |

*Table 23 ISG UV-VIS-Nir fit results*

| | ISG 9.808 MGy | | ISG 5.121 MGy | |
|---|---|---|---|---|
| Assignment | $cm^{-1}$ | nm | $cm^{-1}$ | nm |
| BOHC (32) | 18461.18 | 541.68 | 18335.08 | 545.40 |
| BOHC (32) | 28108.20 | 355.77 | 28375.57 | 352.42 |
| ET/E' center (32,36) | 32622.40 | 306.54 | 32721.04 | 305.61 |

UV-Vis-NIR is ideal for initial identification of peaks but the technique suffers from a lack of sensitivity with smaller peaks, for example the $Fe^{3+}$, being completely obscured by larger neighbouring peaks at higher doses. While the use of UV-Vis-NIR has the potential to reveal EPR-silent defects, due to issues related to lack of reference data and sensitivity to glass composition, it is proposed that in its current form the use of UV-Vis-NIR in defect identification should be considered complementary to EPR (32).

EPR is able to give more detailed information on the defects present. However, analysis of EPR data is typically more complex than UV-Vis-NIR data, requiring the use of detailed simulations to fit data. This is compounded by the majority of gamma radiation induced defects in borosilicate glass being of either a trapped electron defect or an oxygen hole center defect type, and due to this there is a great deal of peak overlap. With the exception of $Fe^{3+}$ found at ~4 g the defects in borosilicate glass all tend to fall between 1.8 – 2.1 g. Attempts have been made to overcome this through the use of UV light to recombine defects and collection of data at higher EPR bands. The use of higher EPR bands has only been partially successful as, due to the inherent disorder present in an amorphous structure, there is a great deal of g strain present, which has not been allowed for in previous work (45–47).

The lack of consideration of g strain in current literature is likely due to the dominant use of X band EPR, resulting in there being no requirement for it to be considered in previous work involving the analysis of glass (37,45–47,113). Where studies have been carried out on varying but related glass formulations using the same EPR band across all samples the homogeneous random nature of disorder found, by definition, in an amorphous material results in little change in peak width between the different EPR spectra (47). The presence of g strain only becomes apparent when a higher EPR band is used to analyse two identical glass samples.

Theoretically both peak width, which is determined by hyperfine coupling, and g factor are independent of EPR band, and peak resonance is dependent on EPR band and g factor. This is demonstrated by equation 6 where B is peak resonance, h is Planck's constant, f is spectrometer frequency or band, $m_B$ is the Bohr magneton, and g is g factor. The result of this equation is typically that the peaks become better resolved as field strength is increased where, theoretically, the peaks will become better separated while experiencing minimal peak broadening. In the data collected here this does not happen and the peak width instead increases with increasing field strength, indicating the presence of previously unobserved g strain in glass. While this is not unexpected it has prevented the full simulation of EPR spectra.

$$B = \frac{h\,f}{m_B g}$$

*Equation 6 B= Peak resonanance, h=Planks constant, f= spectrometer frequency/ band, $m_b$=Bohr magneton g= g factor*

Initial attempts at simulating X band EPR spectra collected from MW glass irradiated to a total dose of ~5 MGy were successful. As indicated by the different absorbance values observed near the UV edge in UV-Vis-NIR collected from irradiated glass, the defects present in glass have different sensitivities to UV light. Unlike thermal annealing that typically results in the recombination of all defects UV light can be used to recombine these defects at different rates. When electronic defects present in glass are recombined their relative magnitude in the EPR spectrum will change however the g values and peak width should remain mostly unchanged. This combined with the more selective recombination of electronic defects when exposed to UV light (seen in the form of changes in peak intensity observed in the time delay EPR spectra shown in figure 34 and 35) enables the EPR simulation to be caried out in stages. This process starts with simulating the EPR spectrum post UV exposure in order to simulate the more UV stable defects and ends with the simulation of the EPR spectrum pre UV exposure. This has enabled the use of literature

data collected from alkali borosilicate glass in the gradual build-up of a complete complex EPR simulation for MW (39,45,46).

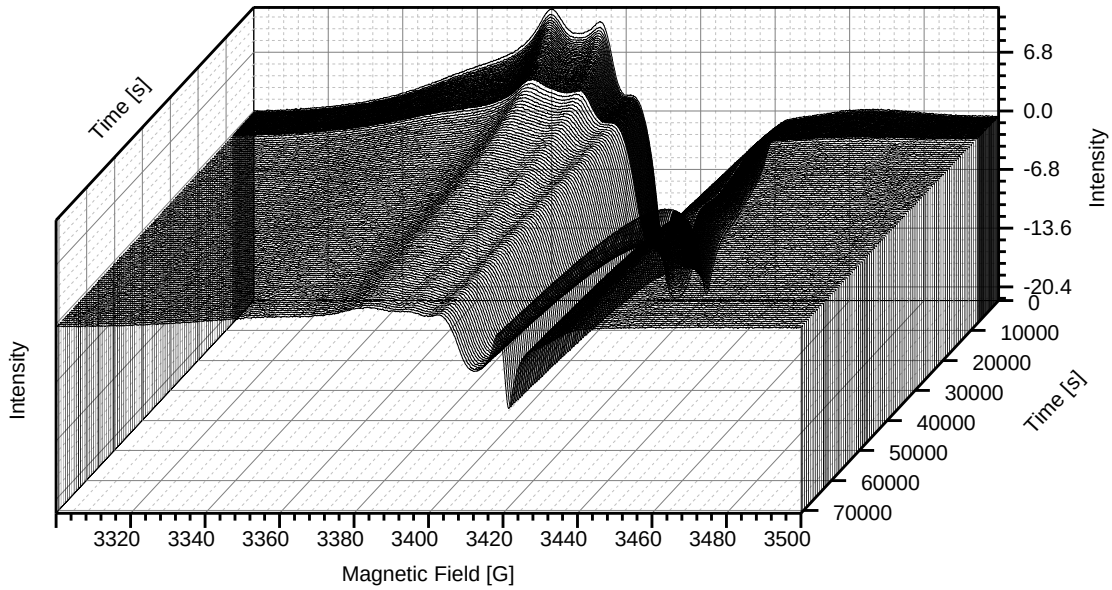


*Figure 34 Full MW time delay UV EPR plot showing defect recombination rate*

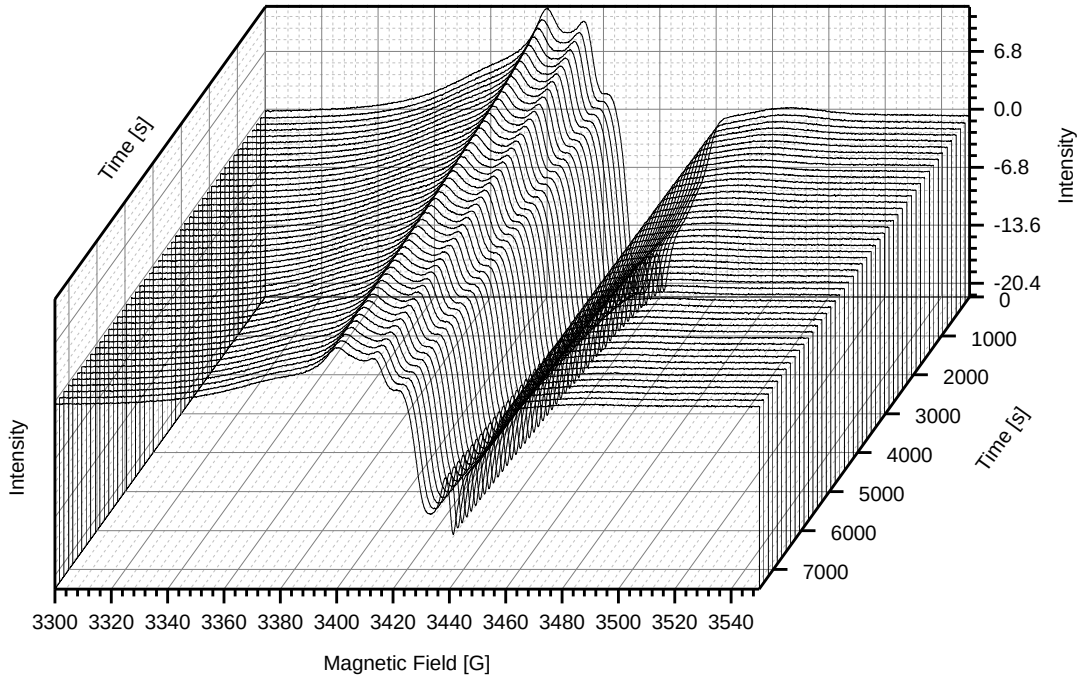


*Figure 35 First 2.5 hours of MW time delay UV EPR plot shown for clarity*

The initial X band MW EPR simulation and the results of this are shown in figure 36 and table 24. In order to track the UV degradation of defects the g values and linewidth were fixed and percentage contribution of these values was allowed to vary before being normalised against E'. E' was chosen as a reference point as this was the last defect to recombine in the thermal annealing of an MW like glass carried out in literature indicating it is the most stable defect present (36). Plotting the change in contribution over time reveals the variable stability of these defects to UV light exposure as shown in figure 37.

*Table 24 MW X band EPR simulation parameters*

| Defect | E' | BOHC | POR | $HC_1$ | NBOHC | $BO_3$ | BOSi |
|---|---|---|---|---|---|---|---|
| Nucs | | B | | | | | |
| g values | 1.9983 | 2.0300 | 2.0007 | 1.9892 | 2.0275 | 2.0085 | 1.9914 |
| g values | | 2.0099 | 2.0051 | 2.0137 | 2.0462 | 2.0365 | 1.9998 |
| g values | | 2.0065 | 2.0212 | 2.0113 | 2.0485 | 2.0036 | 2.0168 |
| A strain | | 40.4674 | | | | | |
| A strain | | 44.2967 | | | | | |
| A strain | | 34.9832 | | | | | |
| $Lwpp_{gauss}$ | 0.5636 | 1.3214 | 0.0223 | | | 0.2748 | 0.7935 |
| $Lwpp_{lorentz}$ | | | 0.5362 | 0.3199 | 2.4281 | 0.5315 | |
| Weight | 0.0226 | 2.1994 | 1.3577 | 0.2280 | 0.6003 | 0.1888 | 0.3964 |

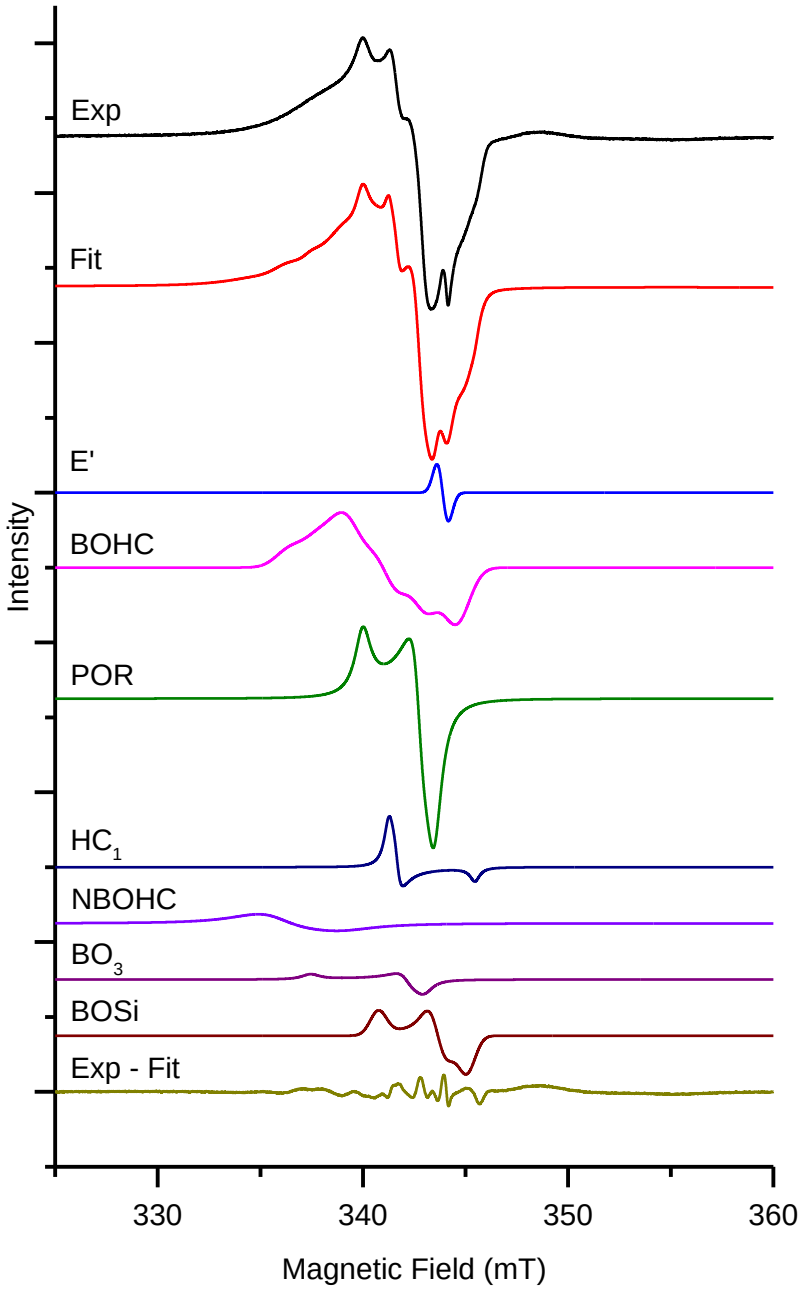


*Figure 36 MW X band EPR defects simulated, shown fitted to data collected pre UV exposure and offset for clarity*

The line shapes (shown in figure 37) were produced from plotting the proportion of defects with E'norm as a reference point and show an excellent match for two phase exponential decay when fitted with the ExpDec2 function in OriginPro 9.1. From this function two half-lives can be derived, a fast half-life ($t_{\text{half-life 1}}$) that with the exception of $BO_3$ is

approximately 30 min for all defects present in MW and a slow half-life ($t_{\text{half-life 2}}$) that potentially displays a dependence on the UV-Vis-NIR absorbance of the defect (shown in table 25). This two factor half-life dependence of defect recombination results in the selective recombination of defects when recombining with UV light. This is observed to some degree in both MW and CaZn but it has not been possible to calculate exact values for CaZn as it was not possible to fit the CaZn EPR spectrum.

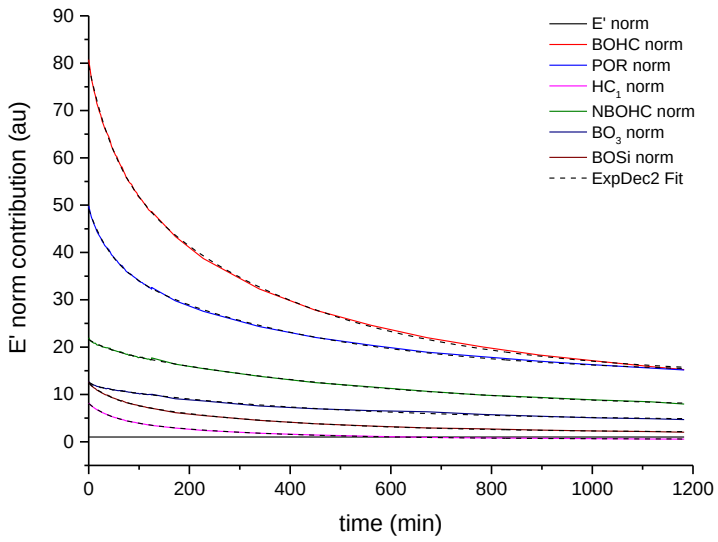


*Figure 37 Normalised MW electronic defect contribution calculated through simulating EPR spectra*

*Table 25 Half-lives calculated by fitting data shown in figure 37 with ExpDec 2 function*

| | $y = A1*exp^{(-x/t1)} + A2*exp^{(-x/t2)} + y0$ | |
|---|---|---|
| Defect | $t_{\text{half-life 1}}$ (min) | $t_{\text{half-life 2}}$ (min) |
| BOHC | 34.45 | 266.54 |
| POR | 30.95 | 284.56 |
| ET center ($HC_1$) | 30.25 | 192.04 |
| NBOHC | 28.99 | 398.00 |
| $BO_3$ | 10.79 | 307.41 |
| BOSi | 30.70 | 232.58 |

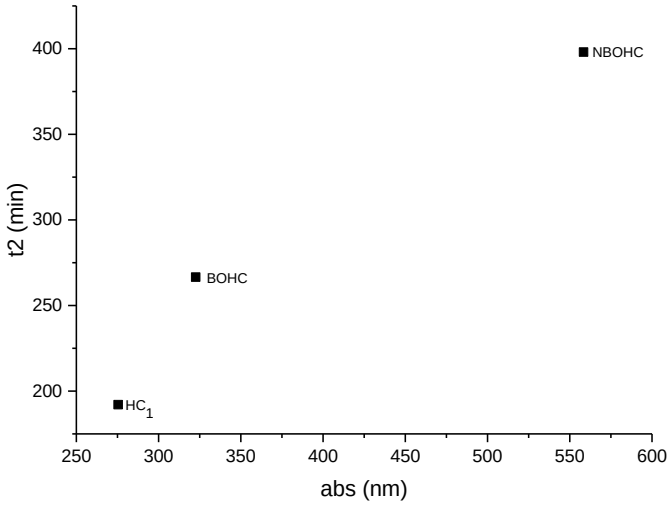


*Figure 38 $T_{half\text{-}life2}$ plotted against tentatively identified absorbance frequency of selected defects present in MW*

Given that the $t_{\text{half-life 1}}$ is near identical in most defects observed in MW while the $t_{\text{half-life 2}}$ shows a relationship with the previously identified UV-Vis-NIR absorbance frequency of electronic defects (shown in figure 38) it is proposed that in future work this may be used to identify defects that are both EPR active and have detectable UV-Vis NIR absorbance through selective recombination with laser light. This would enable the conclusive

identification of defects through UV-Vis-NIR which would enable the study of many of the proposed EPR silent defects.

Due to the presence of g-strain, and difficulties with the UV light set up related to the use of a mercury arc lamp in the presence of a strong magnetic field necessitating the use of ex-situ UV exposure, it has not been possible to fully apply this method to Q band data. This has prevented the production of an EPR simulation for MW that can be applied to both X Band and Q band EPR data.

When the X band simulation is carried out at Q band frequency and overlaid with Q band EPR data collected from MW the presence of g-strain becomes clearly visible in the lack of resolution seen in Q band data (as shown in figure 39).

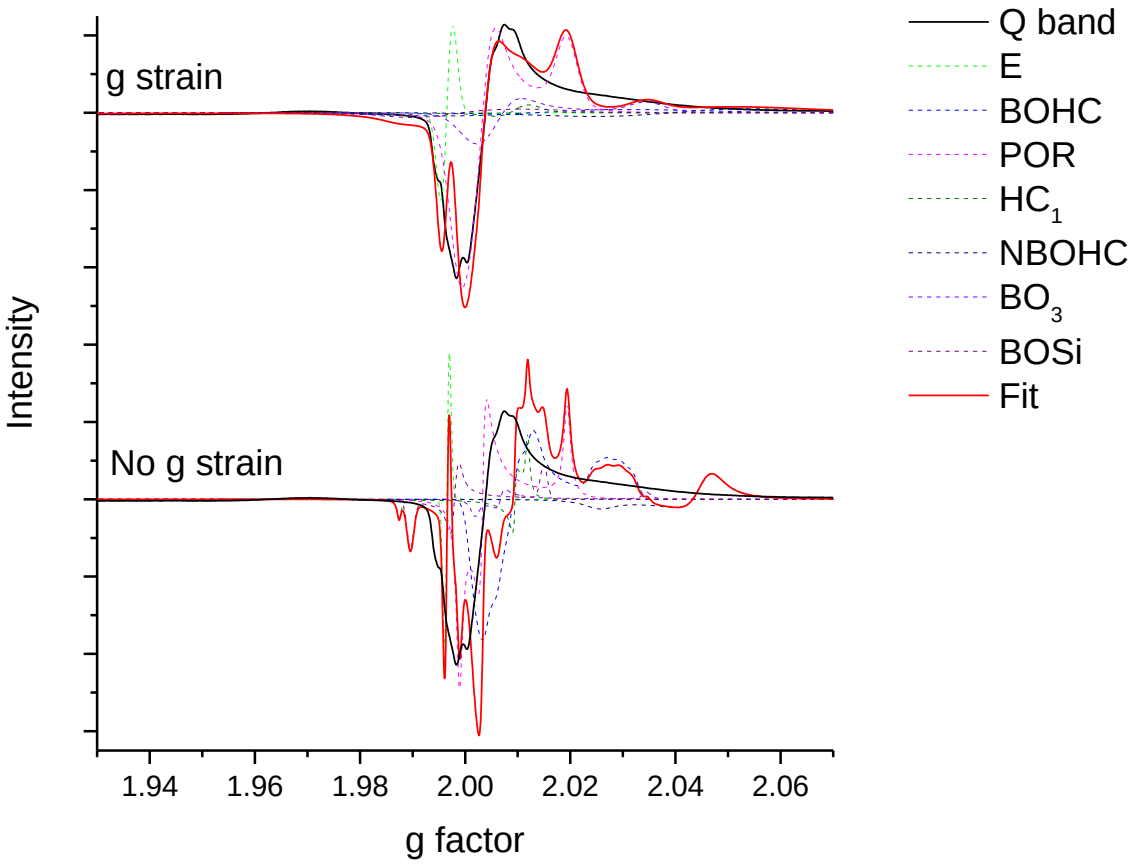


*Figure 39 Q band MW simulation using values calculated by simulating X band exp showing the effects of adding g-strain, overlaid with MW 5MGy Q band EPR. Normalised to g value for clarity*

The addition of g-strain to the initial X band EPR fit does not produce a reasonable match and given the deviation from previous literature g values also seen in the X band fit it is likely that there are signals present, such as the broad and poorly resolved sodium colloid signal, potentially observed at ~1.97 g in figure 40, that have not been allowed for in the current X band simulation (36). The indirect simultaneous fitting of X and Q band EPR data collected from MW has been attempted and the results are shown in table 26 and figure 40. This fit shows significant deviations from both EPR spectra collected at different bands and has a poor match between ratios of defect components found in the initial X band fit. While a slight variation in defect ratios between the two data sets is expected, due to the naturally occurring slow recombination of defect over time, the variation seen between the X band and Q band data falls outside the ratios observed in the X band data during the intentional full recombination of defects with UV light.

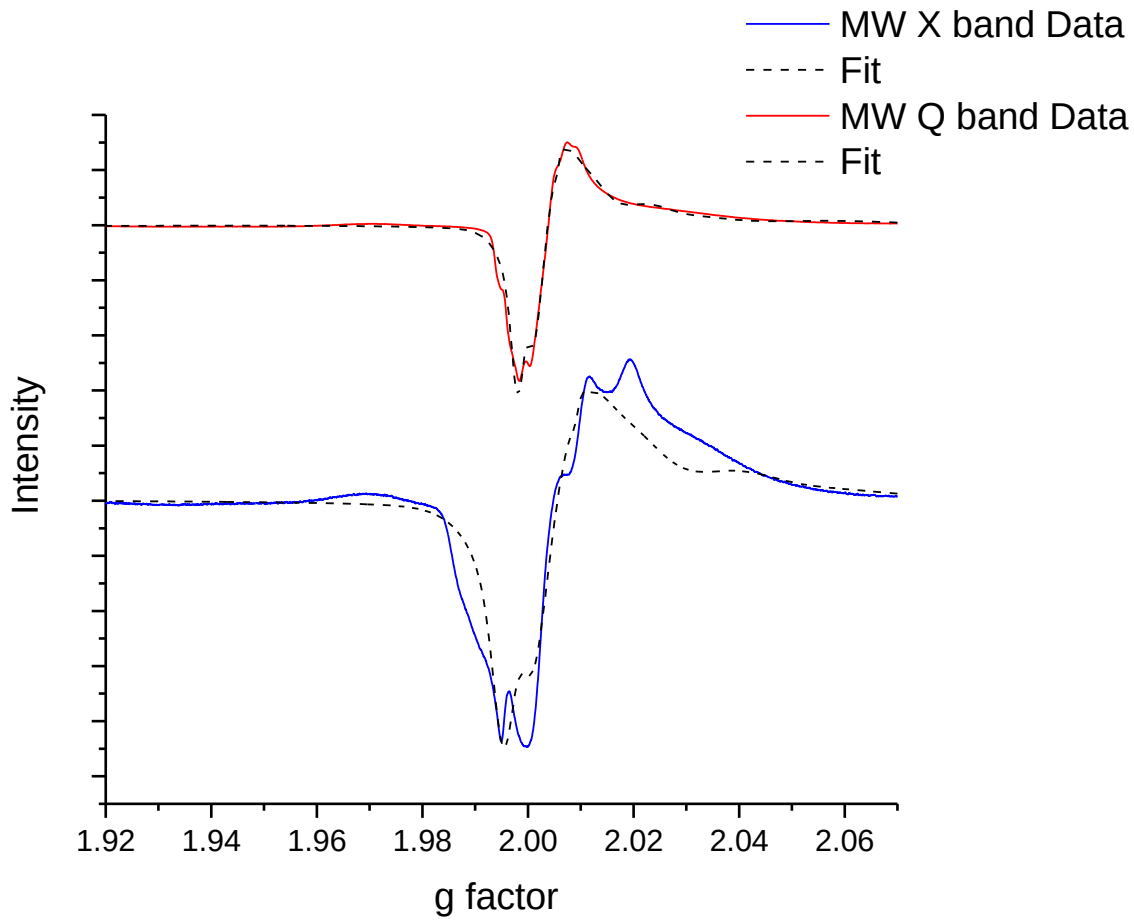


*Figure 40 Results of indirect simultaneous simulation and fitting of MW X band and Q band data collected pre UV exposure. Normalised to g value for clarity*

*Table 26 Results obtained from simulating MW X and Q band EPR spectra collected pre UV exposure*

| Defect | E' | BOHC | POR | $HC_1$ | NBOHC | $BO_3$ | BOSi |
|---|---|---|---|---|---|---|---|
| Nucs | | B | | | | | |
| g values | 1.9977 | 2.0306 | 2.0010 | 2.0034 | 2.0020 | 2.0111 | 1.9974 |
| g values | | 2.0081 | 1.9989 | 2.0103 | 2.0097 | 2.0393 | 2.0013 |
| g values | | 2.0061 | 2.0060 | 2.0070 | 2.0584 | 2.0049 | 2.0219 |
| A strain | | 40.1857 | | | | | |
| A strain | | 43.8786 | | | | | |
| A strain | | 35.2922 | | | | | |
| g strain | 0.0025 | 0.0117 | 0.0049 | 0.0073 | 0.0202 | 0.0540 | 0.0089 |
| $Lwpp_{gauss}$ | 0.4844 | 0.2669 | 0.0223 | | | 0.5463 | 0.5107 |
| $Lwpp_{lorentz}$ | | | 0.5042 | 0.3199 | 1.0228 | | |
| Weight | 0.0414 | 0.4809 | 0.8415 | 0.3782 | 0.7544 | 0.7994 | 0.7777 |

It is proposed that due to the complex overlapping nature of the defects present the complete fitting of MW data is only possible through the use of direct simultaneous fitting,

such that the presence of g-strain can be fully allowed for and the underlying minor defect centres can be fully simulated. It is not currently possible to directly simultaneously fit EPR spectra using EasySpin, therefore it has not been possible to fully simulate the EPR spectra of MW. This demonstrates the complex interactions that occur in glass as a result of gamma irradiation.

As it has not been possible to produce a full fit for MW and, as no g value reference data for calcium borosilicate or aluminosilicate glass can be found, it has not been possible to produce a reasonable start point to aid in the proper identification and calculation of g values for the strong, sharp, UV-unstable defect seen in CaZn shown in figure 41 and 42. Due to the inclusion of calcium and the presence of greater quantities of aluminium the CaZn EPR spectra is expected to be more complex than MW with the large sharp UV unstable peak likely to be anisotropic and potently composed of two closely overlapping signals originating from both the calcium associated HC defect and calcium colloids as indicated by the Q band data shown in figure 43 (47,48). What the UV exposure of CaZn has revealed is that overall the defects present in CaZn are more unstable to UV light exposure than the defects present in MW, which is somewhat unexpected given the two glasses have closely related formulations.

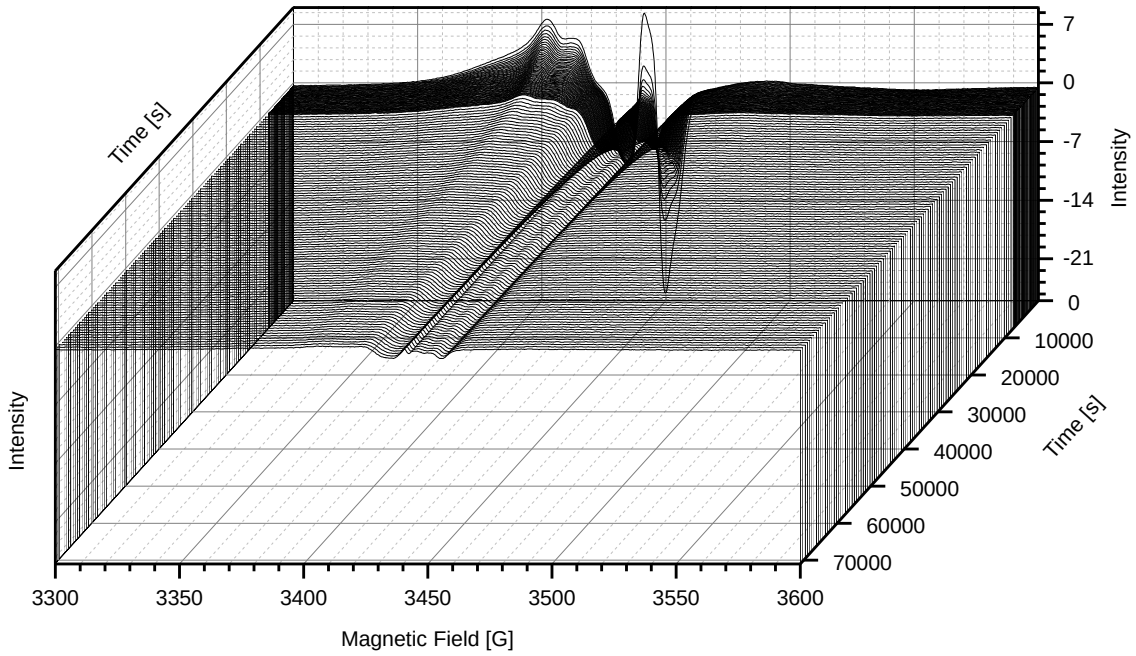


*Figure 41 Full CaZn time delay UV EPR plot showing defect recombination rate*

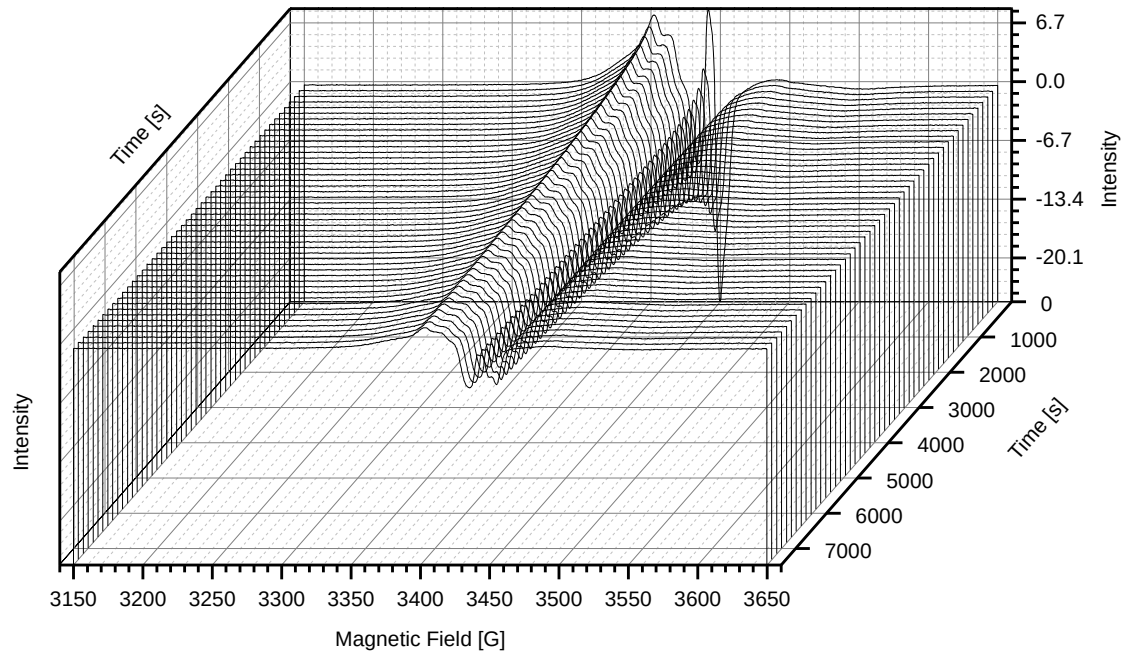


*Figure 42 First 2.5 hours CaZn time delay UV EPR plot shown for clarity*

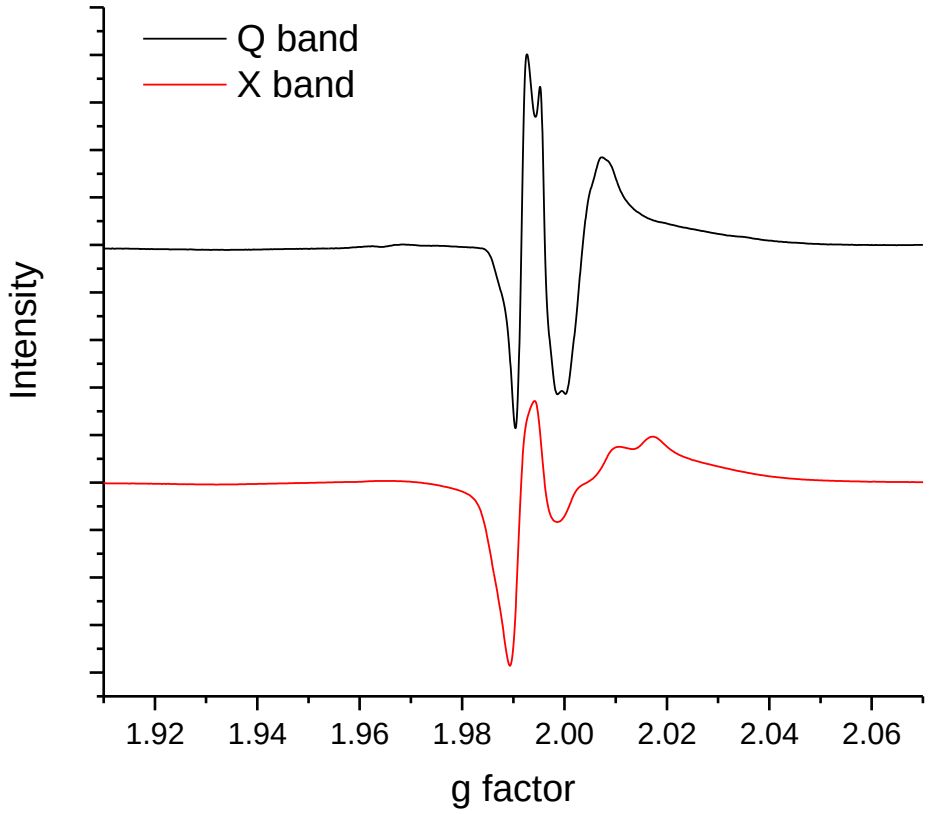


*Figure 43 CaZn Q and X band EPR data normalised to g factor for clarity*

EPR data was collected from a previously irradiated ISG sample which was not exposed to UV light at any stage. The ISG EPR spectrum shown in figure 44 also contained a sharp peak with a comparable g value to the strong sharp peak seen in CaZn and a large broad peak at ~1.97g. However the sharp peak was not as strong as the sharp peak seen in CaZn and the broad peak at ~ 1.97g was weakest in CaZn. Given the general instability of the Ca associated defect observed in CaZn and the duration of time that passed between the sample being irradiated and the EPR spectrum being collected, the sharp peak is taken as an indication there is a related unstable calcium associated defect also present in ISG but that this defect is likely to have started to recombine before the measurement was taken. As ISG has the highest sodium content of all the glasses studied here while CaZn has the lowest sodium content of the glasses studied this also provides further evidence that the

broad peak at ~1.97g observed in MW and ISG corresponds to very small amounts of sodium colloid formation.

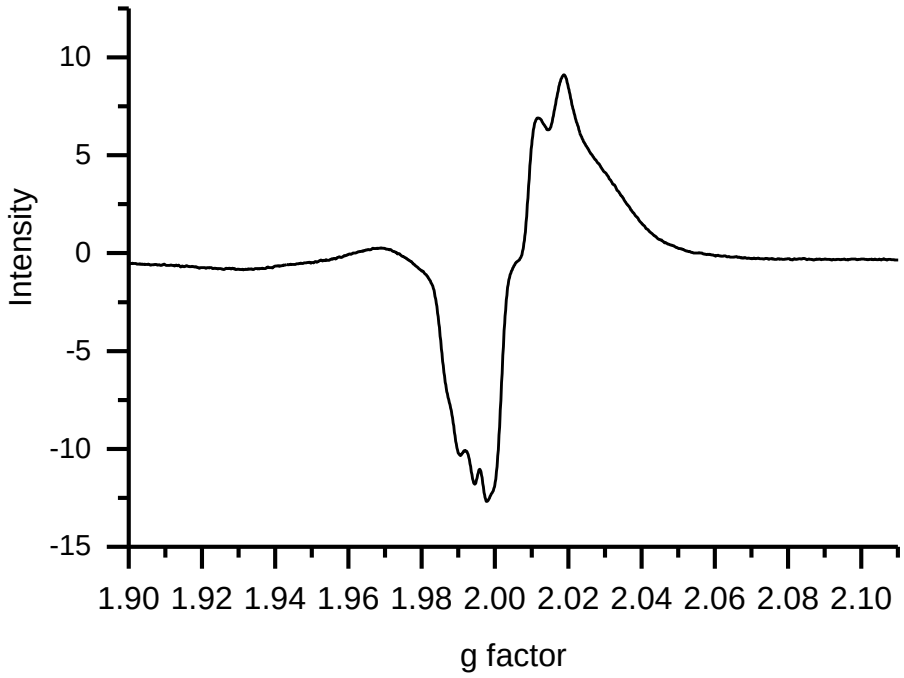


*Figure 44 ISG X band EPR spectrum normalised to g-factor for clarity*

### 3.4.3. Phase Separation

Varying development of Bragg peaks taken to be an indication of gamma radiation induced crystalline phase separation have been observed in high energy X-ray scattering data collected from glass following irradiation to a total dose of ~8 MGy (shown in figure 46 and 47). This crystalline phase separation has not been previously documented in current literature, although this is likely to be due to the use of high energy X-rays to generate PDF data not being commonplace. Where limited amounts of phase separation is present, peak broadening due to the small crystal size is expected to result in peaks being lost against the strong amorphous signal originating from the bulk glass structure, which has potentially been seen here where XRD collected from glass post irradiation up to doses of ~10 MGy did not shown any indication of Bragg peaks.

Irradiation induced phase separation is not an unknown phenomenon. Phase separation has previously been observed in electron irradiated sodium borosilicate glass; however, while inhomogeneous regions corresponding to phase separation were found no indication of crystalline regions was observed by Sun *et.al* (128). Comparable gamma irradiation induced phase separation has also been proposed by McGann *et.al* as being responsible for anomalous behaviour seen in a series of gamma irradiated MW based simulant glasses but again no evidence of crystalline regions were found (43). Given these studies, the crystalline phase separation of the simplified simulant glass ISG, seen in the X-ray scattering data is not entirely unexpected. Despite the widespread use of this glass in radiation studies, ISG was only intended for use as a reference glass in leaching studies. MW and CaZn base glasses are designed to contain HLW, so the extent of crystalline phase separation observed in these glasses is entirely unexpected. This phase separation has prevented the full use of the X-ray scattering data collected from irradiated glass in the creation of a PDF. This data was collected with the aim of quantifying structural changes that occur in gamma irradiated glass. The presence of large quantities of an unidentified competing phase makes the X-ray data collected unsuitable for use in the creation of a PDF, as the resulting data will consist of two complex overlapping PDF datasets. This makes the data semi-quantitative at best and prevents the fitting of both overlapping data sets present in the PDF.

Further evidence of phase separation has been observed in these glasses using an optical microscope. During inspection of the glass surface finish post-irradiation to a dose of ~10 MGy small bright regions shown in figure 45 were observed in certain CaZn and ISG samples; these glass samples were X-ray amorphous when analysed using a standard laboratory XRD. No indication of crystalline regions was observed in glass irradiated to a dose of ~5 MGy.

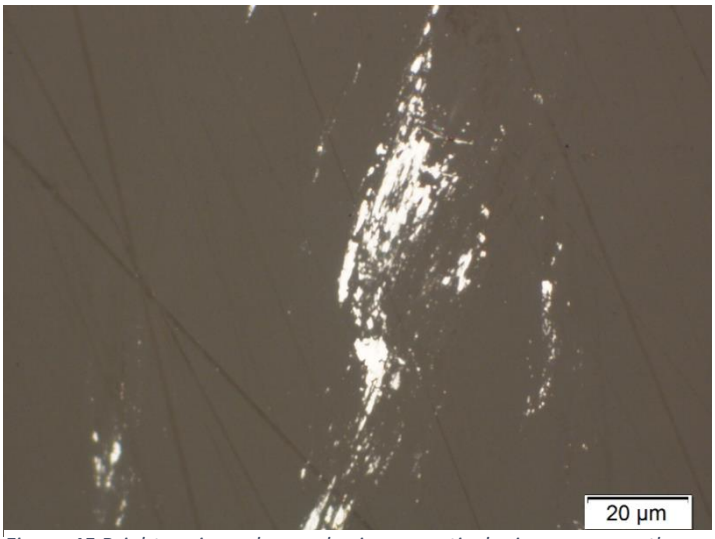


*Figure 45 Bright regions observed using an optical microscope, on the surface of a CaZn sample irradiated to a total dose of 10 MGY*

The same set of Bragg peaks has been observed in all three glasses and the intensity of the peaks present increased with amount of aluminium present in the glass, with the glass with the highest aluminium quantity (ISG) having the strongest Bragg peaks present and the glass with the lowest alumina quantity (MW) having the weakest Bragg peaks present as shown in figure 46.

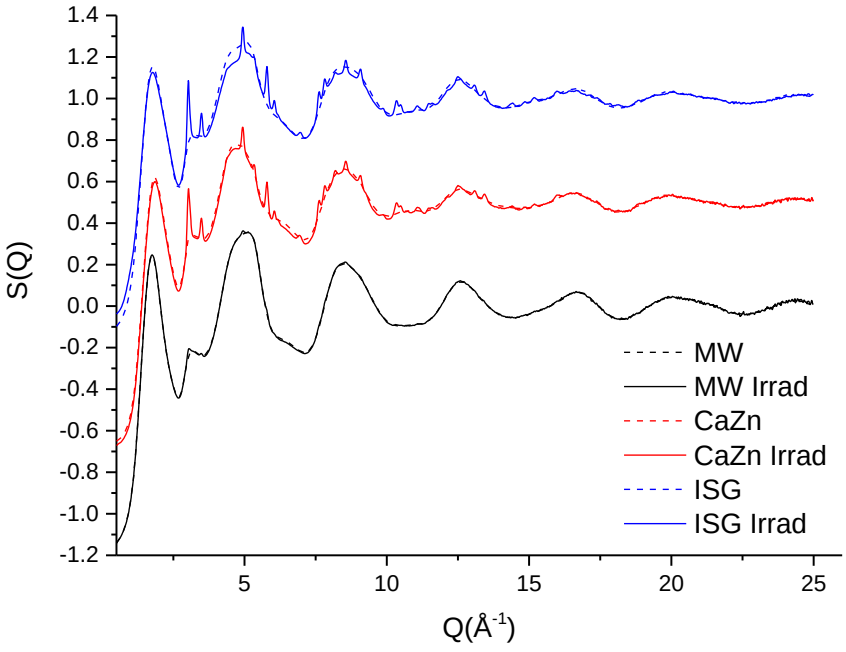


*Figure 46 Overlaid irradiated and unirradiated S(Q) collected from MW, CaZn, and ISG*

In an attempt to identify the crystalline impurity present Q has been converted to d spacing using equation 7 and the data for the pristine sample has been subtracted from the irradiated data.

$$d = \frac{2\pi}{Q}$$

*Equation 7 d = d spacing Q = Q spacing*

To demonstrate the same crystalline phase is present in all the glasses the subtracted data has been baselined to remove the effects of changes to the bulk S(Q) and normalised to the highest peak using OriginPro 9.1. Following this a near identical set of Bragg peaks with d spacings of ~ 1.27, 1.80, and 2.08 Å (shown in figure 47) has been observed in all glass. It has not been possible to identify the crystalline phase or phases formed in these glasses using these d spacing values but based on common elements shared between the glasses the crystalline phase is likely to be aluminum and oxygen based, and may contain silicon, boron and sodium.

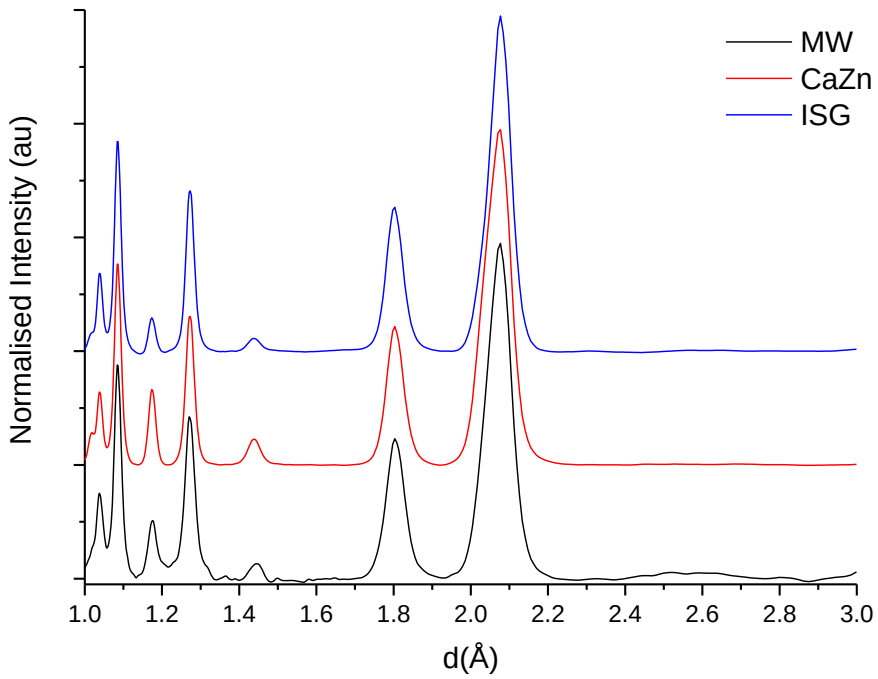


*Figure 47 Normalised d spacing plot of phase separation present in irradiated MW, CaZn, and ISG*

The presence of small quantities of separated phases, invisible at the X-ray wavelength range used in standard laboratory XRD, provides an explanation for difficulties found in modeling gel layer controlled leaching behaviour of glass post irradiation. The gel layer behaviour of simple pristine glasses has been reliably modelled but previous atomistic models with a focus on ballistic effects of radiation have been unable to fully explain the experimental gel layer formation behaviour observed past a certain dose threshold (23,25). It is proposed here that this is due to regions of micro crystalline phase separation forming in the irradiated glass and disrupting stage 1 glass alteration and initial gel layer behaviour before becoming incorporated into the gel layer as a mature gel layer forms over time. This proposed change in the alteration mechansim of irradiated glass would result in both the previously unexplained observed increase in water reactivity at the gel layer/glass interface seen in experiments involving isotopic exchange of irradiated glass, and the reduction in undesirable irradiation effects post gel layer formation and maturation (25).

## 3.5. Conclusion

An attempt at quantifying the impact of gamma radiation on three different glass formulations has been made and this work has provided a foundation for future studies into the impact of gamma radiation on glass structure. Further work in combination with a strong pristine glass baseline produced through atomistic modeling is needed to fully characterise the electronic defects and structural changes taking place in these glasses.

It is proposed that in order to fully understand the impact of gamma radiation on glass electronic defects should be fully characterised and considered separately from structural effects. The distinction between electronic and structural changes is necessary because it is highly likely that structural changes and electronic defects have very different dose thresholds. While electronic defects can be observed at low doses, indications of structural

changes observed in the phase separation seen in the X-ray scattering data, and during sample preparation in the form of a small amount of shrinking and the samples becoming harder to polish only occurred at high (>5 MGy) doses. While it was not possible to quantify these changes, due to Covid-19 related time constraints and lack of equipment, combined with the high energy X- ray scattering data and optical microscope observations this provides further evidence of the presence of different dose thresholds. These dose thresholds should be studied in detail through the use of varying doses and the careful recombination of electronic defects monitored through EPR to enable Raman measurements to be collected with the presence of minimal interference from the fluorescent background.

# 4. The Impact of Gamma Radiation and Steel Contact On The Leaching Behaviour of UK Base Glass.

## 4.1. Abstract

The alteration rates of unirradiated samples of MW and CaZn base glass and samples irradiated to doses of ~ 5 and 10 MGy have been investigated using an MCC-1 based leaching method combined with a 316 stainless steel sample holder designed to simulate a glass-steel crevice environment. A crevice environment can be formed by localised regions of container breach occurring as the container and overpack barriers present in the GDF eventually fail.

This study has revealed specific radiation-induced changes in the rate of silicon, boron and sodium loss from glass that occur during both the crevice and non crevice leaching of both these glasses. These changes have been tentatively linked to the gamma irradiation induced structural changes occurring in MW and CaZn discussed in the author's previous work. The ability to link changes in leaching behaviour to structural changes occurring in the glass has revealed justification for specific variations in both leachate pH and normalised [Si] leachate content that only occur when the glass is leached in the steel crevice environment. These changes are far more prominent in CaZn and are accompanied by an absence of zinc enrichment in the gel layer. It has been proposed that the changes in leachate chemistry and CaZn gel layer composition originate from a specific interaction between the glass and steel that will only occur in the crevice environment. The differences in normalised [Si] leachate concentration and zinc enrichment seen in the CaZn gel layer, and normalised [Si] leachate concentration seen in MW suggest these changes originate from some form of electrochemical interaction occurring between the glass and steel in the crevice environment and that this interaction may be enhanced by the accumulation of certain elements, such as zinc, in the glass gel layer.

## 4.2. Introduction

The 309 steel containers holding the UK's vitrified waste will ultimately be moved to a GDF for long term disposal. Water will penetrate the natural and manmade barriers of the GDF over many hundreds to thousands of years and the glass will be exposed to groundwater. Once the glass is exposed to water the slow degradation of glass, known as alteration, will begin. The alteration process is broadly categorised into three stages (56). Stage 1, is the initial fast alteration of the glass occurring in the early stages of water contact. Stage 2, is the slower gel layer controlled alteration of glass. Stage 3 is the resumption of fast alteration occurring as a result of changes in leachate chemistry, or physical or chemical damage to the glass gel layer (56).

In order to understand this behaviour two standard test methods, the PCT and MCC-1, are typically used as a means of studying the alteration behaviour of glass (61,62). The PCT uses glass powder to produce a high glass surface area to water volume ratio in order to study stage 2 bulk glass alteration behaviour (61). The MCC-1 test uses glass monoliths with a fixed glass surface area to volume ratio in order to study stage 1 alteration behaviour and surface effects (62).

In previous work both MW and CaZn have been well studied using variants of the MCC-1 and PCT tests (129–133). These tests have largely neglected to fully consider container interactions in the early stages of glass alteration. The impact of iron and other steel corrosion products has been well studied using ISG and this is generally agreed to have a negative impact on glass alteration, however, the actual container interactions have again largely been ignored (57,63,64,134). This is despite negative container interaction being discussed in early work (59). A single study is known where the possibility of negative interactions with the container bulk has been raised in work involving ISG and this study has been expanded to include other simple glass formulations (60,65). In these studies it is

proposed that a feedback loop involving the glass steel-interface may form, and it is proposed here that this feedback loop has the potential to be further amplified by increased glass reactivity caused by exposure to ionising radiation.

The interaction between glass and steel is important as it is likely that the initial stages of container breach will consist of localised corrosion leading to small holes forming in the container, as it is corroded by ground water ingress. Densification of borosilicate glass as a result of radiation exposure has been previously observed and the small volume reduction associated with densification may result in the glass pulling away from the container walls where, combined with holes in the container caused by localised corrosion, pockets of water may form between the container walls and glass. (135). The chemistry inside these pockets is expected to differ from the surrounding groundwater chemistry and this may result in the increased duration of stage 1 glass alteration through disrupting gel layer formation (65). In order to investigate this hypothesis, a modified version of the MCC-1 test combined with a self-designed crevice assembly sample holder has been used here. The crevice assembly has been designed such that a glass monolith can be clamped between the two sides of the holder creating a series of crevices simulating the environment formed in these pockets of water.

## 4.3. Experimental

### 4.3.1. Glass Preparation

The glass was prepared using the method given in Brown and cast into ingots (136). The glass ingots were wet cut into 1.4 mm thick sections using a diamond wafering blade and the pre-set glass setting on a Struers Acutom cutting machine with the feed rate varied between 0.1 and 0.04 mm/s to minimise sample breakage. The monoliths were mounted on the surface of a resin block using cyanoacrylate adhesive and wet polished using SiC wet/dry polishing paper starting at 15 µm and moving to 5 µm, with the surface finish

inspected at regular intervals using an optical microscope. The monoliths were removed from the resin block and soaked in acetone to remove adhesive residue. Following this further wet polishing with 5 µm paper was done to remove any remaining residues and minimise any potential surface effects originating from the adhesive used. Polishing compound was not used, due to concerns about potential effects of an aluminum containing polishing compound on the glass surface chemistry. The polished slices were cut into monoliths measuring approximately 0.1 x 1 x 1 cm with two monoliths typically obtained from each slice.

Randomly selected polished glass monoliths were gamma irradiated to doses of ~ 5 and ~ 10 MGy using a Foss Therapy Services 812 $^{60}$Co gamma irradiator as described in Brown with exact dose and dose rate shown in table 27 and 28 (reproduced from (136)). The irradiated monoliths were repolished after irradiation to remove potential surface changes occurring as a result of being irradiated in ambient atmosphere. Prior to leaching, all monoliths were cleaned ultrasonically for a minimum of 5 minutes in ethanol and rinsed with ultra-pure water, then dried in an oven set at 90°C until constant mass. The dried monoliths were immediately placed in the clean water filled Parr vessels.

*Table 27 Dose and dose rate for ~ 10 MGy samples used. Samples were irradiated in two sessions due to length of time required to reach target dose.*

| Glass | MW monoliths | CaZn monliths |
|---|---|---|
| Duration h | 402 | 402 |
| Ave dose rate Gy/min | 209 | 202 |
| Total dose MGy | 5.042 | 4.866 |
| Duration h | 373 | 404 |
| Ave dose rate Gy/min | 215 | 206 |
| Total dose MGy | 9.854 | 9.863 |

*Table 28 Dose and dose rate for ~ 5 MGy samples used*

| Glass | MW monoliths | CaZn monliths |
|---|---|---|
| Duration h | 465 | 441 |
| Ave dose rate Gy/min | 179 | 189 |
| Total dose MGy | 4.998 | 4.999 |

### 4.3.2. Leaching Method

The leaching runs were carried out in a 90°C oven, in ultra-pure 18 MΩ water, using commercially available 22 mL 316 stainless steel series 4700 Parr vessels supplied by NNL and a fixed glass surface area to solution volume ratio of 20 $m^{-1}$. The surface area to volume ratio was calculated for each individual monolith using the assumption that all sides of the glass were exposed to water. In order to determine a suitable duration an initial leaching run was carried out at a 28 and 42 day interval using only CaZn laid flat on the base of the Parr vessel (full details shown in figure s1 in the supplementary section). Due to the aluminum and calcium in its formulation CaZn is expected to alter slower than MW. The two initial CaZn leaching runs showed near identical leachate pH, normalised boron ([B]), normalised silicon ([Si]) and normalised sodium ([Na]) content levels and near identical gel layer formation when EDX line scanned (as shown in figure 48). This was taken as an indication that stage two alteration was reached during the 28 day leaching interval. Based on these results a leaching run time length of 28 days for both glasses was used in all further investigations.

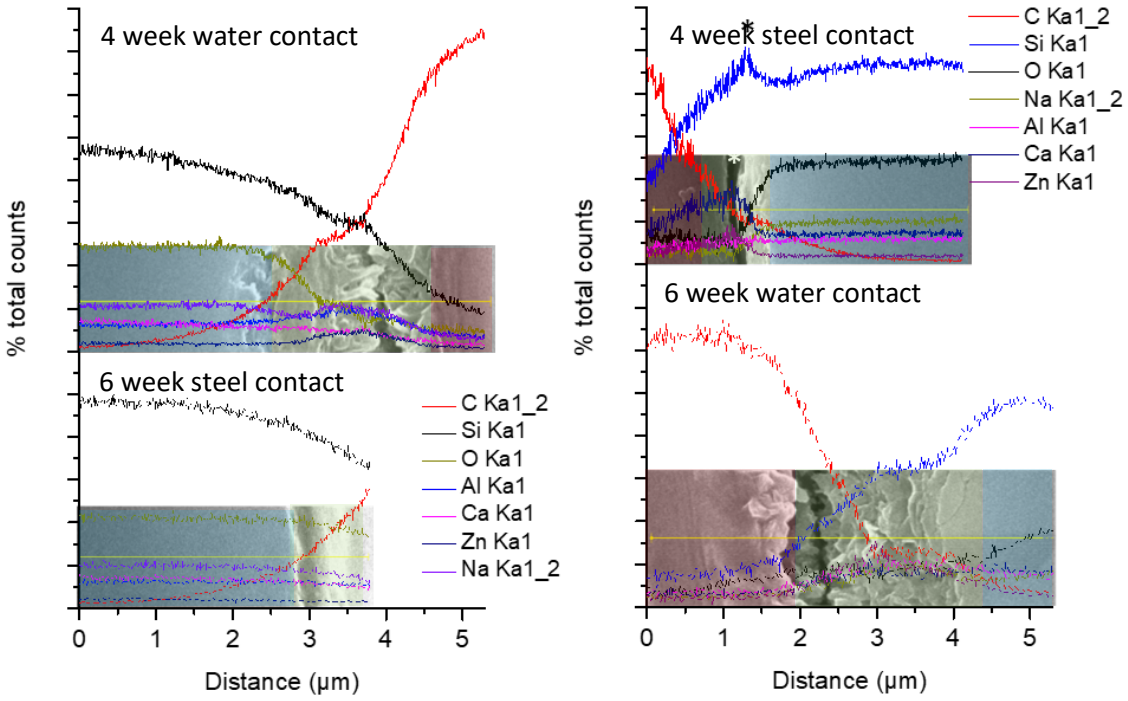


*Figure 48 EDX line scan plots of cross sections of the steel contact and water contact side of 4 and 6 week leached CaZn monoliths. Glass highlighted in blue, approximate gel layer highlighted green and resin highlighted red. 4 week run plotted as solid line and 6 week run plotted as dashed line( * indicates distortion caused by normalisation process and resin pulling away from glass during analysis).*

Each leaching run consisted of two sets of batch leaching experiments consisting of a minimum of three replicates of each glass sample and a blank ran with only water present, and the results were averaged across each batch (full details of each individual run shown in tables s2 to s6 in the supplementary section). Three separate leaching runs were carried out with the monolith laid flat on the base of the Parr vessel (full details shown in table s2 to s4) in order to partially mimic the method used by Guo *et al,* and two separate leaching runs were carried out with the glass monolith held in the crevice holder shown section 4.3.2.2. (full details shown in table s5 to s6) (60,65). In all leaching runs carried out with the monolith laid flat on the base of the parr vessel the side of the monolith exposed to water is referred to as water contact, and the side of the monolith placed flat on the base of the parr vessel is referred to as steel contact in all samples (as shown in figure 49). Wheres in all leaching runs carried out using the crevice holder the side of the monolith held against the ridged side of the holder is referred to as steel crevice contact, and the side of the

monolith held against the flat side of the holder is referred to as steel flat contact (as shown in figure 49).

After each leaching run the Parr vessels were removed from the oven and placed in an iced

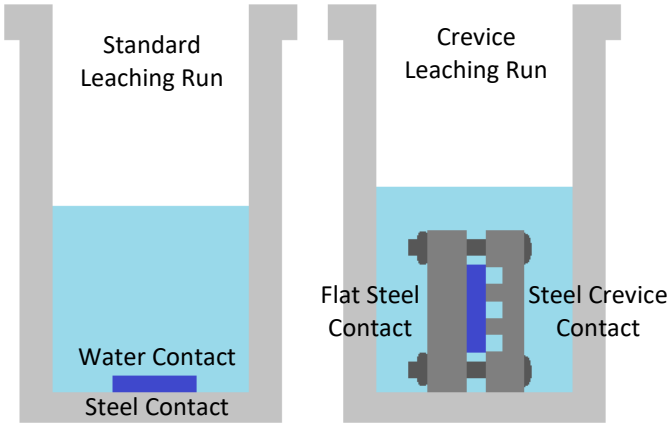


*Figure 49 Simplified diagram (not to scale) of leaching runs prior to parr vessels being sealed, showing notations used. Dark blue rectangle represents glass monoliths used.*

water bath to speed cooling. Once cooled the Parr vessels were opened and the leachate decanted into sealed PTFE vials and placed in a laboratory fridge to prevent microbial growth. The glass monoliths were rinsed thoroughly in the glass leachate, then transferred to a clean watch glass and allowed to dry in a 50°C oven to constant mass.

#### *4.3.2.1. Parr Vessel Cleaning*

Prior to first use in the leaching runs all Parr vessels used were cleaned according to the following method, loosely based on the cleaning steps recommended in PCT method (61).

The Parr vessels were cleaned ultrasonically in water, then degreased with ethanol before being rinsed with distilled water to remove any residues present. Following these steps, the vessels were filled two thirds to three quarters full with 1 wt% (0.16 M) nitric acid, sealed and placed in an oven set at 90°C for approximately 18 hours to strip any residues present on the steel. The nitric acid filled vessels were allowed to cool to room temperature before being emptied and the nitric acid disposed of. The PTFE gasket was removed, as this had become brittle due to degradation caused by nitric acid, and the vessel rinsed 3 times with

distilled water ensuring the lid was thoroughly rinsed. A fresh PTFE gasket was fitted and the vessel filled two third to three quarters of the way with ultra-pure water, sealed then placed in an oven set at 90°C for 24 hours, then allowed to cool to room temperature. The water pH was measured at pH 6 – 6.7 with a digital pH meter before the vessels had been placed in the oven and pH 5.6 – 7.2 after being removed from the oven and allowed to cool. The vessels were placed in a drying oven set at 90°C and allowed to dry. Once dried, the vessels were reassembled with the lids loosely fastened.

The cleaning procedure used was modified in subsequent leaching runs to remove the need for a fresh PTFE gasket for each leaching run as follows. Instead of being filled with 1 wt% (0.16 M) nitric acid sealed and placed in an oven the Parr vessels were filled with 1 wt% (0.16 M) nitric acid, covered with foil and placed in a water bath set at 90°C for 8 hours, then allowed to cool overnight before the nitric acid was disposed of.

#### *4.3.2.2. Crevice Holder Manufacture and Cleaning*

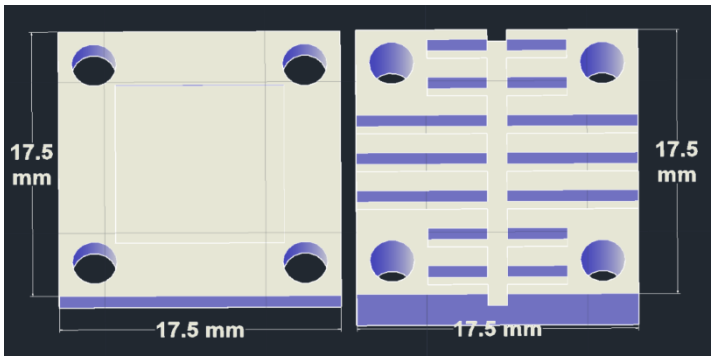

*Figure 50 Crevice holder CAD design*

The crevice holders were machined from 316 stainless steel using the custom design shown in figure 50. This design is based loosely on the crevice washer used in the ASTM G48 – 11 procedure for investigating crevice corrosion in steels and is fastened using 316 stainless steel nuts and bolts (74). The crevice holder assembly, and nuts and bolts were cleaned using the same procedure used for the Parr vessels. Prior to each crevice leaching run the glass monolith was placed in the recess present in the base section (shown on the left side of figure 50) and the crevice assembly was closed with the bolts fastened in a figure eight pattern to evenly distribute pressure on the glass monolith. The crevice

assembly was placed in the water filled Parr vessel on its side with the channel openings facing up. The Parr vessel was then sealed and sonicated for 15 minutes to dislodge any trapped air bubbles from the crevice assembly before being placed in the 90°C oven.

### 4.3.3. Leachate Analysis.

Following each leaching run the unfiltered leachate solution sodium and boron concentration was determined by University of Manchester Microanalysis Laboratory using a Thermo iCAP 6300 ICP-OES system. Prior to ICP-OES analysis the leachate was diluted 1:1 and acidified to 1% m/v nitric acid concentration, using a 2% m/v nitric acid solution prepared from stock using ultra-pure water.

It was not possible to determine the silicate content using this ICP-OES system and the silicon content was instead determined using the molybdenum blue colorimetric method given below (137).

All chemicals used in determination of silicon concentration were supplied and stored in plastic bottles or prepared as a stock solution using Nalgene volumetric flasks to prevent silica contamination and deionised ultrapure 18 MΩ water was used throughout. Prior to each set of leachate silicon analysis appropriate quantities of the following were prepared; $H_2SO_4$ 1 M and 0.05 M; oxalic acid–tartaric acid 0.5 M–0.5 M; ammonium molybdate 5% m/v; ascorbic acid 2% m/v; a standard silicate solution diluted to an appropriate concentration range (0 ppm, 5 ppm, 10 ppm, 20 ppm, 40 ppm, 80 ppm) from a 1000 ppm premixed silicate standard solution.

Prior to analysing each batch of glass leachate a calibration curve was prepared using the set of prediluted silicate standard solutions as follows. A 100mL plastic beaker was placed in a 25°C water bath and positioned on a hotplate stirrer using a temperature probe to control the water bath temperature. A 12mm PTFE coated stir bead was added to the 100 mL beaker followed by 20 mL of $H_2SO_4$ (0.05 M) and 2 mL of silicate standard solution. The

solution was stirred for 20 min to ensure proper mixing and heating of the solution. Following stirring 20 mL of ultrapure 18 MΩ water was added to the beaker, followed by 10 mL of absolute ethyl alcohol, and 15 mL of ammonium molybdate (5%). The solution was again stirred for 20 min to allow for complete formation of a yellow silicomolybdate complex in the colourless solution. Finally, 10 mL of oxalic acid–tartaric acid (0.5 M–0.5 M), and 5 mL of ascorbic acid (2%) were added to the yellow solution and the solution was stirred for 20 min to enable the complete reaction of the yellow silicomolybdate complex to form the molybdenum blue complex necessary for colorimetric analysis.

Following preparation of a calibration curve the leachate solutions were analysed using a similar molybdenum blue method. As the leachate solutions were all stored in sealed plastic vials, and placed in a standard laboratory fridge to prevent microbial growth, prior to analysis all leachate solutions were placed in a 50°C water bath, and thoroughly shaken to enable redissolution of any partiality soluble precipitates that may have settled out of solution. The CaZn leachate was analysed undiluted and the MW leachate was diluted to a 1:10 ratio with ultrapure 18 MΩ water to ensure the silicate concentration fell in the analysis range.

The neat CaZn leachate and diluted MW leachate was analysed using the following method. A 100mL plastic beaker was placed in a 25°C water bath and positioned on a hotplate stirrer using a temperature probe to control the water bath temperature. A 12mm PTFE coated stir bead was added to the 100 mL beaker followed by 20 mL of $H_2SO_4$ (0.05 M) and 2 mL of glass leachate. The solution was stirred for 20 min to ensure proper mixing and heating of the solution. Following stirring 20 mL of ultrapure 18 MΩ water was added to the beaker and if necessary, the pH was adjusted to 1.4 by adding $H_2SO_4$ (1 M) dropwise. Following pH adjustment, 10 mL of absolute ethyl alcohol, and 15 mL of ammonium molybdate (5%) was added to the beaker and if silica was present in the leachate the

solution begun to change from colourless to a very pale yellow, due to silicomolybdate formation. The solution was again stirred for 20 min to allow for complete formation of the yellow silicomolybdate complex in solution. Finally, 10 mL of oxalic acid–tartaric acid (0.5 M–0.5 M), and 5 mL of ascorbic acid (2%) were added to the solution and the solution was stirred for 20 min to enable the complete reaction of the yellow silicomolybdate complex to form the molybdenum blue complex necessary for colorimetric analysis.

The spectrophotometric determination of silicon solution content was performed at a range of 700-900 nm using a Cary UV-VIS-NIR spectrometer in dual beam mode, and PMMA cuvettes to prevent Si uptake from the cuvette, with the peak of interest located at ~812 nm. All measurements were made using 10 mm path length cuvettes with ultrapure water used as a baseline.

The silicon, sodium, and boron solution concentration for each experimental run was normalised against silicon content in the glass using a method based on Abraitis with the equation modified to use glass surface area: solution volume ratio (Sa:V) in the place of monolith size as shown in equation 8 (138). Where $[i]_{raw}$ is the mol/dm$^3$ of element i in the leachate, $SaV_{mean}$ is the mean Sa:V ratio in a given set of leaching runs, SaV is the individual Sa:V ratio, $v_{si}$ is the atom % of silicon in a glass, $v_i$ is atom % of element i in a glass and $m_i$ is the molar mass of element i. To allow for the slight variations in Sa:V and different glass formulations the solution concentration was normalised against glass silicon content of the glass using equation 8. This method was chosen as it better allows for slight variations in Sa:V ratio

$$[i] = [i]_{raw} \times \frac{SaV_{mean}}{SaV} \times \frac{v_{si}/28.0855}{v_i/m_i}$$

*Equation 8*

### 4.3.4. Monolith Analysis

Once cooled the dried glass monoliths were stored in double sealed bags to minimise moisture absorption by the dried gel layer. The monolith surfaces were analysed before and after leaching using an Olympus GX71 invert optical microscope in bright field mode. Selected monoliths were analysed used a Senterra Raman microscope and the following settings 532 nm laser set at 20 mW, 50x magnification, an integration time of 15 s, 30 coadditions and a 25x1000 µm aperture.

SEM and SEM-EDS analysis was caried out using a Quanta FEG 250 Scanning Electron Microscope operating at an acceleration voltage of 15 – 20 kV, equipped with an Oxford Xmax$^N$ 80 EDS detector. Individual monoliths of CaZn and MW from each leaching run were mounted in cross section using a 3D printed sample holder, encased in Araldite 2020 two part epoxy resin using a 4 cm diameter sample cup, and wet polished to a 5 µm surface using silicon carbide paper to enable SEM analysis of gel layer cross sections and a fragment of CaZn was broken from an unirradiated leached sample to enable comparison with resin mounted glass monoliths. All samples were gold coated prior to imaging and single images were taken using a Back Scattered Electron (BSE) detector. EDS elemental mapping was carried on the non-resin coated sample using a 2 min collection interval to allow for this sample shifting during measurement. The resin mounted samples were EDS mapped and EDS line scanned using 5 to 10 min intervals to allow for the resin shifting under the electron beam. All linescans were normalised and plotted against total counts for clarity.

## 4.4. Results and Discussion

A modified MCC-1 test using a surface area to volume ratio of 20 cm$^{-1}$ instead of the specified 10 cm$^{-1}$ was used to ensure the glass monoliths and crevice assembly could be placed in the Parr vessel, without changing the volume of water used in the two types of

leaching. To enable a comparison between a steel containing environment as used in Guo *et al.* and a true steel crevice environment the glass monoliths were placed flat in the base of the water filled Parr vessel while the monolith used in the crevice contact leaching runs were held between the two sides of the steel crevice sample holder (60,65). Stainless steel Parr vessels were used as this method is intended to be proof of concept for future work involving simulant glasses and in situ irradiation. With the aim of simulating both conditions that may occur if container breach occurs in the earlier and later stages of waste lifetime.

The leachate solution concentrations of silicon, boron, and sodium were used as a means of tracking the rate of glass leaching. Silicon was chosen as a marker element as gel layer formation rate and stability is controlled by silicon leachate concentration with a constant silicon leaching solution concentration considered to be an indication that a stable gel layer has formed and stage 2 of glass alteration has been reached (77). Boron and sodium were chosen as glass alteration marker elements as these are present in all glasses studied here and are widely considered to be unable to be reincorporated into the gel layer as secondary products. To allow for the different glass formulations the solution concentration was normalised against glass silicon content of the glass using equation 8.

The initial silicon concentration results (shown in table s2 supplementary) showed that the MW leachate has a silicon solution concentration nearly a factor of 10 larger than CaZn. This was taken as an indication that MW base glass leaches faster than CaZn under these conditions and this pattern is observed throughout, regardless of dose or steel crevice contact. In all glass monoliths a cloudy white gel layer with clear striations corresponding to where the glass monoliths were poured was observed after the gel layer had been carefully dried (as shown in figure 51).

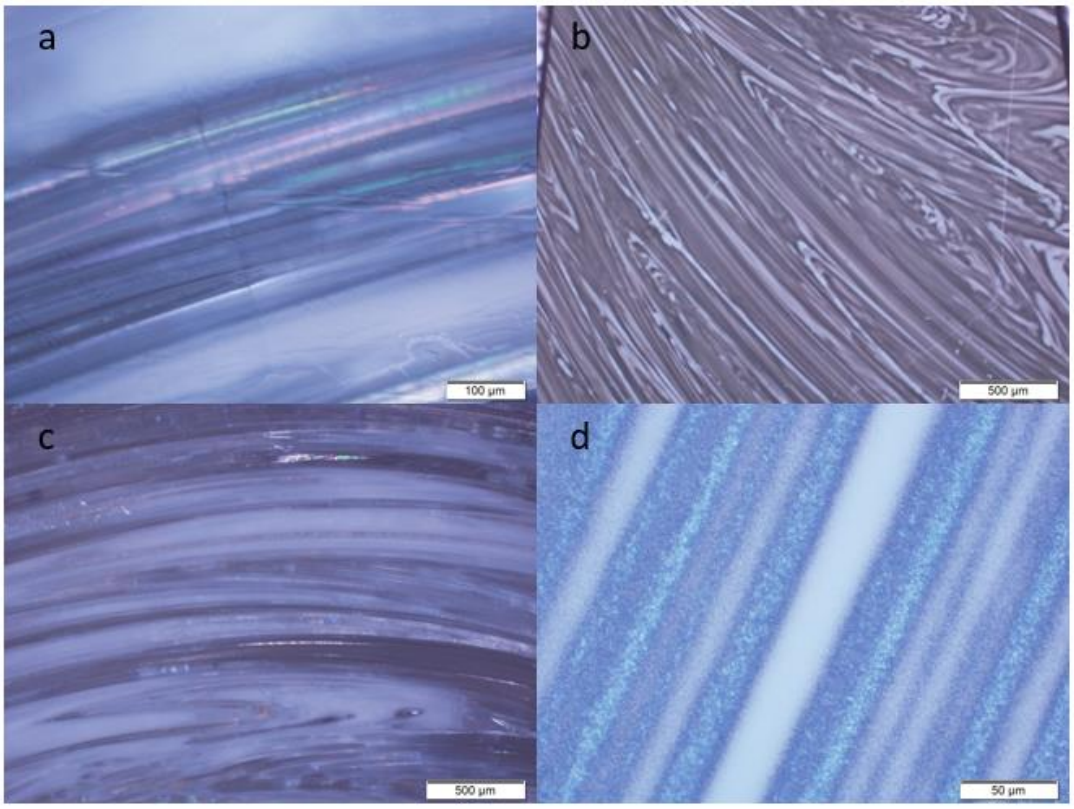


*Figure 51 Gel layer striations observed using an optical microscope in unirradiated MW (a) and CaZn (b), and 10 MGy MW (c) and CaZn (d)*

The glass was prepared from frit which minimised the potential of phase separation occurring due to glass preparation methods, the striations are potentially related to the previously observed formation of boron rich and boron poor regions within borosilicate glass (139). It has been proposed that the high boron regions, observed though NMR, will be more reactive than boron poor areas and this corresponds to the variations in gel layer region appearance observed (139). This is somewhat supported by Raman data where it was only possible to collect data without a significant glass background from the cloudy region of MW samples (shown in figure 52). The Raman signal obtained from the cloudy portion of the MW gel layer showed a broadening and shifting to lower wavenumber of the Si-O peak at ~500 $cm^{-1}$ and a reduction in peak height in the $Q_n$ region (850 – 1300 $cm^{-1}$) consistent with an amorphous silicate. Due to the thinness of the gel layer formed on samples of CaZn it was not possible to collect Raman data that did not show a glass

background; however, the changes in the Si-O and $Q_n$ region of the CaZn Raman signal were consistent with the formation of a thin layer of amorphous silicate (shown in figure 52).

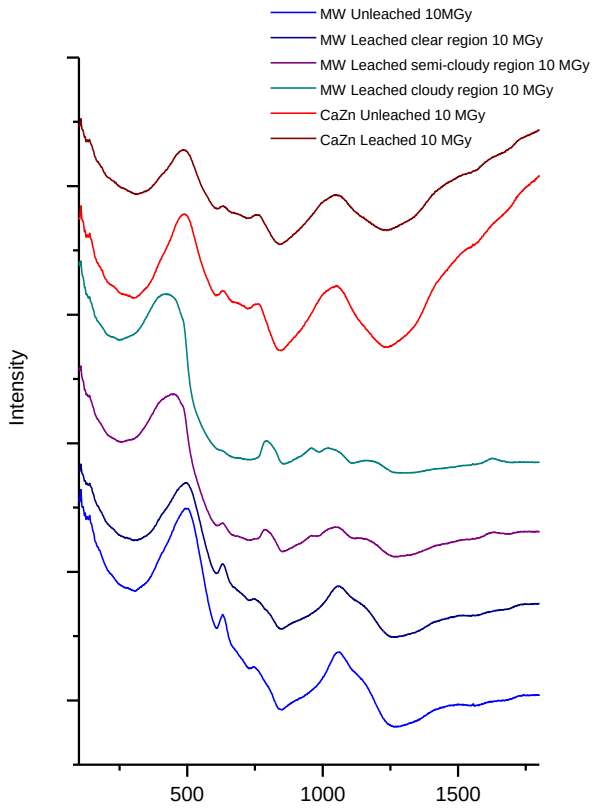


*Figure 52 Raman spectra of MW and CaZn Gel layer*

In the unirradiated samples the dried gel layer formed on MW was thicker than the gel layer formed on CaZn but more prone to delaminating during the drying process, resulting in an overall more fragile gel layer than the thinner gel layer formed on CaZn. This required careful handling to prevent the MW gel layer flaking off. In regions where the gel layer had flaked (as shown in figure 53) the underlying glass surface appeared pitted when viewed using an optical microscope suggesting significant degradation had occurred over the relatively short leching duration. The MW gel layer became noticeably more opaque and more fragile with increased dose. The CaZn gel layer also became more opaque, but did not become more fragile with increased opacity, suggesting a thicker and more stable gel layer had formed in CaZn as result of irradiation.

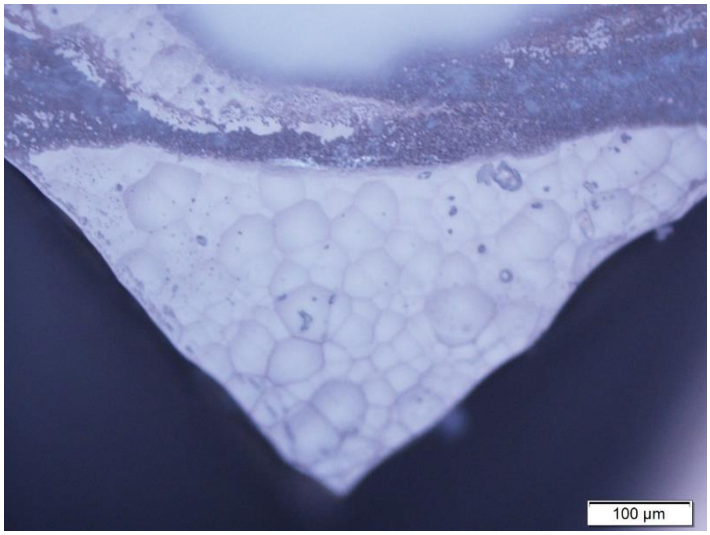


*Figure 53 Optical microscope image of pitting seen under MW gel layer*

The MW gel layer side in contact with the stainless steel Parr vessel dried to a shiny surface finish in all samples. The CaZn gel layer in contact with the stainless steel Parr vessel was typically poorly formed in the center of all glass monoliths. This matches the observation made by Guo *et al.* in leaching runs carried with deionised water and ISG (65). This was present in all CaZn samples and may suggest that water had not made proper contact with the CaZn glass. However complete gel layer formation was observed in MW, suggesting that instead this may be related to interactions with the stainless steel Parr vessel base.

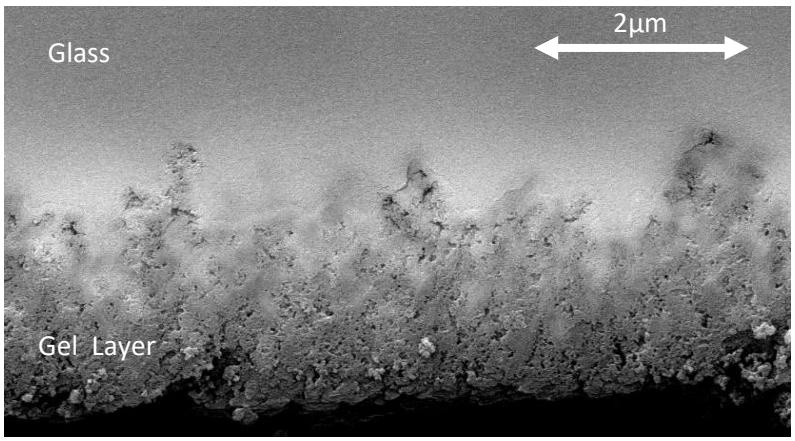


*Figure 54 BSE SEM image of dried CaZn gel layer cross section observed without the use of resin*

A well-formed gel layer was also only observed on the fully water exposed side of the sample of unirradiated leached CaZn broken off a glass monolith and analysed using SEM-EDS (shown in figure 54). Although due to the tool used to break off the glass fragments

causing visible damage to the gel layer this could not be taken as conclusive evidence of improper gel layer formation on the non crevice steel contact CaZn samples. When analysed through SEM-EDS with elemental mapping the leached surface clearly showed the expected sodium depletion and some calcium loss from the gel layer (shown figure s26 supplementary). A small amount of potential zinc loss was also observed, which is not expected as zinc is typically considered to be insoluble. However, due to difficulties in mounting this sample and the tendency of this sample to shift during imaging a comparatively short measurement time was used and the Na Kα line overlapping the Zn Kα line leads to difficulty in distinguishing these lines resulting in a high degree of uncertainty in this measurement.

The EDS mapping and EDS line mapping (normalised line mapping data shown in figure 55 and 56, raw line mapping data shown supplementary figures s6 – s15, and EDS mapping data shown supplementary figures s17 – s36) of the resin-encased sample cross sections demonstrated that minimal smearing across the surface occurred during resin encased sample preparation with the carbon content originating from the resin undergoing a large drop over a distance of less than 2 μm as the analysis region changes from resin, to gel layer, then unleached glass. The EDS line mapping showed that the gel layer formed on the side of the monolith exposed to water noted as water contact was typically ~10 - 25% thicker than the steel contact gel layer in all samples. A distinctive boundary was observed between glass and gel layer in MW, while the boundary between gel layer and glass was less distinct in CaZn. Due to uncertainties originating from MW gel layer delamination combined with variations in gel layer thickness believed to originate from differences in boron content in regions of the glass, and the lack of distinction between glass and gel layer seen in CaZn, the exact gel layer thickness is not discussed in any detail here. The CaZn gel layer region was typically in the 1 - 5 μm order of magnitude while the delaminated MW gel layer was in the 50 – 100 μm.

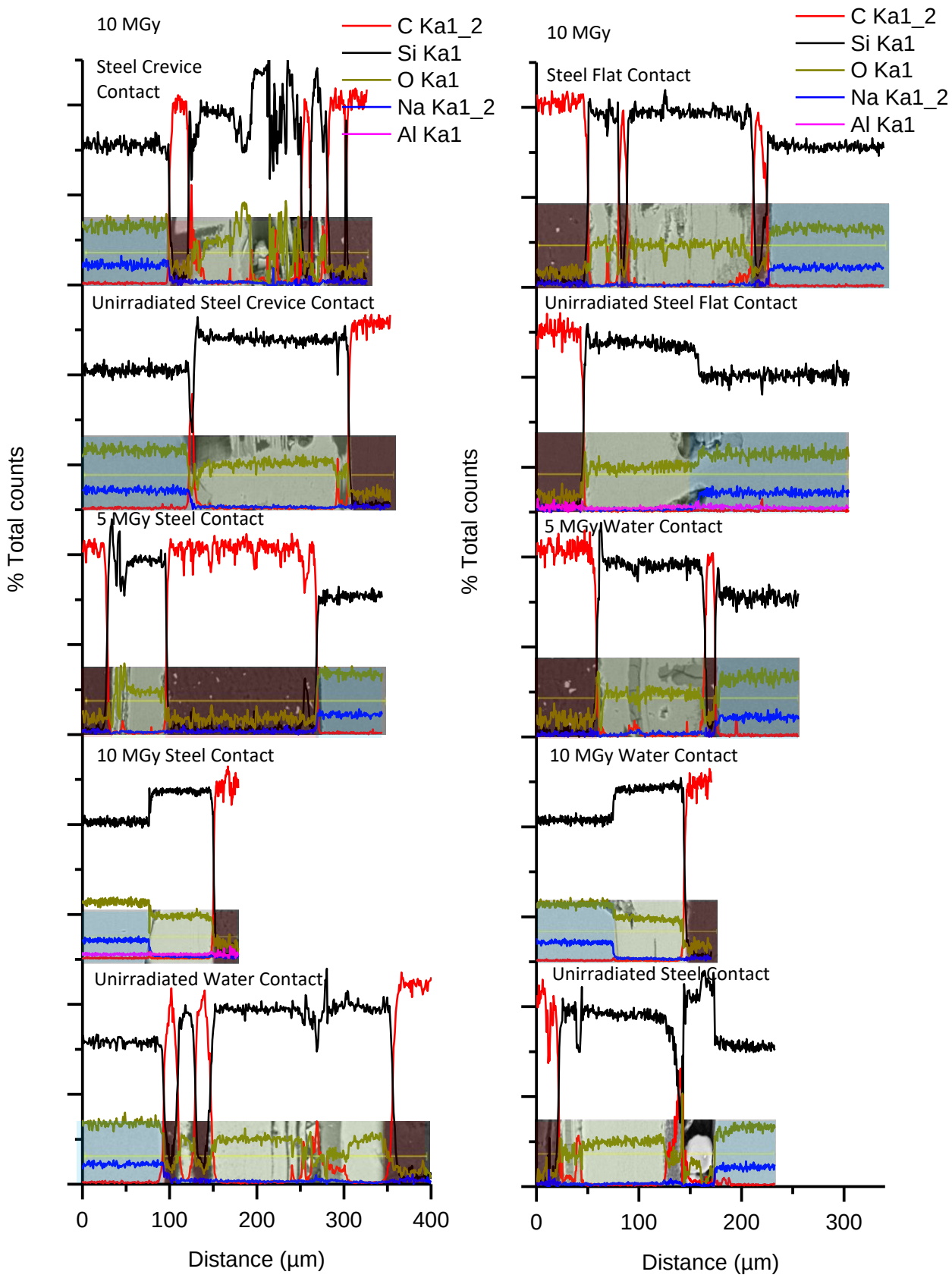


*Figure 55 Normalised MW SEM EDS Line scans shown overlaid with image of gel layer region used for data collection. Glass highlighted blue, gel layer highlighted green, and resin highlighted red.*

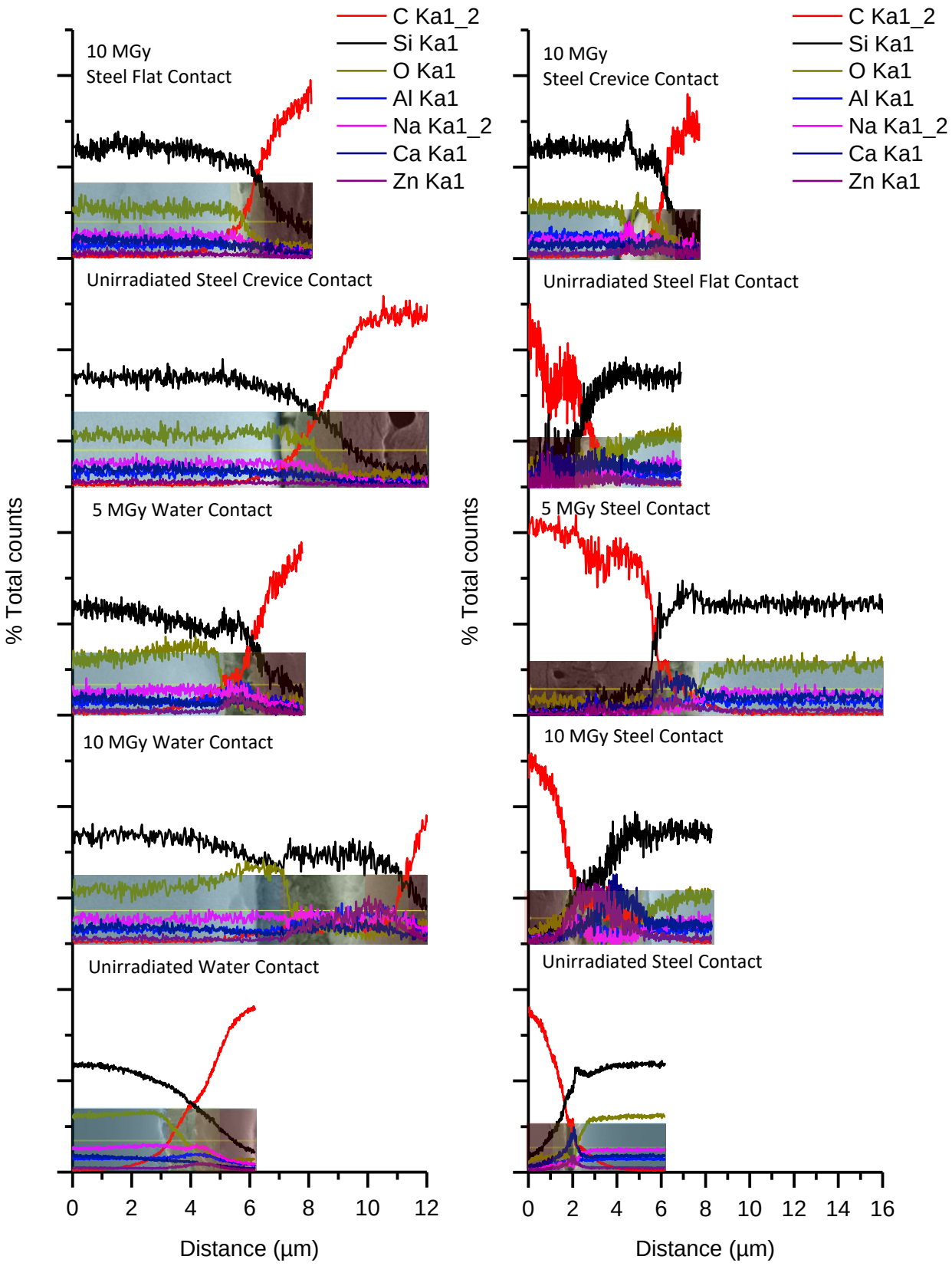


*Figure 56 Normalised CaZn SEM EDS Line scans shown overlaid with gel layer region used for data collection. Sudden spikes in unirradiated and 10 MGy steel contact are artifacts in normalisation caused by resin shrinkage during measurements. Glass highlighted blue, gel layer highlighted green, and resin highlighted red. Note that red and green overlap in many samples due to lack of clear boundary between resin and gel layer.*

In all the non-crevice CaZn samples a thin but well-formed gel layer was observed in cross sections of the water contact side and a thin poorly formed gel layer was observed in cross sections of the steel contact side as shown in figure 56 and 57. This is in contrast to cross sections of the MW gel layer that showed it was well formed on both sides but had undergone significant delamination from the glass surface during the drying process used as shown in figure 58. Following irradiation, an uneven surface finish was observed across the gel layer cross section, indicating the hardness and porosity of the thin CaZn gel layer may have changed. This in combination with the resin being damaged by the electron beam during long measurements led to difficulty in imaging the gel layer to determine its thickness and resulted in artefacts when collecting EDS line scans.

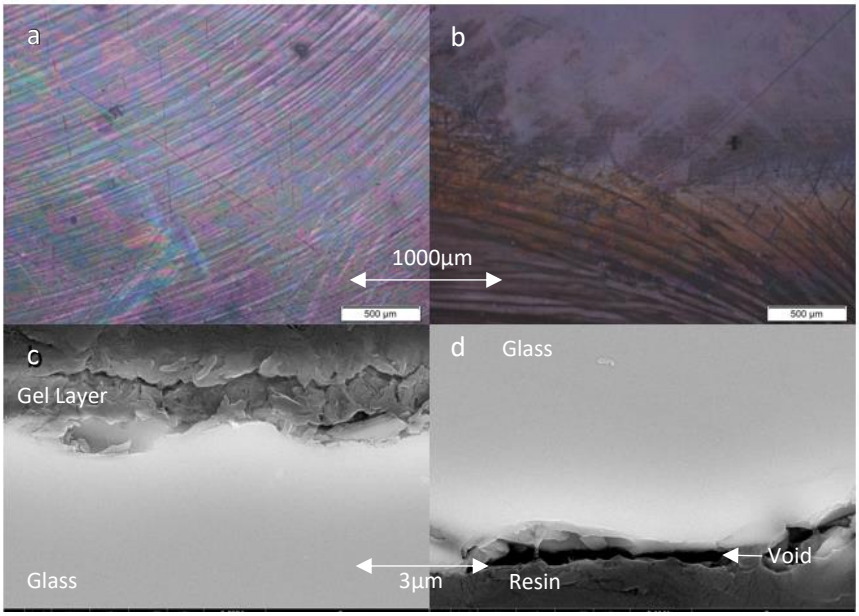


*Figure 57 Optical microscope images (top a and b) showing CaZn water contact gel layer (a) and poorly formed steel contact gel layer (b) and BSE images (bottom, c and d) of cross sections of unirradiated CaZn showing thin gel layer (c) and voids formed by resin shrinking (d).*

Throughout all samples of non crevice contact CaZn a consistent yet small reduction in sodium content and a slight enrichment of zinc was observed in the gel layer cross section (shown in figure 56), indicating the apparent zinc loss observed through initial EDS mapping was an artifact caused by the Na Kα and Zn Kα line overlap combined with the short collection time used leading to poor resolution. In addition to the increase in zinc content,

a very slight drop in calcium content was also observed in the unirradiated CaZn gel layer. This is not consistent with previous studies where enrichment of zinc in the gel layer is typically accompanied by an increase in calcium content (132,140). However, some caution must be taken in this interpretation as a vapour hydration based leaching method was used in these studies instead of the MCC-1 based test used here (132,140). It has been suggested by Corkhill *et al*. that an equillibrium process involving calcium and silicon may be present in bulk solution leaching experiments that may result in small regions of calcium silicate hydrate precipitation on the gel layer surface (78).

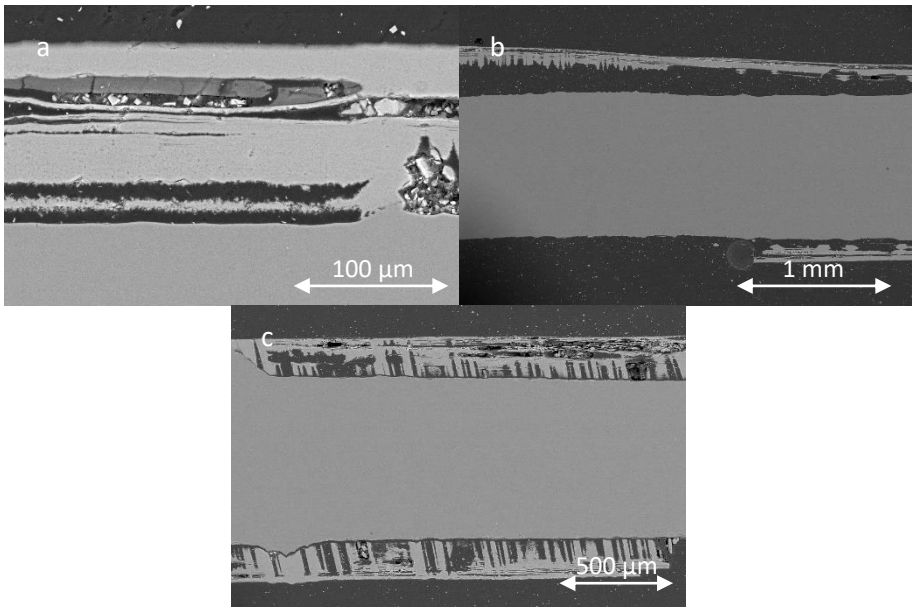


*Figure 58 MW gel layer cross section showing striations and delamination seen in a) standard leached unirradiated sample, b) standard leached 5 MGy sample, and c) 10 MGy crevice leached sample. All samples leached in 18 MΩ water for 28 days at 90 °C..*

The gel layer formed on the CaZn sample irradiated to a dose of 5 MGy showed the expected slight increase in zinc enrichment and calcium content (shown in figure 56), when cross sectioned. This indicates the ion mobility within the glass had increased as indicated by the increase in alkali ion exhange observed by Ojovan and Lee, but otherwise did not greatly differ in appearance from the gel layer formed on unirradiated glass (116). This is in contrast to the gel layer formed on a sample of MW irradiated to a dose of ~5 MGy which became noticeably thicker and seemed shown an increase in the number of multiple layers and voids present compared to the unirradiated glass (as shown in figure 58 and 59) . As

the gel layer was dried prior to being encased in resin and cross sectioned it is not possible to comment whether these voids and layers were present in the hydrated gel layer or are a form of degradation caused by the drying process.

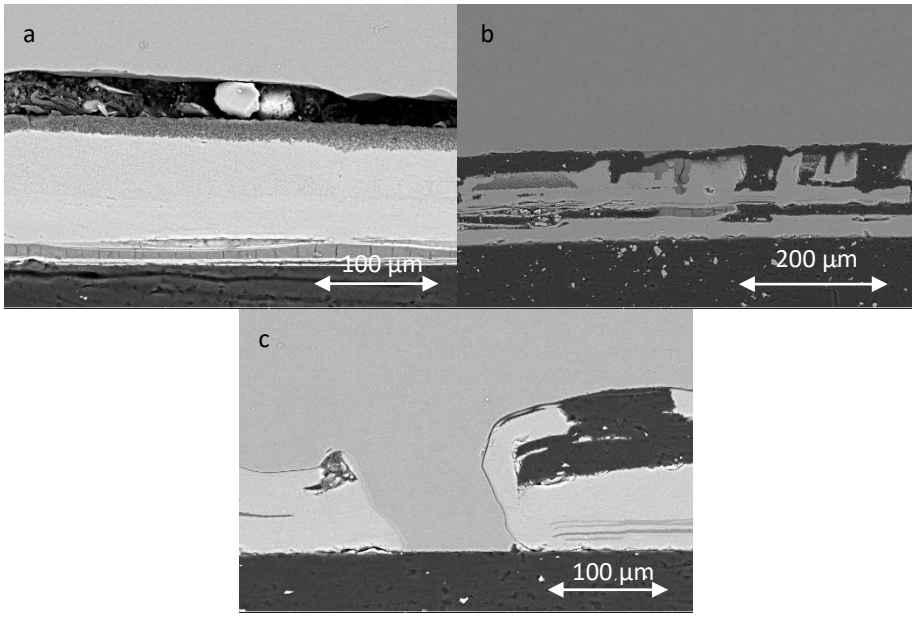


*Figure 59 MW gel layer cross section showing striations and delamination seen in standard leached a) unirradiated, b) 5 MGy, and c) 10 MGy samples. All samples leached in 18 MΩ water for 28 days at 90 °C.*

Cross sections of both the gel layers of samples of CaZn and MW irradiated to a total dose of ~10 MGy showed a large degree of variation in their thickness with the MW sample displaying a reduction in the layering seen compared to the unirradiated and ~5 MGy MW samples (as shown in figure 58 and 59).

These layers were observed in the ~10 MGy crevice contact sample where regions containing small unidentified grains were observed between the layers (as shown in figure 60). While no visible evidence of regions of increased aluminum content corresponding to the micro crystalline regions proposed by Brown were found during SEM imaging, of either the MW or CaZn ~10 MGy samples investigated, a great deal of variation in gel layer thickness was seen (136). This variation in gel layer thickness adds weight to the proposed

irradiation induced phase separation of glass, followed by reincorporation into gel layer mechansim discussed in Brown (136).

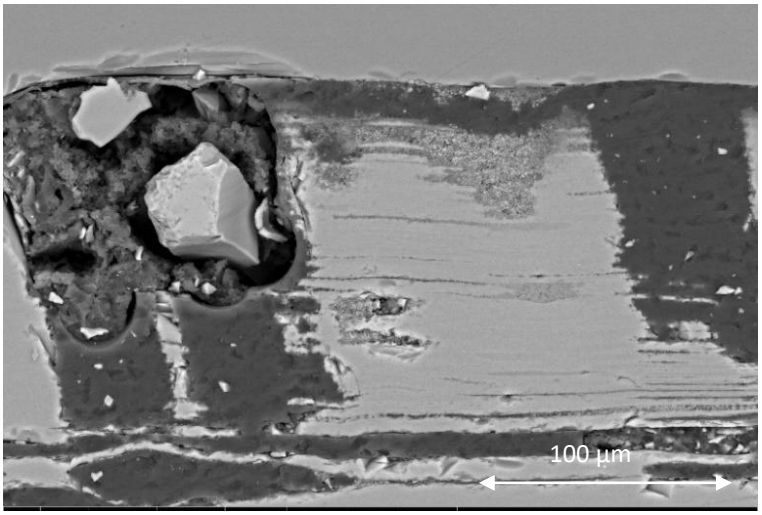


*Figure 60 Cross section of gel layer formed on MW 10 MGy flat steel crevice contact sample showing small grains*

The gel layer observed on the surface of both sides of all the crevice contact samples was typically thinner than the non crevice samples with the thinnest regions of gel layer formation seen on the glass covered by the steel on the crevice side of the holder. The glass gel layer formed adjacent to this region and on the flat side of the crevice holder showed marks corresponding to the tool marks present on the steel crevice holders suggesting a possible link between steel surface area and rate of glass gel layer formation (shown in figure 61).

When cross sectioned and EDS line scanned the gel layer observed in the crevice contact CaZn samples showed a slightly reduced quantity of calcium and zinc enrichment compared to the non crevice samples (as shown in figure 56). The lack of calcium and zinc gel layer enrichment may indicate that an improper gel layer has formed due to the differences in exposed glass surface area to solution volume ratio caused by the crevice holder. However when these compositional changes are combined with changes in leachate marker element concentration and pH discussed in later sections this indicates there is an interaction taking place between the zinc originating from the glass and stainless steel.

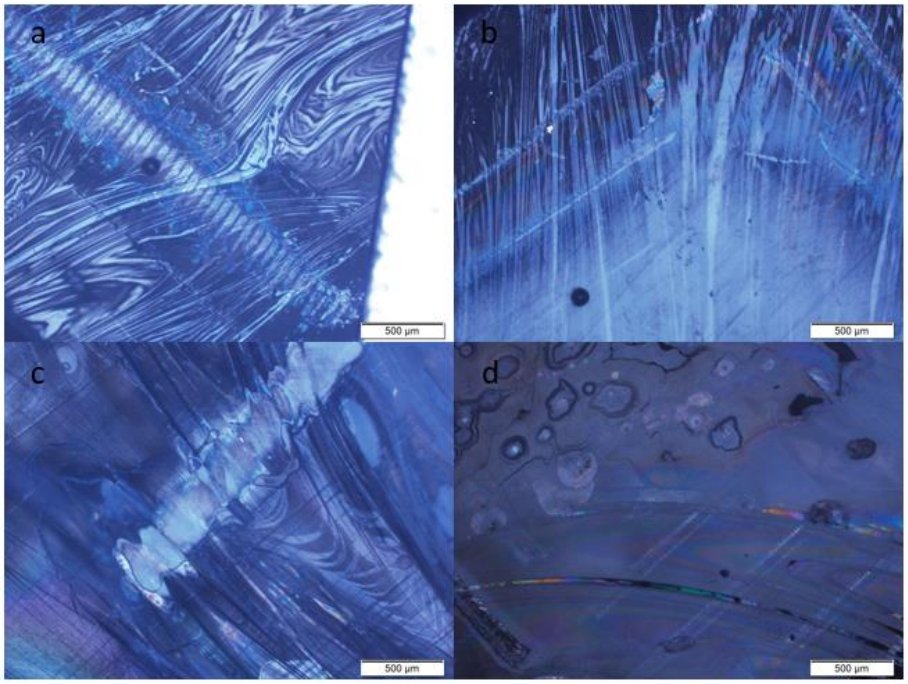


*Figure 61 Optical microscope images of gel layer formed on unirradiated CaZn crevice contact (a), CaZn flat steel contact (b), MW crevice contact (c), and CaZn crevice contact (d) samples.*

While no significant composition changes were observed during the EDS analysis of the MW crevice contact sample gel layer cross section, extensive surface microcracking was observed during optical microscope analysis (shown in figure 62). Cracking was not seen in any of the non crevice contact samples and the same drying method was used for all samples. If the cracking was present prior to drying then the observation of microcracking in the gel layer surface is significant. It has been previously proposed that the increased surface area associated with a cracked gel layer surface may lead to short periods of stage 3 like glass alteration behaviour (141). The combination of surface changes and changes in gel layer cross section appearance observed during SEM analysis suggests that, while the chemical composition of the MW gel layer does not undergo significant changes, the structure of the gel layer formed does change due to the environment formed in the steel crevices and these changes may lead to a less resistant gel layer.

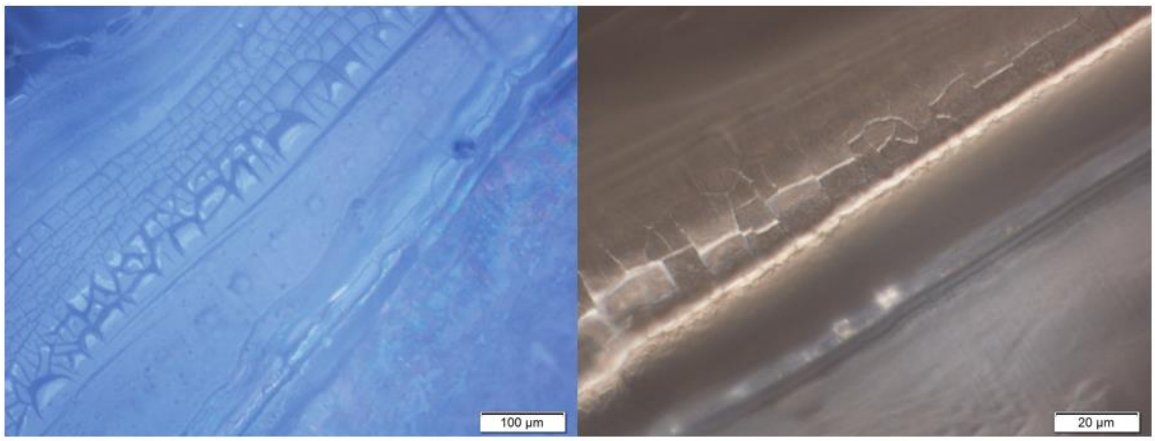


*Figure 62 Optical microscope images of unirradiated and 10 MGy MW gel layer within steel crevices showing cracking observed in crevice contact samples*

In all non-crevice contact glass leaching runs the leachate pH showed an overall increase with dose whereas the crevice contact glass samples showed a very slight decrease in leachate pH with dose as shown in figure 63. The MW leachate pH was typically higher than the CaZn leachate pH, creating an environment that encourages the overall more rapid leaching rate present in MW. When this change in leachate pH is combined with the normalised concentration of marker elements the impact of gamma radiation on individual glass stage 1 leaching behaviour supports the presence of structural changes within the glass.

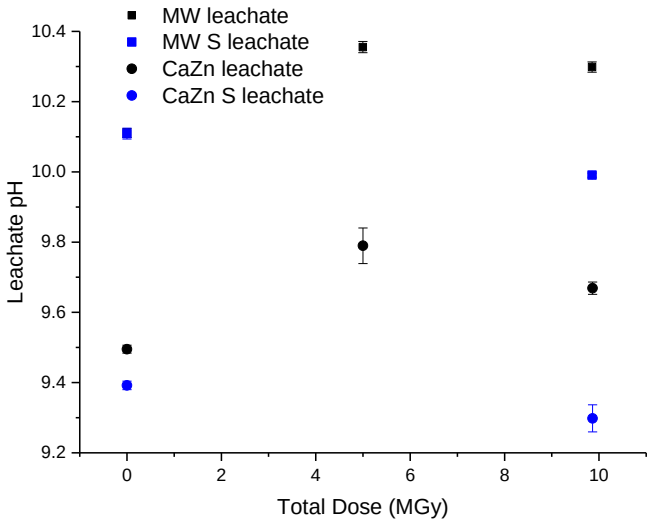


*Figure 63 MW and CaZn Leachate pH vs dose plots. S denotes crevice contact leaching runs. Error bars show standard deviation of measurement set.*

In MW the [Si] leachate concentration (shown in figure 64) near doubles at a dose of ~5 MGy then potentially decreases slightly at a dose of ~10 MGy. This pattern is not reflected in the [Na] and [B] loss (shown in figure 65) instead these undergo a possible drop at ~5 MGy followed by a slight increase at ~10 MGy resulting what are overall very slight changes that are not statistically significant. This behaviour further indicates specific changes in the glass structure leading to greatly increased silicon loss and the potential for a very slight reduction in boron loss, with the overall effect of these radiation induced changes resulting in a more reactive silicate glass network and thicker gel later formation.

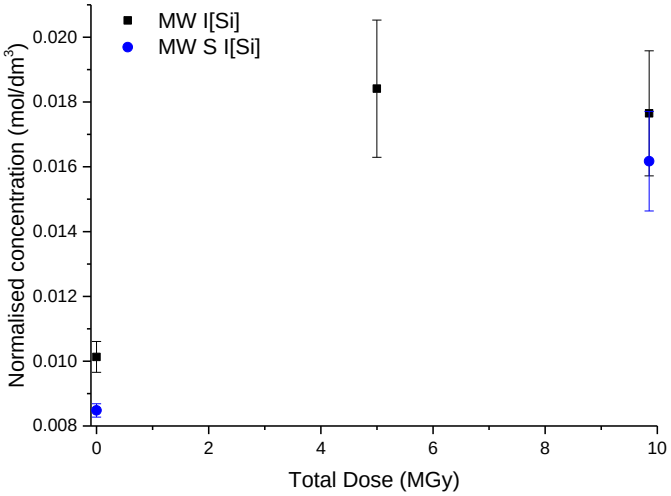


*Figure 65 Plot of MW [Si] leachate concentration vs dose. S denotes crevice contact leaching runs. Error bars show standard deviation of measurement set.*

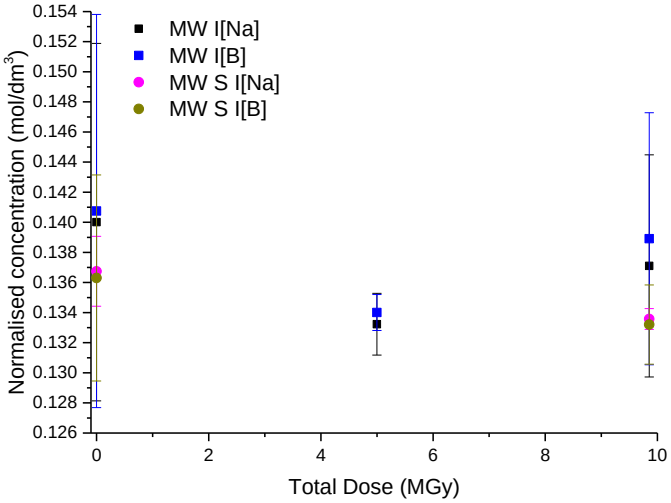


*Figure 64 Plot of MW [B] and [Na] leachate concentration. S denotes crevice contact leaching runs. Error bars show standard deviation of measurement set.*

The CaZn [Si] leachate concentration (shown in figure 66) does not follow the pattern seen in MW. In CaZn the [Si] concentration drops slightly at a dose of ~5 MGy then increases at a dose of ~10 MGy. The change in [Si] seen at a dose of ~10 MGy is the only statistically significant change in [Si] observed in CaZn. Given the potential phase separation observed by Brown in Pair Distribution Function Data the sudden increase in [Si] loss from CaZn at high doses is not unexpected, what is unexpected given the change in pH observed at a dose of ~5 MGy is the lack of statistically significant change in [Si] loss at ~5 MGy (136).

Given the changes in zinc gel layer content seen in the EDS analysis of the ~5 MGy CaZn gel layer cross section analysis the drop in [Si] leachate solution concentration (shown in figure 66) is potentially linked to a slight increase in glass reactivity leading to faster gel layer formation combined with increased ion mobility resulting in greater [Zn] enrichment within the gel layer with the overall effect of these leading to the rapid formation of a more resistant gel layer. The [Na] and [B] leachate concentration (shown in figure 67) also shows a drop followed by a slight increase similar to those seen in MW resulting in an overall drop in [B] concentration and a slight change in [Na] concentration.

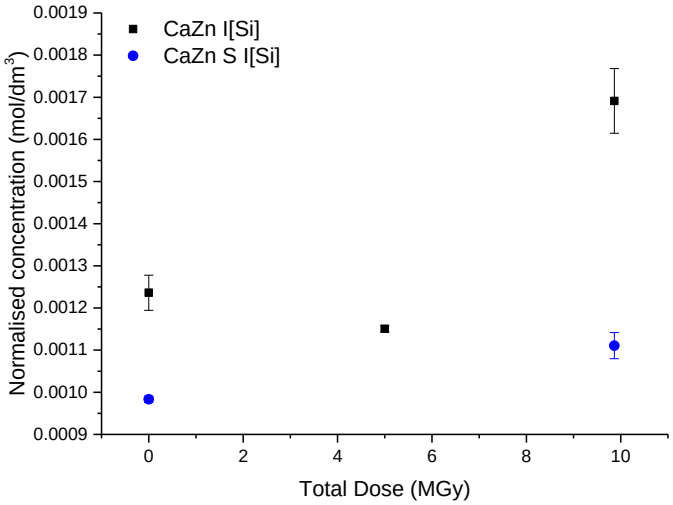


*Figure 66 Plot of CaZn [Si] leachate concentration vs dose. S denotes crevice contact leaching runs. Error bars show standard deviation of measurement set.*

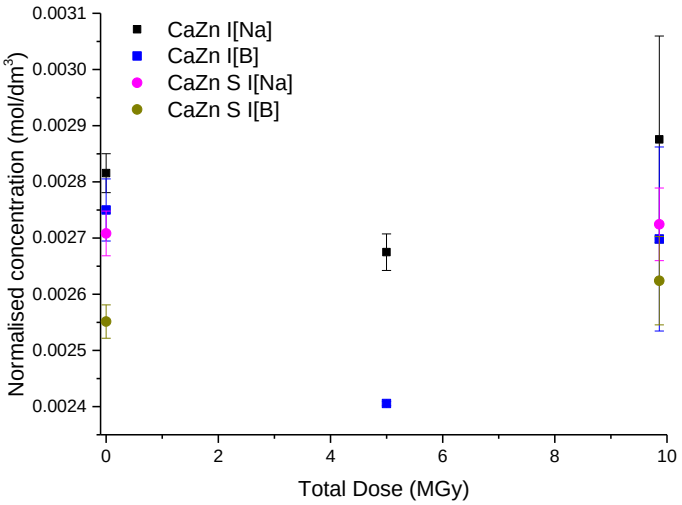


*Figure 67 Plot of CaZn [B] and [Na] leachate concentration. S denotes crevice contact leaching runs. Error bars show standard deviation of measurement set.*

The potential drop in [B] loss seen in MW, despite a large irradiation induced increase in [Si] loss and the potential drop in [B] loss compared to only very slight changes in [Na] seen in CaZn, indicates specific structural changes related to the $BO_3$:$BO_4$ ratio have taken place within the glass. Given that a higher $BO_4$ content is known to lead to a reduction in boron loss and a drop of $3.4x10^{-4}$ mol/dm$^3$ in the CaZn [B] leachate concentration occurs at ~5 MGy (shown in figure 67), combined with a slight ($6.7x10^{-3}$ mol/dm$^{-3}$) though not statistically significant drop in MW [B] leachate concentration at 5MGy (shown in figure 65) (23,142). The observed reduction in boron loss could suggest that more $BO_4$ is formed as a result of exposure to gamma radiation as indicated by an increased quantity of $Q_4$ units observed in Raman data collected by Brown from MW and CaZn glass samples irradiated to a total dose of ~10MGy (136,143). The increase in both [B] and [Na] loss seen between doses of ~5 and ~10 MGy is likely to be related to the phase separation observed in Browns previous PDF work (23,136,142). The proposal that a change in $BO_3$:$BO_4$ ratio is responsible for the drop in B loss is further supported by changes in Raman signal corresponding to an increase in four coordinate diborate and boroxol rings, previously documented for an MW like glass irradiated to a dose of ~5 MGy (36).

Three possible explanations are proposed for the variation in change in B loss seen between the two glasses. The first is that this is due to differences in the silicon/boron ratio in the glass network. This has been previously proposed in literature, where it was shown that a change in silicon/boron ratio will change the impact that $BO_3$:$BO_4$ ratio has on boron loss (23). However, given the difference in silicon/boron ratio is less than 1 and the increased aluminium content of CaZn is expected to reduce the impact of changes in $BO_4$ content, the difference in [B] loss at a dose ~5 MGy is highly unlikely to simply be due to differing Si/B ratio (23).

The second is that this difference is related to the boron anomaly, that typically results in a sudden change in glass properties seen at a $BO_3$:$BO_4$ ratio of approximately 50:50. After this point the effects of changes in $BO_3$:$BO_4$ ratio are reduced. This has been documented as potentially impacting the rate of boron loss in atomistic models of sodium borosilicate glass leaching but does not seem to have been well documented in experimental work (23). Based on the $BO_3$:$BO_4$ ratios, observed in unirradiated glass in the PDF work discussed in Brown *et.al*, the $BO_3$:$BO_4$ ratio of 59:41 observed in MW lies closer to a potential point where the impact of a changes in $BO_4$ will be reduced, compared to CaZn where the $BO_3$:$BO_4$ ratio of 67:32 sits at point where an increased $BO_4$ content will have a larger impact on boron loss (111). The presence of boron anomaly related effects is further supported by the minimal change in [B] loss observed at doses as high as of ~10 MGy in MW. This would be expected, if the relationship between boron loss and $BO_3$:$BO_4$ ratio followed the pattern shown in figure 68 (23).

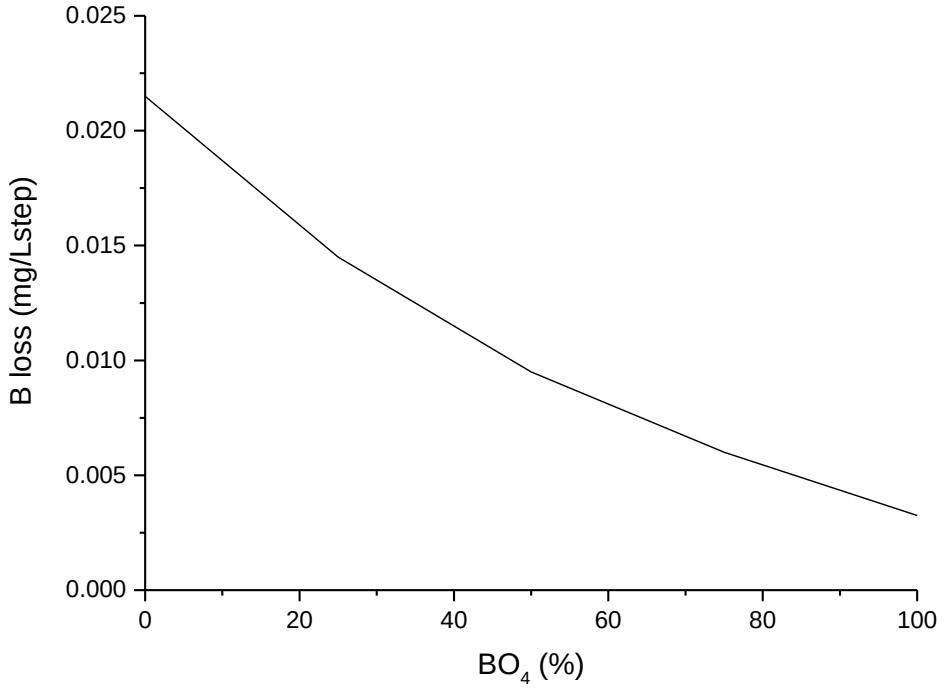


*Figure 68 $BO_4$ % Vs B loss plot adapted from (23)*

The previous two explanations make the assumption that the increase in $BO_4^-$ does not greatly vary between the two glasses, the third explanation is that amount of $BO_4^-$ in CaZn undergoes a large increase at a dose of ~5 MGy, compared to MW, resulting in the observed drop in [B] leachate concentration and that this is associated with the early stages of proposed aluminium-related phase separation discussed in Browns previous work, occurring at a dose of ~5 MGy in CaZn (136). This proposal is made on the basis that, within the glass network the negatively charged $[AlO_4]^-$ will be preferentially charge compensated first by $Ca^{2+}$ then by $Na^+$ reducing the amount of $BO_4^-$ formed within the glass melt. Then, when redistribution of aluminium occurs, as a result of phase separation, the irradiation-induced conversion of $BO_3$ to $BO_4^-$ becomes more favourable as the $BO_4^-$ is able to be better charge balanced by the network modifiers distributed throughout the glass network (13). However this explanation does not properly account for the very slight changes in [Na] leachate concentration seen in CaZn with increased dose and this does not seem to be

reflected in the Raman data discussed in Brown, though some caution must be taken in this interpretation, due to Raman baseline issues encountered in this study (136). In the absence of conclusive data regarding the irradiation induced changes in $BO_3$:$BO_4$ ratio and irradiation induced changes in leachate marker element the boron anomaly proposal combined with a slightly greater increase in $BO_4$ concentration in CaZn is presented as the most likely justification for the difference in changes in both [B] and [Na] leachate concentration with increased dose seen in MW and CaZn.

The differences between [Si] loss behaviour in unirradiated MW and CaZn are due to the presence of aluminium, calcium and zinc in CaZn. The intermediates aluminium and zinc have been demonstrated to be part of the glassy network, with the NMR data discussed in Brown *et.al* showing that in unirradiated glass the aluminium is all four coordinate and is primarily present as a $[Al(OSi)_4]^-$ structural unit (111). Based on the PDF data discussed in later work and previous EXAFS and XANES work on CaZn, the assumption is made that zinc will form similar structural units within the glass (99,136). Both these intermediates will improve glass durability in the early stages of alteration though through reducing the amount of NBO thereby increasing the $Q_n$ number. Despite this, both these intermediates will display slightly different behaviour within the gel layer. Zinc is largely insoluble and its impact on glass durability in the early stages of glass leaching is mainly due to it leaching from the glass slowly and accumulating as an insoluble band within the gel layer (140). In the later stages of glass alteration precipitation of insoluble zinc silicates may induce stage 3 glass alteration (56,132). By contrast, aluminium is more readily soluble compared to zinc with the impact of aluminium on glass durability being the combination of aluminium slowing the kinetics of glass alteration, hardening the glass network by forming small clusters of network modifiers resulting in shallower water penetration, and aluminium becoming reincorporated into the gel layer once dissolved (144). The overall impact of aluminium and its ability to become reincorporated into the glass gel layer is somewhat

debated with it being proposed that overall aluminium may lead to an increased rate of glass alteration, due to formation of both insoluble phases in solution and secondary phases within the gel layer (138,144,145). This may have occurred to some extent here where the sudden increase in silicon leach rate was observed in CaZn at a dose of ~10 MGy. The impact of the network modifier calcium on glass alteration is less direct and somewhat dependant on the charge competition present within the structure, with it being proposed that the lower hydration free energy of calcium silicate compared to other alkali silicates may be responsible for stabilising the glass structure during alteration (130).

The differing changes in [Si] loss from glass with dose demonstrates the stabilising influence of zinc and aluminium in the CaZn glass network, reducing the impact of silicon NBO formation, and potentially the quantity of NBO formed. The MW and CaZn Raman data discussed in previous work and the changes in [Si] loss seen here demonstrates the differences in structural reorganisation taking place involving silicon NBO and bridging oxygen formation that occur at different radiation doses (136). Within this data set, the changes in CaZn $Q_n$ environment at a dose of ~5 MGy were more subtle than those seen in MW and this is reflected in the leaching data, where a slight change in [Si] leachate concentration occurs in CaZn as a result of structural changes in glass network being able to compensate for the negative effects of changes in NBO. The same compensation does not take place within MW and this is reflected in the increased [Si] loss at ~5 MGy. The MW Raman data, discussed in the third chapter, shows the corresponding increase in $Q_1$ and $Q_2$ within the silicate network responsible for the increased [Si] loss seen at a dose of ~5 MGy. Whilst, the MW ~10 MGy Raman data shows evidence of structural reorganisation leading to a drop in $Q_1$ and increase in $Q_3$, that is reflected in the slight change in [Si] loss seen at ~10 MGy.

The lack of large changes in the ~10 MGy CaZn Raman data, discussed in chapter three, and the sudden increase in CaZn [Si] leachate concentration at a dose of ~10 MGy, also supports the previous proposal that phase separation involving aluminium takes place. The loss of the stabilising influence of aluminium associated small network modifier clusters distributed throughout the glass structure, potentially being partially responsible for the sudden drastic increase in [Si] loss seen (144). As the proposed calcium associated defect, discussed in more detail in the third chapter, has only previously been observed within a certain silicon/aluminium range, the change in [Si] leachate concentration also introduces the potential that this defect and its formation maybe related to the redistribution and clustering of aluminium and its associated network modifiers (47).

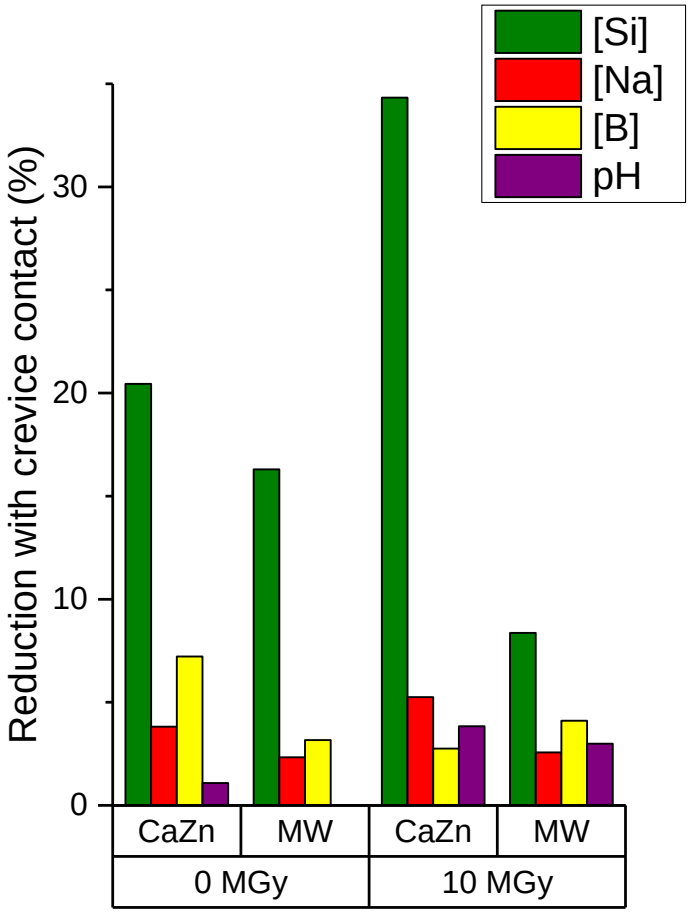


*Figure 69 Plot showing % reduction in leachate marker element concentration and pH in the crevice contact leaching runs compared to non crevice experiments.*

The previous section was primarily focused on glass leaching done in close contact with stainless steel, with the glass resting on the base of the stainless steel Parr vessels. The influence of true steel crevice contact adds to the complex and varied glass alteration mechanism. In the absence of any chemical or electrochemical interactions with the steel crevice environment a, near equal, overall slight reduction in all leachate marker element concentrations is expected due to the effective reduction in glass surface area exposed to the water (Sa:V ratio was calculated using the assumption the entire glass surface is exposed to water) combined with slower diffusion of alteration controlling elements in solution. While this has been observed to a certain extent, it does not occur in equal quantities across all elements in both glasses (as shown in figure 69). This suggests that a specific interaction between the glass and steel occurs within the crevice holder. Further evidence of this interaction with the holder is provided by SEM-EDS analysis of the glass gel layer, and the changes seen on the surface of the steel holder when the holder was removed from the leachate solution. In all leaching runs a coating was clearly present on the crevice holder and while this coating was not analysed due to time constraints, given the changes proposed in Guo *et al.* and the drop in [Si] leachate content seen in all crevice contact investigations, it is likely to be silicate based (60). This is significant as, if silicon is removed from the leaching environment in the early stages of glass alteration by processes, such as the sorption of silicates onto the surface of stainless steel, then the duration of stage one glass alteration will be extended (65). As this is the stage where the negative impact of radiation damage on glass is at its most significant, the loss of silicon from solution has the potential to lead to greatly accelerated glass alteration in the early stages of container breach, through inhibiting gel layer formation and maturation leading to hydrolysis being the dominant glass alteration process.

Of note is the overall reduced impact of gamma irradiation on [Si] leachate concentration in the crevice contact MW compared to CaZn. Given the higher [Si] leachate concentration

seen in MW with increased dose this suggests that the silicon uptake of stainless steel is partially dependent on silicon solution concentration to steel surface area ratio with the high [Si] content in the irradiated MW leachate able to form a complete coating on the steel, resulting in an overall smaller % drop in leachate marker element concentration. This is not entirely unexpected considering sorption of silicates onto the surface of metallic iron, and stainless steel, has been well documented (64,65,133).

The large change in [Si] leachate concentration observed with increased dose in CaZn (shown in figure 69) and the changes in reduction in zinc gel layer content between the crevice and non crevice CaZn leaching runs suggests that the interaction between CaZn and steel in the crevice environment is chemically distinct from the interactions occurring during all other leaching runs.

The lack of zinc enrichment observed in the CaZn crevice contact gel layer combined with the greater zinc accumulation with increased dose observed in the CaZn gel layer in the non-crevice leaching runs, and the reduction in [Si] leachate concentration seen in the both the CaZn unirradiated and irradiated crevice leaching runs, may indicate there is a potential galvanic reaction, occurring between steel and the zinc originating from the zinc enriched gel layer, that encourages crevice corrosion characteristics. In Guo *et al*. the presence of acidic attack was used as an indication of crevice corrosion, and no evidence of crevice corrosion was seen in the leaching run carried out in deionised water (65). However, in Guo *et al,* a flat steel coupon was pressed against the flat glass surface creating a very narrow poorly formed crevice (65). This is in contrast to the results observed here where a crevice holder based on ASTM G48 – 11 procedure for investigating crevice corrosion in stainless steels was used. In these experiments a lower pH was observed in all CaZn leaching runs, and the ~10 MGy dose MW leaching run where the crevice sample holder was used. This suggests that in leaching runs carried out in ultra-pure water it is only possible for crevice

corrosion to occur in the presence of a true crevice environment, where ions from the glass leaching process have accumulated in sufficient quantities due to the reduced diffusion rate in the crevice, to cause a sufficient change in water conductivity. This may be further enhanced in the presence of a saline environment though further investigations should be carried out to confirm this.

This potential galvanic reaction is proposed based on the previously documented cathodic deposition of orthosilicate onto steel, combined with the use of zinc as a sacrificial anode with steel, and the presence of a crevice environment which further increases the likelihood that a suitable environment for an electrochemical reaction to take place will occur in the space between the steel crevice and glass surface (146). While the electropotential of aluminum indicates an electrochemical reaction between aluminum and steel is possible. This reaction is likely to have minimal impact, as aluminum from glass is soluble, and in CaZn does not accumulate in the gel layer in the same quantities as zinc. The impact of aluminum accumulation in the gel layer expected during the early stages of leaching, is likely to be limited to slightly increased silicate uptake of steel, as demonstrated by the work involving ISG carried out by Guo *et al.* and the changes in MW [Si] leachate concentration and pH seen here (65).

Based on the changes seen in the CaZn glass gel layer and leachate marker element concentration it is proposed that in this electrochemical reaction the zinc in the glass will act as an anode encouraging its dissolution from the glass gel layer and the stainless steel will act as a cathode with silicate being deposited from solution onto the surface of the steel through cathodic deposition. This process is indicated by the loss of zinc from irradiated glass in the crevice environment combined with the large drop in [Si] leachate concentration seen in both CaZn crevice runs.

Considering the proposal that zinc primarily bonds to the silicate portion of the network, which will be degraded by radiation leading to increased silicon loss from glass, this loss of protective zinc accumulation in the gel layer will further weaken the already radiation damaged glass network. At the same time the removal of silicon from solution by interactions occurring in the crevice environment that may include cathodic deposition onto the steel surface will significantly delay the formation and maturation of the gel layer, extending the more rapid stage 1 glass alteration and amplifying the negative effects of radiation. Indication that the protective effects of zinc are lost and the negative effects of irradiation are enhanced is seen in the unexpected increase in [B] leachate concentration in the ~10 MGy CaZn crevice assembly run compared to both the unirradiated CaZn crevice assembly and MW crevice assembly runs. Furthermore, given that the $Zn^{2+}$ produced by this reaction is amphoteric, additional evidence of zinc loss from glass is potentially seen in the smaller increase in pH observed in CaZn compared to MW although, further work is needed to confirm that changes in zinc leachate concentration occur.

The eventual complete covering of steel due to cathodic deposition of silicon on to the steel surface would be sufficient to ultimately stop the proposed galvanic reaction and may slow the long term corrosion rate of the container within the crevice environment. At the same time this reaction and associated reactions with the steel would be consuming silicon, from solution extending stage 1 glass alteration while the loss of zinc from the glass surface would temporarily increase the rate of stage 2 glass alteration both of which will delay glass gel layer maturation amplifying the negative effects on radiation on glass alteration. Additionally, if the formation of extensive microcracking in the gel layer, as seen in the MW gel layer, was present prior to the gel layer being dried this would lead to repeated periods of rapid glass alteration as the gel layer surface volume changes. This increased glass alteration rate within the crevice also has the potential to lead to the slow expansion of the crevice between the glass and steel.

## 4.5. Conclusion

The impact of both gamma radiation and steel contact changes the alteration behaviour of MW and CaZn base glass. The gamma radiation induced changes in glass structure can have either a positive or a negative impact on glass alteration behaviour, depending on the glass formulation and total dose used. Given the strong dependence on glass formulation demonstrated here the impact of steel contact and gamma radiation should be further explored using a range of simulant glasses.

The impact of a steel crevice environment on glass alteration has been shown to be distinctive from steel simply being near the glass and a potential reaction involving intermediates and modifiers removed from the glass during alteration and the steel surface has been proposed to justify the changes in leaching behaviour observed between MW and CaZn. This mechanism requires further investigation, involving non-metallic crevice holders, to conclusively prove steel crevices are responsible for the unexpected drop in [Si] leachate concentration and increase in [B] and [Na] leachate concentration and to model the long term consequences of this proposed interaction. There are strong indications, both in this work and in literature, that some form of reaction takes place between selected glasses when placed directly against typically unreactive metals that undergo crevice corrosion (65). If a localised aggressive environment that encourages crevice corrosion of stainless steel were to formed by the actual UK HLW glass, this may be further accelerated by the high levels of magnesium present in HLW glass containing Magnox waste and the known impact of radiation on metal corrosion, which is also potentially accelerated by the radiation produced from the elements contained within the glass (81,147). Due to this, further work with simulant glasses under radiation conditions is needed to fully investigate the impact this interaction will have on the degradation of HLW glass in a GDF environment. Due to the nature of the system used here, minimal modification would be required in order to run these experiments.

# 5. Summary

The hypothesis “In GDF conditions contact with steel, and radiation-induced changes in glass structure, will increase glass leaching rate in the early stages of container breach” has been partially proven for UK base glass, but, further work is needed to fully explore the implications of this on actual HLW glass alteration in a GDF environment. Strong evidence of phase separation resulting in the formation of microcrystalline regions following exposure to high dose (>8 MGy) gamma radiation has been found, in both the high energy X-ray scattering data and in sudden changes in leaching behaviour. These changes were not observed where a lower dose was used, despite the extensive electronic defect formation seen, suggesting that the formation of electronic defects and the formation of structural changes in a glass will have vastly different dose thresholds. The focus on electronic defect formation occurring at low doses combined with the crystalline phase separation becoming lost against the strong amorphous glass background at the wavelength range used by standard laboratory XRD instruments has resulted in the impact of gamma radiation on glass structure being under-emphasised in current research.

A mechanism involving the structural rearrangement and clustering of aluminum and its associated charge balancing network modifiers, has been proposed to explain the formation of the crystalline regions of phase separation, and the strong UV unstable potential calcium colloid associated electronic defects observed in CaZn and other calcium containing aluminosilicate glasses. This proposal is made based on the increase in Bragg peak intensity seen as the quantity of aluminum in the glasses increases, and the drastic change in CaZn leaching behaviour observed at a ~10 MGy dose. It has not been possible to characterise the crystalline regions using the currently available data, leading to uncertainly as to the potential impact of these regions on glass leaching rate is due to the effective loss of the stabilising influence of aluminum distributed throughout the glass network, or the

crystallites themselves being partially soluble. The increased solubility of the small crystals would better fit the general observation, that the impact of gamma radiation damage on glass leaching is reduced once a stable gel layer is formed. However, the impact of aluminium in solution on mature gel layer formation is highly debated, and because of this the observed change in leaching behaviour could equally be due to dissolution of aluminium from aluminum-rich regions of the glass followed by reuptake and distribution of aluminum throughout the gel layer stabilising the mature gel layer, through the same mechanism that would occur during gel layer maturation in unirradiated glass.

The initial results of the steel crevice leaching runs show strong evidence that glass in contact with steel in a crevice environment will display a slight increase in the leaching rate during the early stages of container breach, due to the reaction of soluble silica in solution with the steel. This rate will be further influenced by radiation damage to the glass and crevice corrosion of steel that may be encouraged by elements released in to the crevice environment following accumulation in the gel layer. Due to the differing effects of multicomponent irradiation on glass structure, in particular, the different changes in $BO_3$:$BO_4$ ratio seen as result of ion beam irradiation compared to changes seen with gamma radiation, further work is needed to understand the overall impact of multicomponent radiation on glass structure and steel interactions. The need for further work has been proposed based on the strong evidence of gamma irradiation induced structural rearrangement, seen here in both the analysis, and leaching experiments caried out using high dose gamma irradiated glass.

Conclusive evidence of structural changes has been partially obscured by electronic defect associated florescence observed in the Raman analysis of irradiated glass, and a method of removing these electronic defects with minimal changes to the glass structure in future work has been demonstrated. This method has not been explored in detail due to lack of

sample availability. In order to conclusively identify which of the mechanisms proposed in the fourth chapter are responsible for the observed variations in [B] leachate concentration and provide a better insight into the structural changes occurring the exact changes in $BO_3$:$BO_4$ ratio occurring in high dose gamma irradiated glass should be probed using $^{11}$B-MAS-NMR prior to repeating the leaching experiments.

In addition to irradiation induced structural rearrangement, the changes seen in the glass gel layer composition of the crevice leached CaZn samples, indicate a possible reaction that may influence both the uptake of silicate by steel and the solubility of certain glass components is occurring. This reaction could greatly delay the maturation of the gel layer and this delayed gel layer maturation would further emphasise the negative effects of radiation on glass alteration, while the loss of typically insoluble glass components from the gel layer through the environment formed in the crevice would further impact the long term gel layer properties. The possibility of reactions occurring between steel and elements in solution originating from the glass, becomes all the more important, when the high magnesium levels present in the Magnox waste stream are considered. When galvanic potentials are considered magnesium is more reactive towards steel than zinc and therefore more likely to act as an anode, further increasing the rate of this reaction. Due to the high magnesium levels in HLW waste glass containing Magnox waste a detailed understanding of the electrochemistry that may lead to enhanced crevice corrosion of steel in this environment is needed, in order to fully model the impact of this on both the glass and steel. In the MW crevice leaching runs the gel layer formed differs in appearance from the gel layer formed during the non crevice leaching runs suggesting that the chemistry within the crevice environment will change leading to variations in the leaching mechanism. The exact chemistry of the crevice environment is beyond the scope of the glass focused study here and has not been explored.

The PDF work carried out here has the potential to provide a foundation for atomistic modeling of UK base glass, and has demonstrated proof of concept for the combined use of NMR and simultaneous fitting of neutron and X-ray PDFs in the derivation of multi component glass PDFs. This proof of concept can be applied to other multicomponent glass formulations, as demonstrated by the ISG analysis carried out. The analysis of ISG was also used to provide method validation as, while there are no known full atomistic models of UK base glass, there are a small number of published full atomistic models of ISG. As demonstrated by the atomistic modeling of ISG, a full atomistic model of UK base glass can be used to better understand the properties and degradation of UK base glass and the impact of high dose radiation on this glass.

A full atomistic model of UK base glass would also aid in further analysis of experimental data collected here and would help to provide a more conclusive link between the irradiation induced changes seen in analytical data and the associated structural changes that have been proposed based on changes in leaching behaviour of the glass with increasing dose. There is strong evidence seen in both literature and the work carried out here that high dose gamma radiation causes structural changes to take place that will result in phase separation taking place. This may impact the alteration behaviour of the glass, but information on the exact mechanism responsible for this behaviour is lacking. Without this information it is not possible to predict the exact effects that gamma irradiation induced structural changes and contact with a steel crevice environment will have on actual HLW glass. Given that, in addition to the gamma radiation studded here, the complex multi component HLW glass will also be exposed to alpha and beta radiation through self-irradiation, the overall impact of radiation damage and steel crevice contact will be determined by the balance of several factors discussed here, which does not currently include the ground water chemistry within the GDF. The overall ground water chemistry will have a significant impact on the proposed electrochemical reaction within the steel

crevice. Further research is required to determine which will be the dominant factor in determining the glass alteration rate, and these factors cannot be fully modelled until a site is chosen for the UK GDF.

# 6. Analytical Theory and Method Development

## 6.1. Analytical Theory

Many of the analytical methods detailed in this thesis are modified when analysing disordered materials such as glass. This section details the theory surrounding their use.

### 6.1.1. Raman Spectroscopy

Glass is a typically a relatively weak Raman scatterer with silicate glasses commonly used as sample containers due to their transparency to visible and near IR lasers (89). To allow for this, a Raman spectroscopy technique known as Raman microscopy is commonly used in the analysis of glass. A typical Raman microscope consists of a monochromatic laser that is focused down an optical microscope, a sample compartment enabling the microscope to be safely focused, and the spectrometer to detect and filter the scattered photons (shown in figure 70) (89). Focusing the laser on a small area enables the use of a high powered laser, while minimising the potential for bulk sample heating and damage, and has the additional benefit of enabling the analysis of very small sample areas and volumes. This is vital when analysing samples that contain very small crystals or display variations in surface chemistry as the laser can be focused to allow the collection of data from these areas. The analysis of a small sample volume does, however, introduce a dependence on surface finish and laser focus, which can result in poor quality Raman spectra if the sample is not properly polished. When analysing glass it has been found that the best signal is obtained on samples with a highly polished surface and the laser focused slightly below the sample surface; this is not unexpected considering both collection volume and the transparent glass studied here.

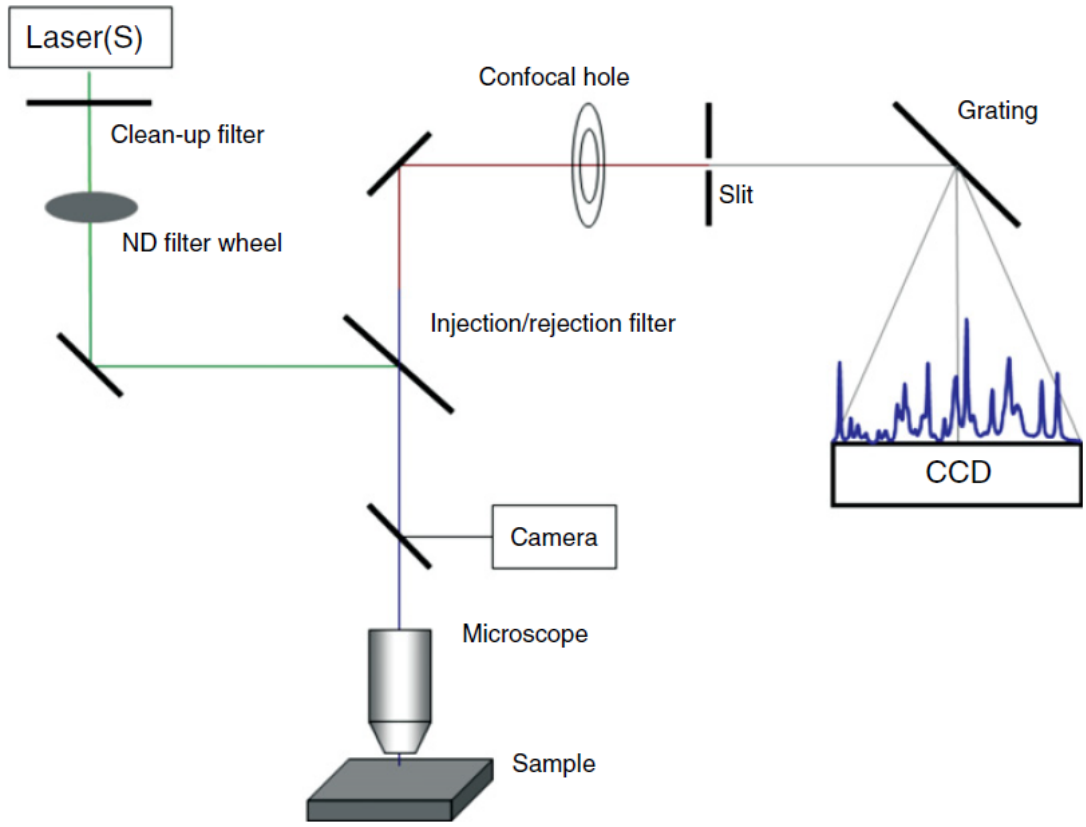


*Figure 70 Simplified diagram showing key parts of the Raman Microscope (taken from (89))*

Raman does not provide direct structural information on amorphous materials; instead information is provided on the vibrational energy transitions of specific polarisable molecular groupings. In Raman active molecular groupings these energy transitions are caused by photons of laser light with a frequency of $v_0$ hitting the group of molecules and exciting these molecules to a virtual state. In molecular groupings excited from a ground state, energy with a frequency of $v_f$ is transferred to the grouping such that the frequency of the scattered light is described by $v_0$-$v_f$, this is known as Stokes shift (as show in figure 71) (89). . In molecular groupings excited to the virtual state from an excited vibrational energy level energy is lost from the grouping as it returns to the ground state where the frequency of the scattered light is described by $v_0$+$v_f$, this is known as Anti Stokes shift (as show in figure 71) (89).

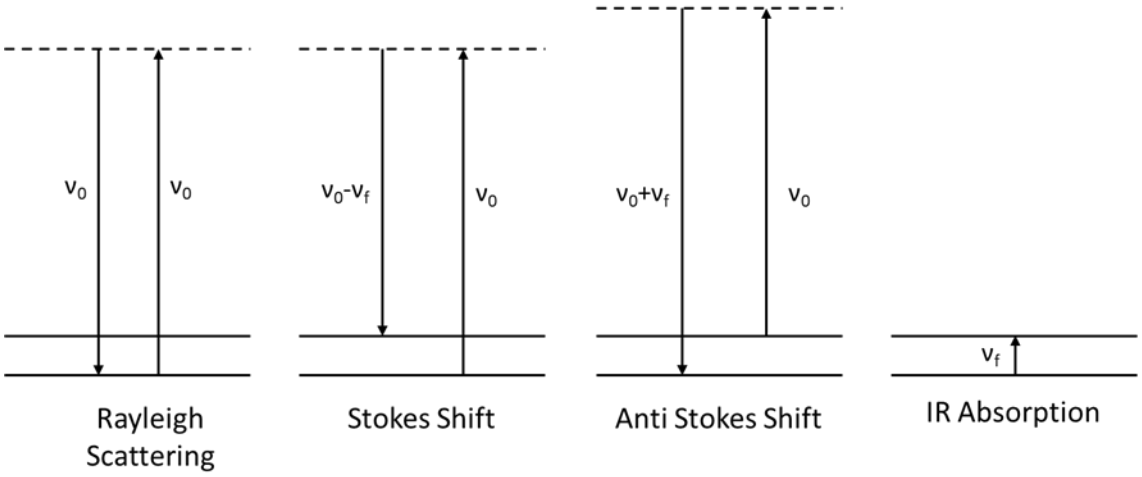


*Figure 71 Simplified diagram of Raman scattering modes. Also shown is Rayleigh scattering which produces a strong peak at 0 Raman shift. Dashed line represents virtual state.*

In borosilicate glass studied using a 532 nm laser these groupings are observed through peaks or bands that are typically observed in the following regions 300–500 $cm^{-1}$ (stretching and bending of Si-O-Si) , 550-850 $cm^{-1}$ (borosilicate and boron ring breathing modes), 800-1200 $cm^{-1}$ (overlapping $Q_n$ groups), and 1200-1700 $cm^{-1}$ (three coordinate boron) as shown in figure 72 (148,149). In glasses with a lower $BO_3$:$BO_4$ ratio the final band is often obscured or distorted by background fluorescence or noise.

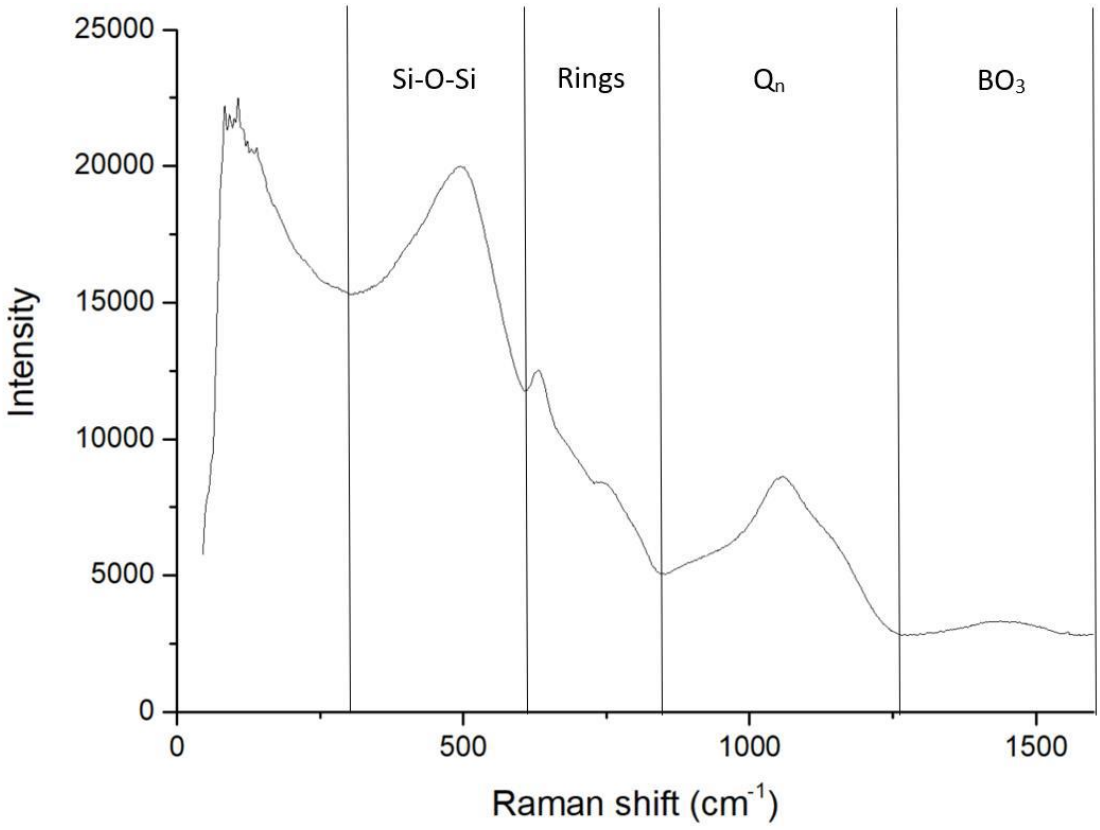


*Figure 72 Example Raman spectrum from this work. Shown pre background correction to demonstrate typical regions observed in borosilicate glass.*

The $Q_n$ region is composed of a series of bands corresponding to the stretching of the Si-O bond, where this bond is strongly influenced by the surrounding $SiO_4$ tetrahedra (79). Within this region, the following five bands can be observed at approximately 850, 900 - 930, 950-1000, 1050-1100, and 1200 $cm^{-1}$, corresponding to tetrahedra containing 4, 3, 2, 1, and 0 NBO respectively (79,94,107). Deconvolution of overlapping bands in the $Q_n$ region is a technique of interest, as this would enable radiation induced structural changes to be easily identified. The convention in current literature is to fit the peaks in this region with Gaussian line shapes, instead of the typical Lorentzian line shapes used in conventional Raman. However, there is a body of literature that suggests the peaks in this region have a mixed Lorentzian-Gaussian line shape (107). This provides an explanation for both the poor fits and the variations in line width and wavenumber seen in initial fittings discussed later in this work. Theoretically, in a homogeneous glass, there should be little variation in line

widths within the $Q_n$ region and the wavenumbers should not greatly deviate from the expected range (107). Due to this and potential interference from varying fluorescent backgrounds it has only been possible to estimate the $Q_n$ ratios using Raman.

There is some debate as to how a baseline and background subtraction should be applied to Raman spectra of glass with two main opinions seen. Either the background is noise and fluorescence, and should be removed for the sake of clarity. Or the technique and data processing require further development in order to extract data from the background fluorescence, and that by applying a baseline to the Raman spectrum useful data is being removed and the spectra are needlessly distorted. Additionally the many broad and overlapping bands seen in Raman spectra of amorphous material may introduce further uncertainty in applying a background.

The fluorescent background is typically most strongly observed in gamma-irradiated glass and it is proposed that this likely to be related to radiation-induced electronic defects. This is not entirely unexpected when the typical Raman laser wavelength of 532 nm and the deconvoluted UV-Vis-NIR spectrum of gamma irradiation induced defects in borosilicate glass (discussed in section 3.3.4) and EPR spectra of irradiated glass are considered, in combination with a model proposed by Williams and Eyring (150). In this model, designed to explain temperature dependence of fluorescence, three energy levels with differing Stokes shifts are proposed: a normal level, a metastable level consisting of trapped electrons, and an excited level that can participate in fluorescence (150). Some electrons are trapped in the metastable level, from which they can be easily promoted to the excited level, where the emissive transition to the normal level then occurs resulting in the observed fluorescence (150). The UV-Vis-NIR spectra of electronic defects typically show absorbance in the 1000 to 250 nm range with bands corresponding to trapped electrons present. The EPR shows further evidence of trapped electrons, with CaZn potentially having

a greater quantity of unstabilised trapped electrons, resulting in smaller energy level transitions, creating the ideal conditions for fluorescence to take place. A comparable effect has been used to explain the fluorescence observed in strongly luminescent Roman silicate glass when compared to a modern glass analogue (151). What is both unexpected and currently not fully understood is the reduction of fluorescence seen in a poorly annealed ISG glass, that was later gamma irradiated (discussed in detail section 3.4). These observations suggest there are potentially multiple origins for the observed background.

### 6.1.2. UV-Vis-NIR Spectroscopy

UV-Vis-NIR is more commonly used on strongly coloured solutions that can be poured into a standard cuvette, such as in the colourimetric molybdenum blue method, used here for silica content determination. However, transparent solid samples, such as glass, can be analysed in a similar way by using a solid sample holder. These samples must be polished to a reasonable surface finish and have a flat parallel surface on both sides. In addition to this, when carrying out UV-Vis-NIR of glass, care must be taken to ensure that the sample is centred and well aligned with the beam or a large and distinctive detector or grating changeover notch will be observed in the collected spectrum due to distortion of the measured absorbance (an example of this is shown in figure 73). While this issue can be encountered to a lesser degree in liquid UV-Vis-NIR, in solid state UV-Vis-NIR the presence of the changeover notch is typically far more pronounced. Where the notch occurs in a region of interest this can be partially overcome by altering the changeover point.

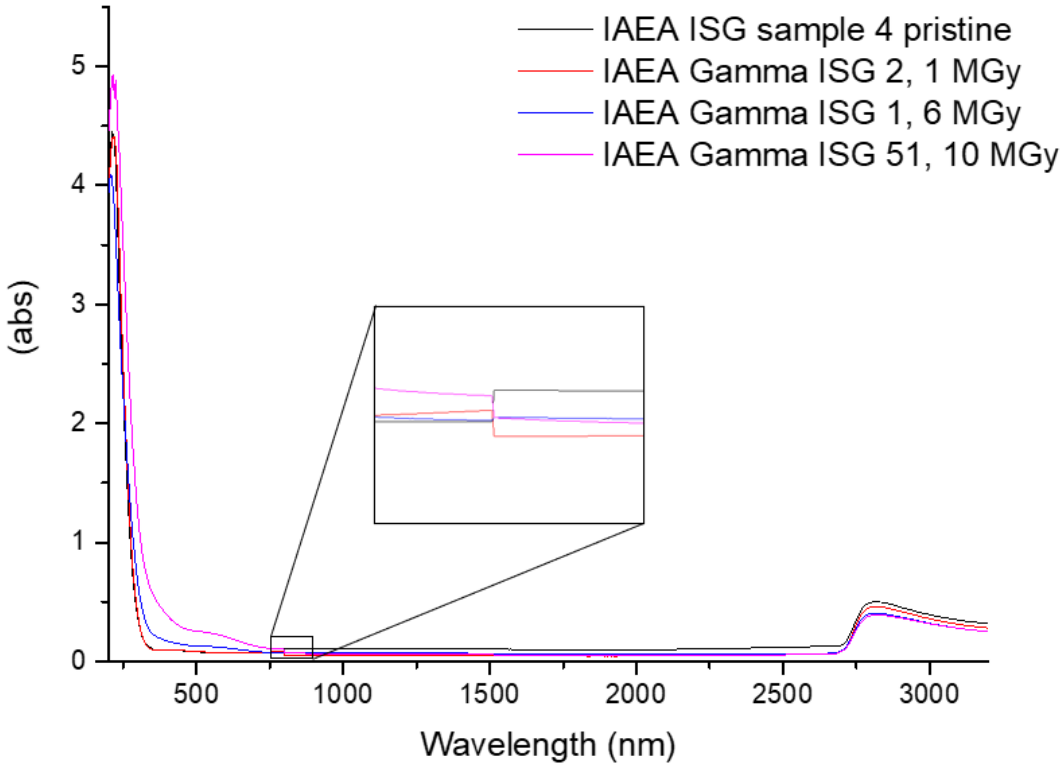


*Figure 73 Change over notch observed in data due to poor sample alignment. Data collected as part of collaborative work later abandoned due to change of supervisor.*

Many elements can cause colour in silicate glass, and some elements need only to be present at ppm level to cause a strong colouration. The colour and its intensity also depends on element quantity, melt temperature and oxidation state. UV-Vis-NIR can be used to characterise these colour centres through the distinct absorption bands present. The amount of water present can also be estimated using a distinct band located in the near IR region.

High dose gamma radiation will induce a strong colour change in previously colourless glass. This colour can vary from dark blue to brown, almost black with absorbance typically observed between 200 nm to 1000 nm. This colouration shows a distinct dose dependence, with previous studies having explored its potential use for emergency dosimetry, and a strong dependence on glass composition (113). This colour change is typically partially or

fully reversible with heat or exposure to UV light. The presence of overlapping electronic defect centres responsible for this colour change can be easily observed through deconvolution of UV-Vis-NIR data.

The method used here is taken from the paper by Rautiyal *et al.* focusing on an MW-like lithium sodium borosilicate and a sodium barium borosilicate glass similar to the Indian Trombay base glass formulation (36). In this method the absorption spectrum of a transparent polished glass monolith is taken pre and post irradiation, the data is converted from absorption to absorbance coefficient (using equation 9) to remove the dependence on path length, rescaled from nm to wavenumber ($cm^{-1}$), and the pristine unirradiated glass spectrum is subtracted from the irradiated glass spectrum (36). This gives a data set containing only the UV-Vis-NIR absorbence caused by the electronic defects present in the glass, that has been rescaled, to enable the spectrum to be fitted with a series of Gaussian peaks to give an indication of the electronic defects present in the glass.

$$\alpha = \frac{ln10 \times a(\gamma)}{t(cm)}$$

*Equation 9 a = sample absorption, t = sample thickness*

As this method is not currently commonly used for the identification of defects in glass, very little reference data is available to aid in identification of the defects present, which has the potential to lead to misidentification of the defects observed. Additionally, any defects with absorptions in the UV range will be obscured by the glass being opaque to UV light, with the wavelength that this occurs at referred to as the UV cut off edge of the glass analysed. This, in combination with the tendency for the UV cut off edge to shift from far UV towards the visible range due to radiation induced structural changes, makes identification of defects with absorbance at higher wavenumbers difficult and demonstrates the value of complementary techniques such as EPR to aid in the identification of defects.

### 6.1.3. Electron Paramagnetic Resonance Spectroscopy

EPR also known as Electron Spin Resonance (ESR) spectroscopy is the study of unpaired electrons in a sample. The fundamental theory of EPR is similar to that of NMR with the only significant difference being that in EPR unpaired electrons are excited and the energy absorbance is measured, not atomic nuclei. In an EPR experiment the sample is held in a fixed microwave field and the magnetic field frequency is swept. As the magnetic field strength is swept the energy levels of the unpaired electron will diverge till the energy difference between the two levels becomes equal to the applied microwave radiation and the microwave energy is absorbed allowing the electron to jump to the higher energy level. This absorbance is measured to give an absorbance spectrum with EPR spectra typically shown as the first derivative of the absorbance spectrum. The power of the applied microwave field can vary depending on the spectrometer type, known as band, used. The most common bands used are X and Q band, due to spectrometer availability, although other bands can be used as shown below in table 29.

*Table 29 Common EPR band shown with their microwave power (λ), frequency (v), and magnetic field strength required for a free electron in a vacuum to transition to a higher energy level ($B(e^-)$).*

| Band | X | P | K | Q | U | V | E | W | F | D |
|---|---|---|---|---|---|---|---|---|---|---|
| λ/cm | 3 | 2 | 1.25 | 0.85 | 0.6 | 0.46 | 0.4 | 0.32 | 0.27 | 0.21 |
| v/GHz | 10 | 15 | 24 | 35 | 50 | 65 | 75 | 95 | 111 | 140 |
| $B(e^-)$/T | 0.33 | 0.54 | 0.86 | 1.25 | 1.8 | 2.3 | 2.7 | 3.5 | 3.9 | 4.9 |

The spectrum is typically shown as first derivative of absorbance in units of mT or Gauss. As demonstrated in table 3 the exact peak position has a strong dependence on the microwave frequency used, because of this values quoted in literature given are in units of g factor. The g factor is calculated using the following equation (equation 10) to remove the dependence on microwave frequency (152).

$$g = h\nu/\mu_B B_0$$

*Equation 10 h = Planck's constant, v = microwave frequency $\mu_B$ = Bohr magneton $B_0$ = magnetic field strength*

An additional feature of EPR is hyperfine splitting. Hyperfine splitting results from the interaction of the magnetic moment of the nucleus and the magnetic moment of the unpaired electron of certain atoms, the quantity of splitting present is determined by the spin state of the nucleus such that spin 1/2 $^{1}H$ will spit a single signal into two hyperfine EPR signals and spin 3/2 $^{11}B$ will give 4 hyperfine EPR signals (152). This leads to an exceptionally complicated splitting pattern, and because of this EPR spectra are typically fitted through simulating spectra.

In UK base glass the signals resulting from multiple radiation-induced defects are all observed in the form of a wide multi component band around 2 g with an additional broad distinct signal observed at approximately 4 g, which corresponds to trace $Fe^{3+}$ present as an impurity in glass. The complex signal at approximately 2 g is expected to correspond to overlapping peroxy radicals, oxygen hole centres and trapped electrons as observed in MW glass and related sodium borosilicate glasses (45). CaZn has an additional signal present (discussed in detail section 3.4.2), believed to be related to the aluminum and calcium present in the glass.

There is anecdotal evidence that states that gamma-irradiated glass is decolorised by exposure to UV light however this has not been fully documented or studied in any great detail. The ability to fit UV-Vis-NIR data of gamma irradiated glass to gain an indication of the electronic defects present demonstrates that specific colour centres may be liked to electronic defects (36), and from this it can be inferred that the decolourisation of irradiated glass is linked to the recombination of radiation induced defects. One other study by Juniewicz *et.al.* relating to the recombination of electronic defects in glass by sunlight is known but does not fully explore the use of UV light for quantifiable recombination of electronic defects (113). The use of UV light to induce defects is well known and commonly used in other areas, because of this, equipment for in situ

measurement of EPR spectra while the sample is being exposed to UV light is widely commercially available. Here this technology has been used to recombine the more unstable electronic defects, revealing the underlying signals enabling the simulation of the electronic defects present. The unexpected stability of certain trapped electron centres further demonstrates the potential for these centres to be stabilised by migration of cationic network modifiers or be located on the clustered cations as proposed by Griscom (37). This stability has the potential to be related to the Na clustering proposed by Rautiyal *et al.* to explain the gamma irradiation induced blue colour change in a NaBaBSi Trombay like glass and an EPR peak observed at ~1.97 g in the same glass (36).

The large yet unstable peak related to aluminum and calcium content seen in CaZn further suggests an electronic defect stabilization process that may be related to mobility of network modifiers and their ability to cluster or form colloids, with any very small calcium colloids formed expected to be reasonably EPR active due the presence of unpaired electrons (47,48). The different abilities of Modifiers to stabilise e centres is supported by evidence of lithium and sodium having comparably greater network mobility, thus being better able to stabilise electronic defects compared to calcium, as observed in the broad asymmetric Li-O and Na-O peak shapes observed in PDF data discussed in section 2.5.2.3.

### 6.1.4. Optical and Scanning Electron Microscopy (SEM).

Both optical and electron microscopy have been used in this study to observe the pristine and leached glass surface pre and post irradiation. All glass samples have been studied using an Olympus GX71 invert optical microscope in bright field mode. SEM and elemental analysis using Energy Dispersive Spectroscopy (SEM-EDS) has been carried out using a Quanta FEG 250 scanning electron microscope on selected pristine and leached glass samples. The fundamental theory of SEM does not greatly change depending on the sample being studied. SEM-EDS is a complementary non-destructive technique making use

of characteristic X-rays emitted when excited electrons in an atom drop to a lower energy level. The energy difference between electronic states is dependent on atomic number and number of electron shells so the technique will not detect elements with an atomic number lower than boron (Z=5) , with many instruments unable to reliably quantify elements with an atomic number lower than sodium (Z=11). Many of the elements in typical alkail borosilicate glass have a lower atomic number than sodium making this technique less than ideal for use in the analysis of bulk alkail borosilicate glass. Additionally only a very small volume of the sample surface is sampled, so information on the inside of the glass sample is not obtained unless the sample is cross sectioned, resulting in the analysis process becoming both more involved and, as the sample is cut during cross sectioning, destructive. This is demonstrated *via* attempts made here to use SEM-EDS to determine the actual sample composition, where a great deal of variation was observed depending on the sample region studied (shown in table 30).

*Table 30 Example of the variation in composition observed during attempted EDS analysis of MW*

| Mol % | Site location | | | | | | |
|---|---|---|---|---|---|---|---|
| | 1 | 2 | 3 | 4 | 5 | Mean | SD |
| $SiO_2$ | 80.1 | 82.4 | 81.3 | 81.6 | 81.3 | 81.3 | 0.8 |
| $Na_2O$ | 13.9 | 14.3 | 13.3 | 13.5 | 13.6 | 13.7 | 0.4 |
| $Al_2O_3$ | 6 | 3.3 | 5.4 | 4.9 | 5.1 | 4.9 | 1.0 |
| $Li_2O$ | ND | ND | ND | ND | ND | ND | NA |
| $B_2O_3$ | ND | ND | ND | ND | ND | ND | NA |
| Total | 100 | 100 | 100 | 100 | 100 | | |

Optical microscopy has been primarily used for inspection of samples pre- and post-leaching. The surface finish of the glass pre-leaching should be largely featureless as a poor surface finish will influence the initial rate of gel layer formation (153). Samples have also been inspected post-irradiation, primarily to ensure that any slight sample density changes expected to occur as a result of high dose radiation do not impact the surface finish (135). A slight change in surface finish was observed in all irradiated samples and the surface

inspection of samples irradiated to a total dose of ~10 MGy revealed shiny areas that may be due to small crystals formed as a result of phase separation (shown in figure 74c) , this was not observed in samples irradiated to a total dose of ~5 MGy. The change in surface finish seen at both doses is likely to be related to the expected density changes, though slight; and irradiation under ambient atmosphere, leading to a very small amount of gel layer formation due to water radiolysis and a slightly elevated temperature in the irradiator.

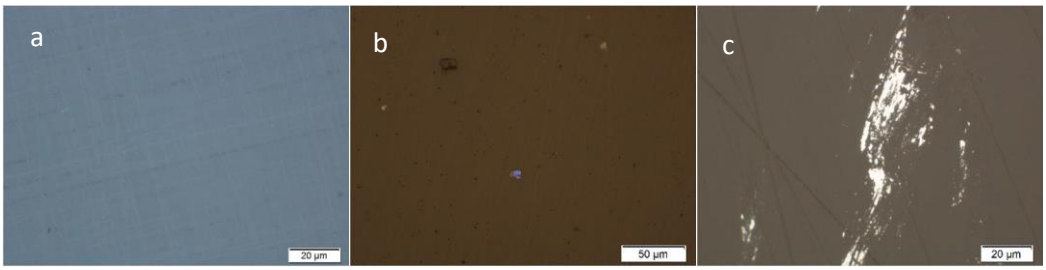


*Figure 74 Microscope images taken from, a) pristine glass surface, b) 10 MGy gamma irradiated ISG, and c) 10 MGy gamma irradiated CaZn. Brown colouration originates from colour change during glass irradiation.*

Optical microscopy, and scanning and transmission electron microscopy used in combination with EDS are typically used to study the glass gel layer (52,63,76). Here optical microscopy has been used to observe the bulk surface of the dried gel layer and SEM has been used to study selected cross sections of the dried gel layer surface and estimate the gel layer thickness. Other methods of estimating gel layer thickness such as those involving leachate concentration of silicate and borate were not used as these methods are not designed for use in leaching systems where silicate can be lost from solution (52,154). Additionally, concerns about the validity of this method have been raised in more recent literature (155). The small sample volume analysed when carrying out SEM-EDS combined with the small gel layer thickness makes the technique well suited for use in mapping the depletion of selected elements from cross sections of the gel layer. This will enable a better understanding of gel layer thickness and composition and how this interacts with the stainless steel container. As boron depletion is expected to occur during gel layer formation

the inability to detect boron is not an issue. With the exception of issues encountered involving the Kα peaks of zinc and sodium closely overlapping creating a possible false positive for zinc loss during short EDX scans (discussed in section 4.4) , this technique is ideal for studying regions of gel layer formation (52,77).

### 6.1.5. Helium Pycnometry

Helium Pycnometry is used to measure the density of solid material making it ideal for measuring the density of glass samples. A typical He Pycnometer such as the Accupyc II 1340 helium pycnometer used here uses gas displacement to calculate the volume of the sample accessible to the gas used (as shown in figure 75) this is known as the skeletal volume of a sample (156). In a typical He Pycnometry experiment the instrument is calibrated using a reference sample of known mass and volume to allow for changes in temperature and any dead space within the instrument. A known mass of sample is placed in a sample cup and the sample cup is sealed in the Pycnometer sample chamber. Gas is allowed to flow into the sample chamber then a valve is opened allowing the same amount of gas to flow into the expansion chamber, the pressure difference between the chambers is used to determine the skeletal volume of a sample. The sample density is calculated using both the mass of the sample and the skeletal volume of the sample.

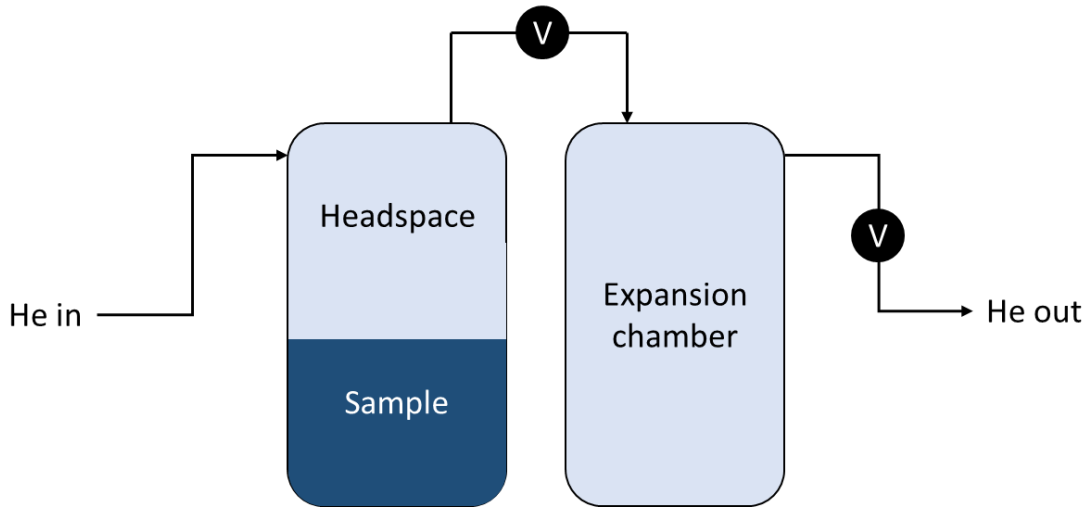


*Figure 75 Simplified diagram of a He Pycnometer. When in use He enters the headspace above the sample and pressure is allowed to equilibrate. Once pressure has equilibrated the value (labeled V) is opened and gas enters the expansion chamber. The pressure difference between the two chambers is used to calculate sample volume. The order of the chambers can be reversed without affecting density measurement*

### 6.1.6. Magic Angle Spinning Nuclear Magnetic Resonance

Solid state NMR is commonly used to analyse a variety of materials and depending on the elements present can be used to build a near full picture of glass structure with some researchers going as far as stating that (referring to XRD being developed before NMR) "The predominance of X-ray diffraction in determining crystal structures led to the establishment of a structural vocabulary incompatible with the nature of the glassy state" (89). In NMR geometrical environments are determined from specific points (corresponding to the nuclei being studied) in a material, this corresponds to the short range order seen in glasses.

In order to be investigated by NMR the target nuclei must be able to generate a magnetic moment, a property that is referred using the spin quantum number. A simple way of determining if a nucleus is NMR active is looking at the number of protons and neutrons, if both are even then the nucleus possesses no overall spin and is not NMR active, if both are odd then the nucleus has and integer spin and is NMR active, and if the sum of the number of protons and neutrons is odd then the nucleus has a fractional spin and is NMR active. In

this thesis two nuclei both with fractional spin quantum numbers have been investigated $^{11}B$ a spin 3/2 nuclei and $^{27}Al$ a spin 5/2 nuclei.

NMR spectroscopy is based on the Zeeman effect. When the material being investigated is exposed to the magnetic field in the spectrometer the Zeeman effect results in previously degenerate spin states splitting into different energy levels and these energy levels scale linearly with the applied magnetic field (as shown in figure 76) (89). The energy difference between the different spin states can be probed using rf fields making NMR spectroscopy possible.

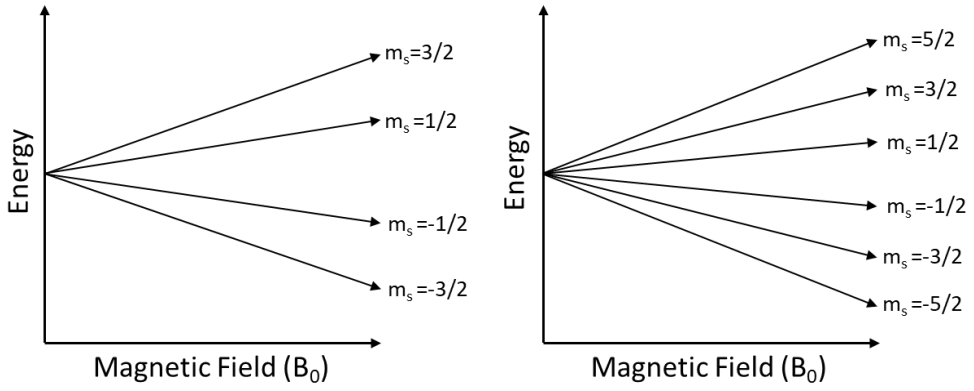


*Figure 76 Example energy level diagram for a spin = 3/2 (left) and spin 5/2 = nucleus in an applied magnetic field.*

While the Zeeman effect makes NMR possible magnetic shielding is what gives the characteristic chemical shifts that enable the identification of specific molecular groups within a structure. The magnetic shielding experienced by the nucleus originates from small magnetic fields generated by electron motion in surrounding bonds.

In nuclides with S > ½ chemical shift, peak broadening, and peak splitting can be further influenced by quadrupolar interactions. These interactions originate from the electric quadrupole moment of the nucleus interacting with the anisotropic field gradient of the surrounding electron density and can produce peaks with complicated shapes (89). The complex peak shapes can be further distorted by the structural disorder of a glass, this

disorder is also typically sufficient to prevent the observation of peak splitting originating from J-couping in a standard glass NMR spectrum (89).

In a typical solid state MAS-NMR experiment the solid being studied is packed into a small rotor so that it can be rapidly spun at an angle to introduce a scaling factor of $3\cos^2\theta - 1$ (where θ is the angle of rotational axis to the magnetic field direction) to undesirable anisotropic spin interactions (89). When a suitable angle is selected the scaling factor becomes zero producing an NMR spectrum containing primarily isotropic spin components. In addition to the angle of rotation the rotor spinning speed used should also be carefully considered. If to slow of a spin rate is used then side bands will be present, these side bands will be reduced at a faster spin rate however, information on site anisotropy can be lost and in some cases such as spectra of nuclei with complex half integer spins these side bands can be used as a reference point providing better resolution (89,157).

Resolution is important when studying glass due to the magnitude of quadrupolar interactions present, including second order anisotropic effects that are not properly averaged by standard MAS NMR. These effects introduce an asymmetric peak broadening that can prevent the interpretation of minor peaks in $^{27}Al$ or $^{17}O$ NMR (89). These effects can be overcome through using 2D MQMAS NMR. 2D MQMAS NMR uses specific pulse sequences to remove anisotropy through refocusing multi quantum dephasings (158).

### 6.1.7. X-Ray and Neutron Pair Distribution Function Analysis

A PDF is the spread of probabilities that a given atom pair will be found with a certain interatomic distance and coordination. This differs from a diffraction pattern where the data shows the spacing between planes of atoms. If diffraction is calculating the precise repeating angular geometric shapes of a cut glass paperweight from the pattern produced when light is shone through the glass, PDFs are calculating the average spacing between swirls within a glass orb using light scattered by the glass. This makes PDFs ideal for use

with amorphous or disordered materials. The calculation of PDFs from X-ray and neutron data is a comparatively new technique that lacks the rigid standardisation of notations found in other areas. While attempts have been made to standardise notation used these have not been entirely successful (159). Here the ATLAS suite of programs has been used to produce the initial neutron PDFs (using the process shown in figure 77) and GudrunX has been used to produce the X-ray S(Q) (88,91). For the simultaneous fitting of PDFs the neutron i(Q) has been converted to S(Q) and both the neutron and X-ray S(Q) have been Fourier transformed using software written in house by University of Kent to give PDFs, that can be simultaneously fitted. To avoid ambiguity the notations and equations used in this thesis are specified in sections 6.1.7.1. – 6.1.7.4. below.

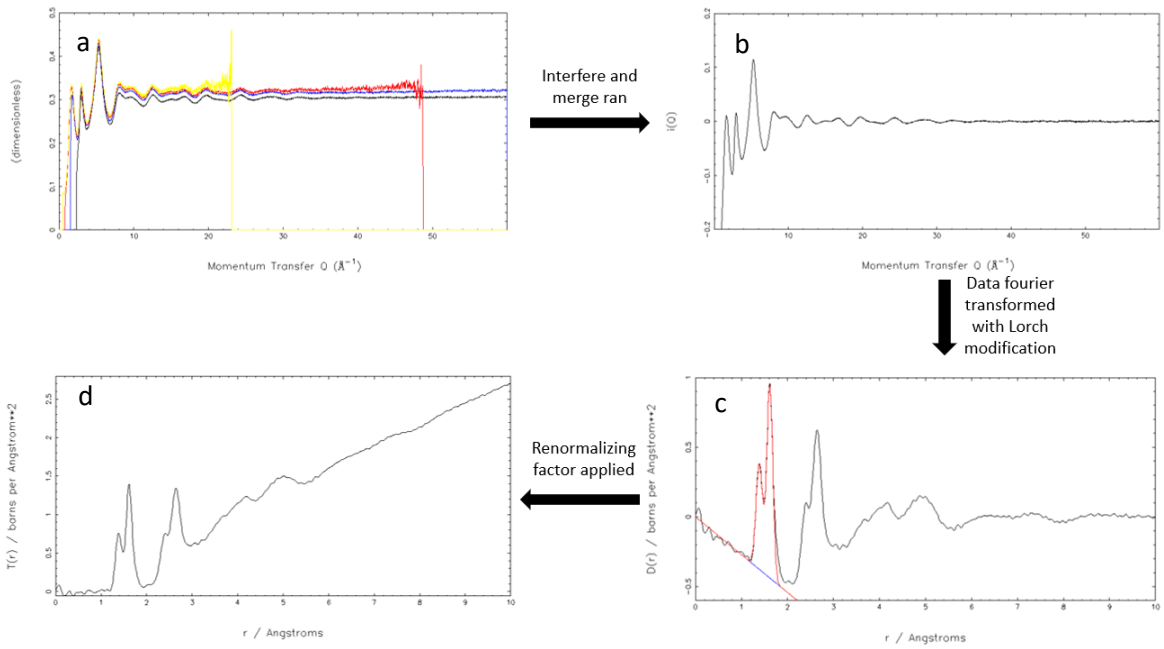


*Figure 77 Example of neutron data correction steps carried out using the ATLAS suite of programmes, a shows uncorrected data, b shows neutron i(Q), c shows D(r), d shows t(r). Shown using ISG as an example.*

### *6.1.7.1. X-Ray and Neutron Scattering*

X-rays used to produce a PDF of a crystalline material can be generated either using a standard laboratory source or synchrotron radiation. Due to loss of energy at high scattering angles more disordered or amorphous materials require the use of a synchrotron

source to produce high energy X-rays required to acquire data with a high enough Qmax to give a usable PDF. Here data has been collected using the i15 beamline at Diamond Light Source (DLS). DLS uses a linac and synchrotron source to accelerate electrons in order to generate high energy photons, these photons are used with a wiggler in the i15 beamline to produce high energy X-rays. The high energy X-rays are monochromated and focused then used in combination with an area detector to collect data.

Neutrons are generated using either a reactor source or a spallation source. Neutrons act as point scatterers when scattered by the nucleus resulting in data typically having a higher Qmax but requiring large sample volumes due to the poor scattering power of the neutron and a more complex data correction process. This process is described in more detail in section 6.2.7. The data used here was collected using the GEneral Materials diffractometer (GEM) beamline at ISIS Neutron and Muon Source. The ISIS Neutron and Muon Source is a spallation source using a proton beam and tungsten plates to generate neutrons and a liquid methane moderator to slow the neutrons to energies required for neutron scattering of the material being analysed (approximately 10 - 100 meV for glass analysis) (89). GEM (shown in figure 78) is designed for the analysis of disordered materials and makes use of a series of detector banks, each designed to collect specific angle ranges of scattered neutrons (89).

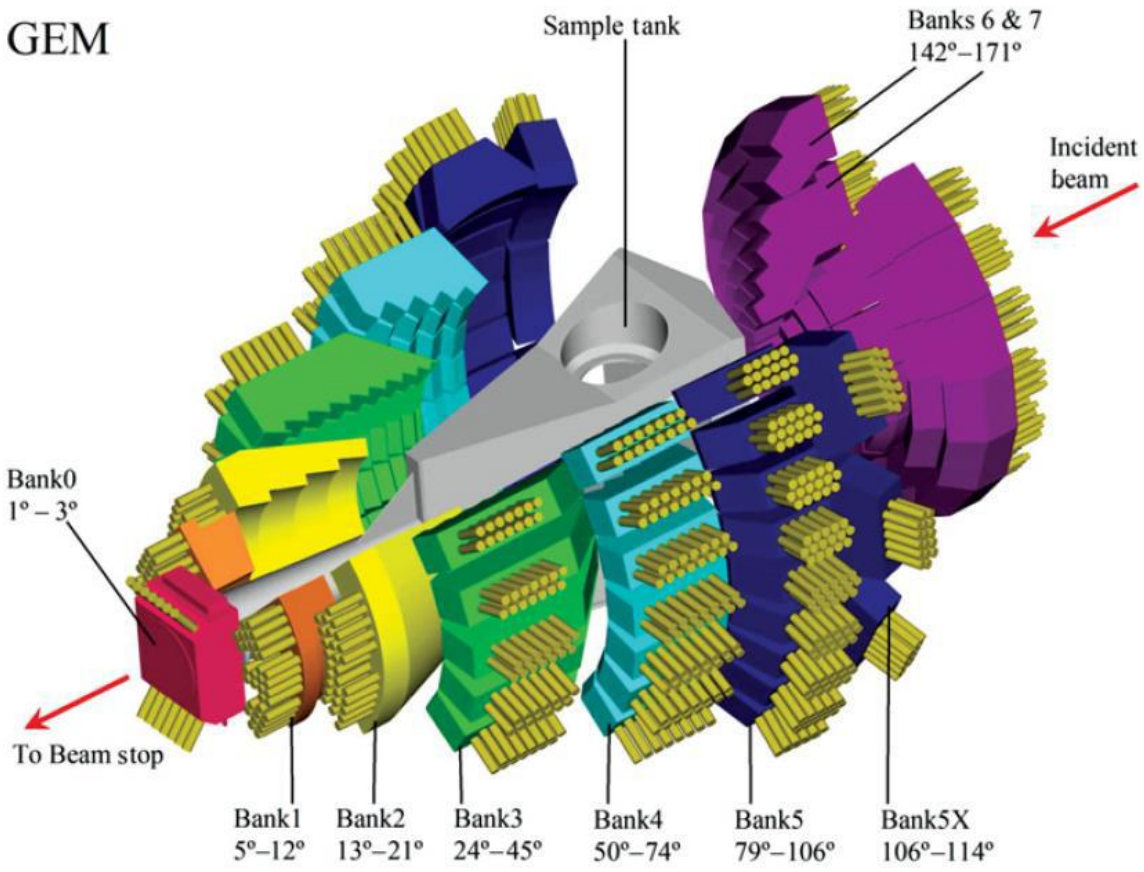


*Figure 78 Diagram showing GEM detector banks (taken from(67))*

X-rays and neutrons will interact with a sample in different ways (as shown table 31). X-rays are scattered by electrons in an atom and neutrons are scattered by the nucleus in an atom, giving neutron scattering a dependence on the isotopes present in a sample. This causes atom pairs in an X-ray PDF to have a different scattering magnitude to atom pairs in a neutron PDF. The differing scattering magnitudes can be calculated and used to simultaneously fit X-ray and neutron PDFs.

*Table 31 Neutron and X-ray scattering magnitudes shown from lowest to highest*

| Atom | Li | Al | Na | Si | Ca | Zn | O | $^{11}$B | Zr |
|---|---|---|---|---|---|---|---|---|---|
| Neutron scattering length/ $b_{coh}$ (fm) | -1.9 | 3.45 | 3.58 | 4.15 | 4.76 | 5.68 | 5.80 | 6.65 | 7.16 |
| Atom | Li | B | O | Na | Al | Si | Ca | Zn | Zr |
| X-ray scattering/ Atom number | 3 | 5 | 8 | 11 | 13 | 14 | 20 | 30 | 40 |

The simultaneous fitting of X-ray and neutron PDFs enables more information to be gained from the PDFs than fitting them individually, as this method is effectively simultaneously solving two different equations with the same answer. Many issues found in neutron PDFs, such as overlapping negative scattering (originating from elements with a negative $b_{coh}$) and positive scattering peaks, are not found in X-ray PDFs as negative scattering does not occur in X-rays. Additionally as neutrons are scattered by the nucleus whereas X-rays are scattered by electrons, atoms that are poor neutron scatterers can be good X-ray scatterers and atoms that are poor neutron scatterers can be good X-ray scatterers.

#### *6.1.7.2. Q Space Functions*

Following corrections to remove container background, background scattering and other undesirable effects present as described in Alderman *et.al.* (90), but immediately prior to application of a modification function and Fourier transformation, the data exists in a form known as Q space. If the Q space data is not of a high enough quality or has not been fully corrected this conversion to "real space" or r space can introduce a large amount of noise and resulting in data loss. To reduce the impact of this, atomistic models produced to fit data can be fitted to a Q space function, usually the S(Q) variant. There are two Q space functions used in this report, S(Q) and i(Q). Q is defined in equation 11 (91).

$$Q = \frac{4\pi sin\theta}{\lambda}$$

*Equation 11 Q = momentum transfer for elastic scattering, 2Θ = scattering angle, λ = neutron wavelength*

The differential neutron scattering of Q is given by equation 12

$$\frac{d\sigma}{d\Omega} = i(Q) + I^S(Q)$$

*Equation 12 $I^s(Q)$ = neutron self-scattering, i(Q) = distinct scattering.*

The differential X-ray scattering is given by equation 13

$$\frac{d\sigma}{d\Omega} = i(Q) + \sum_{i=1}^{n} c_i f_i(Q)^2$$

*Equation 13 i(Q) = distinct scattering, $c_i$ = atomic fraction of elemental sample components, $f_i(Q)$ = Q dependant scattering factor*

This equation varies slightly from the differential neutron scattering equation due to X-ray scattering power decreasing with angle, while neutrons act as point scatterers and do not lose scattering power at high angles.

The neutron distinct scattering can be converted to S(Q) by using the following (equation 14) (92)

$$S(Q) = 1 + \frac{i(Q)}{[\sum_{i=1}^{n} c_i \bar{b}_i]^2}$$

*Equation 14 i(Q) = distinct scattering, $c_i$ = atomic fraction of elemental sample components, $\bar{b}$ = coherent neutron scattering.*

The conversion of neutron i(Q) to S(Q) is a rescale that removes the dependence on neutron scattering making the data unitless. A comparable function (shown below in equation 15), with $f_i(Q)$ representing the X-ray scattering factor and the denominator often referred to as the sharpening function, is used to produce the X-ray S(Q) from the distinct scattering (92).

$$S(Q) = 1 + \frac{i(Q)}{[\sum_{i=1}^{n} c_i f_i(Q)]^2}$$

*Equation 15 i(Q) = distinct scattering, $c_i$ = atomic fraction of elemental sample components, $f_i(Q)$ = X-ray scattering factor.*

#### *6.1.7.3. The Modification Function*

A key part of converting the Q space data to r space is the modification function. A modification function supresses termination ripples that result from Fourier transforming a

finite data set. Two modification functions are used here the Lorch Function (shown in equation 16) and the Step Function (shown in equation 17).

The Lorch Function will supress termination ripples but will result in a slight loss of resolution through peak broadening, whereas the Step Function is equivalent to not using a modification function. The Step Function does not supress termination ripples but will reduce the amount of peak broadening present. Using the Step Function is only practical where Q space data has been collected to a high Q value. The use of the Step Function can enable closely overlapping peaks to be distinguished, although termination ripples can entirely obscure smaller peaks.

$$M(Q) = \begin{cases} (\sin \Delta \mathrm{rQ})/\Delta \mathrm{rQ} \ . & Q \leq Q_{max} \\ 0 & Q \geq Q_{max} \end{cases}$$

*Equation 16*

$$M(Q) = \begin{cases} 1 & Q \leq Q_{max} \\ 0 & Q \geq Q_{max} \end{cases}$$

*Equation 17*

#### *6.1.7.4. r Space Functions*

The r space function, also known as a PDF, is produced from the Q space data; the larger the Qmax of the data collected the higher the resolution of the resulting PDF. The r space is commonly described using three differing notations T(r), G(r), and D(r) with T(r) typically used in the study of glass. Each function corresponds to a slightly differing equation with different sources often quoting different variants of the equations depending on if the data has been produced from an S(Q) or i(Q) (88,91). To prevent confusion the D(r) and T(r) variants used in the work are quoted below (equation 18 and 19). (91,92,159).

$$D(r) = \frac{2}{\pi} \int_0^\infty Q\, x(Q)\, M\, sin(rQ)\, dQ$$

*Equation 18 x(Q) = i(Q) or [S(Q) - 1] M = modification function*

$$T(r) = T^o(r) + D(r)$$

*Equation 19*

The $T^0(r)$has two variants. The variant used with a D(r) generated from an S(Q) is shown in equation 19. For a T(r) produced from a D(r) generated from a neutron i(Q) an additional term is added to the $T^0(r)$, as shown in equation 20.

$$T^o(r) = 4\pi\rho_o r$$

*Equation 20 $\rho_0$ = number density of the sample, r = scalar distance between pairs of atoms,*

$$T^o(r) = 4\pi\rho_o r(\sum_l c_l \bar{b}_l)^2$$

*Equation 21 $\rho_0$ = number density of the sample, r = scalar distance between pairs of atom, $c_l$ = atomic fraction of element l in sample, $\bar{b}_l$ = coherent neutron scattering of element l*

The T(r) can also be described as the sum of weighted partial functions where $T^n(r)$ represents the neutron T(r) and $T^x(r)$ represents the X-ray T(r) (91,92).

$$T^n(r) = \sum_{l,j} c_l \bar{b}_l \bar{b}_j t_{lj}(r)$$

*Equation 22 $c_l$ = atomic fraction of element l in sample, $\bar{b}_l$ = X-ray scattering factor of element l, $\bar{b}_j$ = X-ray scattering factor of element j, $t_{lj}(r)$ = partial corelation function of atom pair lj*

$$T^x(r) = \sum_{l,j} c_l a_l(Q) a_j(Q) t_{lj}(r)$$

*Equation 23 $c_l$ = atomic fraction of element l in sample, $a_l(Q)$ = coherent neutron scattering of element l, $a_j(Q)$ = coherent neutron scattering of element j, $t_{lj}(r)$ = partial corelation function of atom pair lj*

As seen in equation 19 the T(r) is produced from D(r) using a renormalising factor known as the $T^0(r)$ constant (shown in equation 20 and 21). The $T^0(r)$ shifts the data so that it oscillates about 0. This enables the data set to be directly fitted with a set of Gaussian peaks representing the partial corelation function $t_{lj}$ seen in equation 22 and 23. From fitting a PDF with a series of weighted partial corelation functions the bond length, coordination, and σ values of atom pairs can be calculated from the peak position, area,

and peak width respectively. As demonstrated by equation 22 and 23, theoretically these values are the same regardless of if they have been extracted from an X-ray or neutron PDF.

### 6.1.8. Atomistic Modeling

While atomistic modeling has not been used a brief introduction to the technique and is provided in order to give context for the PDF work carried out using MW, CaZn and ISG.

In order to create or verify and refine an atomistic model high quality experimental data on the atom pairs present, the distribution of interatomic distances between the atom pairs and the coordination numbers present within a structure is needed. Once this data has been acquired atomistic models can be created through the use of Monte Carlo (MC) methods or Molecular Dynamics (MD). The basic MC method uses random sampling to approximate values with the new values accepted only if they result in a lower system energy or a system energy increase associated with a Boltzmann factor larger than a randomly generated number (160). This is further refined in variants, such as Kinetic Monte Carlo, which applies transition state theory to MC methods, and Reverse Monte Carlo which is typically used to fit data but requires careful application of constraints. MD calculates the motion of atoms as a function of time by integrating the equations of motion.

However, due to the many aspects of its disordered nature discussed previously, much of the traditional guidance used to aid in the creation and evaluation of atomistic models of related crystalline structures, such as Lowenstein's rule, does not apply to glass. Using atomistic models fitted to experimental data of amorphous materials, it has been demonstrated that the structure that best explains the experimental observations is not necessarily the lowest system energy structural configuration for a material (20). This goes

against some of the standard methods used when determining the accuracy of a structure through traditional MC and demonstrates the need for high quality experimental data.

Experimental data is used to aid in determining the short and intermediate range order displayed in a glass. By definition short range order refers to the interactions between the pairs of atoms in a glass, whereas intermediate range order describes how these atom pairs arrange in small groupings, such as the $Q_n$ number or distribution of borate ring structures. Short range order data, such as the coordination environment, can be gained through techniques such as Extended X-ray Absorption Fine Structure (EXAFS) and Nuclear Magnetic Resonance (NMR) analysis, whereas PDF data can give information on both short and intermediate range order. However, the line between short and long range order is often blurred in PDF data analysis, where the separation between pairs of atoms is used to define short and long range order. The O-O atom pair in the $SiO_4$ tetrahedra atom pair is typically considered the cut off point for short range order in a silicate glass despite not strictly being a standalone atom pair.

The distinction between intermediate and short range order becomes important when analysing PDF data of oxide glasses containing multiple network components, such as boron, silicon, and aluminum using MD based atomistic modeling. The change in distances between the O-O atoms surrounding each individual network component is sufficient for the PDF to show multiple O-O peaks due to the differing short range order surrounding each oxide pair, if this is not considered then this region of the PDF will show a poor fit between experimental data and model (21).

## 6.2. Method

The methods given below have been detailed briefly in previous sections. This section is intended to provide an overview of the origins and development of these methods.

### 6.2.1. Raman Spectroscopy

Raman data was collected from all samples using a Senterra Ramanscope Spectrometer. An initial set of measurement parameters were selected based on literature values and varied to allow for a fault in the instrument preventing the use of 50x magnification (28,36,115). During this investigation it was found that using a slit aperture instead of the more standard pinhole reduced the fluorescence observed from irradiated glass, for the sake of consistency the same settings were used in the initial investigation of glass samples and these are given as follows. A 532 nm laser set at a power of 5 mW with a 20x magnification lens combined with a collection time of 60 s with 30 accumulations and a 25x1000 µm aperture.

These parameters were further refined for use with 50x magnification at a later date and with the exception of ISG which was excluded from latter studies due to covid related time constraints. The raman collection parameters used were a 532 nm laser set at a power of 20 mW with a 50x magnification lens and a collection time of 15 s with 30 accumulations and a 25x1000 µm aperture was used. As the laser was better focused and focused on a smaller area allowing for better heat dissipation (heat increases the recombination rate of electronic defects found in gamma irradiated glass) a higher laser power combined with a shorter collection time was used to enable more efficient use of limited lab access time.

To further improve signal to noise and minimise the impact of any slight inhomogeneity raman spectra used in the study of irradiated glass were collected from multiple fragments of glass from the same batch and irradiation run and the spectra averaged. Despite coming from the same batch of glass it was found that in many cases the background showed a dose dependence (background applied shown in figure s 37 - s 41 )

The data was baseline corrected by eye, temperature and excitation line corrected using a method adapted from Long, and normalised to the highest peak position (91). As all the

Raman spectra were collected at room temperature the method adapted from Long was applied primarily to remove the wavelength dependency of Raman intensities, in glass this tends to over emphasise the Si-O-Si region (300–500 $cm^{-1}$) peaks and under emphasise the $Q_n$ region (1200-1700 $cm^{-1}$) peaks (148,149).

Where the $Q_n$ region was fitted either the default PsdVoigt1 function (shown in equation 24) or the default PsdVoigt2 function (shown in equation 25) in OriginPro 9.1. The Voigt function was not used as when using this function it is not possible to constrain peak width without also constraining the Gaussian Lorentzian peak character. A pseudo voigt function was chosen over a Gaussian function based on the proposal by Bancroft *et.al* that peaks in the $Q_n$ region will have a mixed Gaussian Lorentzian character (107).

$$y = y_0 + A\left[m_u \frac{2}{\pi}\frac{w}{4(x-x_c)^2 + w^2} + (1-m_u)\frac{\sqrt{4\ln 2}}{\sqrt{\pi}\,w} e^{-\frac{4\ln 2}{w^2}(x-x_c)^2}\right]$$

*Equation 24 PsdVoigt1 function used by OriginPro 9.1 $y_0$=offset, A = area, w=full width half max, mu= Gaussian Lorentzian character, $x_c$=center*

$$y = y_0 + A\left[m_u \frac{2}{\pi}\frac{w_L}{4(x-x_c)^2 + w_L^2} + (1-m_u)\frac{\sqrt{4\ln 2}}{\sqrt{\pi}\,w_G} e^{-\frac{4\ln 2}{w_G^2}(x-x_c)^2}\right]$$

*Equation 25 PsdVoigt2 function used by OriginPro 9.1 $y_0$=offset, A = area, $w_G$= Gaussian full width half max, $w_L$= Lorentzian full width half max, mu= Gaussian Lorentzian character, $x_c$=center*

The following peak position constraints were also applied to the $Q_n$ region: 900 -930 ($Q_1$), 950-1000 ($Q_2$), 990-1040 (Al-O), and 1050 – 1100 $cm^{-1}$ ($Q_3$) (77,92,93). The $Q_4$peak was fitted without constraints and due to the low quantity of alumina present in MW and noise seen in the $Q_n$ it was not possible to fit the Al-O peak separately in all raman spectra and instead a four peak fit was carried out.

### 6.2.2. UV-Vis-NIR Spectroscopy

All UV-VIS-NIR measurements were carried out using a Cary 5000 UV-Vis-NIR spectrophotometer operated in dual beam mode. The scan rate was kept at the default

setting of 600 nm/min, and the scan range was changed depending on the investigation carried out, the glass monoliths were scanned from 3300 – 190 nm and the molybdenum blue solution was scanned 900 - 700 nm with the grating and detector changeover changed from 800 nm to 750 nm to prevent possible interference from the changeover point. The glass monoliths were scanned with air as a baseline and the molybdenum blue measurements were carried out with water as a baseline.

#### 6.2.2.1. Monolith Measurements

The thickness of the polished glass monoliths was measured using a set of digital calipers and the monoliths were mounted on a solid sample holder with a 10mm square aperture using reusable adhesive putty. Prior to each measurement set beam alignment was checked using zero order mode to ensure the aperture was not obstructing measurements. Initial measurements were carried out at half beam hight to compensate for the solid sample holder being poorly aligned. The sample holder alignment was latter corrected and MW and CaZn measurements were repeated at full beam height. The spectra were averaged across a minimum of three different samples and the data was processed using the method given in Rautiyal *et.al*. (36). The resulting rescaled and normalised spectra were fitted using the default Gauss function in OriginPro 9.1. (shown below in equation 26).

$$y = y_o + \frac{A}{w\sqrt{\frac{\pi}{2}}} e^{-2\frac{(x-x_c)^2}{w^2}}$$

*Equation 26 $y_0$ = offset, A = area, w = width, and $x_c$ = center*

The method used in Rautiyal *et.al* is somewhat novel hence the decision to use this method in combination with EPR to identify electronic defects, both to help verify this method and demonstrant the complementary use of UV-Vis-NIR (36). One small modification has been made to this method, in the equation given by Rautiyal *et.al* ln10 has been approximated to 2.303, this approximation has not been used here (36).

#### 6.2.2.2. Molybdenum Blue Method

The molybdenum blue method used for the colourimetric determination of solution silica content was based on the method given by Yang *et.al*. (137). This method was chosen as the results of the study had been verified using ICP-OES and displayed a relative error of 1.5%. The same method stated below was used to produce the calibration curve and analyse the glass leachate. A new calibration curve was prepared for each batch of molybdenum blue mixed and a fresh ascorbic acid solution was prepared for each set of measurements and kept refrigerated when not in use.

All chemicals used in determination of silicon concentration were supplied and stored in plastic bottles or prepared as a stock solution using Nalgene volumetric flasks to prevent silica contamination and deionised ultrapure 18 MΩ water was used throughout. Prior to each set of leachate silicon analysis appropriate quantities of the following were prepared; $H_2SO_4$ 1 M and 0.05 M; oxalic acid–tartaric acid 0.5 M–0.5 M; ammonium molybdate 5% m/v; ascorbic acid 2% m/v; a standard silicate solution diluted to an appropriate concentration range (0 ppm, 5 ppm, 10 ppm, 20 ppm, 40 ppm, 80 ppm) from a 1000 ppm premixed silicate standard solution. As the leachate had previously been refrigerated the leachate was placed in a 50°C water bath a thoroughly shaken before use to enable redissolution of any particulates that had settled out of solution. The warm CaZn glass leachate was analysed undiluted and the warm MW leachate was diluted by a factor of 10 to ensure the Si concentration fell in a suitable range for analysis using this method.

In order to determine the silicone concentration and prevent silica contamination from glass a 100mL plastic beaker was used. This beaker was placed in a 25°C water bath and positioned on a hotplate stirrer and a temperature probe was placed in the water bath to control the water bath temperature. A 12mm PTFE coated stir bead was added to the 100 mL beaker followed by 20 mL of $H_2SO_4$ (0.05 M) and 2 mL of either silicate standard

solution or glass leachate was added. The solution was stirred for 20 min to ensure proper mixing and heating. Following stirring 20 mL of ultrapure 18 MΩ water was added to the beaker, followed by 10 mL of absolute ethyl alcohol, and 15 mL of ammonium molybdate (5%). The solution was again stirred for 20 min to allow for complete formation of a yellow silicomolybdate complex in the colourless solution. Finally, 10 mL of oxalic acid–tartaric acid (0.5 M–0.5 M), and 5 mL of ascorbic acid (2%) were added to the yellow solution and the solution was stirred for 20 min to enable the complete reaction of the yellow silicomolybdate complex with the ascorbic acid to form the molybdenum blue complex necessary for colorimetric analysis.

The fully reacted molybdenum blue complex was the analysed using a 10 mm path length PMMA cuvette to prevent silica contamination from glass or quartz. Ultra-pure water was used as a baseline and the baseline was reran for each set of calibration measurements, set of CaZn leachate measurements, and set of MW measurements each set of measurements used the same cuvettes for the baseline and spectrophotometric determination of silicon solution content. The peak of interest was predicted to be located at ~812 nm and the highest point between 802 and 822 nm was used for silicon solution determination (137).

### 6.2.3. Electron Paramagnetic Resonance Spectroscopy

Initial EPR measurements were carried out using a Bruker EMX Nano X band EPR spectrometer, quartz glass tubes and small slices of unpolished glass monoliths. Three sets of measurement settings were used as shown in table 32. The widescan settings were used to collect a wide swept scan showing both the gamma irradiation induced electronic defects and the $Fe^{3+}$ center, the G factor settings were used to collect data from the gamma irradiation induced electronic defects, and the Fe center settings were used to collect a scan of the $Fe^{3+}$ center.

*Table 32 EPR scan settings used for X band measurements*

| | Widescan | G factor | Fe center |
|---|---|---|---|
| Center Field / G | 2300 | 3400 | 1600 |
| Sweep Width / G | 3000 | 500 | 1900 |
| Sweep Time / s | 42 | 7 | 26.7 |
| Sample g Factor | 2 | 2 | 2 |
| Receiver Gain / dB | 35 | 35 | 70 |
| Modulation Amplitude / G | 2 | 2 | 4 |
| Number of Scans | 16 | 16 | 16 |
| Attenuation / dB | 20 | 20 | 20 |

The widescan setting was used as an initial scan on all pristine glass samples prior to and following irradiation to gain an overview of the irradiation induced electronic defects. In these scans the $Fe^{3+}$ region was typically poorly resolved and the electronic defects showed very slight peak broadening compared to using a narrower scan range leading to a loss of resolution. Attempts were made to improve the resolution of the Fe center by changing the settings used but these were not successful and few changes were observed in this region.

EPR measurements were carried out on both 10 MGy irradiated samples of MW, CaZn, and ISG and 5 MGy irradiated samples of MW and CaZn. No significant changes were observed in the G factor scans of 10 MGy and 5 MGy irradiated MW and CaZn glass (as shown in figure 79).

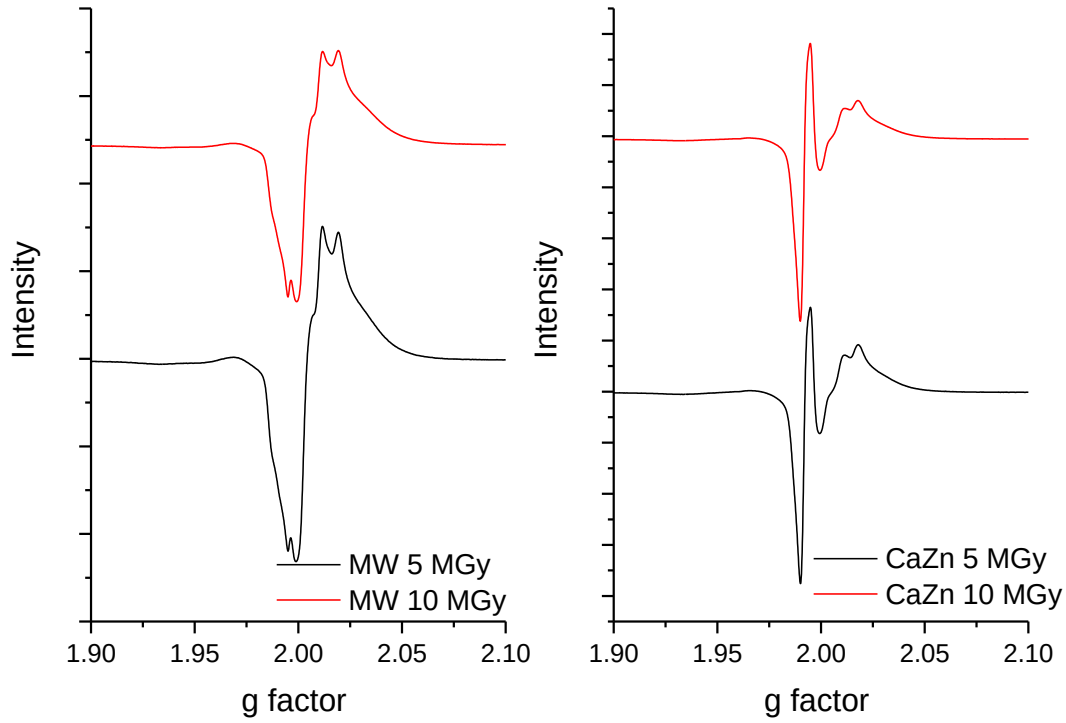


*Figure 79 EPR data collected from glass irradiated to a dose of 5 MGy and 10 MGy, normalised to g factor for clarity.*

Based on these results a dose of 5 MGy and the G factor settings were chosen for the UV induced controlled defect recombination.

The X band UV induced defect recombination was carried out in situ using a Brucker UV irradiation system equipped with a LSB610 100 W mercury arc lamp (spectral irradiance shown figure 80) and a fiber optic cable. The fiber optic cable was set up in a manner that resulted in the glass sample being exposed to the full light emissions of the UV lamp.

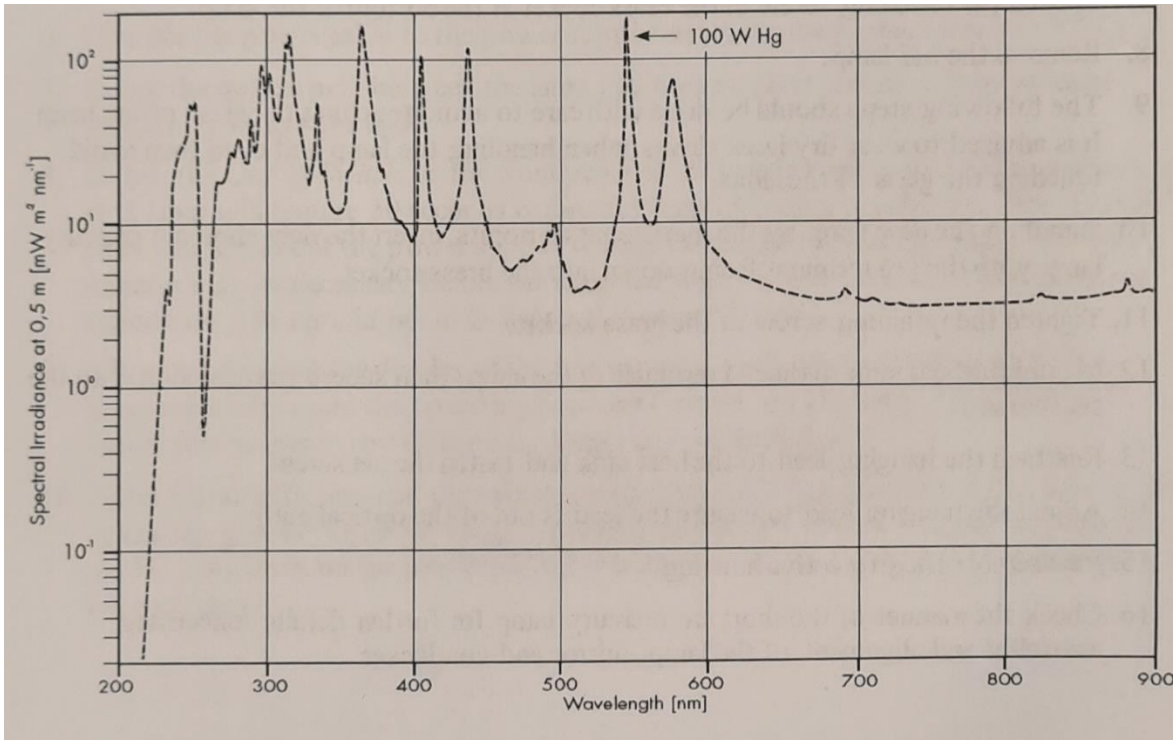


*Figure 80 UV light emission spectra as shown in Bruker UV irradiation system guide.*

EPR measurements were taken pre UV exposure from samples of MW and CaZn. In situ UV exposure measurements were taken at 3 min intervals for the first 2.5 h and then at 22 min intervals for a total of 21 hours. The time delay EPR spectra was plotted using OriginPro9.1 and the EPR spectra of MW was fitted stepwise using values from literature (39,45,46) starting with fitting the BOHC and E center of glass that had been exposed to UV light for 21 hours using the commands shown below where ## represents values that can be varied. The final set of fits was carried out by varying only the Sys.Weight parameters for each EPR scan collected during the time delay EPR process.

```
 % Read epr data

clear,clf,clc
[B,MW1] = eprload('MW 5MGy gamma Gfactor 2 overnight scan');%change to
curent file
BG2 = (B{1,1})/10; % extacts correct B value and converts to mT
Btime = (B{1,2})/60; %extracts run time s and converts to min
run =1; %insert UV run number to change plot
spcMWr = (MW1(:,run)); % converts selected UV run into format readable by
plot
```

```
Exp.mwFreq = (9.420);
Exp.Range = [min(BG2) max(BG2)];
Btitle = (Btime (:,run)); %adds run time to title min
plot(BG2,spcMWr);
title(Btitle);

%% Fit data need to fit E, and BOHC first then add in POR folowed by
others
%E'
Sys1.g = [1.9567];
Vary1.g = ## ;
Sys1.lwpp = [0.563583];
Vary1.lwpp = ##;

%BOHC
Sys2.Nucs = 'B';
Sys2.g = [1.98836 1.96825 1.96483];
Vary2.g = [## ## ##];

Sys2.A = [40.4674 44.2967 34.9832];
Vary2.A = [## ## ##];
Sys2.lwpp = [1.32135 ]; %0.03825
Vary2.lwpp = [##];

% POR
Sys3.g = [1.95906 1.9635 1.97957];
Vary3.g = [## ## ##];
Sys3.lwpp = [0.0223493 0.536158];
Vary3.lwpp = [## ##];

%HC1
Sys4.g = [1.94758 1.97206 1.96964];
Vary4.g = [## ## ##];
Sys4.lwpp = [0 0.319937]; %[0.0225974 0.455049];
Vary4.lwpp = [## ##];

%NBOHC
Sys5.g = [1.98582 2.0046 2.0069];
Vary5.g = [## ## ##];
Sys5.lwpp = [0 2.42808];%[0.202767 2.4268];
Vary5.lwpp = [## ##];

%BO3
Sys6.g = [1.96689 1.99484 1.96199];
Vary6.g = [## ## ##];
Sys6.lwpp = [0.274792 0.531454];
Vary6.lwpp = [## ##];

%BOSi
Sys7.g = [1.94971 1.95814 1.97513];
Vary7.g = [## ## ##];
Sys7.lwpp = [0.79345]; %0.0159337
Vary7.lwpp = [##];

%setting up fit
Sys1.weight = 0.083236249;
Vary1.weight = ##;
Sys2.weight = 1.665649568;
Vary2.weight=##;
```

```
Sys3.weight = 1.495571646;
Vary3.weight=##;
Sys4.weight = 0.067112439;
Vary4.weight=##;
Sys5.weight = 0.82075347;
Vary5.weight=##;
Sys6.weight = 0.482001147;
Vary6.weight=##;
Sys7.weight = 0.228152407;
Vary7.weight=##;

esfit(@pepper,spcMWr,{Sys1,Sys2,Sys3,Sys4,Sys5,Sys6,Sys7},{Vary1,Vary2,Var
y3,Vary4,Vary5,Vary6,Vary7},Exp);
```

It was not possible to fit data collected from CaZn using this method as literature references to use as starting points could not be found for several of the peaks present.

Further EPR measurements were collected using Bruker EMX Plus Q band EPR spectrometer from powdered samples of MW and CaZn irradiated to a dose of 5 MGy using a Foss Therapy Services 812 $^{60}$Co irradiator and loaded in to quartz glass capillary tubes. Exact spectrometer frequency was measured using an external monitor during collection and the parameters were varied to give the set of parameters shown in table 33. These settings were used for scans of the ex situ UV exposed glass. A wide scan and attempts to individually scan the Fe region showed extensive peak broadening and due to time constraints multiple scans of these regions were not carried out.

*Table 33 EPR scan setting used with Q band measurements.*

| | EPR settings |
|---|---|
| Center Field / G | 12250 |
| Sweep Width / G | 1000 |
| Sweep Time / s | 60 |
| Sample g Factor | 2 |
| Receiver Gain / dB | 35 |
| Modulation Amplitude / G | 5 |
| Number of Scans | 8 |
| Attenuation / dB | 20 |

Ex situ Q band UV EPR measurements were carried out using a dark box fitted with a xenon arc lamp. Q band EPR measurements were taken at 5, 10, 15, 30, 60 and 120 min UV exposure intervals and the temperature in the dark box was monitored to ensure it did not exceed 50 °C to prevent excessive temperature-related recombination of EPR active defects. Attempts were made to use a mercury arc lamp to perform in situ UV exposure measurements however, due to the length of the available fiber optic attachment, it was not possible to prevent the magnetic field of the spectrometer interfering with the lamp. The spectra produced from the Q band measurements showed unexpected line broadening, despite this the spectra produced were typically better resolved. Attempts were made using the same set of easy spin commands stated previously with the addition of the Sys.gstrain command to allow for the presence of g strain using SimOpt.Method=perturb2 to calculate the g strain values. These attempts were not successful.

### 6.2.4. Optical and Scanning Electron Microscopy

An Olympus GX71 optical microscope running in bright field mode was used to inspect the surface of all glass monoliths pre and post polishing to ensure no surface imperfections were present that may impact the leaching results.

SEM and SEM-EDS analysis was caried out using a Quanta FEG 250 Scanning Electron Microscope operating at an acceleration voltage of 15 – 20 kV, equipped with an Oxford $Xmax^N$ 80 EDS detector. All samples were mounted on standard sample tabs using carbon tape and gold coated prior to SEM imaging. The monolith surfaces were not studied using SEM as pre leaching these were largely featureless when viewed using an optical microscope. Post leaching the gold coating and high vaccuum process used for SEM caused the gel layer on MW to fully delaminate, while the gel layer on CaZn showed no features of interest when viewed using an optical microscope.

A small portion of a single leached CaZn sample was broken off using a pair of glass nips and positioned on a sample tab using carbon tape to enable the analysis of a cross section of the leached gel layer using SEM EDS. Due to the mounting method used the sample tended to shift while collecting images. Due to this shifting it was only possible to carry out EDS elemental mapping using a 2 min collection intervals.

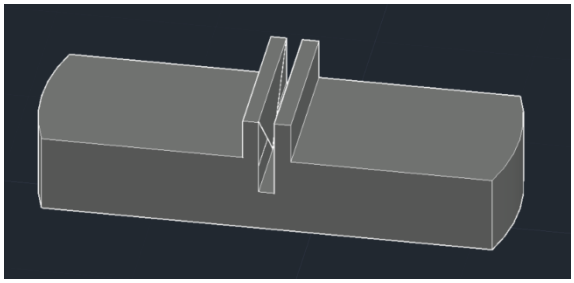

*Figure 81 Model of sample holder used to encase glass monoliths in resin*

In order minimise shifting and enable cross sections to be taken from all leached glass monoliths individual samples of CaZn and MW from each leaching run were held in a 3D printed sample holder (shown in figure 81) and encased in Araldite 2020 two part epoxy resin using a 4 cm diameter sample cup (as shown in figure 82).

The resin encased samples were removed from the sample cup and ground and polished to reveal cross sections of the glass monoliths. The final surface imaged was wet polished to a 5 µm surface using silicon carbide paper.

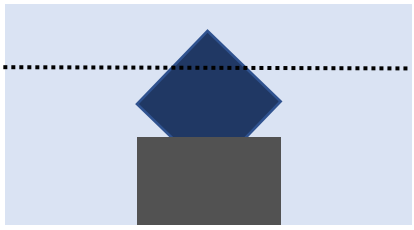

*Figure 82 Simplified diagram showing resin encased glass monolith with dashed line representing approximate depth of polishing and grinding. Resin shown pale blue, glass monolith shown dark blue, and sample holder shown grey*

The resin mounted samples were EDS mapped and EDS line scanned. Some shifting was present and the Araldite resin showed signs of being damaged by the electron beam during long measurements. Due to this EDS line scanning was carried out at 5 to 10 min. The resulting line linescans were normalised and plotted against total counts for clarity.

### 6.2.5. Helium Pycnometry

An Accupyc II 1340 helium pycnometer was used to carry out density measurements of the glass powers prepared with $^{11}B$ isotopically enriched boric acid. Prior to analysing the glass

the pycnometer was calibrated using a 10 $cm^3$ calibration sphere placed in a standard 10 $cm^3$ sample cup. Following calibration a known quantity of powder (shown table 5 section 2.3.3.) was measured into the same standard 10 $cm^3$ sample cup and run with 20 purge fill cycles. Multiple purge fill cycles were run as this resulted in an improved standard deviation within the measurement sets.

### 6.2.6. Magic Angle Spinning Nuclear Magnetic Resonance

All experimental NMR spectra were acquired in partnership with researchers at University of Liverpool using methodology developed with the aid of Aine Black.

All experimental spectra were collected at 9.4 T on a 400 MHz Bruker Avance III HD spectrometer using a Bruker 4 mm HXY MAS probe in double resonance mode. The nuclear spin quantum number (I) and Larmor resonance frequency (ν0) of each nucleus are given below. Glass powder samples were packed into commercial 4 mm zirconia Bruker rotors and spun at MAS frequencies of either 8 and 10 kHz as specified. Experimental 1D MAS NMR spectra were fitted using a version of the Czjzek distribution (161) using the software DMFit (162). Spectra were optimised to achieve the best possible fit with a less than 5 percent error.

$^{11}B$ (I = 3/2, ν0 = 128.38 MHz) MAS NMR spectra were acquired a using small nutation angle rotor-synchronised Hahn echo pulse sequence of $\pi/18 - \tau - \pi/9 - \tau - acq$ with τ corresponding to one rotor period. Short flip angles of π/18 (using radiofrequency field (rf) amplitude of 50 kHz) and π/9 were used to ensure that fully quantitative spectra were obtained (85). The spin-lattice relaxation time ($T_1$) was measured via a saturation recovery pulse sequence. A recycle delay of 20 seconds was determined to be sufficiently long to allow for complete longitudinal relaxation, this corresponds to a delay longer than 5x $T_1$. The saturation recovery data were fitted using $I(t) = I(0)\ (1-\exp(-t/T_1))$ where t is the varying time between pulses. Pulses were optimised for the trihedral boron site, an π/18

pulse corresponds to a pulse length of 0.22 μs; a 10-degree pulse on the trihedral site and a less than 10-degree pulse on the tetrahedral boron site. A radiofrequency field (rf) amplitude of 50 kHz as measured on the reference $NaBH_4$ was used on all three glasses. A MAS rate of 8 kHz was used for CaZn and MW glass, 10 kHz was used for ISG. $^{11}B$ shifts were referenced externally to the field-independent $NaBH_4$ signal at -41.4 ppm that corresponds to the primary reference $BF_3.Et_2O$ resonating at 0.0 ppm.

$^{27}Al$ (I = 5/2, ν0 = 104.26 MHz) MAS NMR spectra were acquired using one pulse sequence with a π/2 flip angle. A radiofrequency field amplitude of 56 kHz as measured on the reference, 0.1 M $Al(NO_3)_3$, was used for all three glass compositions. A recycle delay of 2 seconds was found to be sufficiently long to allow for complete longitudinal relaxation this corresponds to a delay longer than 5x $T_1$ where $T_1$ is the spin-lattice relaxation time measured via a saturation recovery pulse sequence. A MAS rate of 10 kHz was used for the MW and ISG glasses, a MAS rate of 8 kHz was used for CaZn glass. $^{27}Al$ shifts were referenced externally to the field-independent 0.1 M $Al(NO_3)_3$ in $H_2O$ resonating at 0.0 ppm. 2D $^{27}Al$ Multi-Quantum MAS (MQMAS) (86) spectra were recorded on all samples to conclusively determine the number of aluminium sites in the glass network. The 2D Triple quantum MQMAS experiments (86), carried out with a z-filter pulse sequence, (87) were recorded to determine the number of aluminium sites in the glass network. An rf amplitude of 56 kHz was used for the excitation and reconversion pulses and an rf amplitude of 3 kHz was used for the soft selective pulse. Pulse durations were then optimised for each composition with 64 t1 increments of 16.7 μs collected with a recycle delay of 1.5 s.

### 6.2.7. X-Ray and Neutron Pair Distribution Function Analysis

Due to the amorphous nature of glass high quality PDF data is needed to gain useful information. While X-ray PDFs can be produced using a laboratory X-ray diffractometer, the

high Q max values needed to extract meaningful data can only be obtained using high energy X-rays such as those generated by synchrotron sources.

The X-ray scattering measurements were performed at ambient temperature at the i15 beamline at Diamond Light Source (Didcot, UK) using high energy synchrotron X-rays with a photon energy of 76.69 keV (wavelength λ = 0.161669 Å). Small quantities of unirradiated and irradiated glass powder was loaded into a 1.1 mm polyamide tube with a wall thickness of 0.05 mm and the ends of the tube were sealed with a small quantity of cyanoacrylate adhesive. The sealed polyamide tubing was placed on the end of a glass capillary and samples were mounted so that the glass capillary was not in the X-ray beam. Measurements were carried out at 10 minute intervals using a Perkin Elmer XRD 1611 CP3 area detector, with a hold time of 2 minutes used between measurements to prevent detector shadows. Data was collected from an empty tube to act as a background, and sample measurements were carried out with sample spinning used and the sample position shifted slightly for each measurement to reduce damage caused by high energy X-ray radiation.

Due to the different scattering power of neutrons, neutron measurements require a greater quantity of material to collect meaningful data, additionally naturally occurring $^{10}B$ has a large neutron cross section that would prevent the collection of meaningful data. In order to overcome this glass was prepared using $^{11}B$ enriched boric acid for use in the neutron measurements. It was only possible to produce limited quantities of $^{11}B$ enriched glass, this glass was not irradiated to ensure sufficient glass was available to carry out high quality neutron measurements.

Neutron scattering measurements were carried out at ambient temperature using the GEM beamline of the ISIS pulsed neutron source (Didcot, UK). Samples of glass were placed in a 10.3 mm vanadium can. The packing height and weight of the sample were recorded and

used to calculate the packing fraction for use in sample corrections. A rod of vanadium-niobium null alloy and an empty sample can were also measured to enable calculation and subtraction of the sample background.

In both the X-ray and neutron data sets and the appropriate version of Gudrun was used to merge different data collection runs and remove the background. Two variants of Gudrun are available GudrunX for the analysis of X-ray data and GudrunN for the analysis of neutron data (88). GudrunX was used to produce the X-ray S(Q) which was fourier transformed to give the X-ray T(r) using software written in house at University of Kent (92).

The correction and processing of the neutron data was more involved than the X-ray data this is in part due to the detector bank design used in GEM that results in separate data sets that must be merged to give the i(Q) this was carried out using the ATLAS suite of programs to analyse and normalise the data using the technique described by Alderman *et al.* (90,91).

Using the technique described in Alderman *et al.* each individual glass neutron T(r) data sets used here was analysed as follows (90,91). GudrunN was used to subtract the background and merge the data collected from each detector bank. The PLATOM command in ATLAS was used in combination with XSECT to calculate self-scattering. The self-scattering was then subtracted from each data bank and banks 5,4,3 and 2 were merged using the commands INTERFER and MERGE with the aid of corrections calculated using an excel workbook provided by A. Hannon (GEM beamline officer) (163). This produces a single merged set of i(Q) data. In this case the i(Q) covered the range 0.5 to 60 $Å^{-1}$; to fill the data sets to 0 the LOWQ command was run with the ranges of ~0.55-0.75 $Å^{-1}$. The resulting data sets were fourier transformed using the i2t command and Lorch function to Qmax= 60 $Å^{-1}$ to produce the D(r). The region between ~0.5-1.75 Å in the D(r) was fitted for each data

set using PNFIT to enable calculation of $D_{exp}(r)$ (experimental differential correlation function) from the slope of this region as detailed in Alderman *et.al.* (164). The $T_0r$ was calculated using XSECT from the sample density obtained though He pycnometry. The $T_0r$ was used in combination with the $D_{exp}(r)$ to calculate the renormalising factor as follows - $T_0r/ D_{exp}(r)$. This was applied to the full range of i(Q) which was fourier transformed using both a step and Lorch function to produce the fully corrected neutron T(r).

In all glasses the first three peaks of neutron T(r) produced from the i(Q) were fitted using QpenGenie (91). In order to fit the latter peaks the neutron i(Q) was converted to S(Q) using equation 14 (shown in section 6.1.7.2.) then fourier transformed using software written in house at University of Kent to enable simultaneous fitting of both the neutron and X-ray data using NXfit (92). This conversion of i(Q) to S(Q) and the $T_0r$ calculation both have a strong dependency on sample composition. Due to the limited quantity of $^{11}B$ glass available detailed information sample composition was not known during the early stages of analysing the neutron data this introduced a slight nonlinear portion in the early (pre B-O) peak region of the neutron data, this was disregarded during data fitting.

# 7. References


1. Harrison MT. Current Challenges in the Vitrification of Nuclear Wastes in the UK. In: Vitrogeowastes Vitrification and Geopolymerization of Wastes for Immobilization or Recycling. Congress Center 'Ciutat d'Elx' · C/ Filet de Fora, 1, 03203 Elche, Alicante; 2017. p. 33–76.

2. Harrison MT. Vitrification of High Level Waste in the UK. Procedia Mater Sci. 2014 Jan 1;7:10–5.

3. Kaspar TC, Ryan JV, Pantano CG, Rice J, Trivelpiece C, Hyatt NC, et al. Physical and Optical Properties of the International Simple Glass. Npj Mater Degrad. 2019 Apr 3;3(1):15.

4. 2019 UK Radioactive Waste Inventory [Internet]. Nuclear Decommissioning Authority; 2019 Dec [cited 2021 Apr 23] p. 70. Available from: https://ukinventory.nda.gov.uk/wp-content/uploads/2020/01/2019-Waste-Report-Final.pdf

5. Basic Principles of Radioactive Waste Management [Internet]. Office for Nuclear Regulation, the Environment Agency, the Scottish Environment Protection Agency and Natural Resources Wales.; 2015 [cited 2019 Oct 24]. Available from: http://www.onr.org.uk/wastemanage/basic-principles.pdf

6. Dunnet B. Review of the Development of UK High Level Waste Vitrified Product. Nexia Solutions; 2007.

7. Harrison MT. The Effect of Composition on Short- and Long-term Durability of UK HLW Glass. Procedia Mater Sci. 2014;7:186–92.

8. Shelby JE. Introduction to Glass Science and Technology. 2nd ed. Cambridge: The Royal Society of Chemistry; 2005.

9. Frankberg EJ, Kalikka J, García Ferré F, Joly-Pottuz L, Salminen T, Hintikka J, et al. Highly Ductile Amorphous Oxide at Room Temperature and High Strain Rate. Science. 2019 Nov 15;366(6467):864.

10. Zachariasen WH. The Atomic Arrangement in Glass. J Am Chem Soc. 1932 Oct 1;54(10):3841–51.

11. Greaves GN, Sen S. Inorganic Glasses, Glass-forming Liquids and Amorphizing Solids. Adv Phys. 2007 Jan 1;56(1):1–166.

12. Doweidar H. Consideration of the Boron Oxide Anomaly. J Mater Sci. 1990 Jan 1;25(1):253–8.

13. Cormier L, Ghaleb D, Delaye JM, Calas G. Competition for Charge Compensation in Borosilicate Glasses: Wide-angle X-ray Scattering and Molecular Dynamics Calculations. Phys Rev B. 2000 Jun;61(21):14495–9.

14. Shelby JE. Thermal Expansion of Alkali Borate Glasses. J Am Ceram Soc. 1983;66(3):225–7.

15. Yiannopoulos YD, Chryssikos GD, Kamitsos EI. Structure and Properties of Alkaline Earth Borate Glasses. Phys Chem Glas. 2001;42(3):164–72.

16. Stoch P, Stoch A. Structure and Properties of Cs Containing Borosilicate Glasses Studied by Molecular Dynamics Simulations. J Non-Cryst Solids. 2015 Mar 1;411:106–14.

17. Vaishnav S, Hannon AC, Barney ER, Bingham PA. Neutron Diffraction and Raman Studies of the Incorporation of Sulfate in Silicate Glasses. J Phys Chem C. 2020 Mar 5;124(9):5409–24.

18. Hannon AC, Vaishnav S, Alderman OLG, Bingham PA. The Structure of Sodium Silicate Glass from Neutron Diffraction and Modeling of Oxygen-Oxygen Correlations. J Am Ceram Soc. 2021 Jun 30;104(12):6155–71.

19. Isard JO. The Mixed Alkali Effect in Glass. J Non-Cryst Solids. 1969;1(3):235–61.

20. Sivaraman G, Csanyi G, Vazquez-Mayagoitia A, Foster IT, Wilke SK, Weber R, et al. A Combined Machine Learning and High-Energy X-ray Diffraction Approach to Understanding Liquid and Amorphous Metal Oxides. J Phys Soc Jpn. 2022 Sep 15;91(9):091009.

21. Lu X, Ren M, Deng L, Benmore CJ, Du J. Structural Features of ISG Borosilicate Nuclear Waste Glasses Revealed from High-Energy X-ray Diffraction and Molecular Dynamics Simulations. J Nucl Mater. 2019;515:284–93.

22. Bouty O, Cammelli S, Solari PL. Structural Insights for the International Simple Glass by Combining X-ray Absorption Spectroscopic Analysis and Atomistic Modelling. J Non-Cryst Solids. 2018 Nov 1;499:434–40.

23. Jan A, Delaye JM, Gin S, Kerisit S. Monte Carlo Simulation of the Corrosion of Irradiated Simplified Nuclear Waste Glasses. J Non-Cryst Solids. 2019 Sep 1;519:119449.

24. Chroneos A, Rushton MJD, Jiang C, Tsoukalas LH. Nuclear Wasteform Materials: Atomistic Simulation Case Studies. J Nucl Mater. 2013;441(1):29–39.

25. Jan A, Anoop Krishnan NM. Diminished Diffusion in the Aged Hydrated Gels of Irradiated Borosilicate Glasses. J Phys Chem C. 2022 Sep 8;126(35):15037–45.

26. Weber WJ. Radiation and Thermal Ageing of Nuclear Waste Glass. Procedia Mater Sci. 2014;7:237–46.

27. Malkovsky VI, Yudintsev SV, Ojovan MI, Petrov VA. The Influence of Radiation on Confinement Properties of Nuclear Waste Glasses. Juoi JM, editor. Sci Technol Nucl Install. 2020 Aug 1;2020:8875723.

28. Boizot B, Ollier N, Olivier F, Petite G, Ghaleb D, Malchukova E. Irradiation Effects in Simplified Nuclear Waste Glasses. Accel Appl Res Technol. 2005 Oct 1;240(1):146–51.

29. Weber WJ. Radiation Effects In Nuclear Waste Glasses. Nucl Instrum Methods Phys Res. 1988;B32:471–9.

30. The Ionising Radiations Regulations 2017 [Internet]. 2017. Available from: https://www.legislation.gov.uk/uksi/2017/1075/contents/made

31. Tilley RJ. Defects in Solids. John Wiley & Sons; 2008.

32. Ehrt D, Ebeling P. Radiation Defects in Borosilicate Glasses. Glass Technol. 2003;44(2):46–9.

33. Griscom DL, Merzbacher CI, Weeks RA, Zuhr RA. Electron Spin Resonance Studies of Defect Centers Induced in a High-Level Nuclear Waste Glass Simulant by Gamma-Irradiation and Ion-Implantation. J Non-Cryst Solids. 1999;258(1):34–47.

34. Ollier N, Rizza G, Boizot B, Petite G. Effects of Temperature and Flux on Oxygen Bubble Formation in Li Borosilicate Glass under Electron Beam Irradiation. J Appl Phys. 2006;99(7):073511.

35. Ehrt D, Vogel W. Radiation Effects in Glasses. Nucl Instrum Methods Phys Res Sect B Beam Interact Mater At. 1992 Mar 1;65(1):IN1-8.

36. Rautiyal P, Gupta G, Edge R, Leay L, Daubney A, Patel MK, et al. Gamma Irradiation-Induced Defects in Borosilicate Glasses for High-Level Radioactive Waste Immobilisation. J Nucl Mater. 2021 Feb 1;544:152702.

37. Griscom DL. E.S.R. Studies of Radiation Damage and Structure in Oxide Glasses not Containing Transition Group Ions: A Contemporary Overview with Illustrations from the Alkali Borate System. J Non-Cryst Solids. 1974 Jan 1;13(2):251–85.

38. Griscom DL. Electron Spin Resonance Studies of Trapped Hole Centers in Irradiated Alkali Silicate Glasses: A Critical Comment on Current Models for HC1 and HC2. J Non-Cryst Solids. 1984 Apr 1;64(1):229–47.

39. Griscom DL. ESR and Optical Studies of Alkali-Associated Trapped-Electron Centres in Alkali Borate Glasses Irradiated at 77 K. J Non-Cryst Solids. 1971 Nov 1;6(4):275–82.

40. Radioactive Wastes in the UK:A Summary of the 2016 Inventory [Internet]. NDA; [cited 2019 Nov 20]. Available from: https://ukinventory.nda.gov.uk/wp-content/uploads/sites/18/2017/03/High-Level-Summary-UK-Radwaste-Inventory-2016.pdf

41. Leay L, Harrison MT. Bubble Formation in Nuclear Glasses: A Review. J Mater Res. 2019;34(6):905–20.

42. Mougnaud S, Tribet M, Renault JP, Gin S, Peuget S, Podor R, et al. Heavy ion radiation ageing impact on long-term glass alteration behavior. J Nucl Mater. 2018 Nov 1;510:168–77.

43. McGann OJ, Bingham PA, Hand RJ, Gandy AS, Kavcic M, Zitnik M, et al. The Effects of Gamma-Radiation on Model Vitreous Wasteforms Intended for the Disposal of Intermediate and High Level Radioactive Wastes in the United Kingdom. J Nucl Mater. 2012;429:353–67.

44. Abdelouas A, Ferrand K, Grambow B, Mennecart T, Fattahi M, Blondiaux G, et al. Effect of Gamma and Alpha Irradiation on the Corrosion of the French Borosilicate Glass SON 68. MRS Online Proc Libr. 2003 Dec 1;807(1):397–402.

45. Wang TT, Zhang XY, Sun ML, Du X, Guan M, Peng HB, et al. γ-Irradiation Effects in Borosilicate Glass Studied by EPR and UV–Vis Spectroscopies. Nucl Instrum Methods Phys Res Sect B Beam Interact Mater At. 2020 Feb 1;464:106–10.

46. Boizot B, Petite G, Ghaleb D, Calas G. Radiation Induced Paramagnetic Centres in Nuclear Glasses by EPR Spectroscopy. Nucl Instrum Methods Phys Res Sect B Beam Interact Mater At. 1998 May 1;141(1):580–4.

47. Gac AL, Boizot B, Jégou C, Peuget S. Aluminosilicate Glasses Structure Under Electron Irradiation: An EPR Study. Nucl Instrum Methods Phys Res Sect B Beam Interact Mater At. 2017 Sep 15;407:203–9.

48. Braithwaite RSW, Flowers WT, Haszeldine RN, Russell M. The Cause of the Colour of Blue John and other Purple Fluorites. Mineral Mag. 2018/07/05 ed. 1973;39(304):401–11.

49. Lean C. Regulating a Geological Disposal Facility to Protect the Environment [Internet]. Creating a Better Place. 2021 [cited 2022 Apr 14]. Available from: https://environmentagency.blog.gov.uk/2021/12/01/regulating-a-geological-disposal-facility-to-protect-the-environment/

50. Geological Disposal Facilities for Radioactive Waste [Internet]. Vienna: International Atomic Energy Agency; 2011. (Specific Safety Guides). Available from: https://www.iaea.org/publications/8535/geological-disposal-facilities-for-radioactive-waste

51. Trauth KM, Hora SC, Guzowski RV. Expert Judgment on Markers to Deter Inadvertent Human Intrusion into the Waste Isolation Pilot Plant. Sandia National Laboratories Albuquerque; 1993.

52. Gin S, Ribet I, Couillard M. Role and Properties of the Gel Formed During Nuclear Glass Alteration: Importance of Gel Formation Conditions. J Nucl Mater. 2001;298(1):1–10.

53. Tribet M, Mir AH, Gillet C, Jegou C, Mougnaud S, Hinks JonathanA, et al. New Insights about the Importance of the Alteration Layer/Glass Interface. J Phys Chem C. 2020 May 7;124(18):10032–44.

54. Gin S, Guittonneau C, Godon N, Neff D, Rebiscoul D, Cabié M, et al. Nuclear Glass Durability: New Insight into Alteration Layer Properties. J Phys Chem C. 2011 Sep 29;115(38):18696–706.

55. Frankel GS, Vienna JD, Lian J, Scully JR, Gin S, Ryan JV, et al. A Comparative Review of the Aqueous Corrosion of Glasses, Crystalline Ceramics, and Metals. Npj Mater Degrad. 2018;15.

56. Vienna JD, Ryan JV, Gin S, Inagaki Y. Current Understanding and Remaining Challenges in Modeling Long-Term Degradation of Borosilicate Nuclear Waste Glasses. Int J Appl Glass Sci. 2013;4(4):283–94.

57. Dillmann P, Gin S, Neff D, Gentaz L, Rebiscoul D. Effect of Natural and Synthetic Iron Corrosion Products on Silicate Glass Alteration Processes. Geochim Cosmochim Acta. 2016;172:287–305.

58. Bart G, Zwicky HU, Aerne ET, Graber T, Z'berg D, Tokiwai M. Borosilicate Glass Corrosion in the Presence of Steel Corrosion Products. MRS Proc. 1986;84:459.

59. Buckwalter CQ, Pederson LR. Inhibition of Nuclear Waste Glass Leaching by Chemisorption. J Am Ceram Soc. 1982 Sep 1;65(9):431–6.

60. Guo X, Gin S, Lei P, Yao T, Liu H, Schreiber DK, et al. Self-Accelerated Corrosion of Nuclear Waste Forms at Material Interfaces. Nat Mater. 2020 Jan 27;19:310–6.

61. ASTM C1285-14, Standard Test Methods for Determining Chemical Durability of Nuclear, Hazardous, and Mixed Waste Glasses and Multiphase Glass Ceramics: The Product Consistency Test (PCT), ASTM International, West Conshohocken, PA, 2014, www.astm.org [Internet]. West Conshohocken, PA: ASTM International; 2014. Report No.: ASTM C1285-14. Available from: https://www.astm.org/Standards/C1285-14.htm

62. ASTM C1220-17, Standard Test Method for Static Leaching of Monolithic Waste Forms for Disposal of Radioactive Waste [Internet]. Conshohocken, PA: ASTM International; 2017. Report No.: ASTM C1220-17. Available from: https://www.astm.org/Standards/C1220.htm

63. Burger E, Rebiscoul D, Bruguier F, Jublot M, Lartigue JE, Gin S. Impact of Iron on Nuclear Glass Alteration in Geological Repository Conditions: A Multiscale Approach. Appl Geochem. 2013;31:159–70.

64. McVay GL, Buckwalter CQ. Effect of Iron on Waste-Glass Leaching. J Am Ceram Soc. 1983;66(3):170–4.

65. Guo X, Gin S, Liu H, Ngo D, Luo J, Kim SH, et al. Near-Field Corrosion Interactions Between Glass and Corrosion Resistant Alloys. Npj Mater Degrad. 2020 Apr 3;4(1):10.

66. Dayal RK. 4 - Crevice Corrosion of Stainless Steel. In: Khatak HS, Raj B, editors. Corrosion of Austenitic Stainless Steels [Internet]. Woodhead Publishing; 2002. p. 106–16. Available from: https://www.sciencedirect.com/science/article/pii/B978185573613950010X

67. Laycock NJ, Stewart J, Newman RC. The Initiation of Crevice Corrosion in Stainless Steels. Corros Sci. 1997 Oct 1;39(10):1791–809.

68. Bengtsson M. Investigation of Galvanic Corrosion between Graphite Gaskets and Stainless Steel Flanges. [Sweden]: Uppsala Universitet; 2015.

69. Buss S, Herbert A, Rivett M, Rukin N. Perspectives on Protection of Deep Groundwater. UK: Environment Agency; 2020 Oct p. 75. Report No.: SC180015.

70. Qiu J, Wu A, Li Y, Xu Y, Scarlat R, Macdonald DD. Galvanic Corrosion of Type 316L Stainless Steel and Graphite in Molten Fluoride Salt. Corros Sci. 2020 Jul 1;170:108677.

71. Tucker WC, Brown R, Russell L. Corrosion Between a Graphite/Polymer Composite and Metals. J Compos Mater. 1990;24(1):92–102.

72. Aylor DM, Murray JN. The Effect of a Seawater Environment on the Galvanic Corrosion Behavior of Graphite/Epoxy Composites Coupled to Metals. Bethesda MD: Naval Suface Warfare Center Carderock Div; 1992.

73. Liu Q, Sun H, Yin H, Guo L, Qiu J, Lin J, et al. Corrosion Behaviour of 316H Stainless Steel in Molten FLiNaK Eutectic Salt Containing Graphite Particles. Corros Sci. 2019 Nov 1;160:108174.

74. ASTM G48-11(2020)e1, Standard Test Methods for Pitting and Crevice Corrosion Resistance of Stainless Steels and Related Alloys by Use of Ferric Chloride Solution [Internet]. West Conshohocken: ASTM international; 2020. Report No.: ASTM G48-11(2020)e1. Available from: www.astm.org/Standards/G48.htm

75. Gin S, Abdelouas A, Criscenti LJ, Ebert WL, Ferrand K, Geisler T, et al. An International Initiative on Long-Term Behavior of High-Level Nuclear Waste Glass. Mater Today. 2013;16(6).

76. Curti E, Crovisier JL, Morvan G, Karpoff AM. Long-Term Corrosion of Two Nuclear Waste Reference Glasses (MW and SON68): A Kinetic and Mineral Alteration Study. Appl Geochem. 2006 Jul 1;21(7):1152–68.

77. Fisher AJ, Harrison MT, Hyatt NC, Hand RJ, Corkhill CL. The Dissolution of Simulant UK Ca/Zn-Modified Nuclear Waste Glass: Insight into Stage III Behavior. MRS Adv. 2020 Jan 1;5(3):103–9.

78. Corkhill CL, Cassingham NJ, Heath PaulG, Hyatt NC. Dissolution of UK High-Level Waste Glass Under Simulated Hyperalkaline Conditions of a Colocated Geological Disposal Facility. Int J Appl Glass Sci. 2013 Dec 1;4(4):341–56.

79. Peuget S, Tribet M, Mougnaud S, Miro S, Jégou C. Radiations Effects in ISG Glass: from Structural Changes to Long-Term Aqueous Behavior. Npj Mater Degrad. 2018 Aug 20;2(1):23.

80. Backhouse DJ, Fisher AJ, Neeway JJ, Corkhill CL, Hyatt NC, Hand RJ. Corrosion of the International Simple Glass Under Acidic to Hyperalkaline Conditions. Npj Mater Degrad. 2018 Sep 10;2(1):29.

81. Magrabi C, Smith W, Larkin M. Development Of The Glass Formulation For The Windscale Vitrification Plant. UK Nucl Fuel Waste Manag Program. 1987;9(1–3):85–106.

82. Short R. Phase Separation and Crystallisation in UK HLW Vitrified Products. Procedia Mater Sci. 2014;7:93–100.

83. Bouty O, Delaye JM, Beuneu B, Charpentier T. Modelling Borosilicate Glasses of Nuclear Interest with the help of RMC, WAXS, Neutron Diffraction and 11B NMR. J Non-Cryst Solids. 2014;401:27–31.

84. Lacaillerie JB d'Espinose de, Fretigny C, Massiot D. MAS NMR Spectra of Quadrupolar Nuclei in Disordered Solids: The Czjzek Model. J Magn Reson. 2008;192(2):244–51.

85. Smith ME, van Eck ERH. Recent Advances in Experimental Solid State NMR Methodology for Half-Integer Spin Quadrupolar Nuclei. Prog Nucl Magn Reson Spectrosc. 1999 Mar 19;34(2):159–201.

86. Medek A, Harwood JS, Frydman L. Multiple-Quantum Magic-Angle Spinning NMR: A New Method for the Study of Quadrupolar Nuclei in Solids. J Am Chem Soc. 1995 Dec 1;117(51):12779–87.

87. Amoureux JP, Fernandez C, Frydman L. Optimized Multiple-Quantum Magic-Angle Spinning NMR Experiments on Half-Integer Quadrupoles. Chem Phys Lett. 1996 Sep 6;259(3):347–55.

88. Soper AK. GudrunN and GudrunX: Programs for Correcting Raw Neutron and X-ray Diffraction Data to Differential Scattering Cross Section. Science & Technology Facilities Council Swindon, UK; 2011.

89. Affatigato M, editor. Modern Glass Characterization. New Jersey: John Wiley & Sons, Inc; 2015.

90. Alderman OLG, Hannon AC, Holland D, Feller S, Lehr G, Vitale AJ, et al. Lone-Pair Distribution and Plumbite Network Formation in High Lead Silicate Glass, 80PbO·20SiO2. Phys Chem Chem Phys. 2013;15(22):8506–19.

91. Hannon A, Howells W, Soper A. ATLAS: A Suite of Programs for the Analysis of Time-Of-Flight Neutron Diffraction Data from Liquid and Amorphous Samples. In: Inst Phys Conf Ser. 1990. p. 193–211.

92. Pickup DM, Moss RM, Newport RJ. NXFit: a Program for Simultaneously Fitting X-ray and Neutron Diffraction Pair-Distribution Functions to Provide Optimized Structural Parameters. J Appl Crystallogr. 2014;47:1790–6.

93. Long DA. Raman Spectroscopy. N Y. 1977;1.

94. Bonfils J de, Peuget S, Panczer G, Ligny D de, Henry S, Noël PY, et al. Effect of Chemical Composition on Borosilicate Glass Behavior Under Irradiation. J Non-Cryst Solids. 2010;356(6):388–93.

95. Neuville DR, Cormier L, Massiot D. Al Coordination and Speciation in Calcium Aluminosilicate Glasses: Effects of Composition Determined by 27Al MQ-MAS NMR and Raman Spectroscopy. Phys Chem Rheol Silic Melts Glas. 2006 May 16;229(1):173–85.

96. Parkinson B, Holland D, Smith ME, Howes A, Scales C. The Effect of Oxide Additions on Medium-Range Order Structures in Borosilicate Glasses. J Phys Condens Matter. 2007;19(41):415114.

97. Du LS, Stebbins JF. Site Connectivities in Sodium Aluminoborate Glasses: Multinuclear and Multiple Quantum NMR Results. Solid State Nucl Magn Reson. 2005;27(1–2):37–49.

98. Pedesseau L, Ispas S, Kob W. First-Principles Study of a Sodium Borosilicate Glass-Former. II. The Glass State. Phys Rev B. 2015 Apr;91(13):134202.

99. Cassingham NJ, Stennett MC, Bingham Paul A, Hyatt NC, Aquilanti G. The Structural Role of Zn in Nuclear Waste Glasses. Int J Appl Glass Sci. 2011 Dec 1;2(4):343–53.

100. Fábián M, Sváb E, Proffen Th, Veress E. Structure Study of Multi-Component Borosilicate Glasses from High-Q Neutron Diffraction Measurement and RMC Modeling. J Non-Cryst Solids. 2008 Jun 15;354(28):3299–307.

101. Du LS, Stebbins JF. Site Preference and Si/B Mixing in Mixed-Alkali Borosilicate Glasses: A High-Resolution 11B and 17O NMR Study. Chem Mater. 2003 Oct 1;15(20):3913–21.

102. Swenson J, Börjesson L, Howells WS. Structure of Borate Glasses from Neutron-Diffraction Experiments. Phys Rev B. 1995 Oct;52(13):9310–9.

103. McKeown DA, Waychunas GA, Brown GE. EXAFS Study of the Coordination Environment of Aluminum in a Series of Silica-Rich Glasses and Selected Minerals within the Na2O-Al2O3-SiO2 System. J Non-Cryst Solids. 1985 Nov 1;74(2):349–71.

104. Hashimoto H, Onodera Y, Tahara S, Kohara S, Yazawa K, Segawa H, et al. Structure of Alumina Glass. Sci Rep. 2022 Jan 11;12(1):516.

105. Bray PJ. NMR and NQR Studies of Boron in Vitreous and Crystalline Borates. Inorganica Chim Acta. 1999 Jun 15;289(1):158–73.

106. Krishnamurthy A, Michaelis VK, Kroeker S. Network Formation in Borosilicate Glasses with Aluminum or Gallium: Implications for Nepheline Crystallization. J Phys Chem C. 2021 Apr 29;125(16):8815–24.

107. Bancroft GM, Nesbitt HW, Henderson GS, O'Shaughnessy C, Withers AC, Neuville DR. Lorentzian Dominated Lineshapes and Linewidths for Raman Symmetric Stretch Peaks (800–1200 cm−1) in Qn (n = 1–3) Species of Alkali Silicate Glasses/Melts. J Non-Cryst Solids. 2018;484:72–83.

108. Wronkiewicz DJ. Effects of Radionuclide Decay on Waste Glass Behavior: A Critical Review [Internet]. United States: Argonne National Lab.; 1993 Dec p. 64. Report No.: ANL-93/45. Available from: http://inis.iaea.org/search/search.aspx?orig_q=RN:25070346

109. Mir AH, peuget S. Using External Ion Irradiations for Simulating Self-Irradiation Damage in Nuclear Waste Glasses: State of the Art, Recommendations and, Prospects. J Nucl Mater. 2020 Oct 1;539:152246.

110. Delaye JM, Peuget S, Bureau G, Calas G. Molecular Dynamics Simulation of Radiation Damage in Glasses. J Non-Cryst Solids. 2011;357:2763–8.

111. Brown NA, Black AG, Hannon AC, Blanc F, Mountjoy G, Patel M, et al. New Insights Into MW, CaZn, and ISG Glass Structure from X-Ray and Neutron Scattering Combined with MAS-NMR. Unpublished.

112. Charpentier T, Martel L, Mir AH, Somers J, Jégou C, Peuget S. Self-Healing Capacity of Nuclear Glass Observed by NMR Spectroscopy. Sci Rep. 2016 May 5;6(1):25499.

113. Juniewicz M, Marciniak A, Ciesielski B, Prawdzik-Dampc A, Sawczak M, Boguś P. The Effect of Sunlight and UV Lamp Exposure on EPR Signals in X-ray Irradiated Touch Screens of Mobile Phones. Radiat Environ Biophys. 2020 Aug;59(3):539–52.

114. Skuja L, Hirano M, Hosono H, Kajihara K. Defects in Oxide Glasses. Phys Status Solidi C. 2005;2(1):15–24.

115. Olivier FY, Boizot B, Ghaleb D, Petite G. Raman and EPR Studies of β-Irradiated Oxide Glasses: The Effect of Iron Concentration. Proc Int Conf Non-Cryst Mater CONCIM. 2005 May 1;351(12):1061–6.

116. Ojovan MI, Lee WE. Alkali Ion Exchange in γ-Irradiated Glasses. J Nucl Mater. 2004 Dec 1;335(3):425–32.

117. Pederson LR, McVay GL. Influence of Gamma Irradiation on Leaching of Simulated Nuclear Waste Glass: Temperature and Dose Rate Dependence in Deaerated Water. J Am Ceram Soc. 1983 Dec 1;66(12):863–7.

118. Denatale JF, Howitt DG. The Gamma-Irradiation of Nuclear Waste Glasses. Radiat Eff. 1985 Jan 1;91(1–2):89–96.

119. Holzwarth U, Gibson N. The Scherrer Equation versus the 'Debye-Scherrer Equation'. Nat Nanotechnol. 2011 Sep 1;6(9):534–534.

120. Assih T, Ayral A, Abenoza M, Phalippou J. Raman Study of Alumina Gels. J Mater Sci. 1988 Sep 1;23(9):3326–31.

121. Marcial J, Ahmadzadeh M, McCloy JS. Effect of Li, Fe, and B Addition on the Crystallization Behavior of Sodium Aluminosilicate Glasses as Analogues for Hanford High Level Waste Glasses. MRS Adv. 2017 Feb 1;2(10):549–55.

122. Mir A, Peuget S, Toulemonde M, Bulot P, Jegou C, Miro S, et al. Defect Recovery and Damage Reduction in Borosilicate Glasses under Double Ion Beam Irradiation. EPL Europhys Lett. 2015;112(3):36002.

123. Wendy Meulebroeck, Kitty Baert, Andrea Ceglia, Peter Cosyns, Hilde Wouters, Karin Nys, et al. The Potential of UV-VIS-NIR Absorption Spectroscopy in Glass Studies. In 2012. Available from: https://doi.org/10.1117/12.975684

124. Fayad AM, Abd-Allah WM, Moustafa FA. Effect of Gamma Irradiation on Structural and Optical Investigations of Borosilicate Glass Doped Yttrium Oxide. Silicon. 2018 May 1;10(3):799–809.

125. Patel KB, Boizot B, Facq SP, Peuget S, Schuller S, Farnan I. Impacts of Composition and Beta Irradiation on Phase Separation in Multiphase Amorphous Calcium Borosilicates. J Non-Cryst Solids. 2017 Oct 1;473:1–16.

126. Beuneu F, Florea C, Vajda P. EPR-Study of Electron-Radiation Induced Ca Colloids in CaF2 Crystals. Radiat Eff Defects Solids. 1995 Dec 1;136(1–4):175–9.

127. Griscom DL, Mizuguchi M. Determination of the Visible Range Optical Absorption Spectrum of Peroxy Radicals in Gamma-Irradiated Fused Silica. J Non-Cryst Solids. 1998 Oct 1;239(1):66–77.

128. Sun K, Wang LM, Ewing RC, Weber WJ. Electron Irradiation Induced Phase Separation in a Sodium Borosilicate Glass. Proc Twelfth Int Conf Radiat Eff Insul. 2004 Jun 1;218:368–74.

129. Aréna H, Godon N, Rébiscoul D, Podor R, Garcès E, Cabie M, et al. Impact of Zn, Mg, Ni and Co Elements on Glass Alteration: Additive Effects. J Nucl Mater. 2016;470:55–67.

130. Farid OM, Ojovan MI, Massoud A, Abdel Rahman RO. An Assessment of Initial Leaching Characteristics of Alkali-Borosilicate Glasses for Nuclear Waste Immobilization. Materials [Internet]. 2019;12(9). Available from: https://www.mdpi.com/1996-1944/12/9/1462

131. Fisher AJ, Imran MNB, Mann C, Gausse C, Hand RJ, Hyatt NC, et al. Short Communication: The Dissolution of UK Simulant Vitrified High-Level-Waste in Groundwater Solutions. J Nucl Mater. 2020 Sep 1;538:152245.

132. Zhang H, Corkhill CL, Heath PG, Hand RJ, Stennett MC, Hyatt NC. Effect of Zn- and Ca-Oxides on the Structure and Chemical Durability of Simulant Alkali Borosilicate Glasses for Immobilisation of UK High Level Wastes. J Nucl Mater. 2015 Jul 1;462:321–8.

133. Werme L, Björner IK, Bart G, Zwicky HU, Grambow B, Lutze W, et al. Chemical Corrosion of Highly Radioactive Borosilicate Nuclear Waste Glass Under Simulated Repository Conditions. J Mater Res. 2011/01/31 ed. 1990;5(5):1130–46.

134. Inagaki Y, Furuya H, Idemitsu K, Arima T. Review of Waste Glass Corrosion and Associated Radionuclide Release as a Part Of Safety Assessment of Entire Disposal System. Glob Environ Nucl Energy Syst-2. 1998 Jan 1;32(3):501–8.

135. Shelby JE. Effect of Radiation on the Physical Properties of Borosilicate Glasses. J Appl Phys. 1980 May 1;51(5):2561–5.

136. Brown NA. Gamma Irradiation-Induced Structural Changes in Glass. Unpublished.

137. Yang H, Li C, Wei C, Li M, Li X, Deng Z, et al. Molybdenum Blue Photometry Method for the Determination of Colloidal Silica and Soluble Silica in Leaching Solution. Anal Methods. 2015;7(13):5462–7.

138. Abraitis PK. Dissolution of a Simulated Magnox Waste Glass in Aqueous Solutions at Temperatures Below 100 Degrees C. University of Manchester; 1999.

139. Bourcier WL. Critical Review of Glass Performance Modeling [Internet]. United States: Argonne National Lab., IL; 1994 Jul. Report No.: ANL-94/17. Available from: https://www.osti.gov/biblio/10178711

140. Cassingham NJ, Corkhill CL, Stennett MC, Hand RJ, Hyatt NC. Alteration Layer Formation of Ca- and Zn-Oxide Bearing Alkali Borosilicate Glasses for Immobilisation of UK High Level Waste: A Vapour Hydration Study. J Nucl Mater. 2016 Oct 1;479:639–46.

141. Ojovan MI. On Alteration Rate Renewal Stage of Nuclear Waste Glass Corrosion. MRS Adv. 2020 Jan 1;5(3):111–20.

142. Bunker BC, Arnold GW, Day DE, Bray PJ. The Effect of Molecular Structure on Borosilicate Glass Leaching. J Non-Cryst Solids. 1986 Oct 2;87(1):226–53.

143. Deshpande VK, Raut AP. Effect of Gamma Irradiation on the Density, Glass Transition Temperature and Electrical Conductivity of Lithium Borosilicate Glasses with Alumina Addition. J Non-Cryst Solids. 2017 Feb 1;457:104–10.

144. Kerisit S, Ryan JV, Pierce EM. Monte Carlo Simulations of the Corrosion of Aluminoborosilicate Glasses. J Non-Cryst Solids. 2013 Oct 15;378:273–81.

145. Ledieu A, Devreux F, Barboux P. The Role of Aluminium in the Durability of Alumino-Borosilicate Glasses. Phys Chem Glas. 2005;46(1):12–20.

146. Rama Mohan TR, Kröger FA. Cathodic Deposition of Amorphous Silicon from Solutions of Silicic Acid and Tetraethyl Ortho-Silicate in Ethylene Glycol and Formamide Containing HF. Electrochimica Acta. 1982 Mar 1;27(3):371–7.

147. Nordlund K, Sand AE, Granberg F, Zinkle SJ, Stoller R, Averback RS, et al. Primary Radiation Damage in Materials Review of Current Understanding and Proposed New Standard Displacement Damage Model to Incorporate in Cascade Defect Production Efficiency and Mixing Effects [Internet]. NEA/NSC; 2015 p. 87. (Nuclear Science). Report No.: 9. Available from: https://www.oecd-nea.org/science/docs/2015/nsc-doc2015-9.pdf

148. Koroleva ON, Shabunina LA, Bykov VN. Structure of Borosilicate Glass According to Raman Spectroscopy Data. Glass Ceram. 2011 Mar 1;67(11):340–2.

149. Yadav AK, Singh P. A Review of the Structures of Oxide Glasses by Raman Spectroscopy. RSC Adv. 2015;5(83):67583–609.

150. Williams FE, Eyring H. The Mechanism of the Luminescence of Solids. J Chem Phys. 1947 May 1;15(5):289–304.

151. Raffaëlly L, Champagnon B. High Temperature Experiments: a way to Observe Raman Scattering in Luminescent Samples. J Raman Spectrosc. 2007 Oct 1;38(10):1242–5.

152. Eaton GR, Eaton SS, Barr DP, Weber RT. Quantitative EPR : A Practitioners Guide. Vienna: Springer International Publishing; 2010. 185 p.

153. Dussossoy JL, Dubois C, Vernaz E, Chambaudet A. Effect of Surface Finish on Nuclear Glass Dissolution Rate. MRS Online Proc Libr. 1991 Dec 1;257(1):109–15.

154. Jollivet P, Angeli F, Cailleteau C, Devreux F, Frugier P, Gin S. Investigation of Gel Porosity Clogging During Glass Leaching. J Non-Cryst Solids. 2008 Nov 15;354(45):4952–8.

155. Kroecker S. Multinuclear NMR Investigation of the Composition-Dependent Structural Role of Pb2+ in Lead Borogallate and Boroaluminate Glasses. 16th International Conference on the Physics of Non-Crystalline Solids; 2022 Jul 13; University of Kent, Canterbury, UK.

156. Nguyen HGT, Horn JC, Bleakney M, Siderius DW, Espinal L. Understanding Material Characteristics Through Signature Traits from Helium Pycnometry. Langmuir. 2019;35(6):2115–22.

157. Samoson A. Satellite Transition High-Resolution NMR of Quadrupolar Nuclei in Powders. Chem Phys Lett. 1985 Aug 23;119(1):29–32.

158. Frydman L, Grant DM, Harris RK. Fundamentals of Multiple-Quantum Magic-Angle Spinning NMR on Half-Integer Quadrupolar Nuclei. In: Encyclopedia of Nuclear Magnetic Resonance. Wiley; 2002. p. 2. (Advances in NMR; vol. 9).

159. Keen DA. A Comparison of Various Commonly Used Correlation Functions for Describing Total Scattering. J Appl Crystallogr. 2001 Apr;34(2):172–7.

160. Cormack AN. Classical Simulation Methods. In: Atomistic Simulations of Glasses [Internet]. 1st ed. Wiley; 2022 [cited 2022 Sep 13]. p. 1–29. Available from: https://doi.org/10.1002/9781118939079.ch1

161. Czjzek G, Fink J, Götz F, Schmidt H, Coey J, Rebouillat JP, et al. Atomic Coordination and the Distribution of Electric Field Gradients in Amorphous Solids. Phys Rev B. 1981;23(6):2513.

162. Massiot D, Fayon F, Capron M, King I, Le Calvé S, Alonso B, et al. Modelling One-and Two-Dimensional Solid-State NMR Spectra. Magn Reson Chem. 2002;40(1):70–6.

163. Hannon AC. INTERFERE and MERGE-Using Microsoft Excel to Choose Parameters for LAD Data.

164. Alderman OL, Hannon AC, Holland D, Umesaki N. On the Germanium–Oxygen Coordination Number in Lead Germanate Glasses. J Non-Cryst Solids. 2014;386:56–60.

# 8. Supplementary

Configuration settings used for processing and correction of Xray PDF data collected from

unirradiated glass, using Gudrun X

```
' ' '       ' '\'

INSTRUMENT      {

XPDF        Instrument name
C:\Users\Student\Xray data\processing\       Gudrun input file directory:
C:\Users\Student\Xray data\processing\       Data file directory
xye         Data file type
StartupFiles\Xray\CrossSec_XCOM.txt         X-ray cross sections file
StartupFiles\Xray\f0_WaasKirf.txt         X-ray form factor file
StartupFiles\Xray\CrossSec_Compton_Balyuzi.txt         X-ray Compton scattering file
0.5  27  0.01         Q-range [1/Å] for final DCS
10  0.01         r-max and r-step for final g(r)

}

BEAM        {

CYLINDRICAL         Sample geometry
2         Number of beam profile values
1.0  1.0          Beam profile values (Maximum of 50 allowed currently)
0.0022  0.0110  100         Step size for absorption and m.s. calculation and no. of slices
5         Step in scattering angle to calculate corrections at: [deg.]
-0.035  0.035  -0.7  0.7         Incident beam edges relative to centre of sample [cm]
-0.035  0.035  -0.7  0.7         Scattered beam edges relative to centre of sample [cm]
*         File containing bremsstrahlung intensity
0         Density of target material [gm/cm^3]
0         Effective target penetration depth [cm]
Na          K-beta filter
0         K-beta filter density [gm/cm^3]
0         K-beta filter thickness [cm]
0         Bremsstrahlung power
0         Detector cutoff [keV]
0         Cutoff width [keV]
*         Lowest scattering angle
*         Highest scattering angle
*         Scattering angle step
0.0         Angle offset [deg.]
*         Anode material:
*         Tube voltage [kV]
0.161669         Wavelength [A]:
0         Theta-theta scanning?
0         Fixed slits?
```

0.0 0.0 -1.0 Footprint length, sample thickness, and depression (all relative to sample dimension):
0.0 0.0 -1.0 Position, width and power for low angle cutoff [deg]:
* Tube current [mA]
* kAlpha1 [A]
* kAlpha2 [A]
* kBeta [A]
0.0 0.00 kAlpha2 and kBeta relative intensities:
0.0 Bremsstrahlung scattering amplitude
10 No. of bremsstrahlung iterations

}

NORMALISATION {

0.0 Azimuthal angle of detector above scattering plane:
0 Divide by <F>^2?
2 Power for Breit-Dirac factor (2 -3)
1 Krogh-Moe & Norman normalisation
0.0 Overlap factor

}

SAMPLE BACKGROUND {

2 Number of files
i15-1-30048_tth_pe2_0.xye SAMPLE BACKGROUND data files
i15-1-30039_tth_pe2_0.xye SAMPLE BACKGROUND data files
1.0 Sample background factor
1.0 Data factor
1.0 Data factor
0 Exclude scans
0 Exclude scans

}

SAMPLE B11 CaZn {

4 Number of files
i15-1-30060_tth_pe2_0.xye SAMPLE B11 CaZn data files
i15-1-30083_tth_pe2_0.xye SAMPLE B11 CaZn data files
i15-1-30083_tth_pe2_1.xye SAMPLE B11 CaZn data files
i15-1-30083_tth_pe2_2.xye SAMPLE B11 CaZn data files
1 Force calculation of sample corrections?
Si Si 0.136388967 0.0 0.0 Sample atomic composition
B B 0.117774803 0.0 0.0 Sample atomic composition
Li Li 0.014707488 0.0 0.0 Sample atomic composition
Na Na 0.044524621 0.0 0.0 Sample atomic composition
Al Al 0.05676171 0.0 0.0 Sample atomic composition
Ca Ca 0.017209484 0.0 0.0 Sample atomic composition
Zn Zn 0.015612343 0.0 0.0 Sample atomic composition

```
O  O  0.597020585   0.0  0.0         Sample atomic composition
*  0  0  0  0         * 0 0 0 0 to specify end of composition input
SameAsBeam          Geometry
0.05  0.055         Inner and outer radii (cm)
5         Sample height (cm)
2.534         Density Units:  gm/cm^3?
TABLES         Total cross section source
2         Sample tweak factor
2.6         Top hat width (1/Å) for cleaning up Fourier Transform
1.16374         Minimum radius for Fourier Transform [Å]
0.07         Width of broadening in r-space [A]
0  0         0   0         to finish specifying wavelength range of resonance
0.0  0.0  1.0         Exponential amplitude, decay [?] and stretch
 3.377930e-03         Sample calibration factor
5         No. of iterations
0.0 0.0 0.0 0.0 0.0 0.0 0.0 0.0 0.0 0.0 0.0 0.0 0.0 0.0 0.0 0.0 0.0 0.0          Fluorescence levels
1.0         Factor to modify multiple scattering (0 - 1)
-0.45         Incident beam polarization factor (-1 -> +1)
1.25         Factor for Compton scattering
0.0         Bremsstrahlung scattering amplitude
10         No. of bremsstrahlung iterations
0         Broadening power
0.0  0.00         kAlpha2 and kBeta relative intensities:
1.0         Data factor
1.0         Data factor
1.0         Data factor
1.0         Data factor
1         Analyse this sample?
0         Exclude scans
0         Exclude scans
0         Exclude scans
0         Exclude scans

}

GO

SAMPLE B11 ISG         {

6          Number of  files
i15-1-30061_tth_pe2_0.xye         SAMPLE B11 ISG data files
i15-1-30077_tth_pe2_0.xye         SAMPLE B11 ISG data files
i15-1-30077_tth_pe2_1.xye         SAMPLE B11 ISG data files
i15-1-30077_tth_pe2_2.xye         SAMPLE B11 ISG data files
i15-1-30077_tth_pe2_3.xye         SAMPLE B11 ISG data files
i15-1-30077_tth_pe2_4.xye         SAMPLE B11 ISG data files
1         Force calculation of sample corrections?
Si  Si  0.15962186   0.0  0.0         Sample atomic composition
Na  Na  0.063061916   0.0  0.0         Sample atomic composition
B  B  0.083311156   0.0  0.0         Sample atomic composition
Al  Al  0.065954665   0.0  0.0         Sample atomic composition
```

```
Ca  Ca  0.014434815   0.0  0.0         Sample atomic composition
Zr  Zr  0.008169122   0.0  0.0         Sample atomic composition
O  O  0.605446467   0.0  0.0          Sample atomic composition
*  0  0  0  0         * 0 0 0 0 to specify end of composition input
SameAsBeam          Geometry
0.05  0.055         Inner and outer radii (cm)
5         Sample height (cm)
2.4484          Density Units:  gm/cm^3?
TABLES         Total cross section source
2         Sample tweak factor
2.6         Top hat width (1/Å) for cleaning up Fourier Transform
1.16374         Minimum radius for Fourier Transform [Å]
0.07         Width of broadening in r-space [A]
0  0         0   0         to finish specifying wavelength range of resonance
0.0  0.0  1.0         Exponential amplitude, decay [?] and stretch
 3.393506e-03         Sample calibration factor
5         No. of iterations
0.0 0.0 0.0 0.0 0.0 0.0 0.0 0.0 0.0 0.0 0.0 0.0 0.0 0.0 0.0          Fluorescence levels
1.0         Factor to modify multiple scattering (0 - 1)
-0.45         Incident beam polarization factor (-1 -> +1)
1.25         Factor for Compton scattering
0.0         Bremsstrahlung scattering amplitude
10         No. of bremsstrahlung iterations
0         Broadening power
0.0  0.00         kAlpha2 and kBeta relative intensities:
1.0         Data factor
1.0         Data factor
1.0         Data factor
1.0         Data factor
1.0         Data factor
1.0         Data factor
1         Analyse this sample?
0         Exclude scans
0         Exclude scans
0         Exclude scans
0         Exclude scans
0         Exclude scans
0         Exclude scans

}

GO

SAMPLE B11 MW         {

6          Number of  files
i15-1-30059_tth_pe2_0.xye         SAMPLE B11 MW data files
i15-1-30076_tth_pe2_0.xye         SAMPLE B11 MW data files
i15-1-30076_tth_pe2_1.xye         SAMPLE B11 MW data files
i15-1-30076_tth_pe2_2.xye         SAMPLE B11 MW data files
i15-1-30076_tth_pe2_3.xye         SAMPLE B11 MW data files
```

```
i15-1-30076_tth_pe2_4.xye         SAMPLE B11 MW data files
1         Force calculation of sample corrections?
Si  Si  0.180275962   0.0  0.0         Sample atomic composition
B  B  0.108641975   0.0  0.0          Sample atomic composition
Li  Li  0.028990559   0.0  0.0         Sample atomic composition
Na  Na  0.058678286   0.0  0.0         Sample atomic composition
O  O  0.600987654   0.0  0.0          Sample atomic composition
Al  Al  0.022425563   0.0  0.0         Sample atomic composition
*  0  0  0  0         * 0 0 0 0 to specify end of composition input
SameAsBeam         Geometry
0.05  0.055         Inner and outer radii (cm)
5         Sample height (cm)
2.4208         Density Units:  gm/cm^3?
TABLES         Total cross section source
2         Sample tweak factor
2.6         Top hat width (1/Å) for cleaning up Fourier Transform
1.16374         Minimum radius for Fourier Transform [Å]
0.07         Width of broadening in r-space [A]
0  0         0   0         to finish specifying wavelength range of resonance
0.0  0.0  1.0         Exponential amplitude, decay [?] and stretch
 3.287798e-03         Sample calibration factor
5         No. of iterations
0.0 0.0 0.0 0.0 0.0 0.0 0.0 0.0 0.0 0.0 0.0 0.0 0.0          Fluorescence levels
1.0         Factor to modify multiple scattering (0 - 1)
-0.45         Incident beam polarization factor (-1 -> +1)
1.25         Factor for Compton scattering
0.0         Bremsstrahlung scattering amplitude
10         No. of bremsstrahlung iterations
0         Broadening power
0.0  0.00         kAlpha2 and kBeta relative intensities:
1.0         Data factor
1.0         Data factor
1.0         Data factor
1.0         Data factor
1.0         Data factor
1.0         Data factor
1         Analyse this sample?
0         Exclude scans
0         Exclude scans
0         Exclude scans
0         Exclude scans
0         Exclude scans
0         Exclude scans

}

GO


END
1
```

Date and time last written:  20220722 16:30:25
X
' ' '  ' '\'

Configuration settings used for processing and correction of Xray PDF data collected from

irradiated glass , using Gudrun X

INSTRUMENT  {

XPDF  Instrument name
C:\Users\Student\Xray data\processing\  Gudrun input file directory:
C:\Users\Student\Xray data\processing\  Data file directory
xye  Data file type
StartupFiles\Xray\CrossSec_XCOM.txt  X-ray cross sections file
StartupFiles\Xray\f0_WaasKirf.txt  X-ray form factor file
StartupFiles\Xray\CrossSec_Compton_Balyuzi.txt  X-ray Compton scattering file
0.5  25  0.01  Q-range [1/Å] for final DCS
25  0.02  r-max and r-step for final g(r)

}

BEAM  {

CYLINDRICAL  Sample geometry
2  Number of beam profile values
1.0  1.0  Beam profile values (Maximum of 50 allowed currently)
0.0022  0.0110  100  Step size for absorption and m.s. calculation and no. of slices
5  Step in scattering angle to calculate corrections at: [deg.]
-0.035  0.035  -0.7  0.7  Incident beam edges relative to centre of sample [cm]
-0.035  0.035  -0.7  0.7  Scattered beam edges relative to centre of sample [cm]
*  File containing bremsstrahlung intensity
0  Density of target material [gm/cm^3]
0  Effective target penetration depth [cm]
Na  K-beta filter
0  K-beta filter density [gm/cm^3]
0  K-beta filter thickness [cm]
0  Bremsstrahlung power
0  Detector cutoff [keV]
0  Cutoff width [keV]
*  Lowest scattering angle
*  Highest scattering angle
*  Scattering angle step
0.0  Angle offset [deg.]
*  Anode material:
*  Tube voltage [kV]
0.161669  Wavelength [A]:
0  Theta-theta scanning?
0  Fixed slits?

```
0.0  0.0  -1.0        Footprint length, sample thickness, and depression (all relative to sample
dimension):
0.0  0.0  -1.0        Position, width and power for low angle cutoff [deg]:
*        Tube current [mA]
*        kAlpha1 [A]
*        kAlpha2 [A]
*        kBeta [A]
0.0  0.00        kAlpha2 and kBeta relative intensities:
0.0        Bremsstrahlung scattering amplitude
10        No. of bremsstrahlung iterations

}

NORMALISATION        {

0.0        Azimuthal angle of detector above scattering plane:
0        Divide by <F>^2?
2        Power for Breit-Dirac factor (2 -3)
1        Krogh-Moe & Norman normalisation
0.0        Overlap factor

}

SAMPLE BACKGROUND        {

2        Number of  files
i15-1-30048_tth_pe2_0.xye        SAMPLE BACKGROUND data files
i15-1-30039_tth_pe2_0.xye        SAMPLE BACKGROUND data files
1.0        Sample background factor
1.0        Data factor
1.0        Data factor
0        Exclude scans
0        Exclude scans

}

SAMPLE B11 CaZn irrad        {

3        Number of  files
i15-1-30063_tth_pe2_0.xye        SAMPLE B11 CaZn irrad data files
i15-1-30084_tth_pe2_0.xye        SAMPLE B11 CaZn irrad data files
i15-1-30084_tth_pe2_1.xye        SAMPLE B11 CaZn irrad data files
1        Force calculation of sample corrections?
Si  Si  12.26466  0.0  0.0        Sample atomic composition
B  B  11.04015  0.0  0.0        Sample atomic composition
Li  Li  4.608996  0.0  0.0        Sample atomic composition
Na  Na  5.15918  0.0  0.0        Sample atomic composition
Al  Al  5.615147  0.0  0.0        Sample atomic composition
Ca  Ca  1.473448  0.0  0.0        Sample atomic composition
Zn  Zn  1.9843  0.0  0.0        Sample atomic composition
O  O  57.85411  0.0  0.0        Sample atomic composition
```

```
*  0  0  0  0        * 0 0 0 0 to specify end of composition input
SameAsBeam         Geometry
0.05  0.055        Inner and outer radii (cm)
5        Sample height (cm)
2.5340        Density Units:  gm/cm^3?
TABLES        Total cross section source
2        Sample tweak factor
2        Top hat width (1/Å) for cleaning up Fourier Transform
1.1312        Minimum radius for Fourier Transform [Å]
0.07        Width of broadening in r-space [A]
0  0        0   0        to finish specifying wavelength range of resonance
0.0  0.0  1.0        Exponential amplitude, decay [?] and stretch
 3.383487e-03        Sample calibration factor
5        No. of iterations
0.0 0.0 0.0 0.0 0.0 0.0 0.0 0.0 0.0 0.0 0.0 0.0 0.0 0.0 0.0 0.0 0.0        Fluorescence levels
1.0        Factor to modify multiple scattering (0 - 1)
-0.45        Incident beam polarization factor (-1 -> +1)
1.25        Factor for Compton scattering
0.0        Bremsstrahlung scattering amplitude
10        No. of bremsstrahlung iterations
0        Broadening power
0.0  0.00        kAlpha2 and kBeta relative intensities:
1.0        Data factor
1.0        Data factor
1.0        Data factor
1        Analyse this sample?
0        Exclude scans
0        Exclude scans
0        Exclude scans

}

GO

SAMPLE B11 ISG irrad        {

4         Number of  files
i15-1-30052_tth_pe2_0.xye        SAMPLE B11 ISG irrad data files
i15-1-30081_tth_pe2_0.xye        SAMPLE B11 ISG irrad data files
i15-1-30081_tth_pe2_1.xye        SAMPLE B11 ISG irrad data files
i15-1-30081_tth_pe2_2.xye        SAMPLE B11 ISG irrad data files
1        Force calculation of sample corrections?
Si  Si  60.201  0.0  0.0        Sample atomic composition
Na  Na  25.251  0.0  0.0        Sample atomic composition
B  B  31.979  0.0  0.0        Sample atomic composition
Al  Al  9.474  0.0  0.0        Sample atomic composition
Ca  Ca  5.692  0.0  0.0        Sample atomic composition
Zr  Zr  1.707  0.0  0.0        Sample atomic composition
O  O  204.318  0.0  0.0        Sample atomic composition
H  H  0.0  0.0  0.0        Sample atomic composition
*  0  0  0  0        * 0 0 0 0 to specify end of composition input
```

```
SameAsBeam          Geometry
0.05  0.055         Inner and outer radii (cm)
5         Sample height (cm)
2.4152          Density Units:  gm/cm^3?
TABLES          Total cross section source
2         Sample tweak factor
1.5         Top hat width (1/Å) for cleaning up Fourier Transform
1.0         Minimum radius for Fourier Transform [Å]
0.07          Width of broadening in r-space [A]
0  0         0   0         to finish specifying wavelength range of resonance
0.0  0.0  1.0         Exponential amplitude, decay [?] and stretch
 2.302785e-03          Sample calibration factor
5         No. of iterations
0.0 0.0 0.0 0.0 0.0 0.0 0.0 0.0 0.0 0.0 0.0 0.0 0.0 0.0 0.0 0.0 0.0          Fluorescence levels
1.0         Factor to modify multiple scattering (0 - 1)
-0.45         Incident beam polarization factor (-1 -> +1)
1.2         Factor for Compton scattering
0.0         Bremsstrahlung scattering amplitude
10          No. of bremsstrahlung iterations
0         Broadening power
0.0  0.00         kAlpha2 and kBeta relative intensities:
1.0         Data factor
1.0         Data factor
1.0         Data factor
1.0         Data factor
1         Analyse this sample?
0         Exclude scans
0         Exclude scans
0         Exclude scans
0         Exclude scans

}

GO

SAMPLE B11 MW irrad         {

5          Number of  files
i15-1-30062_tth_pe2_0.xye         SAMPLE B11 MW irrad data files
i15-1-30078_tth_pe2_0.xye         SAMPLE B11 MW irrad data files
i15-1-30078_tth_pe2_1.xye         SAMPLE B11 MW irrad data files
i15-1-30080_tth_pe2_0.xye         SAMPLE B11 MW irrad data files
i15-1-30080_tth_pe2_1.xye         SAMPLE B11 MW irrad data files
1         Force calculation of sample corrections?
Si  Si  16.63001  0.0  0.0          Sample atomic composition
B  B  10.66462  0.0  0.0          Sample atomic composition
Li  Li  5.893605  0.0  0.0          Sample atomic composition
Na  Na  5.711328  0.0  0.0          Sample atomic composition
O  O  58.74403  0.0  0.0          Sample atomic composition
Al  Al  2.056411  0.0  0.0          Sample atomic composition
*  0  0  0  0         * 0 0 0 0 to specify end of composition input
```

```
SameAsBeam          Geometry
0.05  0.055         Inner and outer radii (cm)
5         Sample height (cm)
2.4208          Density Units:  gm/cm^3?
TABLES          Total cross section source
2         Sample tweak factor
2         Top hat width (1/Å) for cleaning up Fourier Transform
1.1312          Minimum radius for Fourier Transform [Å]
0.07          Width of broadening in r-space [A]
0  0          0   0         to finish specifying wavelength range of resonance
0.0  0.0  1.0         Exponential amplitude, decay [?] and stretch
 3.368465e-03          Sample calibration factor
5         No. of iterations
0.0 0.0 0.0 0.0 0.0 0.0 0.0 0.0 0.0 0.0 0.0 0.0 0.0 0.0          Fluorescence levels
1.0         Factor to modify multiple scattering (0 - 1)
-0.45         Incident beam polarization factor (-1 -> +1)
1.25         Factor for Compton scattering
0.0         Bremsstrahlung scattering amplitude
10         No. of bremsstrahlung iterations
0         Broadening power
0.0  0.00         kAlpha2 and kBeta relative intensities:
1.0         Data factor
1.0         Data factor
1.0         Data factor
1.0         Data factor
1.0         Data factor
1         Analyse this sample?
0         Exclude scans
0         Exclude scans
0         Exclude scans
0         Exclude scans
0         Exclude scans

}

GO


END
1
```

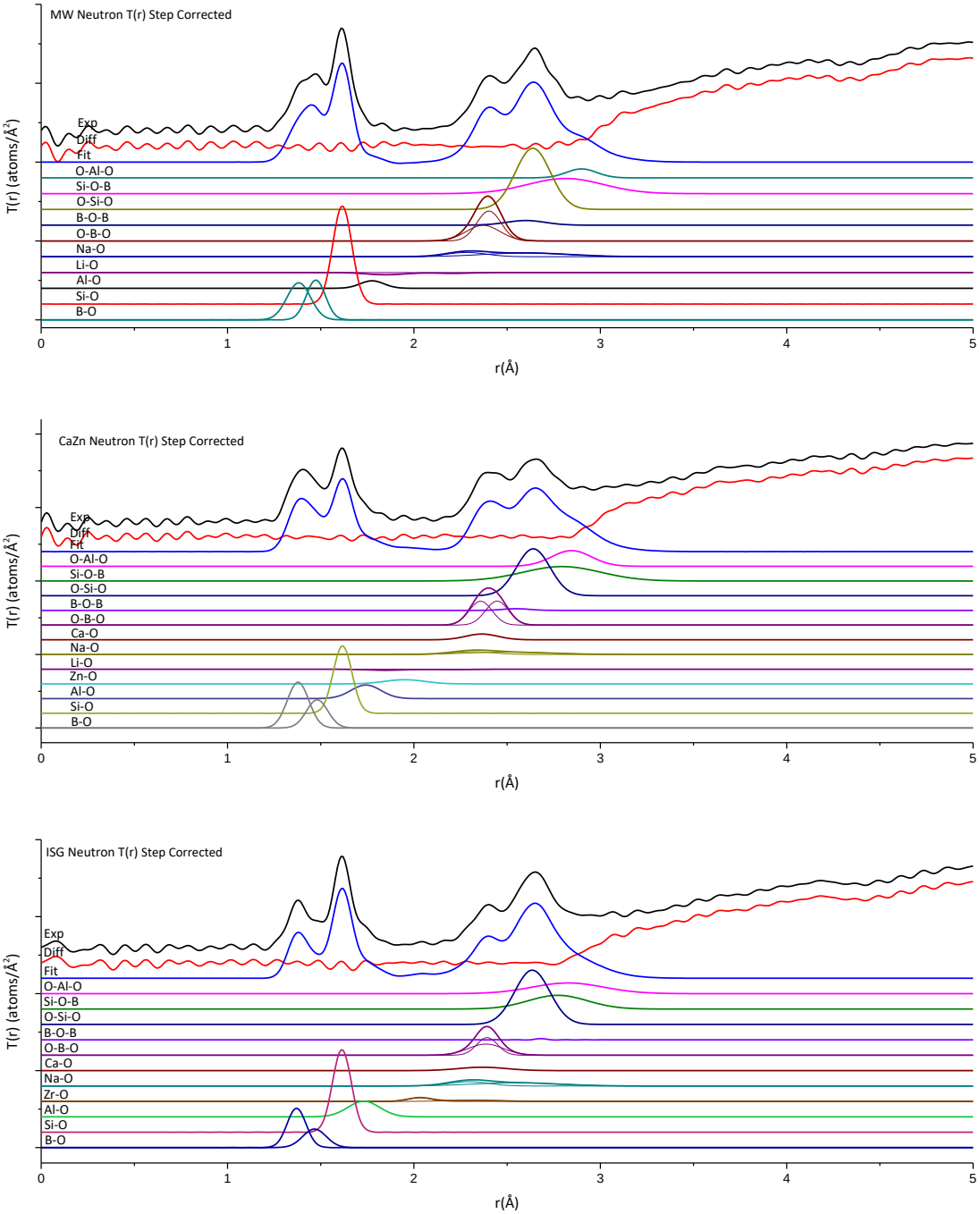


*Figure s 1 Step Corrected neutron T(r) fully fitted and offset for clarity*

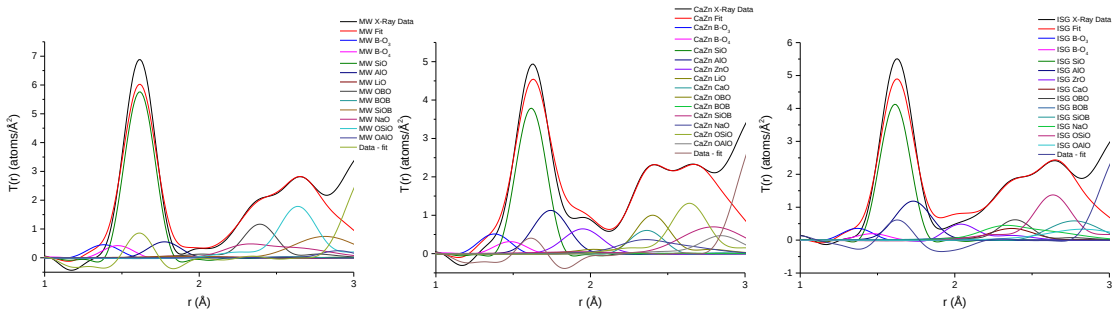


*Figure s 2 Xray T(r) fits*

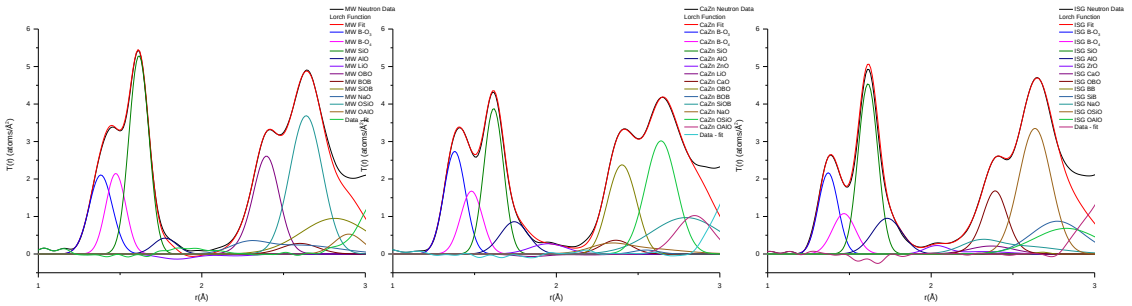


*Figure s 3 Lorch Function neutron T(r) fits*

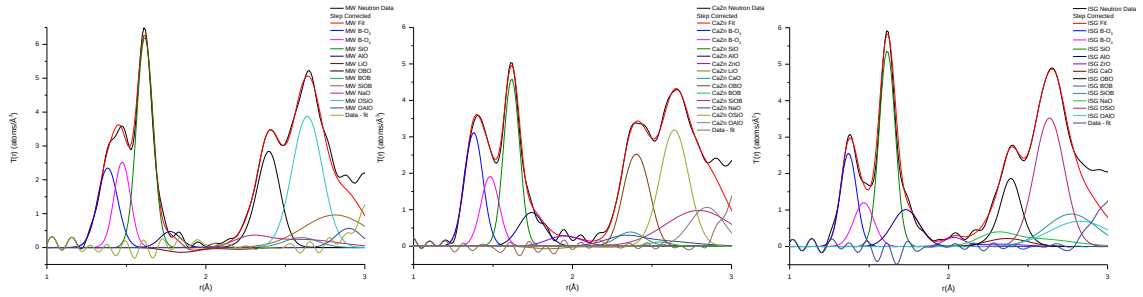


*Figure s 4 Step Corrected neutron T(r) fits*

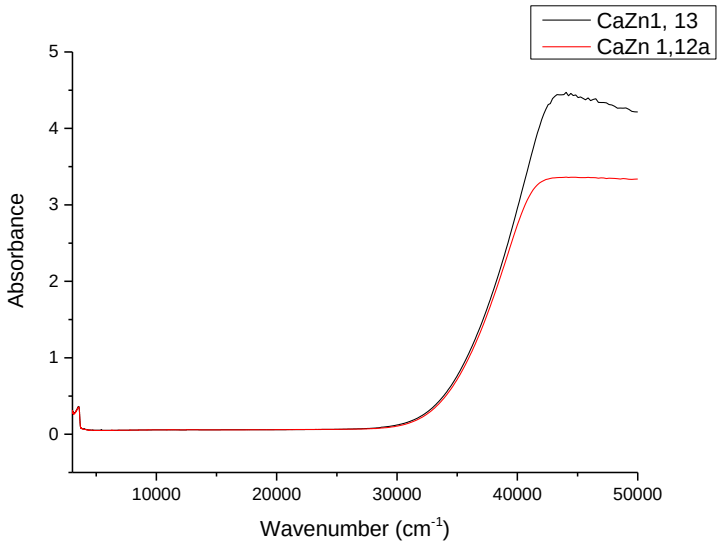


*Figure s 5 UV-Vis-NIR showing CaZn1,13 post XRD analysis and CaZn1,12a not XRD analysed. Shown pre pathlength correction to emphasise possible change in absorbance*

*Table S 1 Table showing full details of test leaching run carried out with glass laid flat on base of Parr vessel to select leaching run duration*

| weeks | Parr Vessel | Monolith ID | Monolith size/ mm | Monolith Surface area/ $cm^2$ | Water volume/mL | Sa:V $m^{-1}$ | leachate pH | leachate Si conc/ mmol/L | leachate B conc/ mmol/L | leachate Na conc/ mmol/L |
|---|---|---|---|---|---|---|---|---|---|---|
| 6 | 1 | CaZn 1,13a | 10.3x 10.5 x 1.3 | 2.7 | 13.5 | 20.0 | 9.4 | 1.04 | 1.13 | 0.46 |
| 6 | 2 | CaZn 1,7a | 10x 9.9x 1.2 | 2.5 | 12.3 | 20.3 | 9.3 | 0.99 | 1.29 | 0.50 |
| 6 | 3 | CaZn 1,11b | 10x 10.1x 1.2 | 2.5 | 12.6 | 19.8 | 9.3 | 1.16 | 1.49 | 0.62 |
| 6 | 4 | n/a | n/a | n/a | 12.8 | n/a | 6.4 | 0.04 | 0.00 | 0.00 |
| 4 | 5 | CaZn 1,13b | 9.9x 10.3x 1.3 | 2.6 | 12.5 | 20.8 | 9.2 | 1.19 | 1.50 | 0.63 |
| 4 | 6 | CaZn 1,7b | 10x 10.2x 1.3 | 2.6 | 12.9 | 20.2 | 9.3 | 1.01 | 1.11 | 0.43 |
| 4 | 7 | CaZn 1,11b | 10.3x 9.9x 1.2 | 2.5 | 12.7 | 19.7 | 9.2 | 1.21 | 1.55 | 0.64 |

*Table S 2 Table showing full details of Leaching run 1 carried out with unirradiated glass laid flat on base of Parr vessel*

| weeks | Parr Vessel | Monolith ID | Monolith size/ mm | Monolith Surface area/ $cm^2$ | Water volume/mL | Sa:V $m^{-1}$ | leachate pH | leachate Si conc/ mmol/L | leachate B conc/ mmol/L | leachate Na conc/ mmol/L |
|---|---|---|---|---|---|---|---|---|---|---|
| 4 | 1 | CaZn 1,15a | 1.2 x 10 x 10.2 | 2.52 | 12.6 | 20.0 | 9.5 | 1.23 | 1.14 | 0.49 |
| 4 | 2 | CaZn 1,15b | 1.2 x 10.1 x 10.2 | 2.55 | 12.7 | 20.1 | 9.5 | 1.18 | 1.15 | 0.47 |
| 4 | 3 | CaZn 1,14a | 1.2 x 10 x 10 | 2.48 | 12.4 | 20.0 | 9.5 | 1.28 | 1.18 | 0.50 |
| 4 | 4 | CaZn1 ,14b | 1.1 x 9.5 x10.5 | 2.44 | 12.2 | 20.0 | 9.5 | 1.26 | 1.18 | 0.50 |
| 4 | 7 | MW 1,8a | 1.2 x 9.7 x 10.4 | 2.5 | 12.5 | 20.0 | 10.1 | 7.92 | 39.96 | 22.07 |
| 4 | 9 | MW 1,8b | 1.2 x 10.1 x 10.3 | 2.57 | 12.7 | 20.2 | 10.1 | 9.54 | 48.06 | 26.48 |
| 4 | 5 | MW 1,7a | 1.4 x 10.3 x 10.1 | 2.65 | 13.3 | 19.9 | 10.1 | 10.63 | 42.59 | 23.81 |
| 4 | 6 | MW 1,7b | 1.4 x 10.3 x 10.2 | 2.68 | 13.4 | 20.0 | 10.1 | 10.22 | 47.62 | 25.62 |
| 4 | 10 | blank | n/a | n/a | 13 | n/a | 5.4 | 0.00 | 0.00 | 0.01 |

*Table S 3 Table showing full details of Leaching run 2 carried out with glass irradiated to a total dose ~10 MGy laid flat on base of Parr vessel*

| weeks | Parr Vessel | Monolith ID | Monolith size/ mm | Monolith Surface area/ $cm^2$ | Water volume/mL | Sa:V $m^{-1}$ | leachate pH | leachate Si conc/ mmol/L | leachate B conc/ mmol/L | leachate Na conc/ mmol/L |
|---|---|---|---|---|---|---|---|---|---|---|
| 4 | 1 | CaZn 1,10a | 10.3x 10.2x 1.2 | 2.59 | 13 | 19.9 | 9.7 | 1.73 | 1.13 | 0.50 |
| 4 | 2 | CaZn 1,6 | 9.1x 9x 1.1 | 2.01 | 10.2 | 19.7 | 9.6 | 1.71 | 1.20 | 0.53 |
| 4 | 3 | CaZn 1,8b | 10.2x 9.3x 1 | 2.23 | 11.6 | 19.2 | 9.7 | 1.64 | 1.09 | 0.48 |
| 4 | 4 | blank | n/a | n/a | 15 | n/a | 5.7 | 0.02 | 0.00 | 0.00 |
| 4 | 5 | MW 1,2a | 9x 9.9x 1.1 | 2.2 | 11 | 20.0 | 10.3 | 18.83 | 45.44 | 24.40 |
| 4 | 6 | MW 1,2b | 10.3x 10.1x 1.2 | 2.57 | 12.6 | 20.4 | 10.3 | 15.57 | 43.55 | 23.90 |
| 4 | 7 | MW 1,5a | 9.8x 9.9x 1.3 | 2.45 | 12.3 | 19.9 | 10.3 | 16.28 | 40.65 | 22.27 |
| 4 | 9 | MW 1,5b | 9.5x9. 8x 1.3 | 2.36 | 11.9 | 19.8 | 10.3 | 19.97 | 46.29 | 25.40 |

*Table S 4 Table showing full details of Leaching run 3 carried out with glass irradiated to a total dose ~5 MGy laid flat on base of Parr vessel*

| weeks | Parr Vessel | Monolith ID | Monolith size/ mm | Monolith Surface area/ $cm^2$ | Water volume/mL | Sa:V $m^{-1}$ | leachate pH | leachate Si conc/ mmol/L | leachate B conc/ mmol/L | leachate Na conc/ mmol/L |
|---|---|---|---|---|---|---|---|---|---|---|
| 4 | 1 | CaZn 1,12a | 9.95x 10.1x 1.28 | 2.53 | 12.66 | 20.0 | 9.8 | 1.16 | 1.02 | 0.47 |
| 4 | 2 | CaZn 2,1b | 10.0x 10.0x 1.29 | 2.55 | 12.74 | 20.0 | 9.8 | 1.14 | 1.02 | 0.47 |
| 4 | 3 | CaZn 2,2a | 10.0x 10.1x 1.3 | 2.56 | 12.83 | 20.0 | 9.7 | 1.15 | 1.02 | 0.46 |
| 4 | 5 | MW1, 10b | 10.0x 10.1x 1.14 | 2.5 | 12.57 | 19.9 | 10.4 | 19.48 | 42.09 | 23.09 |
| 4 | 6 | MW1, 11a | 10x 10.0x 1.2 | 2.5 | 12.48 | 20.0 | 10.3 | 19.73 | 42.44 | 23.60 |
| 4 | 7 | MW1, 12a | 9.51x 9.88x 0.89 | 2.22 | 11.17 | 19.9 | 10.4 | 16.02 | 42.78 | 23.25 |
| 4 | 9 | blank | n/a | n/a | 14.92 | n/a | 4.9 | 0.00 | 0.00 | 0.00 |

*Table S 5 Table showing full details of Leaching run 4 carried out with unirradiated glass held in crevice sample holder*

| weeks | Parr Vessel | Monolith ID | Monolith size/ mm | Monolith Surface area/ $cm^2$ | Water volume/mL | Sa:V $m^{-1}$ | leachate pH | leachate Si conc/ mmol/L | leachate B conc/ mmol/L | leachate Na conc/ mmol/L |
|---|---|---|---|---|---|---|---|---|---|---|
| 4 | 1 | CaZn 2,3a | 1.12 x 9.57 x 9.76 | 2.301 | 11.61 | 19.8 | 9.4 | 0.98 | 1.07 | 0.47 |
| 4 | 2 | CaZn 2,3b | 1.2 x 9.99 x 10.14 | 2.509 | 12.54 | 20.0 | 9.4 | 0.98 | 1.07 | 0.48 |
| 4 | 3 | CaZn 2,6a | 1.36x 10.0x 10.06 | 2.574 | 12.91 | 19.9 | 9.4 | 0.99 | 1.09 | 0.47 |
| 4 | 4 | blank | n/a | n/a | 15 | n/a | 8.8 | 0.03 | 0.07 | 0.04 |
| 4 | 7 | MW 1 ,13 | 0.84 x 10.0x 10.06 | 2.351 | 11.75 | 20.0 | 10.1 | 4.18 | 42.11 | 23.48 |
| 4 | 9 | MW 1 ,15a | 1.21 x 9.58 x 10.02 | 2.394 | 12.1 | 19.8 | 10.1 | 8.62 | 43.50 | 24.19 |
| 4 | 10 | MW 1,15b | 1.17 x 9.70 x 9.29 | 2.247 | 11.52 | 19.5 | 10.1 | 8.45 | 43.16 | 23.96 |

*Table S 6 Table showing full details of Leaching run 5 carried out with glass irradiated to a total dose of ~ 10 MGy held in crevice sample holder*

| weeks | Parr Vessel | Monolith ID | Monolith size/ mm | Monolith Surface area/ $cm^2$ | Water volume/mL | Sa:V $m^{-1}$ | leachate pH | leachate Si conc/ mmol/L | leachate B conc/ mmol/L | leachate Na conc/ mmol/L |
|---|---|---|---|---|---|---|---|---|---|---|
| 4 | 1 | CaZn 1,6 | 1.08 x 9.9 x 9.62 | 2.32 | 11.6 | 20.0 | 9.3 | 1.14 | 1.11 | 0.48 |
| 4 | 3 | CaZn 1 8a | 10.51 x 9.26 x 1.21 | 2.43 | 12.1 | 20.1 | 9.3 | 1.13 | 1.15 | 0.49 |
| 4 | 4 | CaZn 1 10b | 10.09 x 10.18 x 1.27 | 2.57 | 12.7 | 20.2 | 9.3 | 1.07 | 1.07 | 0.46 |
| 4 | 5 | blank | n/a | n/a | 15 | n/a | 6.6 | 0.04 | 0.02 | 0.01 |
| 4 | 6 | MW 1 1 | 9.88 x 9.84 x 1.06 | 2.36 | 11.8 | 20.0 | 10.0 | 14.47 | 42.18 | 23.41 |
| 4 | 7 | MW 1 4a | 9.82 x 9.09 x 1.3 | 2.28 | 11.4 | 20.0 | 10.0 | 17.44 | 42.02 | 23.29 |
| 4 | 9 | MW 1 4b | 9.89 x 9.29 x 1.17 | 2.29 | 11.4 | 20.1 | 10.0 | 16.61 | 42.33 | 23.43 |

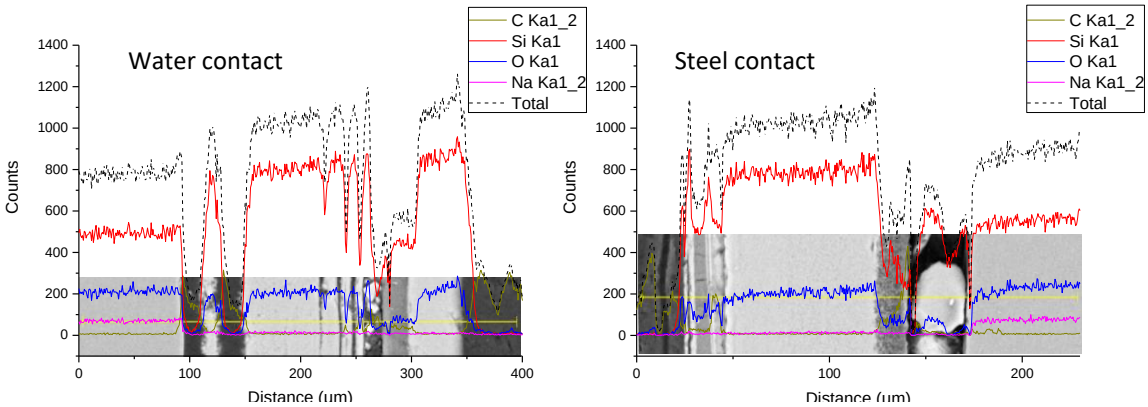


*Figure s 6 Pristine (unirradiated) MW pre normalisation linescan data*

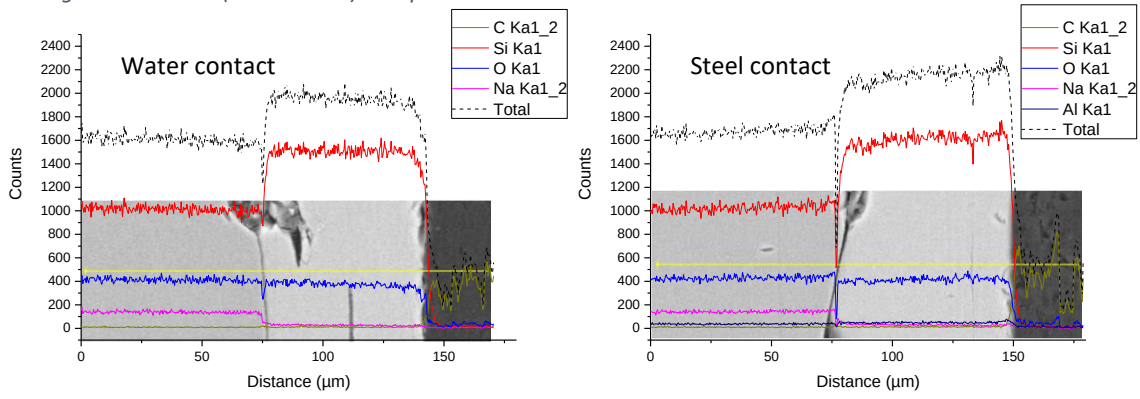

*Figure s 7 10 MGy dose MW pre normalisation linescan data*

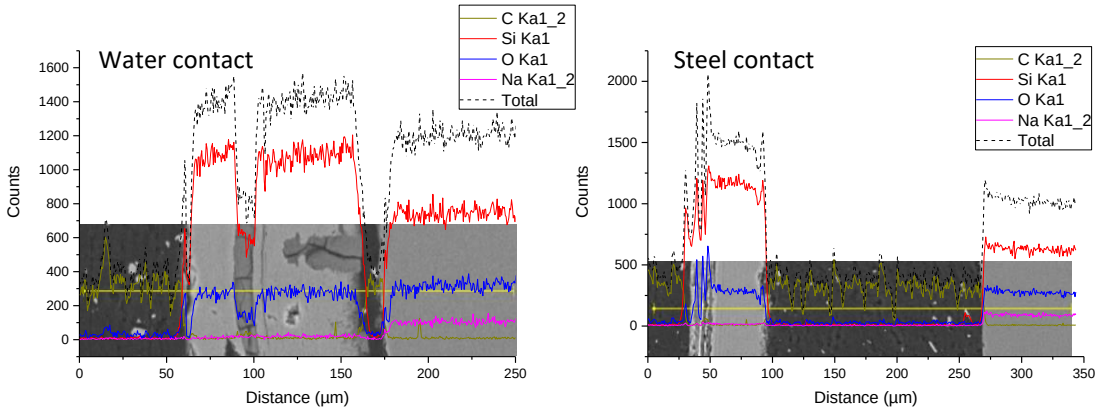


*Figure s 8 5 MGy dose MW pre normalisation linescan data*

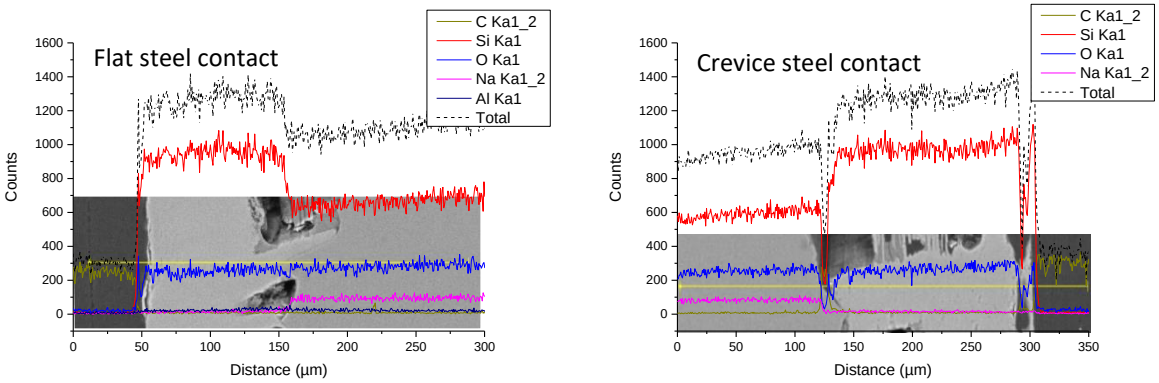


*Figure s 9 Pristine (unirradiated) MW crevice pre normalisation linescan data*

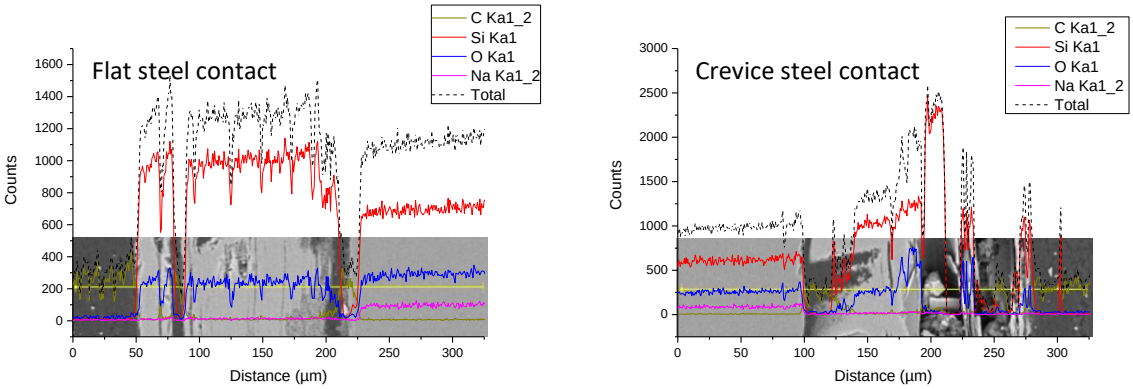


*Figure s 10 10 MGy dose MW crevice pre normalisation linescan data*

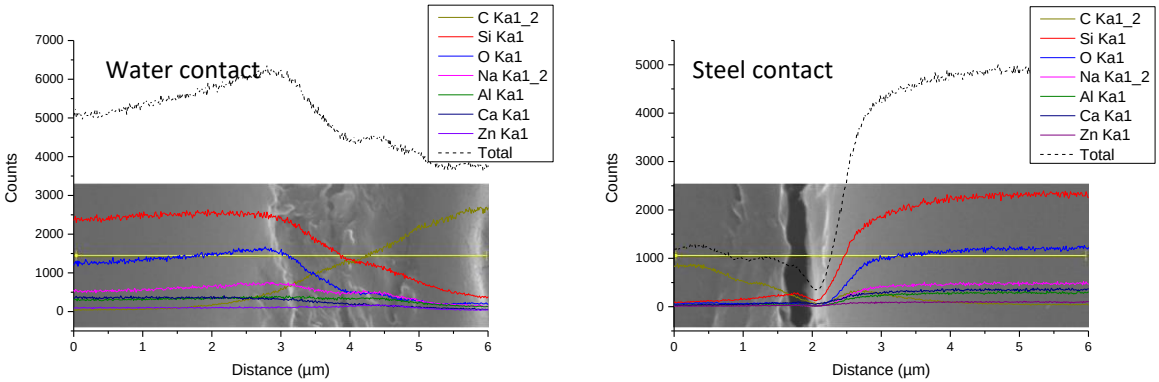

*Figure s 11 Pristine (unirradiated) CaZn pre normalisation linescan data*

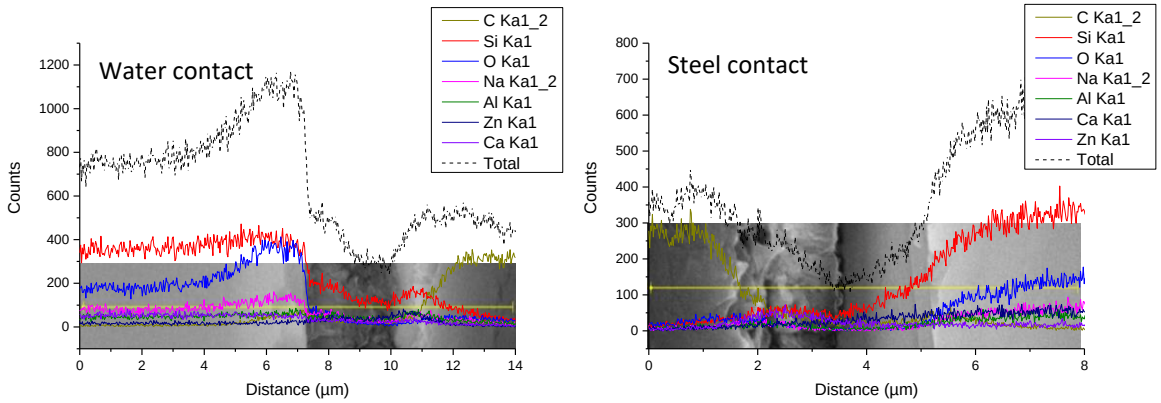


*Figure s 12 10 MGy dose CaZn pre normalisation data*

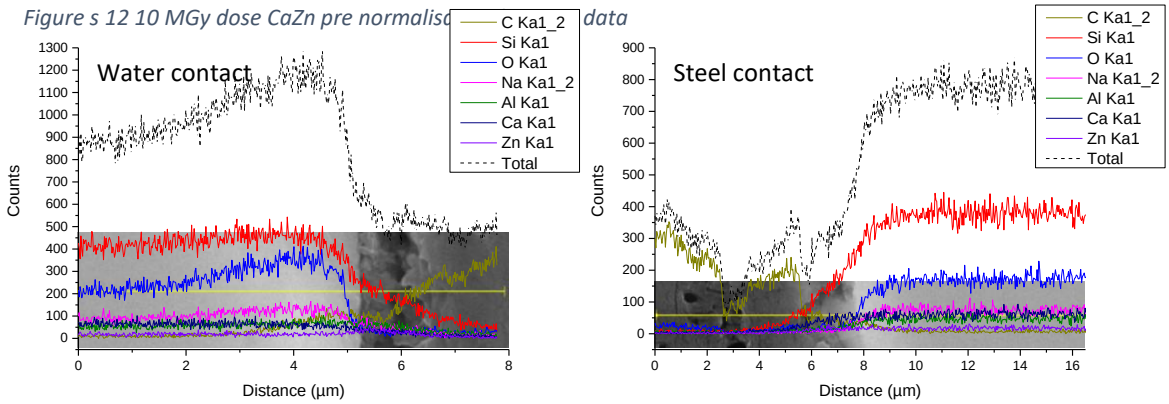


*Figure s 13 5 MGy dose CaZn pre normalisation linescan data*

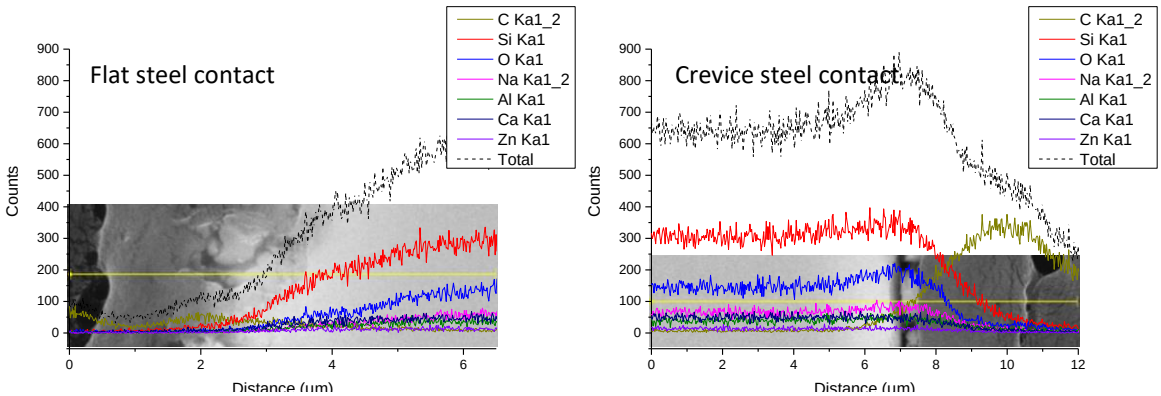


*Figure s 14 Pristine (unirradiated) CaZn crevice pre normalisation linescan data*

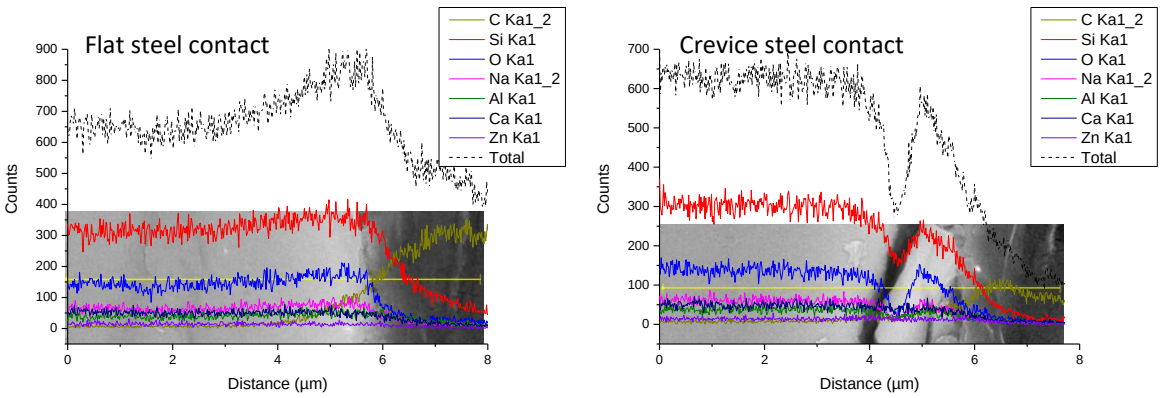


*Figure s 15 10 MGy dose CaZn crevice pre normalisation linescan data*

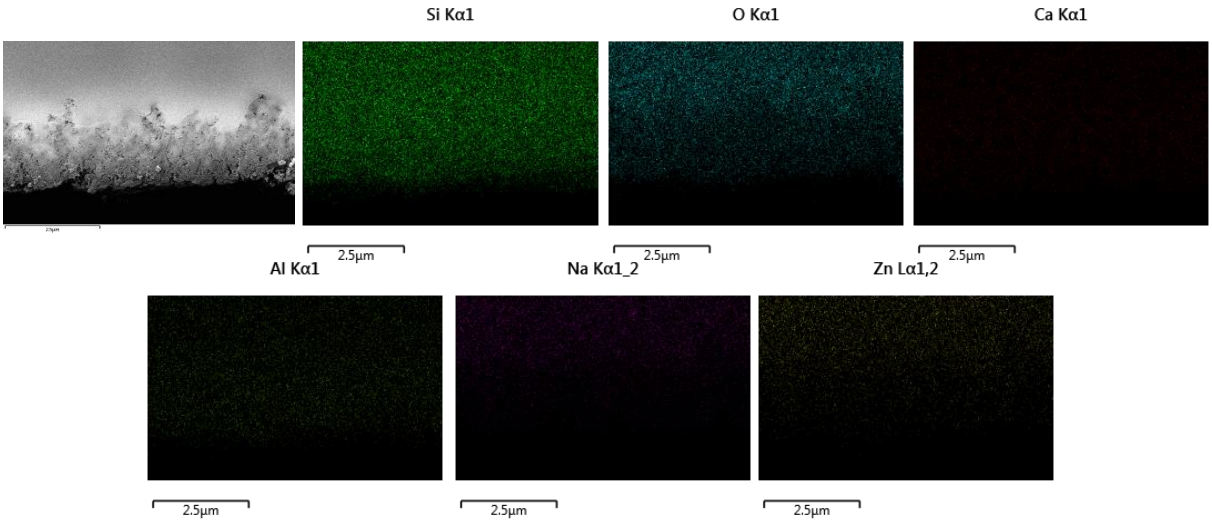


*Figure s 16 EDS Elemental mapping of non-resin encased unirradiated leached CaZn sample*

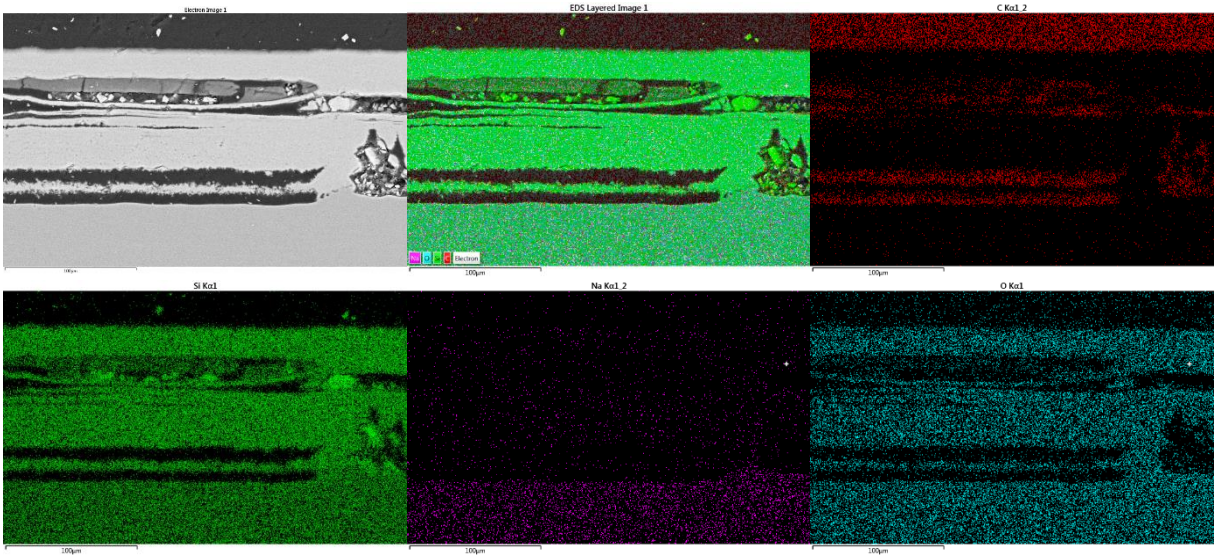


*Figure s 17 Pristine (unirradiated) MW water contact, EDS element maps*

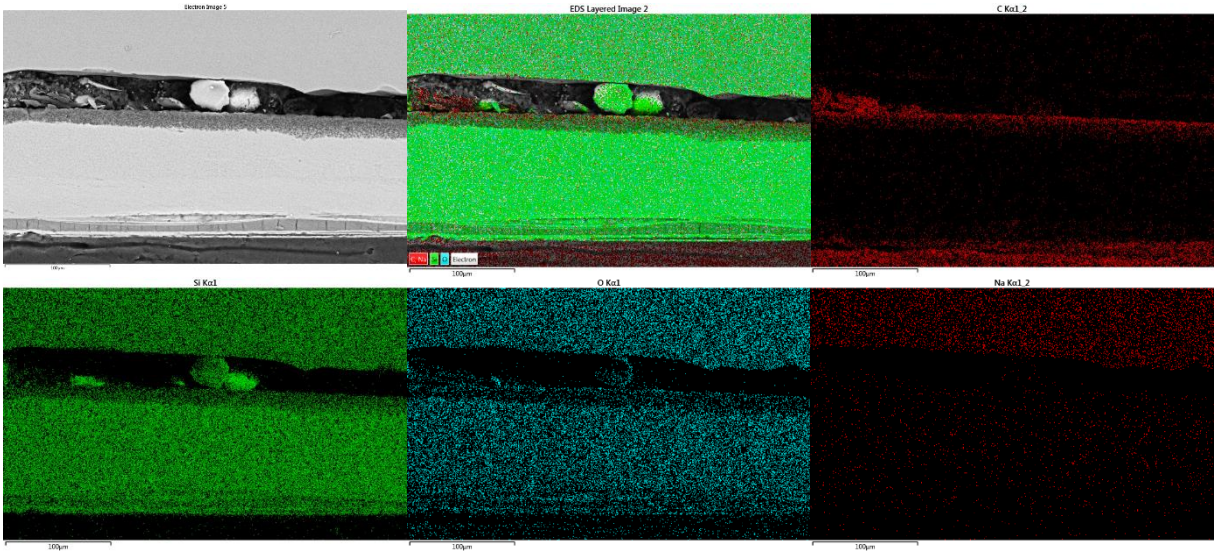


*Figure s 18 Pristine (unirradiated) MW steel contact, EDS element maps*

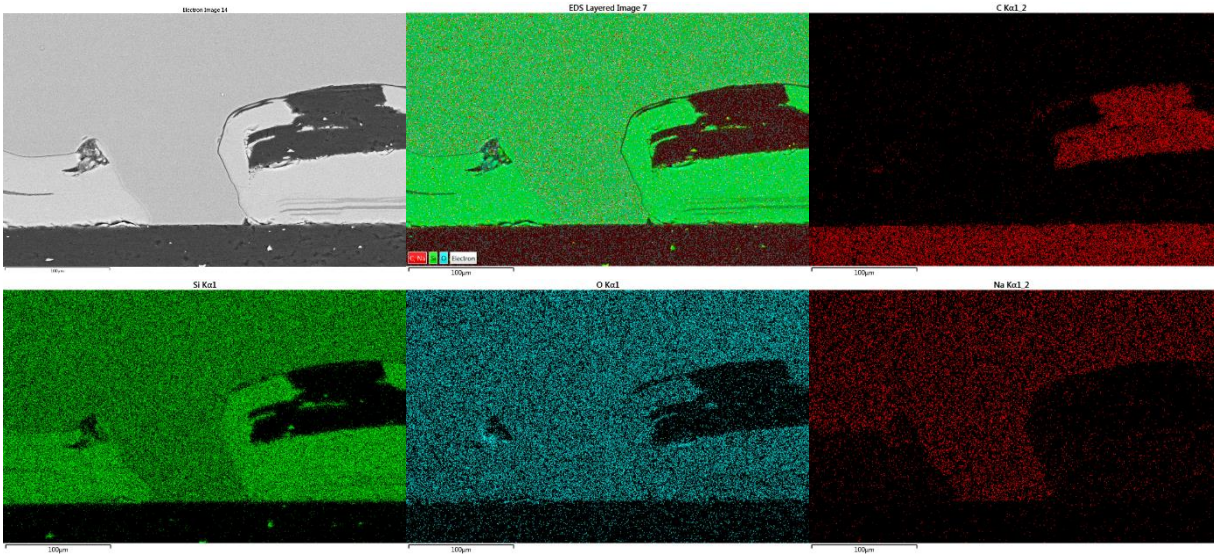


*Figure s 19 MW 10 MGy water contact, EDS element maps*

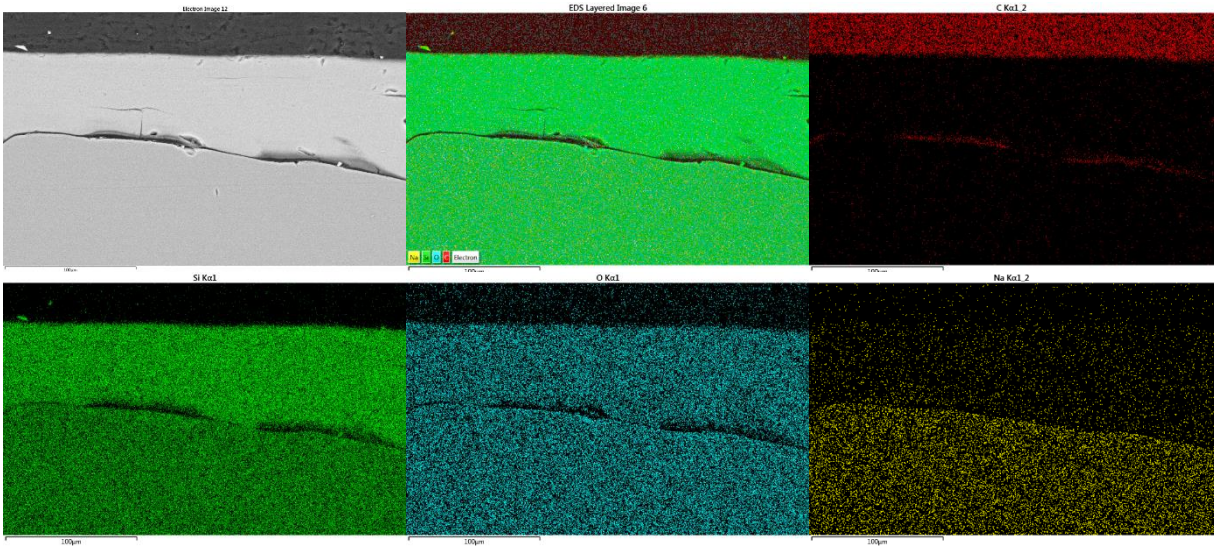


*Figure s 20 MW 10 MGy steel contact, EDS element maps*

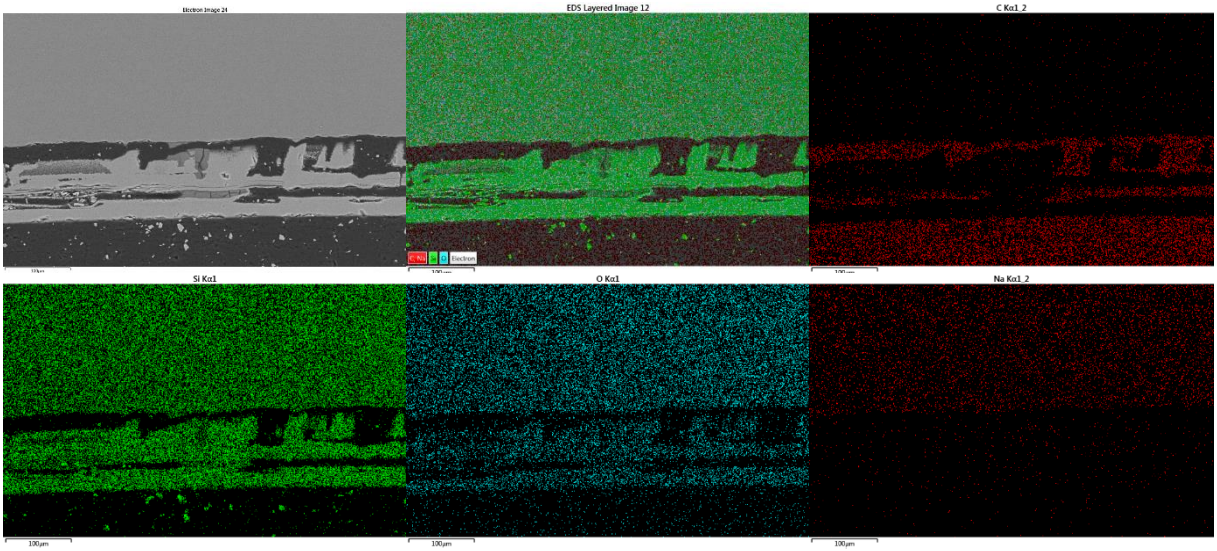


*Figure s 21 MW 5 MGy water contact, EDS element maps*

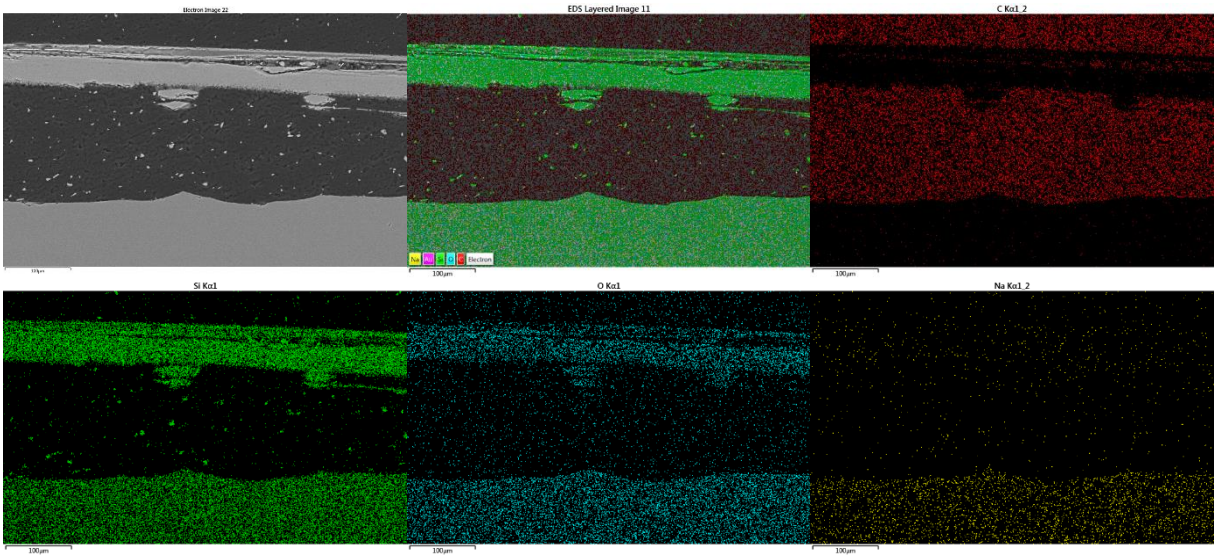


*Figure s 22 MW 5 MGy steel contact, EDS element maps*

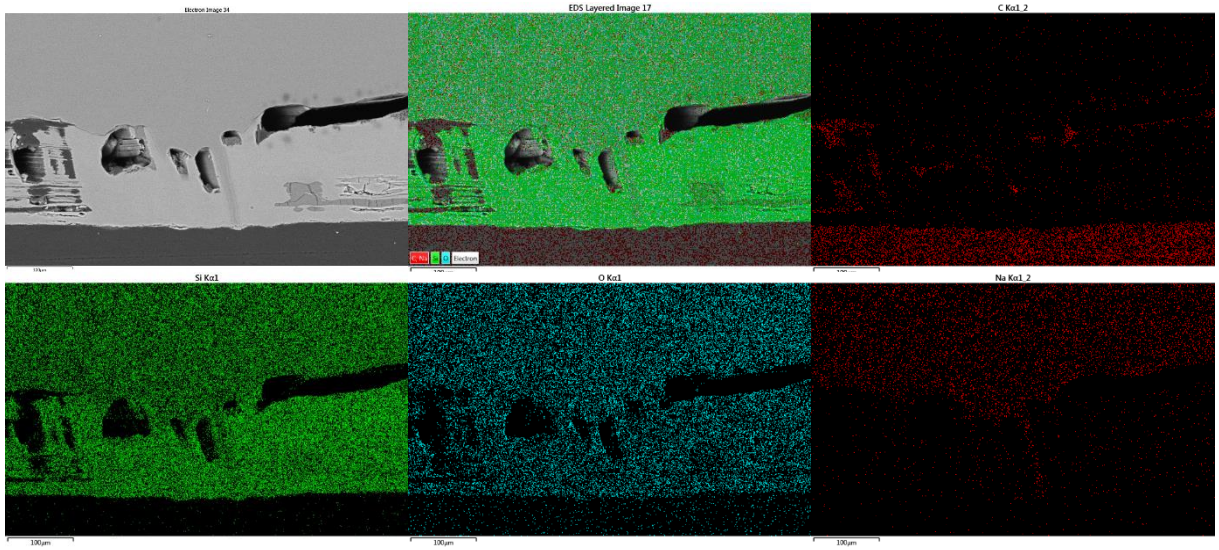


*Figure s 23 Pristine (unirradiated) MW flat steel contact, EDS element maps*

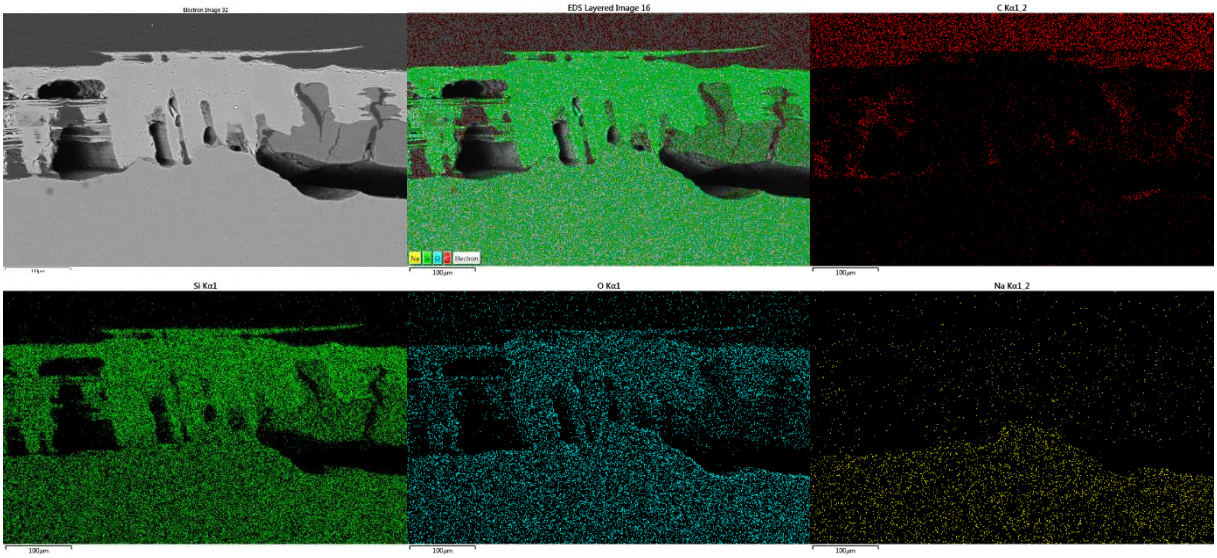


*Figure s 24  Pristine (unirradiated) MW steel crevice contact, EDS element maps*

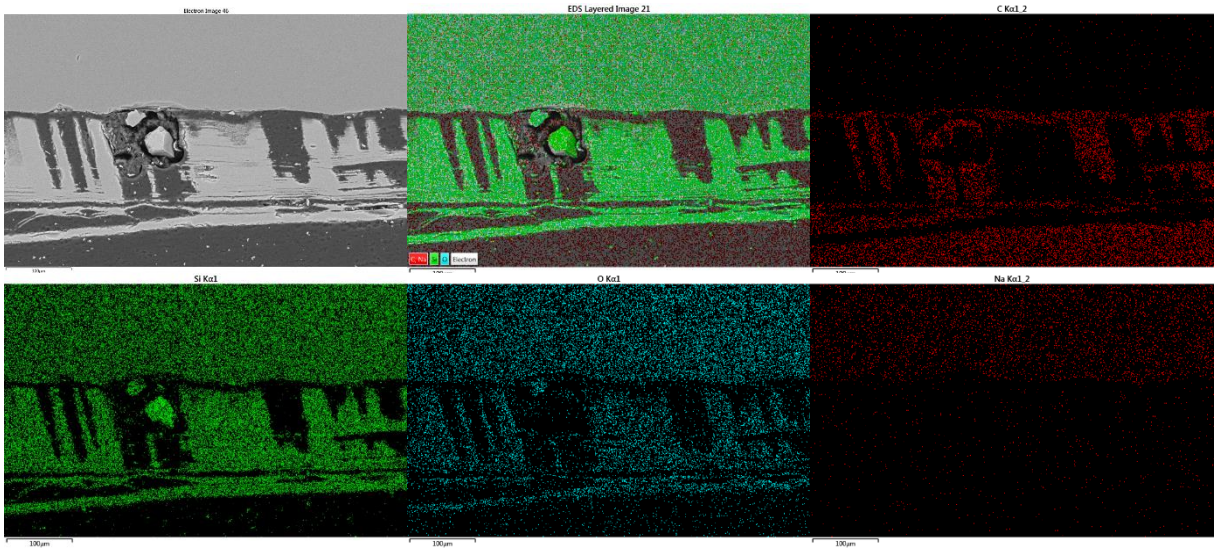


*Figure s 25 MW 10 MGy flat steel contact, EDS element maps*

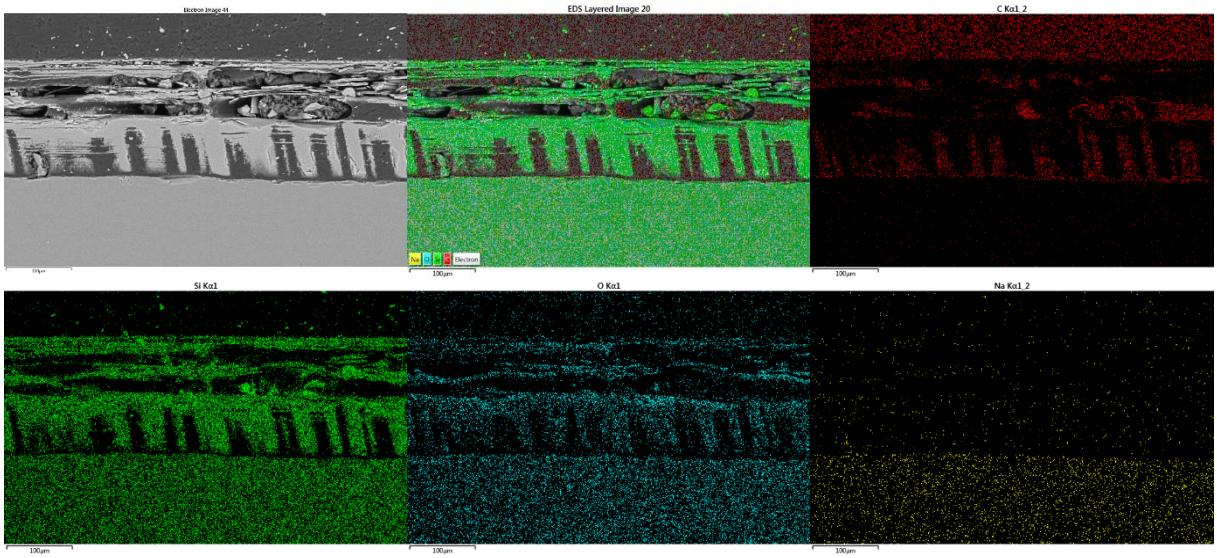


*Figure s 26 MW 10 MGy steel crevice contact, EDS element maps*

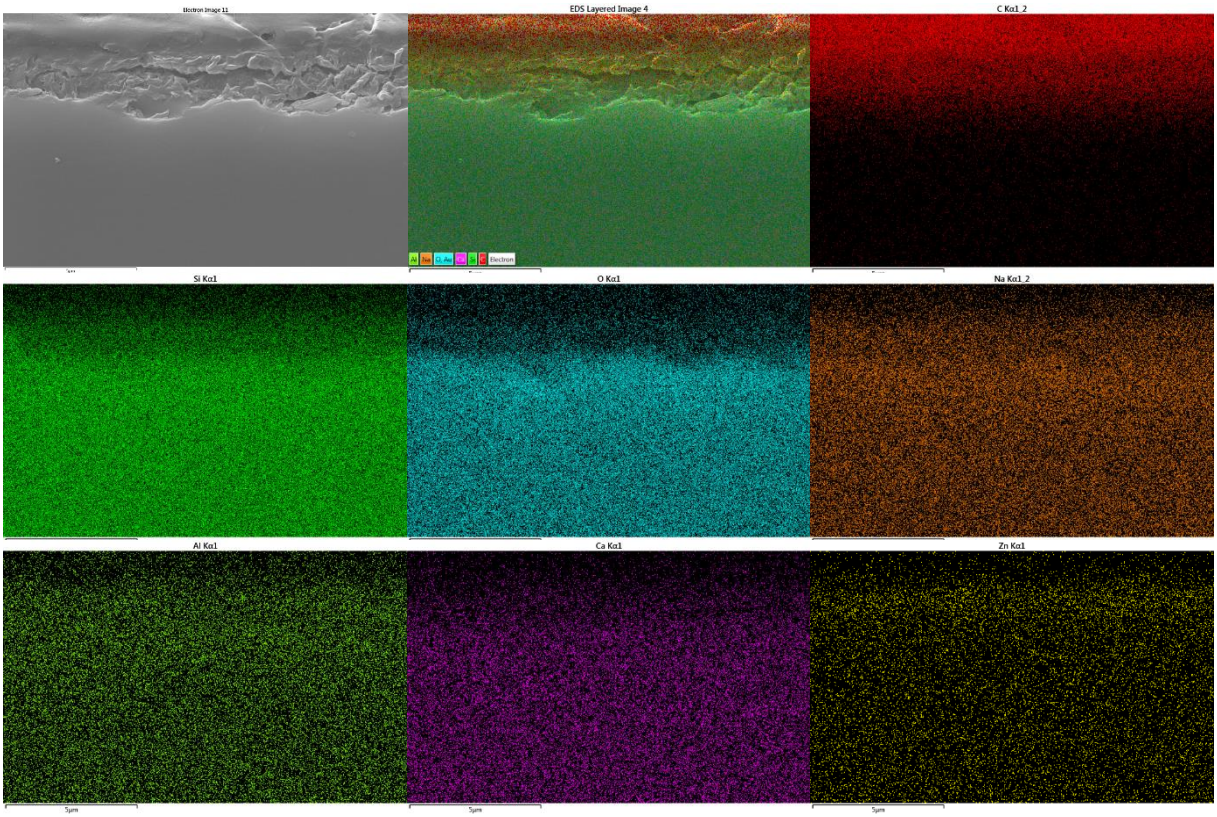


*Figure s 27 Pristine (unirradiated) CaZn water contact, EDS element maps*

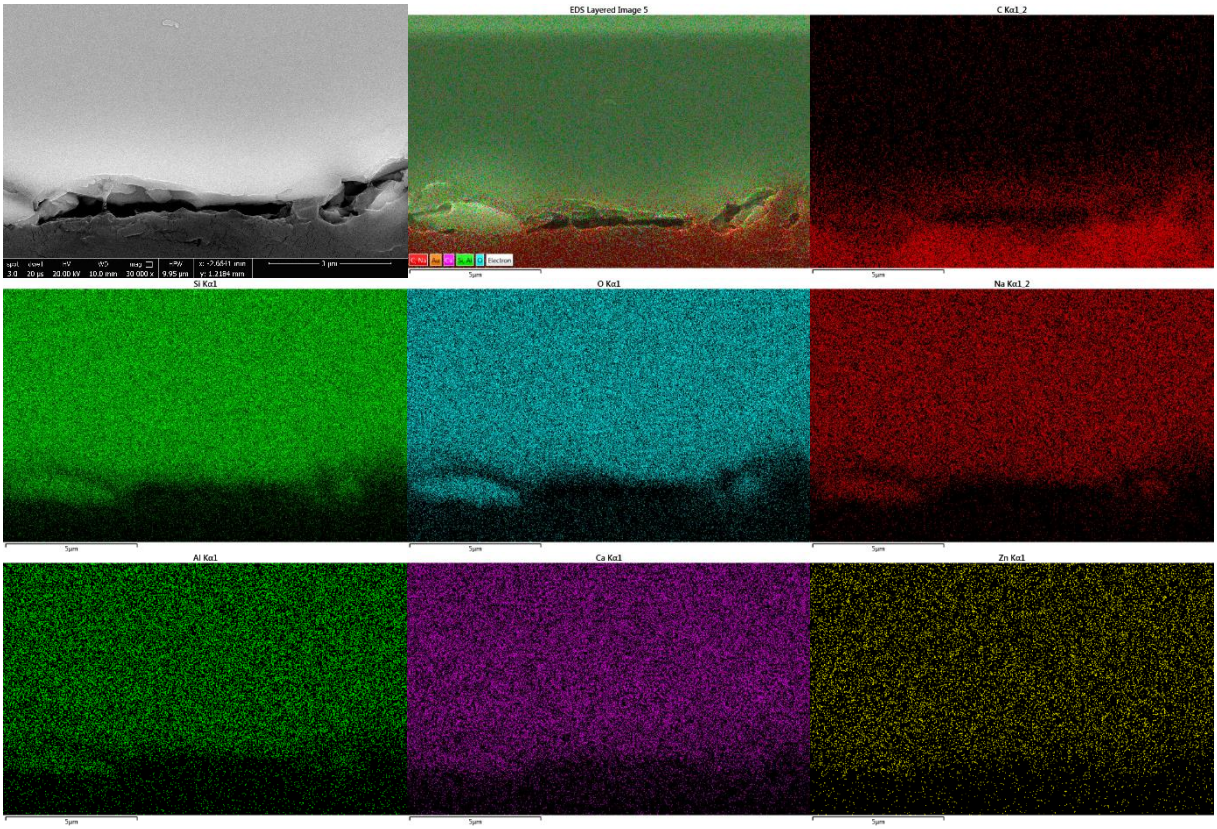


*Figure s 28 Pristine (unirradiated) CaZn steel contact, EDS element maps*

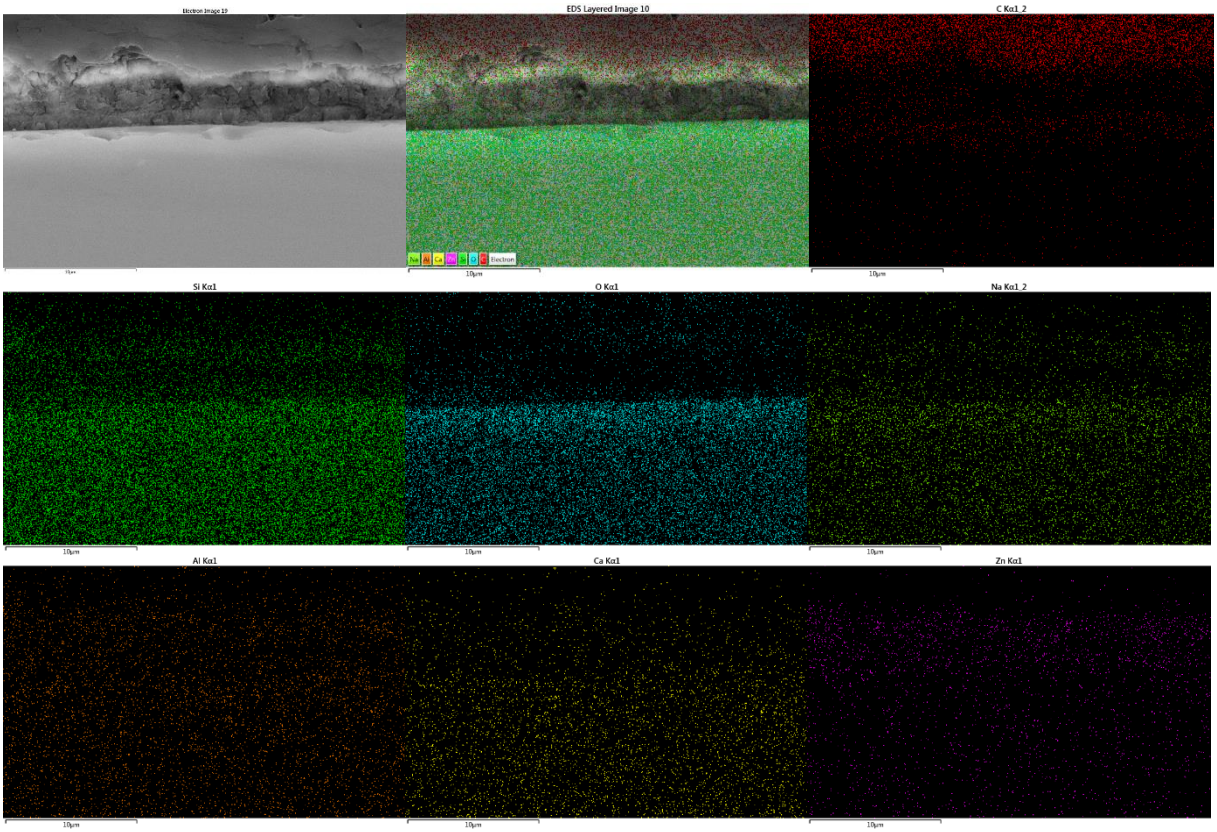


*Figure s 29 CaZn 10 MGy water contact, EDS element maps*

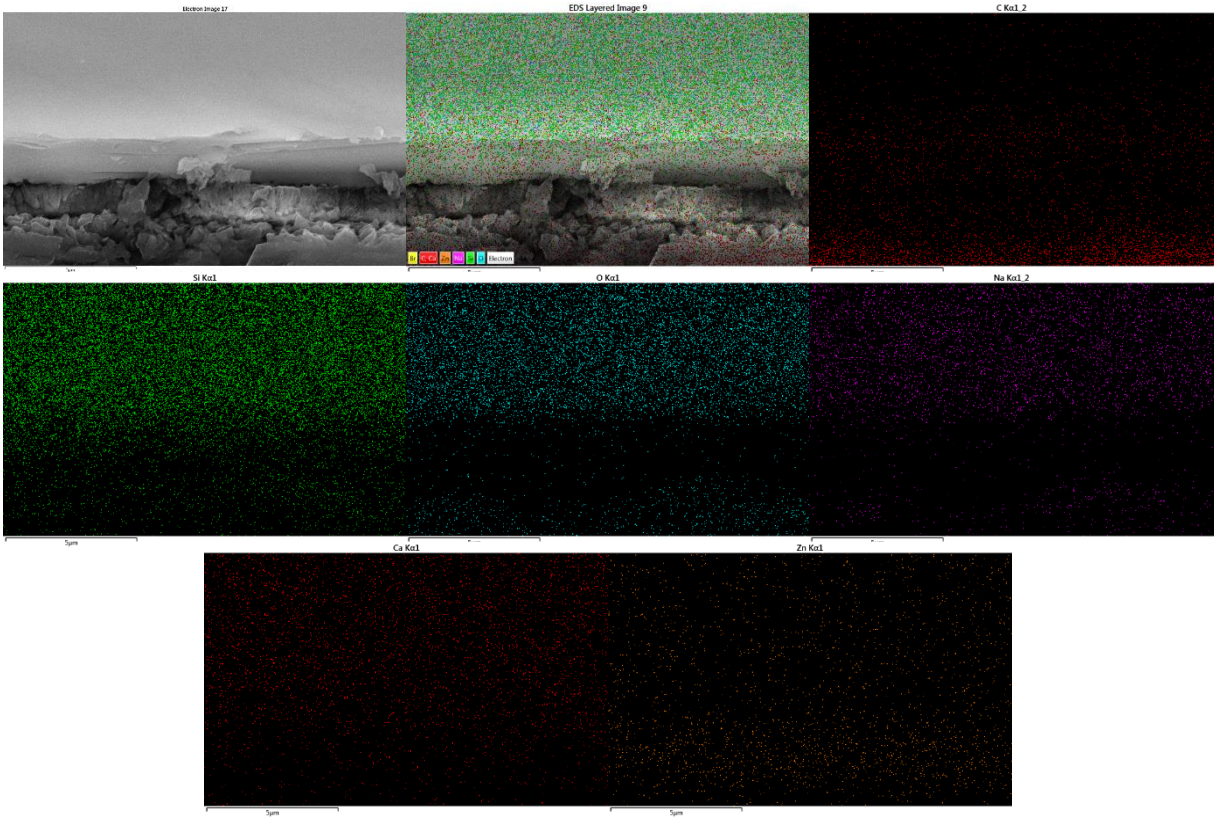


*Figure s 30 CaZn 10 MGy steel contact, EDS element maps*

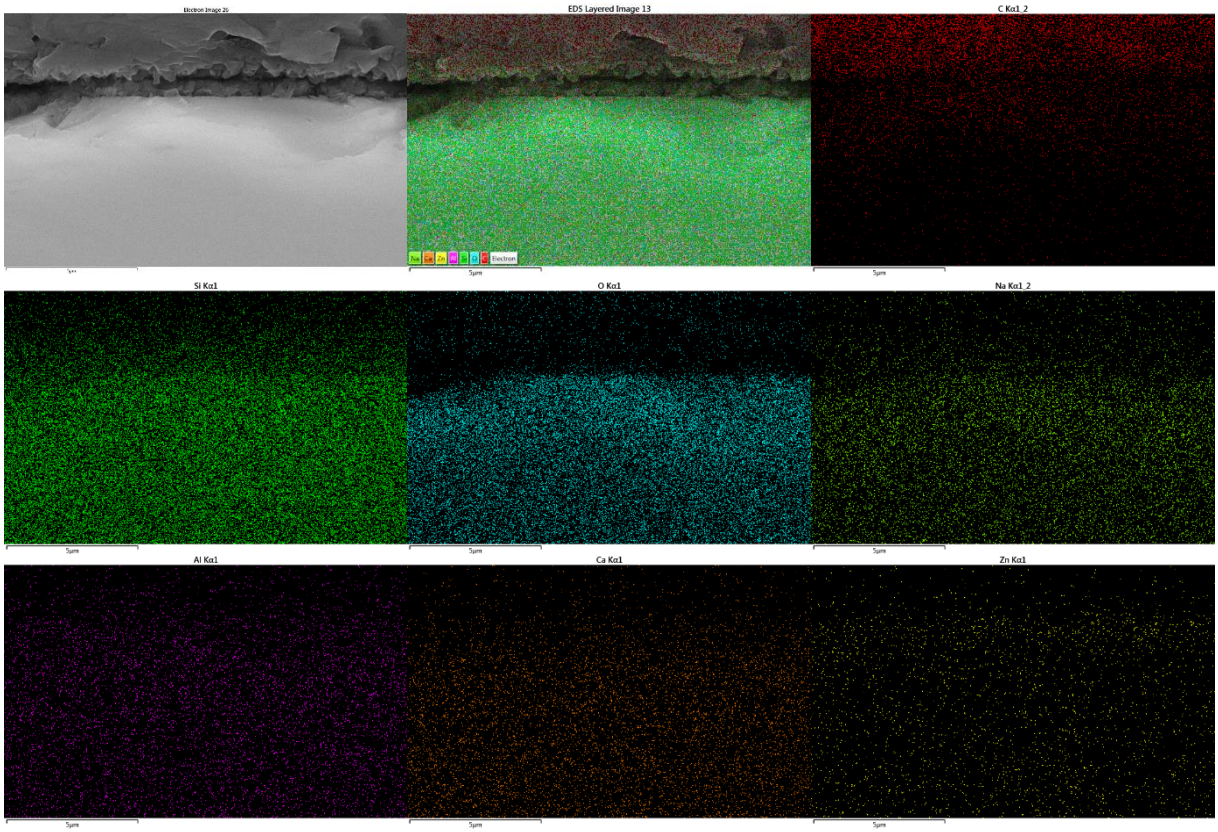


*Figure s 31 CaZn 5 MGy water contact, EDS element maps*

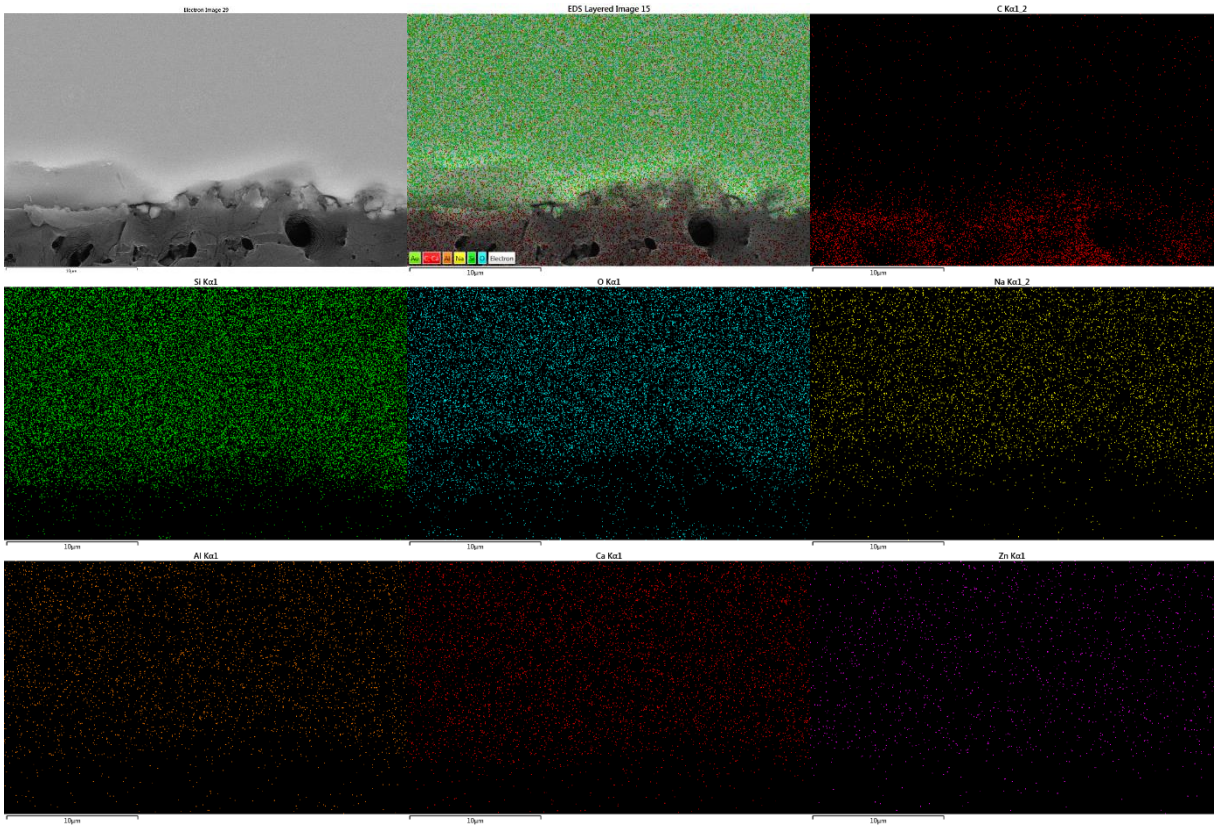


*Figure s 32 CaZn 5 MGy steel contact, EDS element maps*

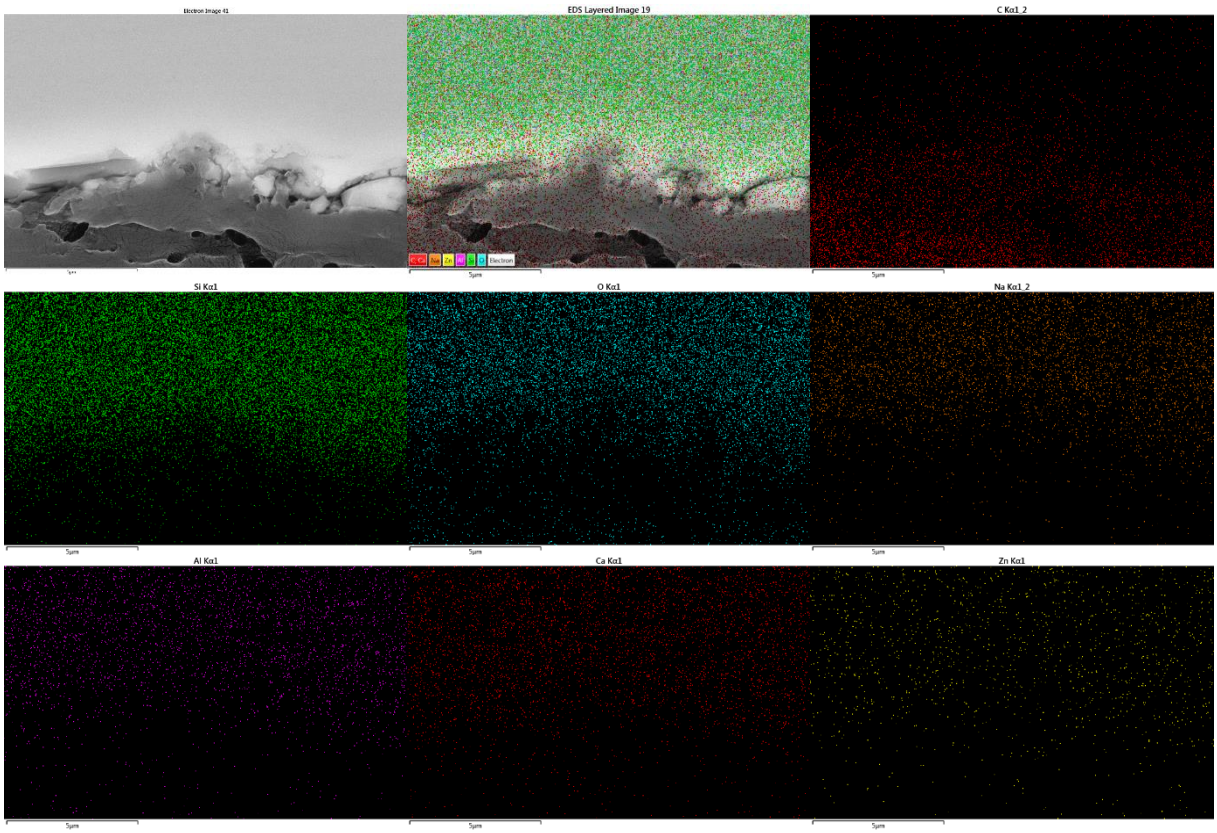


*Figure s 33 Pristine (unirradiated) CaZn flat steel contact, EDS element maps*

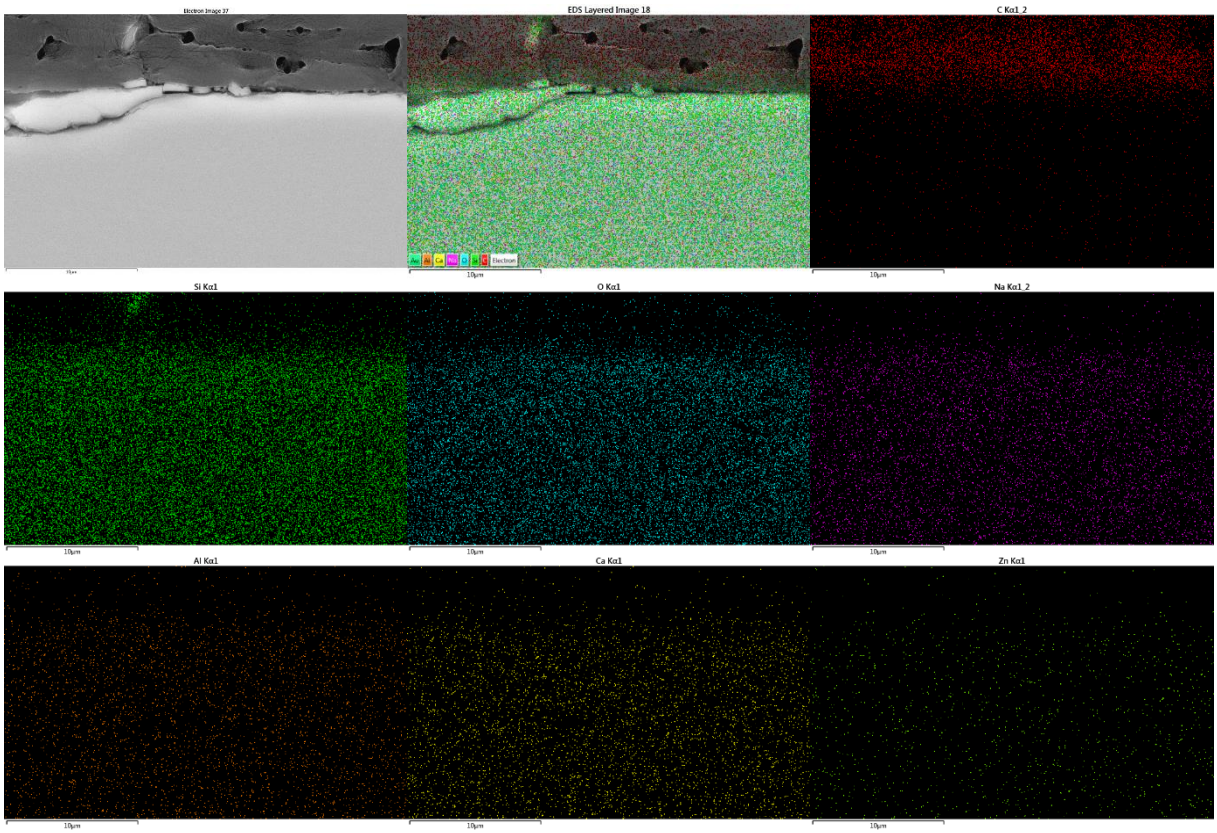


*Figure s 34 Pristine (unirradiated) CaZn steel crevice contact, EDS element maps*

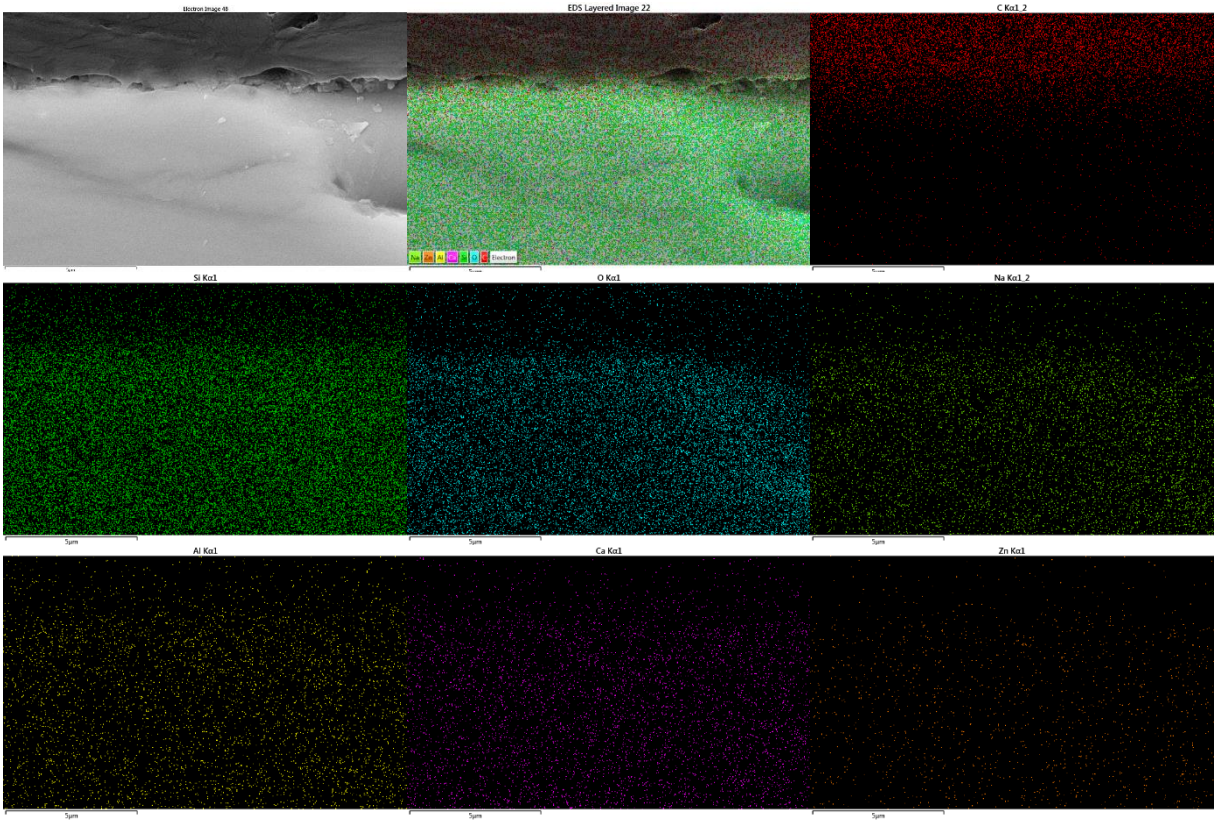


*Figure s 35 CaZn 10 MGy flat steel contact, EDS element maps*

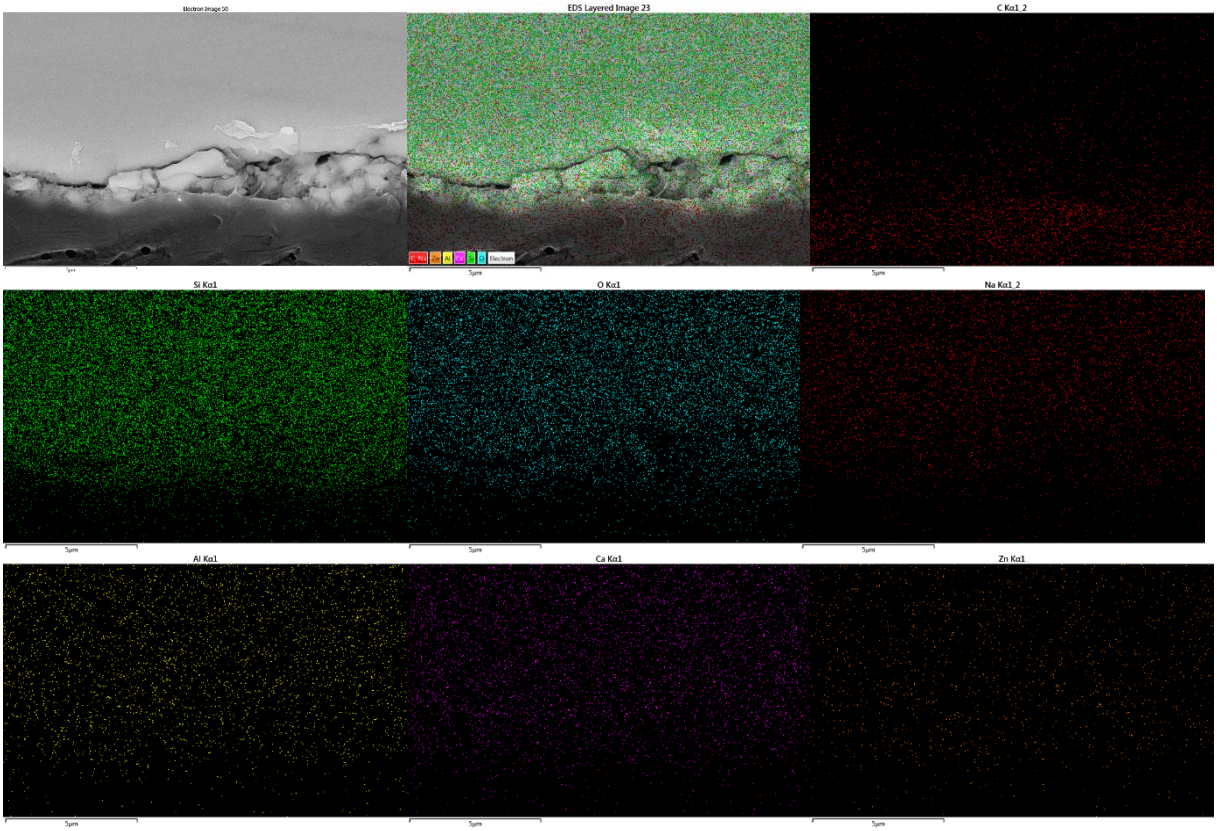


*Figure s 36 CaZn 10 MGy steel crevice contact, EDS element maps*

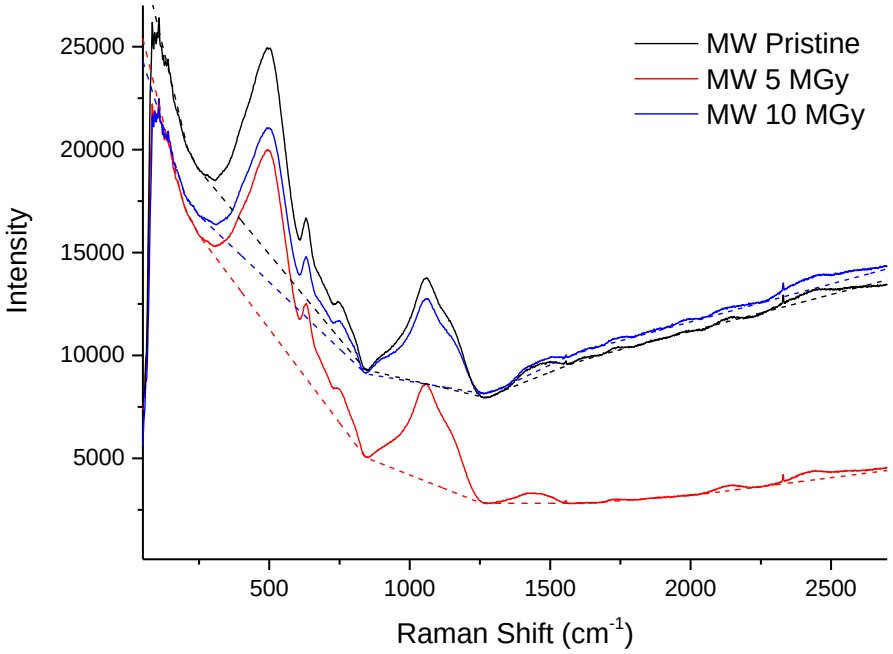


*Figure s 37 Raw Raman spectra of pristine and irradiated MW Glass, with baseline applied shown as dashed line*

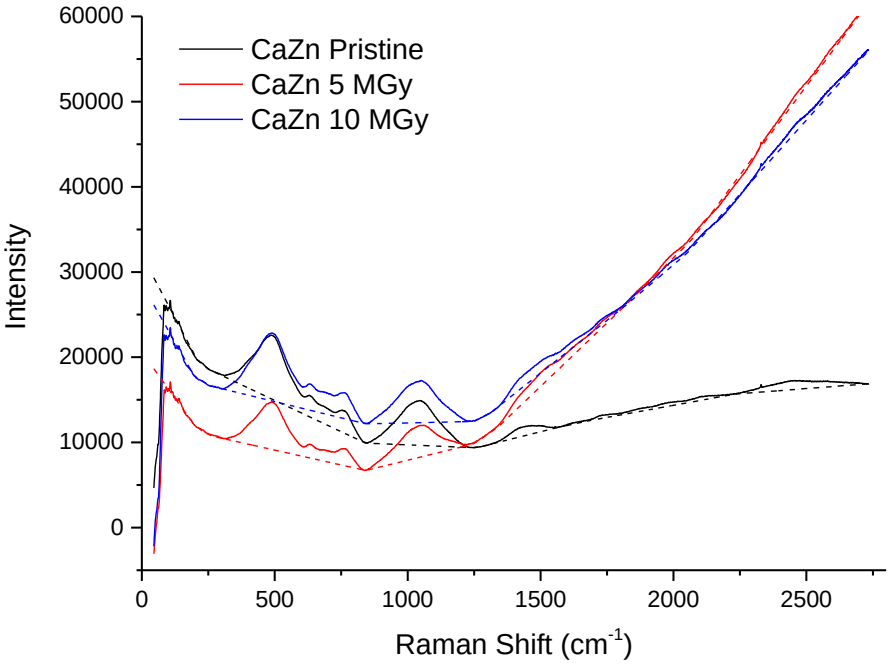


*Figure s 38 Raw Raman spectra of pristine and irradiated CaZn Glass, with baseline applied shown as dashed line.*

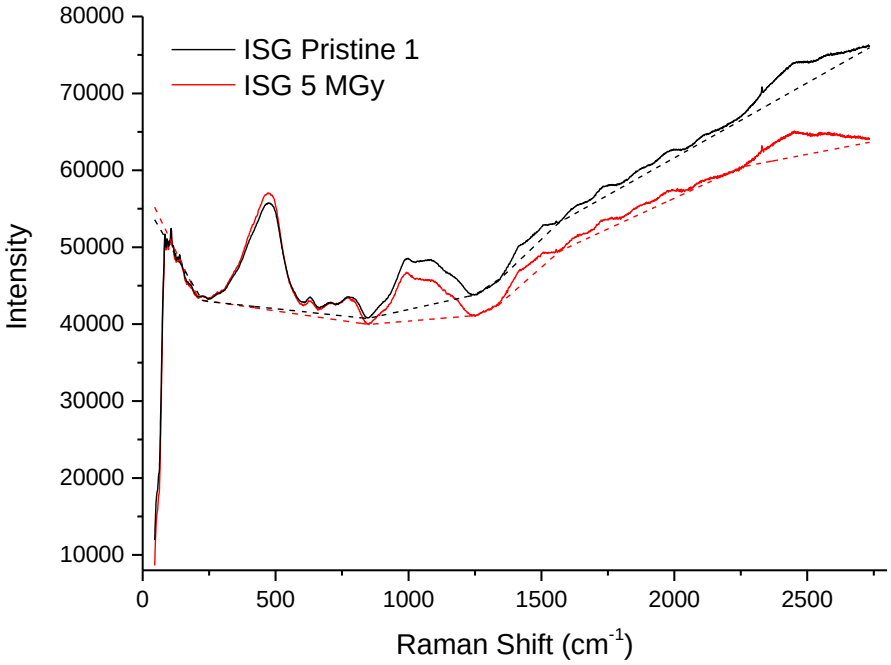


*Figure s 39 Raw Raman spectra of pristine and irradiated ISG Glass carried out at lower magnification settings, with baseline applied shown as dashed line.*

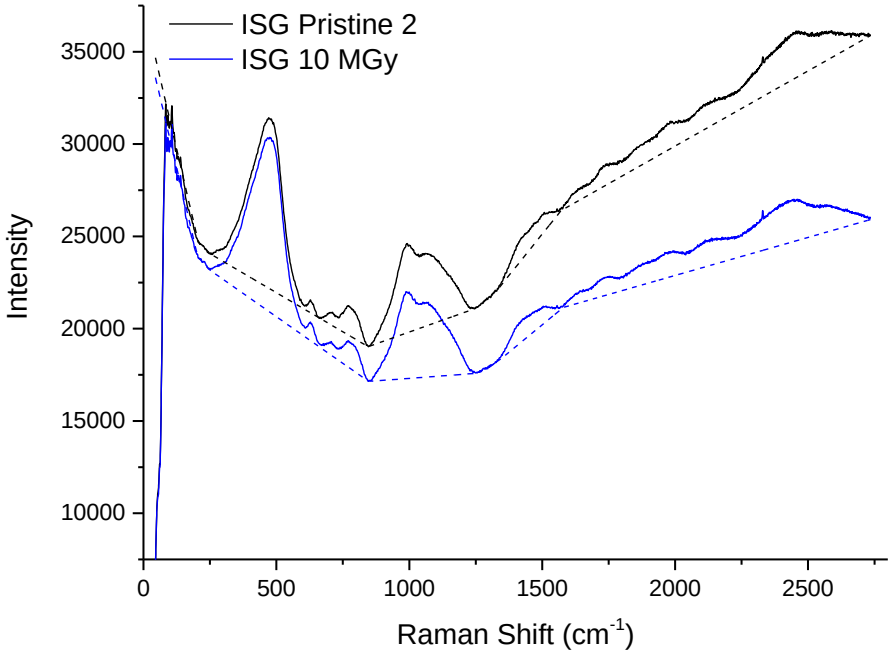


*Figure s 40 Raw Raman spectra of pristine and irradiated ISG Glass carried out at standard magnification settings, with baseline applied shown as dashed line.*

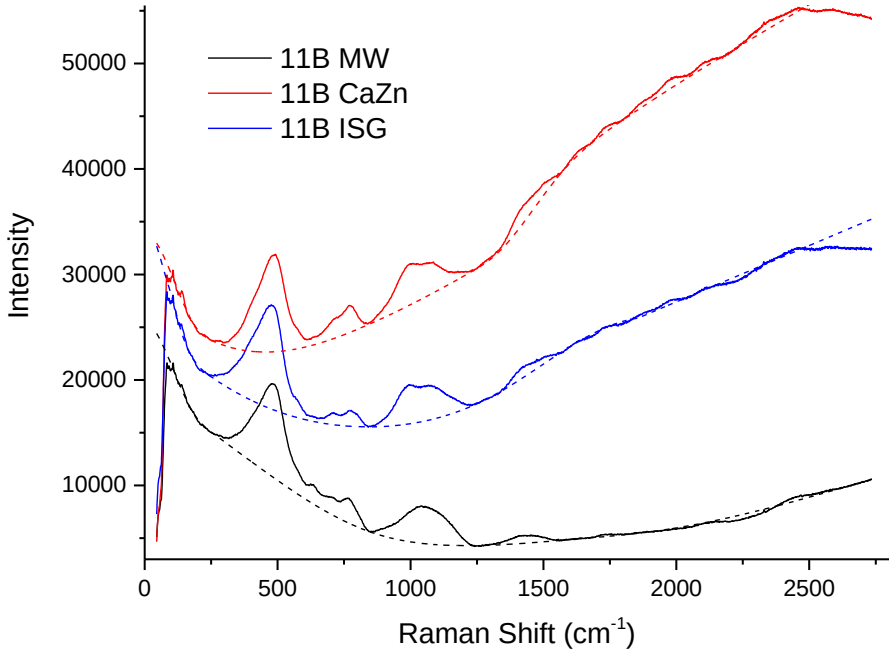


*Figure s 41 Raw Raman spectra of glass prepared with $^{11}B$ isotopically enriched boric acid, with baseline applied shown as dashed line.*